Ph. D. Thesis

Research on a pure spin current source using YPtBi topological semimetal and its device applications

Takanori Shirokura

Supervisor: Associate Professor Pham Nam Hai

Department of Electrical and Electronic Engineering

Tokyo Institute of Technology

Thesis Defense Committee:

Associate Professor Pham Nam Hai (Chair)

Professor Shigeki Nakagawa

Professor Takaaki Manaka

Professor Akira Yamada

Professor Masaaki Tanaka

Associate Professor Shinsuke Miyajima

Abstract

Topological materials, such as topological insulators (TIs), have great potential for ultralow power spin-orbit torque (SOT) spintronic devices thanks to their giant spin Hall effect (SHE) originated from their topological surface states (TSSs). However, the giant spin Hall angle ($\theta_{SH} > 1$) is limited to a few chalcogenide-based TIs with toxic elements and low melting points, making them challenging for device integration during the silicon Back-End-of-Line (BEOL) process. In this thesis, we have focused on a half-Heusler alloy topological semimetal (HHA-TSM), YPtBi, and evaluated the SHE in YPtBi, to overcome this difficulty.

In Chapters 1 and 2, we introduce the background and fundamental physics for spin Hall and ferromagnetic materials. These fundamental phenomena, especially, the Berry phase effects play important roles in this thesis.

In Chapter 3, we propose a generalized angle-resolved second harmonic technique to disentangle the magneto thermoelectric effects and SOT effective fields even in strong perpendicular magnetic anisotropy systems, which is used to precisely evaluate the SHE in YPtBi.

In Chapter 4, we evaluate the SHE in the YPt alloy which is one of the components of YPtBi. Although the SHE in the YPt alloy has the intrinsic contribution, the maximum value of θ_{SH} was 0.08 despite its higher resistivity than that of Pt. This result highlights the importance of the contribution of TSS in YPtBi to the giant SHE.

In Chapter 5, we synthesize YPtBi thin films by using co-sputtering at various substrate temperatures. According to the X-ray diffraction and X-ray fluorescence measurements, YPtBi thin films are stable up to 600^{o}C which is high enough for BEOL process. To evaluate the SHE of YPtBi, we conduct the second harmonic measurement in

CoPt/YPtBi heterostructures. By tuning the electric conductivity of YPtBi and the spin transparency at the CoPt/YPtBi interface, we successfully realize a giant θ_{SH} up to 4.1, which is much higher than those of each element of YPtBi or their non-topological alloys. We find that θ_{SH} is inversely proportional to conductivity which can be explained by the intrinsic mechanism of the SHE. Furthermore, θ_{SH} disappears when YPtBi thickness is 4 nm, indicating that the SHE is governed by TSS, which disappears below 4 nm due to interference of the top and bottom TSS, as well known in other TIs. We then demonstrate SOT magnetization switching in the CoPt/YPtBi heterostructures. Thanks to the giant SHE originated from TSS, a small threshold current density of about 1×10^6 A/cm^2 is observed, which is one order magnitude smaller than that in heavy metals.

In Chapter 6, we evaluate the stoichiometry effect on the SHE in YPtBi. To understand the stoichiometry effect, we investigate the SHE while changing the composition ratio of Y/Pt from 0.5 to 1.9. We find that the θ_{SH} – conductivity relationship is similar to that observed in samples with exact stoichiometry, indicating that the SHE in YPtBi is robust against the change of its stoichiometry.

In Chapter 7, we investigate the SHE in YPtBi grown at low temperature. Although we observe the giant SHE in YPtBi in Chapters 5 and 6, the growth temperature was 600ºC, which was too high for BEOL process. To realize the giant SHE even at low temperature growth, we deposit YPtBi down to 300ºC using low Ar pressure. We then successfully obtain a giant θ_{SH} up to 8.2 by recovering the spin transparency at the CoPt/YPtBi interface and demonstrate efficient SOT magnetization switching by ultralow current density of ~10^5 A/cm^2 in YPtBi grown at 300°C with the Ar gas pressure of 1 Pa.

In Chapter 8, we investigate the SHE in YPtBi grown on SiO_2/Si substrates. We demonstrate high SOT performance of sputtered YPtBi films grown on SiO_2/Si substrates

using buffer layers. We find that a 1 nm-thick Ta buffer layer realizes high quality YPtBi with large θ_{SH} of 1.3 and high conductivity of 1.4×10^5 $\Omega^{-1}m^{-1}$, which is comparable to the most conductive topological insulator BiSb grown on SiO_2/Si substrate.

In Chapter 9, we theoretically propose a bias-field-free spin Hall oscillator (SHO). We find the oscillation condition with no bias-field, and derive analytical solutions for typical parameters such as oscillation frequency, driving current, and so on, which are useful to design bias-field-free SHOs. We also confirm that YPtBi can effectively reduce the driving current for the proposed bias-field-free SHOs.

In chapter 10, we summarize the achievements in this thesis. Our work opens the door to the next generation spintronic devices with YPtBi having both giant θ_{SH} and high thermal stability.

List of abbreviations

GMR	giant magnetoresistance
TMR	tunnel magnetoresistance
AMR	anisotropic magnetoresistance
STT	spin transfer torque
SOT	spin orbit torque
SHE	spin Hall effect
MTJ	magnetic tunnel junction
MRAM	magnetoresistive random access memory
RM	racetrack memory
SRAM	static random access memory
DRAM	dynamic random access memory
SSD	solid state drive
BEOL	back-end-of-line
PMA	perpendicular magnetic anisotropy
IMA	in-plane magnetic anisotropy
IPP	in-plane precession
OPP	out-of-plane precession
HM	heavy metal
TI	topological insulator
TSS	topological surface state
HHA-TSM	half-Heusler alloy-topological semimetal
ARPES	angle resolved photoemission spectroscopy
DOS	density of state

PHE	planar Hall effect
AHE	anomalous Hall effect
ONE	ordinary Nernst effect
ANE	anomalous Nernst effect
SSE	spin Seebeck effect
AC	alternative current
DC	direct current
XRD	X-ray diffraction
XRR	X-ray reflectivity
XRF	X-ray fluorescence spectrometry
TEM	transmission electron microscopy
SQUID	superconducting quantum interference device
AFM	atomic force microscopy

List of symbols

$\hbar$	Dirac constant
e	electron charge
P	spin polarization
M_{S}	saturation magnetization
J_{X}	charge current density for X layer
ρ_{X}	resistivity for X layer
σ_{X}	conductivity for X layer
t_{X}	thickness for X layer
λ_{S}	spin relaxation length
θ_{H}	polar angle for external magnetic field
ϕ_{H}	azimuth angle for external magnetic field
θ_{SH}	spin Hall angle
$\theta_{\mathrm{SH}}^{\mathrm{eff}}$	effective spin Hall angle
$\sigma_{\mathrm{SH}}^{\mathrm{eff}}$	effective spin Hall conductivity
R_{xy}^{ω}	first harmonic resistance
$R_{xy}^{2\omega}$	second harmonic resistance
R_{AHE}	anomalous Hall resistance
R_{PHE}	planar Hall resistance
H_{ext}	external magnetic field
$H_{\mathrm{k}}^{\mathrm{eff}}$	effective magnetic anisotropy field
$H_{\mathrm{FL+OF}}$	sum of the field-like SOT effective field and Oersted field
H_{DL}	damping-like SOT effective field
$\alpha_{\mathrm{ONE}}^{\mathrm{out}}$	ONE caused by a temperature gradient along the z-direction

α_{ONE}	ONE caused by a temperature gradient along the *z*-direction
$\alpha_{\mathrm{ONE}}^{\mathrm{in}}$	ONE caused by a temperature gradient along the *x*-direction
$R_{\mathrm{ANE+SSE}}^{\mathrm{out}}$	ANE/SSE caused by a temperature gradient along the *z*-direction
$R_{\mathrm{ANE+SSE}}$	ANE/SSE caused by a temperature gradient along the *z*-direction
$R_{\mathrm{ANE+SSE}}^{\mathrm{in}}$	ANE/SSE caused by a temperature gradient along the *x*-direction
$J_{\mathrm{th}}^{\mathrm{YPtBi}}$	threshold current density for YPtBi layer
$J_{\mathrm{th0}}^{\mathrm{YPtBi}}$	threshold current density for YPtBi layer at 0 K
Δ	thermal stability factor
$1/\tau_0$	attempt frequency associated with precession of magnetization

Chapter 1. Introduction

In this chapter, we present a brief overview of spintronics. We also explain the concept and generation method for a spin current which plays an important role in manipulation of magnetization in spintronic devices. After that, we explain typical spintronic devices: a magnetoresistive random access memory, racetrack memory, and spin torque oscillator. Finally, we introduce the motivation and outline of this work.

1.1 Spintronics

Spintronics is one of the hottest research fields which uses both charge and spin degrees of freedoms of electrons to realize high performance devices with unique functionality. Electrons can transport both charge and spin with their motions. However, the electron's spin direction is preserved within a spin relaxation length because it is easily affected by some phenomena such as spin orbit interactions and magnon scattering, while the charge degree of freedom is robust against any scattering. Here, the typical value of the spin relaxation length is ranging from few nm to few μm even in high quality crystals, and thus, it had been very challenging to evaluate spin transports by experimental approaches.

At the end of the 20th century, researchers became able to access spin transport phenomena thanks to the improvement of device fabrication and growth technology, so called the nano technology. Starting with the discovery of the anisotropic magnetoresistance (AMR) effect,[1,2] variety of magnetoresistances such as the tunnel magnetoresistance (TMR) effect[3] have been discovered. Especially, the discovery of the giant magnetoresistance (GMR) effect[4] made a big impact on research on spin

transport properties of conduction electrons, and then, spintronics became one of the hottest research fields in nanotechnology. Because these effects can convert magnetic information into an electric signal, they have been applied to sensing applications such as magnetic sensors, magnetic heads for hard disk drives, and so on.

The conduction electron's spin can be used for not only sensing but also magnetization manipulation. A spin current which is a flow of electrons' spin angular momentum can exert torque on magnetization of a magnetic layer via the conservation of angular momentum between conduction and localized electrons.[5,6] After the discovery of spin current, it has been studied intensively from not only academic but also industrial sides because spin current can manipulate magnetization with lower power comparing with an external Oersted field. Therefore, it is expected that the research field on spintronics can be significantly expanded by utilizing spin current, motivated by realization of ultra-low power consumption applications, in addition to interesting physical phenomena provided by the combination of the charge and spin degrees of freedoms.

1.2 Generation method of spin current

The spin current is a transport phenomenon of a spin angular momentum of conduction electrons. As mentioned in Section 1.1, conduction electrons have both the charge and spin degree of freedoms, and thus, we can define the electron flow with up-spin and down-spin, respectively. Under the time reversal operation, both velocity and spin direction are flipped. Because the charge current changes the sign under the time reversal operation, the charge current density J_C should be defined as,

$$J_C = J_\uparrow + J_\downarrow,$$

where $J_{\uparrow}$ and $J_{\downarrow}$ are the current density for up and down spins, respectively. On the other hand, because the spin current is a quantity with the time reversal invariant, the spin current density J_S should be defined as,

$$J_S = J_{\uparrow} - J_{\downarrow}.$$

Here, one can see that non-zero J_S with zero J_C can be realized when $J_{\uparrow} = -J_{\downarrow}$. Such a spin current with no charge current is called the pure spin current, while that with a charge current is called the spin polarized current.

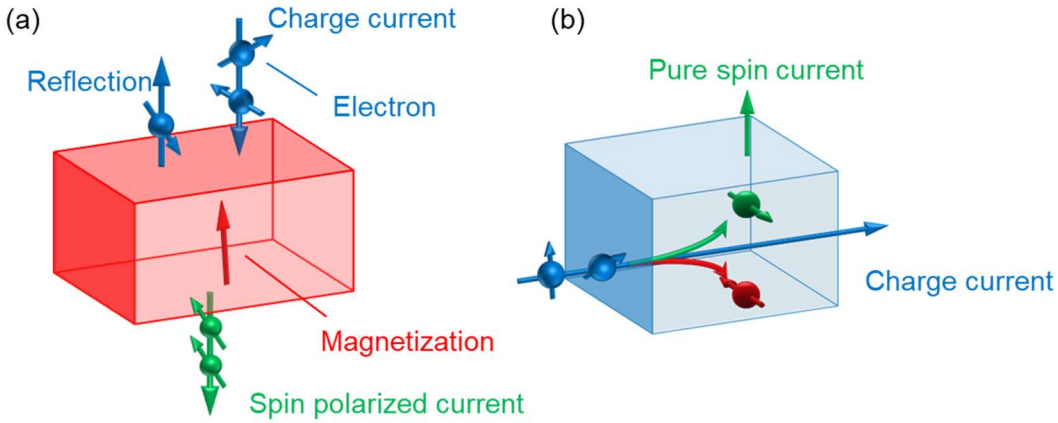

Figure 1.1. Schematic illustration of spin current originated from (a) the spin filtering effect, and (b) spin Hall effect.

The spin polarized current is generally generated by using the spin filtering effect in ferromagnetic materials. Figure 1.1(a) shows a schematic image of the spin filtering effect.[7] When a charge current is injected into a ferromagnetic material, some conduction electrons pass through the interface of the ferromagnetic material and the others are reflected on there. Here, the reflection probability depends on the relative direction between the spin direction of conduction electrons and magnetization in the ferromagnetic material. Because a conduction electron's spin

parallel to the majority spin in the ferromagnetic material has a higher transmittance, the current passing through the ferromagnetic material becomes spin polarized along the magnetization direction. The charge-to-spin conversion efficiency is determined by the spin polarization P, and J_S is given by,

$$J_S = \frac{\hbar}{2e} P J_C,$$

where $\hbar$ is the Dirac constant and e is the electron charge. This mechanism is utilized to generate the spin transfer torque (STT),[5,6] and widely used for magnetization manipulation in commercial magnetoresistive random access memory (MRAM).[8] However, the spin filtering effect requires a large charge current because P is typically 0.6 ~ 0.7 and cannot exceed unity, leading to high power consumption for magnetization manipulation, low bit density due to large size of drive transistors, and risk of device breakdown.

On the other hand, the pure spin current can be generated by using the spin Hall effect (SHE) in non-magnetic materials.[9] Figure 1.1(b) shows a schematic image of the SHE. When a charge current is injected into a non-magnetic material, conduction electrons are deflected by an effective field originated from the spin orbit interaction, and get an anomalous velocity depending on their spin direction. Here, the relationship between the spin angular momentum $\boldsymbol{\sigma}$, wavenumber vector for the charge current $\boldsymbol{k}$, and that for the bending direction $\boldsymbol{k}$' is given by,[9]

$$\boldsymbol{\sigma} \propto \boldsymbol{k} \times \boldsymbol{k}',$$

which means that the pure spin current generated by the SHE is orthogonal to the charge current. When a ferromagnetic layer is attached to a non-magnetic layer, the spin accumulated on the interface caused by the SHE diffuses into the adjacent ferromagnetic layer and generates a spin orbit torque (SOT).[10,11]

The strength of the SHE is denoted by a spin Hall angle θ_{SH}, which defines the relationship between J_S and J_C as,

$$J_S = \frac{\hbar}{2e}\theta_{SH} J_C.$$

Because the spin and charge currents are orthogonal to each other, one can obtain the relationship between the spin current I_S and the charge current I_C,

$$I_S = \frac{\hbar}{2e}\theta_{SH}\frac{S_S}{S_C} I_C,$$

where S_S and S_C are the cross-sectional area for the spin and charge currents, respectively. In generally, S_S is the contact area between the non-magnetic material and adjacent ferromagnetic layers, and S_C is the cross-sectional area of the non-magnetic material, and thus the structure factor S_S/S_C is typically 5 ~ 10 in spintronic applications. This structure factor makes it easier to reduce the drive current than that in the case of the spin filtering effect whose spin and charge current directions are same. This is one of the reasons why the pure spin current generated by the SHE has attracted much attention for low power consumption spintronic devices in recent years.

To improve the charge-to-spin conversion efficiency in the SHE, it is essential to explore spin Hall materials with large θ_{SH}. Because the SHE is originated from the spin orbit interaction, large θ_{SH} has been reported in materials with strong spin orbit interaction such as heavy metals (HMs)[12-17] and topological materials,[18-22] as shown in Figure 1.2. From the viewpoint of the charge-to-spin conversion efficiency including the structure factor, θ_{SH} of ~ 0.1 in HMs corresponds to a similar or slightly higher value than P, whereas $\theta_{SH} > 1$ in topological materials is 1 ~ 2 orders magnitude higher than that. Therefore, $\theta_{SH} \sim 1$ is a critical value for spintronic

applications with low power consumption, high bit density, and high endurance.

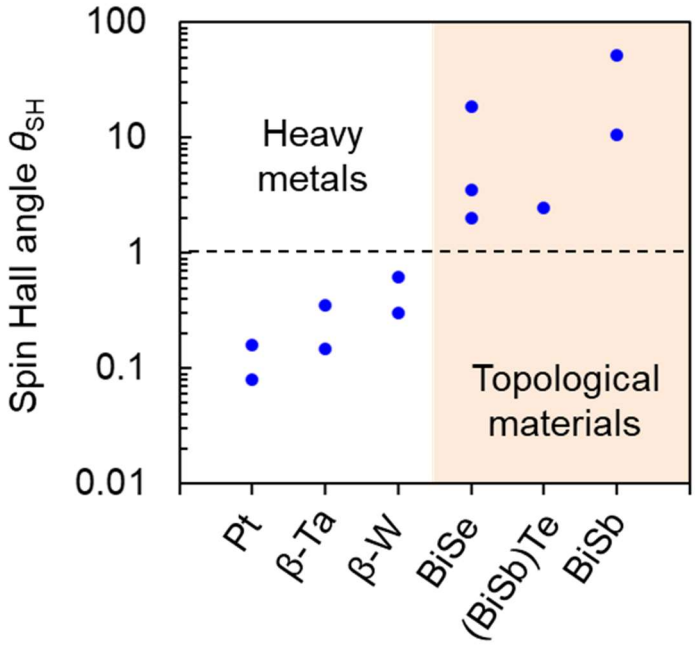

Figure 1.2. Benchmark of spin Hall angle in heavy metals and topological materials at room temperature.[12-22]

1.3 Spintronic devices

1.3.1 Magnetoresistive random access memory

MRAM is one of the most promising emerging non-volatile memories with fast writing and reading speed. The main structure of MRAM is a magnetic tunnel junction (MTJ) which is a sandwich of an insulator by two ferromagnetic (FM) layers. Because each FM layer has different strength of magnetic anisotropy, their magnetization does not flip simultaneously when an external magnetic field or spin current is applied. Here, the magnetic layer with smaller magnetic anisotropy is called the free layer, and the other one with stronger magnetic anisotropy is called the pinned layer.

When a voltage is applied to a MTJ structure, a quantum tunneling current flows because the insulating layer is very thin (~ 1 nm). Then, the resistance of the MTJ is determined by the relative direction of magnetization in both FM layers owning to the TMR effect. Because the magnetization direction in the pinned layer does not change, the resistance of the MTJ device only depends on the magnetization direction of the free layer, indicating that one can read out the magnetization direction in the free layer via the MTJ resistance. Furthermore, the magnetization direction in the free layer can be controlled by an external magnetic field or spin current. Therefore, the MTJ device can work as a memory device, where data is saved as the magnetization direction of the free layer.

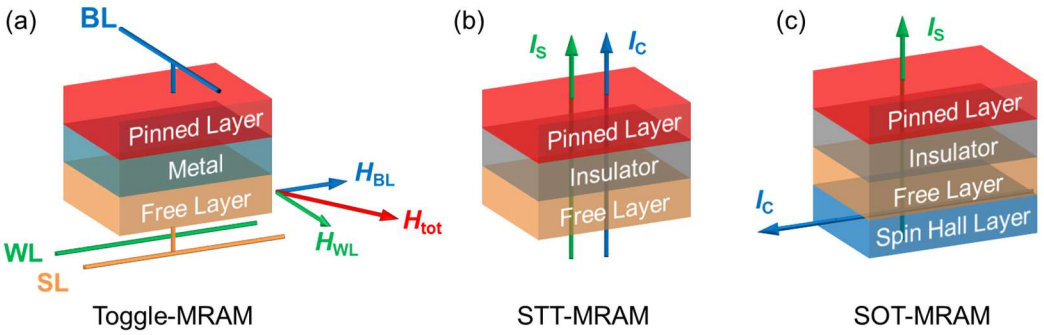

Figure 1.3. Schematic illustration of 1st – 3rd generation MRAMs so called (a) toggle-MRAM, (b) STT-MRAM, and (c) SOT-MRAM, respectively. Here, BL, WL, and SL in (b) are bit, word, and source lines, respectively.

MRAM is classified into three generations by magnetization control methods. Figure 1.3 shows schematic illustrations of MRAMs in each generation. The 1st generation MRAM, so called toggle-MRAM, utilizes an external magnetic field to manipulate magnetization.[23] To manipulate the magnetization in the free layer, currents are applied to both a bit line and word line. Because the magnitude of

synthetic magnetic field H_{tot} is maximized at the cross point of both lines, one can select the device and control its magnetization. However, toggle-MRAM has some disadvantages such as a large writing current and bad device scaling.

The 2nd generation MRAM is STT-MRAM which utilizes a spin polarized current generated by the spin filtering effect in the pinned layer to manipulate the magnetization in the free layer.[24] Because a torque working on magnetization is determined by a spin current "density", STT-MRAM has good device scaling capability. However, STT-MRAM also requires large drive current due to small charge-to-spin conversion efficiency of the spin filtering effect, resulting in high writing power consumption than that of volatile static random access memory (SRAM). Besides, such a large driving current results in low endurance because a large tunneling current may degrade the insulating layer in a MTJ device.

To overcome these problems, the 3rd generation MRAM, so called SOT-MRAM, has attracted much attention.[10,11] SOT-MRAM can manipulate magnetization with smaller driving current than STT-MRAM, because SOT-MRAM utilizes a pure spin current generated by the SHE which has higher charge-to-spin conversion efficiency than that of the spin filtering effect. Furthermore, SOT-MRAM can effectively reduce the power consumption for a magnetization switching because the switching speed is 10 – 100 times faster than STT-MRAM.

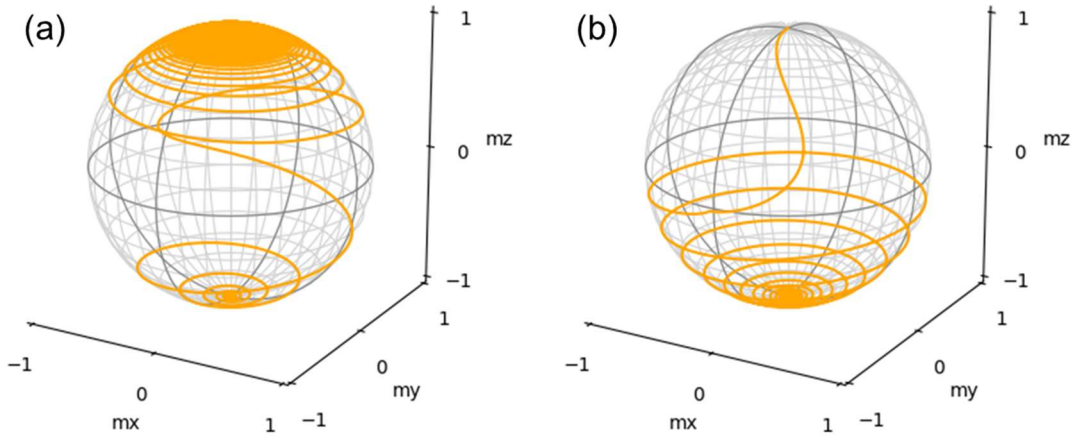

Figure 1.4. Magnetization trajectory of switching by (a) STT, and (b) SOT mechanisms, where orange curves show the time evolution of magnetization motion. Magnetizations are switched from +z- to -z-directions.

Figure 1.4 shows the comparison of magnetization switching trajectory in STT and SOT mechanisms. In case of the STT mechanism, long switching time is required due to a small initial torque which is given by cross product of the magnetization vector in the free layer and the spin polarization vector of spin current whose direction is same as the magnetization direction of the pinned layer. Because those vectors are nearly parallel or anti-parallel, the initial torque is small, and thus, magnetization switching takes on the order of 10 ns. On the other hand, the SOT mechanism can switch the magnetization by the order of 0.1 – 1 ns thanks to the maximized initial torque, because the spin polarization vector can be set orthogonal to the magnetization vector of the free layer.

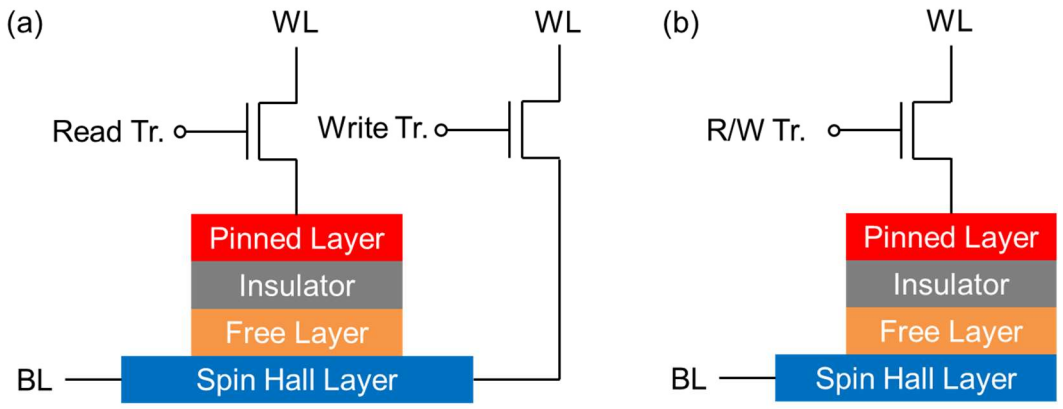

Figure 1.5. Schematic illustration of SOT-MARM with (a) two driving transistors, and (b) one transistor, where BL, WL, and Tr. denote a bit line, word line, and transistor, respectively.

Because the SHE requires an in-plane charge current for spin current generation, two transistors, one for reading and the other for writing, are required for SOT-MRAM as shown in Figure 1.5(a), whereas STT-MRAM uses only one transistor. Although such a separation of reading and writing paths improves the endurance because a writing current, which is larger than a reading current, does not pass through the insulating layer of the MTJ device, this is not suitable for improving bit density. For high bit density, one transistor driven SOT-MRAM is proposed, as shown in Figure 1.5(b).[25] Even though this type can realize high bit density, a writing current may degrade the insulating layer if the writing current is not small enough. Therefore, selecting a spin Hall material with large θ_{SH} is the key point to realize both high bit density and high endurance at the same time.

Table 1.1. Comparison of area, write energy, write time, read energy, read time, and standby power for SRAM, DRAM, STT- and SOT-MRAMs. Here, $Au_{25}Pt_{75}$ is assumed for the spin Hall material of SOT-MRAM.[26,27]

	SRAM	DRAM	STT-MRAM	SOT-MRAM
Area (F^2)	120	6	16	20
E_{Write} (fJ)	26.36	~1000	357.22	15.13
t_{Write} (ns)	0.15	~10	3.80	1.39
E_{Read} (fJ)	4.93	~1000	6.15	3.22
t_{Read} (ns)	0.11	~10	0.37	0.32
$P_{Standby}$ (W)	$\sim 1\times10^{-5}$	$\sim 1\times10^{-1}$	N/A	N/A

Finally, we compare the performance of MRAM and other conventional memories, SRAM[26] and dynamic random access memory (DRAM).[27] Table 1.1 shows comparison of performance of these memories. In this table, $Au_{25}Pt_{75}$ (θ_{SH} = 0.35, conductivity = 1.2×10^6 $\Omega^{-1}m^{-1}$) is assumed for the spin Hall material of SOT-MRAM.[26,28] MRAMs have advantages of smaller cell size and no standby power comparing with SRAM. However, large write current and write energy for STT-MRAM significantly degrade its reliability and offset its advantage of non-volatility. Therefore, SOT-MRAM is suitable for post-SRAM thanks to its comparable writing energy with that of SRAM. Note that, the writing energy and write time can be reduced by improving the performance of the spin Hall material, and thus, SOT-MRAM has a potential to perfectly surpass the performance of SRAM. On the other hand, MRAMs show smaller power consumptions by comparing with those for DRAM including standby power. However, small cell size for DRAM is a strong advantage from the viewpoint of bit density and cost. Therefore, development of new

technologies such as the two-terminal SOT-MRAM, X-point technique, reactive ion etching for ferromagnetic layers are required to replace DRAM by MRAMs.

1.3.2 Racetrack memory

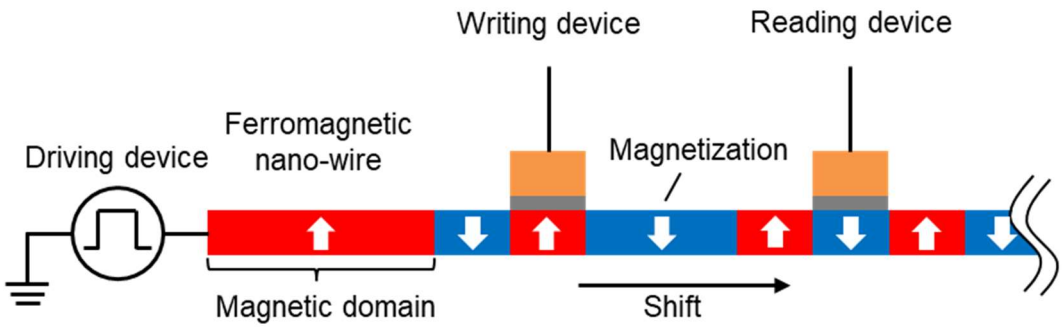

Figure 1.6. Schematic illustration of racetrack memory.

Racetrack memory (RM) is a kind of shift register which utilizes domain wall motion in a ferromagnetic nanowire, originally proposed by S. S. P. Parkin.[29] Figure 1.6 shows a schematic illustration of RM. RM is basically composed of four parts, a ferromagnetic nanowire, driving device (pulse current generator) for domain wall motion, MTJ-based writing device, and MTJ-based reading device. Here, one bit corresponds to the minimum magnetic domain in a ferromagnetic nanowire, and it can be moved along the wire via domain wall motion. Because RM requests only two transistors for writing and reading to handle the whole data in a ferromagnetic nanowire, RM is a promising candidate for next generation non-volatile memory with low cost and high bit density, especially substitution of the three dimensional (3D) NAND flash based solid state drive (SSD).

Table 1.2. Comparison of performance for 3D-NAND Flash, 2D-, and 3D-RMs.

	3D-NAND flash	2D-RM	3D-RM
Bit density	10 Gbit/mm^2	1 ~ 10 Gbit/mm^2	10 ~ 100 Gbit/mm^2
Write time	100 μs	1 ~ 100 ns	1 ~ 100 ns
Read time	10 μs	5 ~ 100 ns	5 ~ 100 ns
Endurance	10^3 ~ 10^5	10^{15}	10^{15}

RM has two types of structure, one is 2D type and the other is 3D type.[29] In the case of 2D-RM, a ferromagnetic nanowire is deposited a flat substrate. Because this structure is easy to fabricate by current technologies, numerous research on RM has been focused on 2D-RM. On the other hand, ferromagnetic nanowires for 3D-RM must be deposited on the side wall of holes with high aspect ratio. 3D-RM can realize higher bit density than that for 2D-RM although deposition process of vertical ferromagnetic nanowires is still challenging. Table 1.2 shows comparison of performance for 3D-NAND flash, 2D-RM, and 3D-RM. Here, we assumed the aspect ratio of 100 for the calculation of bit density for 3D-RM. When we assume a standard value of 10 – 100 nm for the magnetic domain size in ferromagnetic nanowires, 2D- and 3D-RMs can realize the same or higher order bit density comparing with 3D-NAND flash. Furthermore, the bit density easily improves by at least one order of magnitude by using skyrmion which is a special chiral magnetic domain structure in the strong Dzyaloshinsky-Moriya interaction system.[30] Furthermore, RM can reduce the write time by 3 ~ 5 orders of magnitude compared to 3D-NAND flash by using the SOT mechanism, although this comparison include uncertainty due to domain movement time. Read time for RM also can be reduced by 2 ~ 4 orders of magnitude

compared to 3D-NAND flash by using the TMR effect. These times for RM are single bit read/write times, not random access properties which is much more important for actual working time when we construct a circular RM.[31] Here, access time is 10 – 100 ns even in a 10 μm-long ferromagnetic nanowire because a magnetic domain wall can be driven at 100 – 1000 m/s.[32] These results indicate that RM is expected to play an important role as a new high-speed nonvolatile memory alternative to SSD. In particular, RM having high speed and high reliability can be realized by using SOT mechanism which is superior to STT mechanism in terms of write speed and write power consumption.

1.3.3 Spin torque oscillator

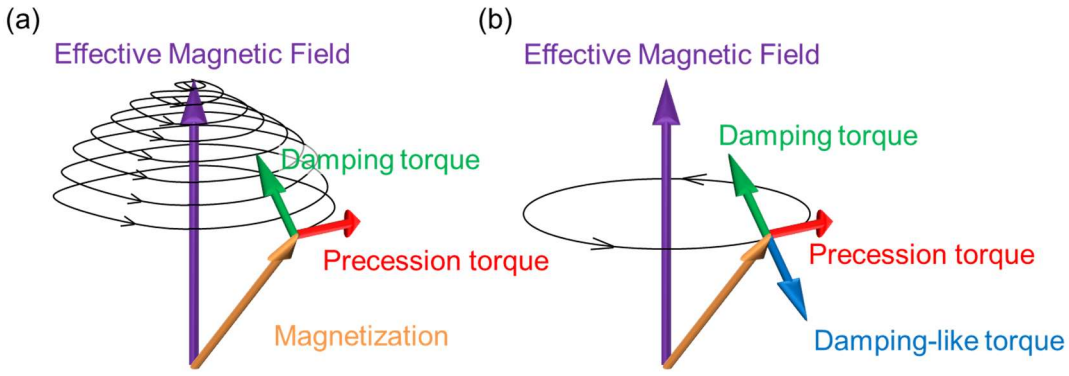

Figure 1.7. Schematic image of magnetization motion under an effective magnetic field (a) without, and (b) with a damping-like torque caused by a spin current.

A spin torque oscillator (STO) is a microwave oscillator which utilizes precession motion of magnetization in a ferromagnetic layer. When an effective magnetic field is applied, the magnetization moves to align to the effective magnetic field to reduce its magnetic energy, where the effective magnetic field is defined by the gradient of magnetic energy against the magnetization direction. At the same time,

the magnetization processes with a high precession frequency of several GHz to few THz, as shown in Figure 1.7(a). Although this precession stops when the magnetization perfectly aligns to the effective magnetic field, one can obtain a sustainable precession by applying a spin torque which cancels out the damping torque, as shown in Figure 1.7(b). This sustainable high frequency oscillation can be extracted as a microwave via dipole emission or voltage signal generated by the GMR or TMR effects, and thus, a ferromagnetic layer can work as a microwave oscillator.

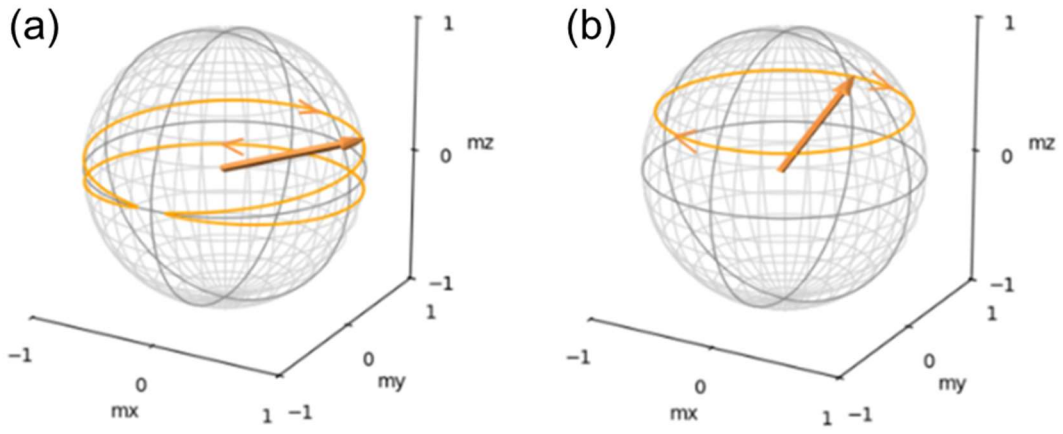

Figure 1.8. Schematic illustration of typical precession trajectory of a magnetization with (a) in-plane precession mode, and (b) out-of-plane precession mode, where the orange arrows and lines indicate the magnetization and oscillation trajectory, respectively.

A prototype of STO was proposed by S. I. Kiselev, *et al.* in 2003.[33] Their STO is driven by STT with in-plane spin polarization generated in Co/Cu GMR multi-stacks. Figure 1.8(a) shows the schematic illustration of their typical trajectory of the magnetization. This precession mode is so called the in-plane precession (IPP) mode because the magnetization continuously goes left and right in the *xy*-plane. They successfully demonstrated ~10 GHz oscillation and high tunability of the oscillation

frequency, controlled by a driving current and an external magnetic field applied opposite to the spin polarization direction. However, their STO did not work at zero-bias field because the magnetization is switched along its spin polarization direction without a bias field. To obtain effective oscillation with no-bias field, STO driven by STT with out-of-plane spin polarization was proposed.[34] In this proposal, a demagnetization field plays the same role as the external magnetic field in the IPP-STO case. In this case, the magnetization can continuously precess around the *z*-axis without a bias field, as shown in Figure 1.8(b). This precession mode is called the out-of-plane precession (OPP) mode, and bias-field-free oscillation in OPP-STOs has been successfully demonstrated.[35] Now, it is recognized that STOs are promising for high frequency communication and microwave assisted magnetic recording because STOs have high oscillation frequency with high quality factor and work even in small device size (nano-meter size). Note that STOs also work as a device for neuromorphic computing thanks to their non-linear output against input current.[36] These facts indicate that STOs can play important roles to internet of things (IoT) technology.

1.4 Motivation and thesis outline

In this chapter, we have explained the history of spintronics, the method for spin current generation, and examples of spintronic devices. We also have emphasized that SOT plays very important roles to realize spintronic devices with ultra-low power consumption. Because SOT is originated from the SHE whose strength is given by θ_{SH}, spin Hall materials with large θ_{SH} (> 1) is necessary to realize ultra-low power consumption spintronic devices. Currently, only few chalcogenide-based topological insulators (TIs) show such a large θ_{SH} thanks to their strong SHE

originated from their topological surface states (TSSs). However, applying TIs to spintronic devices is still challenging due to their toxic elements and poor thermal stability because they are composed of only V and VI group elements. Thus, research on SOT-based spintronic devices has been mainly focused on HMs thanks to their high affinity of silicon Back-End-of-Line (BEOL) process despite their small θ_{SH} of ~ 0.1.

The simple solution to realize ultra-low power consumption spintronic devices is development of a new class of topological materials having both large θ_{SH} and high affinity of BEOL process. Here, we focus on a half-Heusler alloy-topological semimetal (HHA-TSM).[37,38] Half-Heusler alloys consist of three kinds of element XYZ, and one can control the topology of their band structure by choosing the combination of X, Y, and Z without using toxic materials. Because their TSSs have been confirmed not only by first principle calculations but also by angle resolved photoemission spectroscopy (ARPES),[39-42] strong SHE originated from their TSSs is expected. Furthermore, higher thermal stability of HHA-TSM (> 600^{o}C) has been reported,[41] which satisfies with the requirements for BEOL process. Therefore, HHA-TSMs are promising candidates for a spin Hall material which combines the advantage of HMs and TIs. However, there is no report on their spin transport properties. In this thesis, we demonstrate a HHA-TSM, YPtBi, having the following features: “high thermal stability (> 400^{o}C)”, “large θ_{SH} (> 1)”, “toxic material free”, and “can be deposited by sputtering technique”, to pave the way for SOT-based ultra-low power spintronic devices. Then, we also investigate the performance of spintronic applications with YPtBi.

In Chapter 1 and Chapter 2, we introduce the background and fundamental spin

physic, respectively. These two chapters show that the SHE has novel potential for low power consumption spintronic devices and emphasize the importance of the Berry phase from topological surface states. In Chapter 3, we develop a new evaluation method of θ_{SH} for strong perpendicular magnetic anisotropy (PMA) system by considering the ordinary Nernst effect which plays an important role in topological materials. In Chapter 4, we investigate the SHE in a non-topological YPt alloy to clarify the importance of TSSs on the SHE by comparing with the result for YPtBi in following chapters. In Chapter 5, we deposit the topological semimetal YPtBi by using the sputtering technique and demonstrate its strong SHE via second harmonic measurement and current induced magnetization switching. In Chapter 6, we investigate the role of stoichiometry of Y and Pt on the SHE of YPtBi. In Chapter 7, we develop a low temperature growth method for sputtered YPtBi with maintained spin Hall properties. In Chapter 8, we investigate the SHE for sputtered YPtBi on SiO_2 / Si substrate to demonstrate the SHE performance in realistic spintronic devices. In Chapter 9, we propose a new class of STO driven by the SHE with no bias field and investigates its performance using sputtered YPtBi as the spin Hall layer. We conclude this work in Chapter 10.

1.5 References

[1] W. Thomson, Proc. R. Soc. Lond. **8**, 546 (1857).

[2] T. R. McGuire, and R. I. Potter, IEEE Trans. Magn. MAG-1, 1018 (1975).

[3] M. Julliere, Phys. Lett. A **54**, 225 (1975).

[4] M. N. Baibich, J. M. Broto, A. Fert, F. Nguyen Van Dau, F. Petroff, P. Etienne, G. Creuzet, A. Friederich, and J. Chazelas, Phys. Rev. Lett. **6**, 2472 (1988).

[5] J. C. Slonczewski, J. Magn. Magn. Mater. **159**, L1 (1996).

[6] L. Berger, Phys. Rev. B **54**, 9353 (1996).

[7] D. C. Ralph, and M. D. Stiles, J. Magn. Magn. Mater. **320**, 1190 (2008).

[8] S-W. Chung, T. Kishi, J. W. Park, M. Yoshikawa, K. S. Park, T. Nagase, K. Sunouchi, H. Kanaya, G. C. Kim, K. Noma, *et al*. 2016 IEEE IEDM 27.1.1–27.1.4 (2016).

[9] J. E. Hirsch, Phys. Rev. Lett. **83**, 1834 (1999).

[10] I. M. Miron, K. Garello, G. Gaudin, P-J. Zermatten, M. V. Costache, S. Auffret, S. Bandiera, B. Rodmacq, A. Schuhl, and P. Gambardella, *Nature* **476**, 189 (2011).

[11] L. Liu, O. J. Lee, T. J. Gudmundsen, D. C. Ralph, and R. A. Buhrman, Phys. Rev. Lett. **109**, 096602 (2012).

[12] L. Liu, T. Moriyama, D. C. Ralph and R. A. Buhrman, Phys. Rev. Lett. **106**, 036601 (2011).

[13] M.-H. Nguyen, D. C. Ralph and R. A. Buhrman, Phys. Rev. Lett. **116**, 126601 (2016).

[14] L. Liu, C-F. Pai, Y. Li, H. W. Tseng, D. C. Ralph, and R. A. Buhrman, *Science* **336**, 555 (2012).

[15] E. Sagasta, Y. Omori, S. Vélez, R. Llopis, C. Tollan, A. Chuvilin, L. E. Hueso, M. Gradhand, Y. Otani, and F. Casanova, Phys. Rev. B **98**, 060410(R) (2018).

[16] C.-F. Pai, L. Liu, Y. Li, H. W. Tseng, D. C. Ralph and R. A. Buhrman, Appl. Phys. Lett. **101**, 122404 (2012).

[17] Y. Takeuchi, C. Zhang, A. Okada, H. Sato, S. Fukami and H. Ohno, Appl. Phys. Lett. **112**, 192408 (2018).

[18] A. R. Mellnik, J. S. Lee, A. Richardella, J. L. Grab, P. J. Mintun, M. H. Fischer, A. Vaezi, A. Manchon, E.-A. Kim, N. Samarth and D. C. Ralph, Nature **511**, 449 (2014).

[19] M. DC, R. Grassi, J. Y. Chen, M. Jamali, D. R. Hickey, D. Zhang, Z. Zhao, H. Li, P.

Quarterman, Y. Lv, M. Li, A. Manchon, K. A. Mkhoyan, T. Low and J. P. Wang, Nat. Mater. **17**, 800 (2018).

[20] H. Wu, P. Zhang, P. Deng, Q. Lan, Q. Pan, S. A. Razavi, X. Che, L. Huang, B. Dai, K. Wong, X. Han and K. L. Wang, Phys. Rev. Lett. **123**, 207205 (2019).

[21] T. Fan, N. H. D. Khang, S. Nakano, and P. N. Hai, Sci. Rep. **12**, 2998 (2022).

[22] N. H. D. Khang, Y. Ueda and P. N. Hai, Nat. Mater. **17**, 808 (2018).

[23] S. Tehrani, J. M. Slaughter, M. Deherrera, B. N. Engel, N. D. Rizzo, J. Salter, M. Durlam, R. W. Dave, J. Janesky, B. Butcher, Proc. IEEE **91**, 703 (2003).

[24] Y. Higo, K. Yamane, K. Ohba, H. Narisawa, K. Bessho, M. Hosomi, and H. Kano, Appl. Phys. Lett. **87**, 082502 (2005).

[25] G. Yu, Nat. Electron. **1**, 496– 497 (2018).

[26] Y.-C. Liao, C. Pan and A. Naeemi, IEEE J. Explor. Solid-State Computat. **6**, 9 (2020).

[27] T. Schenk, M. Pesic, S. Slesazeck, U. Schroeder, and T. Mikolajick, Rep. Prog. Phys. **83**, 086501 (2020).

[28] L. Zhu, D. C. Ralph and R. A. Buhrman, Phys. Rev. Appl. **10**, 031001 (2018).

[29] S. S. P. PARKIN, M. Hayashi, and L. Thomas, Science **320**, 190 (2008).

[30] Y. Tokura, and N. Kanazawa, Chem. Rev. **121**, 2857 (2021).

[31] Y. Zhang, X. Zhang, J. Hu, J. Nan, Z. Zheng, Z. Zhang, Y. Zhang, N. Vernier, D. Ravelosona, and W. Zhao, Sci. Rep. **6**, 35062 (2016).

[32] K.J. Kim, S. K. Kim, Y. Hirata, S.-H. Oh, T. Tono, D.-H. Kim, T. Okuno, W. S. Ham, S. Kim, G. Go, Y. Tserkovnyak, *et al*. Nat. Mater. **16**, 1187 (2017).

[33] S. I. Kiselev, J. C. Sankey, I. N. Krivorotov, N. C. Emley, R. J. Schoelkopf, R. A. Buhrman, and D. C. Ralph, Nature **425**, 308 (2003).

[34] X. Zhu and J. G. Zhu, IEEE Trans. Magn. **42**, 2670 (2006).

[35] D. Houssameddine, U. Ebels, B. Delaet, B. Rodmacq, I. Firastrau, F. Ponthenier, M. Brunet, C. Thirion, J.-P. Michel, L. Perjbeanu-Buda, M.-C. Cyrille, O. Redon, and B. Dieny, Nat. Mater. **6**, 447 (2007).

[36] J. Torrejon, M. Riou, F. A. Araujo, S. Tsunegi, G. Khalsa, D. Querlioz, P. Bortolotti, V. Cros, K. Yakushiji, A. Fukushima, H. Kubota, S. Yuasa, M. D. Stiles, and J. Grollier, Nature **547**, 428 (2017).

[37] S. Chadov, X. Qi, J. Kübler, G. H. Fecher, C. Felser, and S. C. Zhang, Nat. Mater. **9**, 541-545 (2010).

[38] H. Lin, L. A. Wray, Y. Xia, S. Xu, S. Jia, R. J. Cava, A. Bansil, and M. Z. Hasan, Nat. Mater. **9**, 546-549 (2010).

[39] Z. K. Liu, L. X. Yang, S.-C. Wu, C. Shekhar, J. Jiang, H. F. Yang, Y. Zhang, S.-K. Mo, Z. Hussain, B. Yan, C. Felser, and Y. L. Chen, Nat. Commun. **7**, 12924 (2016).

[40] J. A. Logan, S. J. Patel, S. D. Harrington, C. M. Polley, B. D. Schultz, T. Balasubramanian, A. Janotti, A. Mikkelsen, and C. J. Palmstrøm, Nat. Commun. **7**, 11993 (2016).

[41] A. Kronenberg, J. Braun, J. Minár, H.-J. Elmers, D. Kutnyakhov, A. V. Zaporozhchenko, R. Wallauer, S. Chernov, K. Medjanik, G. Schönhense, M. Kläui, *et al.* Phys. Rev. B **94**, 161108(R) (2016).

[42] M. M. Hosen, G. Dhakal, K. Dimitri, H. Choi, F. Kabir, C. Sims, O. Pavlosiuk, P. Wiśniewski, T. Durakiewicz, J.-X. Zhu, D. Kaczorowski, and M. Neupane, Sci. Rep. **10**, 12343 (2020).

Chapter 2. Fundamental spin physics in spin Hall and ferromagnetic materials

2.1 Spin orbit interaction and its effect on band structure

In this section, we introduce the spin orbit interaction and its effect on the band structure. The spin orbit interaction, which is one of relativistic effects, converts a particle's momentum and spin angular momentum to each other. Because the spin orbit interaction is a relativistic effect, it is embedded in the Dirac equation naturally. However, our interest is the spin orbit interaction in the non-relativistic limit. To obtain the expression of the spin orbit interaction in the non-relativistic limit, we will begin with the time-independent Dirac equation,[1]

$$[c\boldsymbol{\alpha}\ \cdot(\hat{\boldsymbol{p}}+e\boldsymbol{A})+\beta m_0c^2+V]\psi=E\psi$$

$$\alpha_i=\begin{pmatrix}O & \sigma_i\\ \sigma_i & O\end{pmatrix},\qquad \beta=\begin{pmatrix}I & O\\ O & -I\end{pmatrix}$$

where c is the velocity of light, $\hat{\boldsymbol{p}}$ is the momentum operator, $\boldsymbol{A}$ is the vector potential, m_0 is the electron rest mass, V is a potential, E is an eigen energy, σ_i $(i=x,y,z)$ is the Pauli matrix, and I is a 2×2-unit matrix. Here, one can obtain following expression by substituting the relation $\psi=(\psi_{\mathrm{p}}\quad\psi_{\mathrm{ap}})$,

$$\begin{cases}\boldsymbol{\sigma}\cdot(\hat{\boldsymbol{p}}+e\boldsymbol{A})\psi_{\mathrm{ap}}=c^{-1}(E-m_0c^2-V)\psi_{\mathrm{p}}\\ \boldsymbol{\sigma}\cdot(\hat{\boldsymbol{p}}+e\boldsymbol{A})\psi_{\mathrm{p}}=c^{-1}(E+m_0c^2-V)\psi_{\mathrm{ap}}\end{cases}$$

where ψ_{p} and ψ_{ap} are wavefunctions for a particle and anti-particle, respectively. This simultaneous equation tells us that a particle and anti-particle are essentially mixed up together at relativistic limit. The wavefunction in the non-relativistic limit ψ_{nr} can be obtained by solving simultaneously the above equation to find ψ_{p} within the second order of v/c under the normalization condition $\langle\psi_{\mathrm{p}}|\psi_{\mathrm{p}}\rangle+$

$\langle \psi_{\mathrm{ap}} | \psi_{\mathrm{ap}} \rangle = 1$ because the kinetic energy of a particle is much smaller than the resting energy m_0c^2,

$$\psi_{\mathrm{nr}} = \left[1 + \frac{\hat{\boldsymbol{p}}^2 + e\hbar \boldsymbol{\sigma} \cdot \boldsymbol{B}}{8m_0^2c^2} \right] \psi_{\mathrm{p}}.$$

Then, the Dirac equation at the non-relativistic limit, so called the Pauli equation, can be obtained by substituting ψ_{nr} to the Dirac equation and re-approximating it within the second order of v/c,

$$\left[m_0c^2 + \frac{1}{2m_0}(\hat{\boldsymbol{p}} + e\boldsymbol{A})^2 + V + \frac{e\hbar}{4m_0^2c^2} \boldsymbol{\sigma} \cdot (\boldsymbol{\varepsilon} \times \hat{\boldsymbol{p}}) + \frac{e\hbar}{2m_0} \boldsymbol{\sigma} \cdot \boldsymbol{B} - \frac{\hat{\boldsymbol{p}}^4}{8m_0^3c^2} + \frac{e\hbar^2}{8m_0^2c^2} \nabla \cdot \boldsymbol{\varepsilon} \right] \psi_{\mathrm{nr}} = E\psi_{\mathrm{nr}}.$$

Here, the 4th term of the left-hand side in the Pauli equation corresponds to the spin orbit interaction. When a static electric field $\boldsymbol{\varepsilon}$ is given by a central electric field, one can see that the spin orbit interaction term is proportional to $\boldsymbol{\sigma} \cdot \boldsymbol{L}$, where $\boldsymbol{L}$ is the angular momentum of a particle, which is the reason why this term is called as the spin "orbit" interaction.

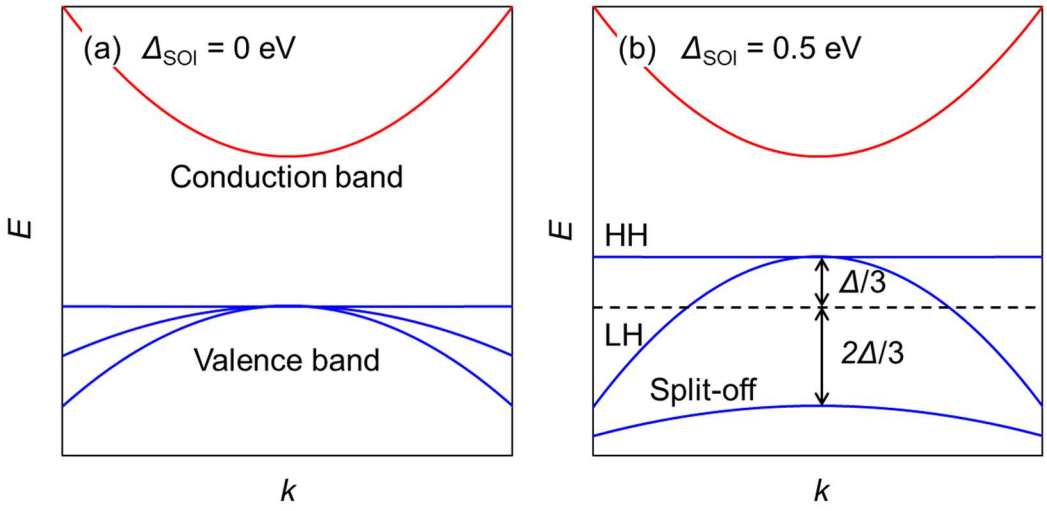

Figure 2.1. Schematic image of band structure around Γ-point calculated by $\boldsymbol{k} \cdot \boldsymbol{p}$ perturbation (a) without, and (b) with the spin orbit interaction whose strength is 0.5 eV.

As mentioned above, the relativistic effects including the spin orbit interaction originates from the mixing effect of a particle and anti-particle. In a vacuum system, the energy barrier between these particles is about m_0c^2 (~MeV), resulting in an ultimately small spin orbit interaction. Whereas the spin orbit interaction can be large in materials because the energy barrier between a particle (electron) and anti-particle (hole) is same scale as their band gap, and thus, it can affect their band structure. Figure 2.1 shows the schematic image of band structure calculated by a Bloch Hamiltonian with $\boldsymbol{k}\cdot\boldsymbol{p}$ perturbation with and without the spin orbit interaction, where HH and LH are heavy and light hole bands, respectively, and Δ_{SOI} is a strength of the spin orbit interaction.[2] The spin orbit interaction can lift up its valence band top as seen in Figure 2.1(b). Note that a part of the conduction band and valence band can be inverted when the spin orbit interaction is strong enough. Such a band inversion also flips the symmetry of wavefunction belonging to their bands, which plays a very important role to change a topological invariant for topological materials as discussed in the following sessions. Therefore, the spin orbit interaction can switch a material from topologically trivial to non-trivial.

2.2 Berry phase

A time evolution for a particle is expressed as a change of a phase for its wavefunction in quantum mechanics, indicating that understanding how a particle gets a phase is necessary to know the particle motion. In this section, we explain the Berry phase which is caused by a parameter change of a Hamiltonian. Now, we consider a Hamiltonian $\hat{H}$ which contains time dependent parameters $\boldsymbol{R}$. Then, the time dependent Schrödinger equation is given by,

$$i\hbar\partial_t|\psi(t)\rangle = \hat{H}[\boldsymbol{R}(t)]|\psi(t)\rangle.$$

If the time evolution of $\boldsymbol{R}$ is slower than the resonance frequency for the system, a n-th eigenstate will belong to same n-th eigenvalue, and then, the solution of the Schrödinger equation is given by,

$$|\psi(t)\rangle = \exp[i\theta(t)]\,|\psi_n[\boldsymbol{R}(t)]\rangle.$$

By substituting $|\psi(t)\rangle$ into the time dependent Schrödinger equation, one can obtain the following expression,

$$i\theta(t) = -\frac{i}{\hbar}\int_0^t dt'\,E_n[R(t')] - i\int_0^t dt'[-i\langle\psi_n[\boldsymbol{R}(t')]|\partial_{t'}|\psi_n[\boldsymbol{R}(t')]\rangle].$$

Here, the 1st term of the right-hand side is the dynamical phase which generally appears when one solves the time dependent Schrödinger equation. The 2nd term is so called the Berry phase which originated by the parameter change of the Hamiltonian.[3] It is now understood that the Berry phase plays an important role for a topological invariant in numerous systems such as a quantum Hall and electric dipole systems. By using a partial integration by t', one can obtain a time-independent expression,

$$\int_0^t dt'[-i\langle\psi_n[\boldsymbol{R}(t')]|\partial_{t'}|\psi_n[\boldsymbol{R}(t')]\rangle] = \int_{\boldsymbol{R}(0)}^{\boldsymbol{R}(t)} d\boldsymbol{R}'\cdot\boldsymbol{A_n}(\boldsymbol{R}'),$$

$$\boldsymbol{A_n}(\boldsymbol{R}') = -i\langle\psi_n(\boldsymbol{R}')|\partial_{\boldsymbol{R}'}|\psi_n(\boldsymbol{R}')\rangle.$$

where $\boldsymbol{A_n}$ is the Berry connection. Here, one can understand that the Berry phase originates from a curvature of a Hamiltonian in a $\boldsymbol{R}$-space because the Berry connection acting on a wavefunction as a covariant derivative has same role with the Riemann connection which reflects a curvature of real space. Although the Berry connection is an important quantity for quantum mechanics, it is not observable because it is not gauge invariant. Therefore, observable Berry phase is defined as a

contour integral of the Berry connection in a $\boldsymbol{R}$-space. Here, similar with the relationship between a magnetic flux density and vector potential, the Berry curvature given by,

$$\boldsymbol{B_n} = \nabla_{\boldsymbol{R}} \times \boldsymbol{A_n} = \sum_{m \neq n} \frac{\langle \psi_n(\boldsymbol{R}) | \partial_{\boldsymbol{R}} \hat{H} | \psi_m(\boldsymbol{R}) \rangle \times \langle \psi_m(\boldsymbol{R}) | \partial_{\boldsymbol{R}} \hat{H} | \psi_n(\boldsymbol{R}) \rangle}{i[E_n(\boldsymbol{R}) - E_m(\boldsymbol{R})]^2}$$

is also observable. The Berry curvature is the origin of the anomalous velocity, and it can be observed in many phenomena such as the anomalous and spin Hall effects.[4]

2.3 Topological insulator

In this section, we explain the fundamental physics of TI which is a foundation for topological materials. In mathematics, topology is one of the research fields which classifies a diagram by focusing on invariants against a mapping function. In condensed matter physics, a wave function is one of the mappings from the $\boldsymbol{k}$-space to the Hilbert space via Hamiltonian. Therefore, one can classify the materials from the viewpoint of the topology by considering the invariant of wave functions. In the following, we construct the expression of topological invariant for TIs.

The quantum Hall effect is one of the topological phenomena in condensed matter physics whose topological invariant is an electric dipole caused by adiabatic change of parameters for a Hamiltonian under the breaking of time reversal symmetry. It is now understood that the topological invariant for the quantum Hall system is the sum of the Berry phase for filled up states.[5] Similar to this, the topological invariant for TIs is also related to be the Berry phase for filled up states because TIs are superposition of the quantum Hall system with the time reversal symmetry. However, the Berry phase is not well-defined topological invariant under the time reversal

symmetry because wave functions forming a Kramers pair get the Berry phase with opposite sign to each other during the adiabatic cycle, as the result, the Berry phase in the system with the time reversal symmetry becomes always zero. To overcome this difficulty, L. Fu and C. L. Kane introduced the time reversal polarization which is defined by the difference of the Berry phase for a Kramers pair.[6] When we consider the 2D (*t*-axis and *k*-axis) 4 bands model for simplify, the time reversal polarization P_θ is given by,

$$\begin{aligned} P_\theta \equiv P_2 - P_1 &= -\int_{-\pi}^{\pi} \frac{dk}{2\pi} A_2 + \int_{-\pi}^{\pi} \frac{dk}{2\pi} A_1 \\ &= -\int_{-\pi}^{\pi} \frac{dk}{2\pi} (-i\langle u_{2,k}|\partial_k|u_{2,k}\rangle) + \int_{-\pi}^{\pi} \frac{dk}{2\pi} (-i\langle u_{1,k}|\partial_k|u_{1,k}\rangle), \end{aligned}$$

where $|u_{1,k}\rangle$ and $|u_{2,k}\rangle$ are wave functions which form the Kramers pair in the valence band. We then introduce the W matrix whose elements are given by the hopping integral via time reversal operator $\hat{\Theta}$ to deform P_θ,

$$P_\theta = \frac{1}{i\pi} \ln \left(\frac{\sqrt{w_{12}(0)^2}}{w_{12}(0)} \frac{w_{12}(\pi)}{\sqrt{w_{12}(\pi)^2}} \right),$$

$$w_{12} = \left\langle u_{1,-k} \middle| \hat{\Theta} \middle| u_{2,k} \right\rangle.$$

Here, we take a difference between P_θ defined at time reversal invariant (t = 0, T/2) to make P_θ gauge invariant by closing the adiabatic loop. Finally, we obtain the topological invariant ν for TIs,

$$\nu = P_\theta \left(\frac{T}{2} \right) - P_\theta(0) \bmod 2,$$

$$(-1)^\nu = \prod_{i=1}^{4} \frac{w_{12}(\Lambda_i)}{\sqrt{w_{12}(\Lambda_i)^2}},$$

where Λ_i is the time reversal invariant momenta (TRIM). The system becomes topologically non-trivial (topological insulator) when $\nu = 1$, and it becomes trivial (normal insulator) when $\nu = 0$. Here, ν should be defined by mod 2 because the

system with even number of differences of P_θ is equivalent to the initial system. One can define ν with *n* bands by using the result of 4 bands,

$$(-1)^\nu = \prod_{i=1}^{4} \frac{\mathrm{Pf}[w(\Lambda_i)]}{\sqrt{\det[w(\Lambda_i)]}}$$

where Pf denotes the Pfaffian. In 2D system, one topological invariant of ν is enough to classify the topology of band structure, whereas 4 topological invariants ν_0, ν_1, ν_2, and ν_3 are required in 3D system.[7] ν_0 is calculated by using w_{12} defined at all time reversal invariant momenta (TRIM) which are totally 8, while the others are calculated at 4 TRIM on each plane, and thus, ν_0 represents the topology of the whole crystal system (strong topological invariant) and the others represent the topology of each crystal plane (weak topological invariant).[7]

We have introduced the topological invariant in the general system with the time reversal symmetry. Here, the calculation of the topological invariant becomes drastically simple and instinctive in the system with both the time and spatial reversal symmetries. In such a system, the product of the W matrix becomes the product of the eigenvalue of the spatial reversal operator $\hat{K}$ at each TRIM.[8] Note that the eigenvalue of $\hat{K}$ is determined by the symmetry of the wavefunction. It indicates that only band inversion can change that eigenvalue because wave functions in a valence band have only *p*-orbital like symmetry without band inversion. As mentioned in Section 2.1, such a band inversion occurs due to the split off for *p*-orbital like valence band caused by the spin orbit interaction. Therefore, materials with strong spin orbit interaction can become a TI when band inversion occurs at odd number of TRIM, and this is the reason why the spin orbit interaction plays an important role for TI.

Here, we consider the physical meaning of the topological invariant in TIs.

According to the previous work, the number of topological invariants corresponds to the number of recombination of Kramers pairs. A Kramers pair should exchange the pair between TRIM at which the topological invariant has different value. Although such an exchange requests continuous connection between neighboring bands, it is forbidden that the existence of electronic states crossing its band gap because we have considered an insulating "bulk" band. To avoid this contradiction, such an electronic state appears as a "surface" state. This TSS is robust against perturbations which preserve the topological invariant such as non-magnetic impurities and defects because the TSS is protected by the topological invariant of bulk wave functions, which is an advantage for realistic devices. Because the TSS should be degenerate at TRIM due to the Kramers' theorem, the TSS has a Dirac dispersion around degenerate points, which brings rich physical phenomena discussed in detail in the next section.

2.4 Fundamental physics of topological surface states

In this section, we explain fundamental properties and a magnetoresistance in TSSs. We now consider a 3D TI thin film, where the length and width are sufficiently larger than the thickness. TSSs appear on the top and bottom planes for the thin film. Here, the effective Hamiltonian for the top-TSS is given by following within the 1st order of $\boldsymbol{k}$,

$$\hat{H} = \hbar\nu_{\mathrm{F}}(\boldsymbol{\sigma} \times \boldsymbol{k}) = \hbar\nu_{\mathrm{F}} \begin{pmatrix} 0 & k_y + ik_x \\ k_y - ik_x & 0 \end{pmatrix} = i\hbar\nu_{\mathrm{F}} k \begin{pmatrix} 0 & e^{-i\theta} \\ -e^{i\theta} & 0 \end{pmatrix},$$

where ν_{F} is the Fermi velocity. The eigenvalues and eigenfunctions for this effective Hamiltonian are given by,

$$E_{\pm} = \pm\hbar\nu_{\mathrm{F}} k, \qquad \psi_{\pm} = \frac{1}{\sqrt{2}} \begin{pmatrix} 1 \\ \mp ie^{i\theta} \end{pmatrix},$$

where + (–) denotes the eigenvalue and eigenfunction for upper (lower) bands, and k = 0 corresponds to the Dirac point. Then, the expectation value of the spin operator is given by,

$$\langle \psi_{\pm} | \boldsymbol{\sigma} | \psi_{\pm} \rangle = \pm (\sin\theta \quad -\cos\theta \quad 0).$$

On the other hand, the velocity of a Dirac electron is given by,

$$\boldsymbol{v} = \frac{1}{\hbar}\frac{\partial E}{\partial \boldsymbol{k}} = \pm \nu_{\mathrm{F}} \frac{\boldsymbol{k}}{k} = \pm \nu_{\mathrm{F}} (\cos\theta \quad \sin\theta \quad 0).$$

These results indicate that the spin and velocity of a Dirac electron are always orthogonal to each other, and the spin direction is determined by the $\boldsymbol{k}$ direction. This relation between the spin and $\boldsymbol{k}$ is called spin-momentum locking. Because electrons cannot change their direction without changing their spin direction, back scattering of electrons is suppressed on TSSs.[9]

Next, we explain the Berry phase of TSS. By using the cylindrical coordinate system for the calculation, one can obtain the Berry connection for upper and lower bands as follows,

$$\boldsymbol{A}_{\pm}(\boldsymbol{k}) = -i \langle \psi_{\pm}(\boldsymbol{k}) | \partial_{\boldsymbol{k}} | \psi_{\pm}(\boldsymbol{k}) \rangle = \begin{pmatrix} 0 & \frac{1}{2k} \end{pmatrix}.$$

Then, one can calculate the Berry phase,

$$\gamma_{\pm} = -\oint_C d\boldsymbol{k} \cdot \boldsymbol{A}_{\pm}(\boldsymbol{k}) = \begin{cases} -\pi & (C \text{ includes the Dirac point}) \\ 0 & (C \text{ does not include the Dirac point}) \end{cases}$$

This result indicates that both upper and lower bands have large Berry phase at the Dirac point. Therefore, TSS, especially at the Dirac point is a hot spot for strong SHE originated from the intrinsic Berry phase effect.

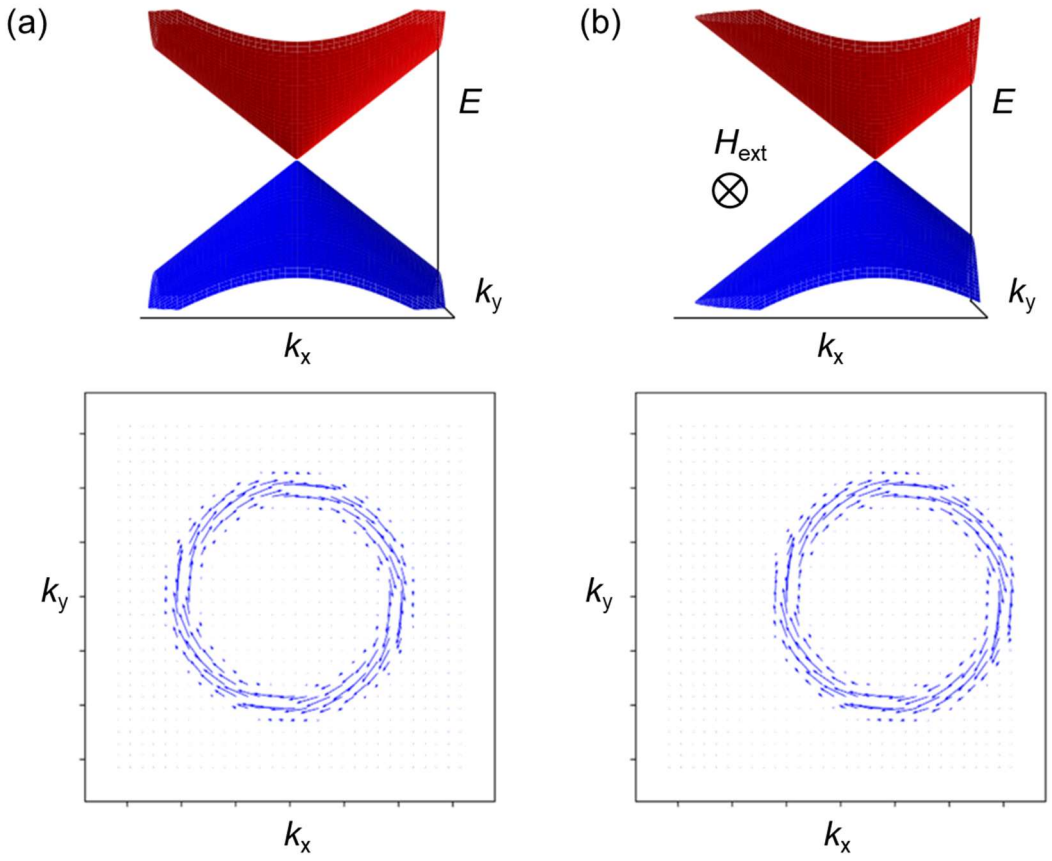

Figure 2.2. Dirac dispersion calculated by effective Hamiltonian with 1st order of *k* under (a) no magnetic field, and (b) magnetic field along the *y*-axis, and corresponding spin distribution, where blue allows show the spin direction on a Fermi surface.

Finally, we explain the magnetoresistance originated from TSS. When we consider the effective Hamiltonian with 1st order of ***k***, the magnetoresistance does not occur because an external magnetic field just shifts the position of Dirac dispersion in ***k***-space maintaining the spin-momentum locking, as shown in Figure 2.2.

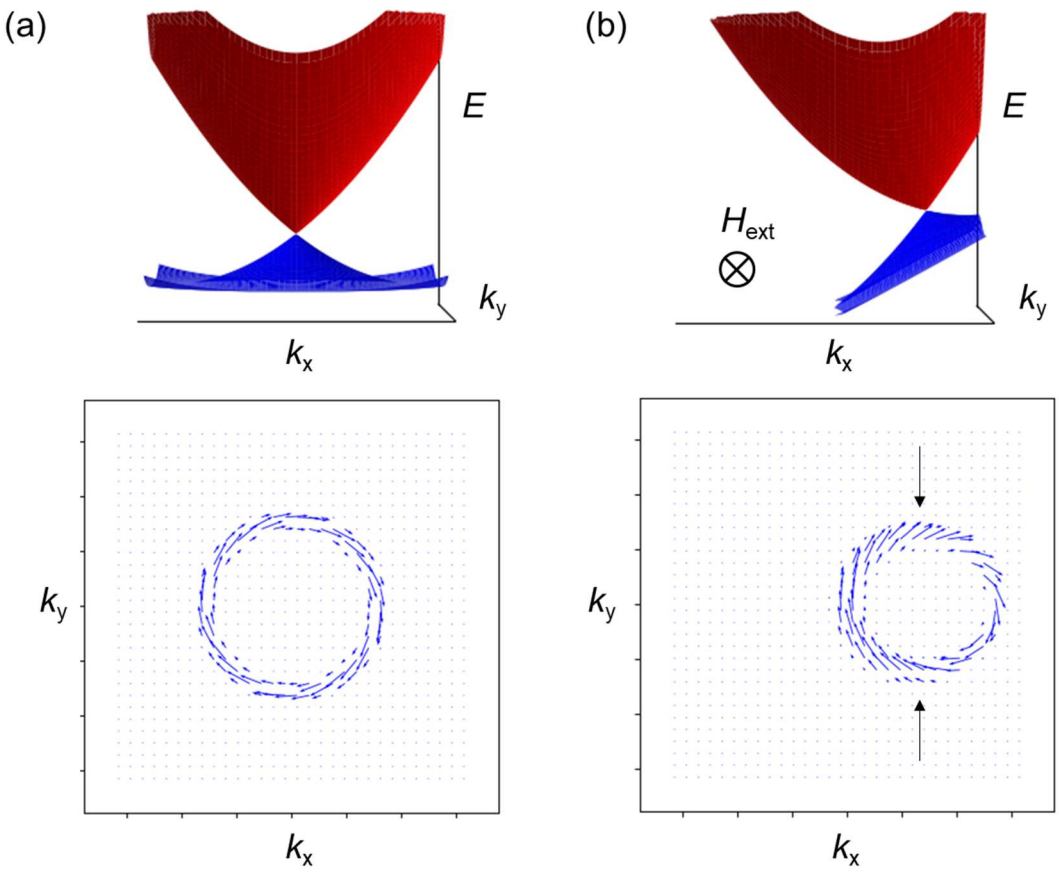

Figure 2.3. Dirac dispersion calculated by effective Hamiltonian with 1st and 2nd orders of *k* under (a) no magnetic field, and (b) magnetic field along the *y*-axis, and corresponding spin distribution, where blue allows show the spin direction on a Fermi surface. Spins are tilting along the *y*-direction at where black arrows are pointing, while the spin-momentum-locking is still maintained along the *x*-direction.

Whereas the spin-momentum locking is easily disturbed by a field when the effective Hamiltonian with higher order ***k***-terms which causes asymmetry of upper and lower bands.[10] In generally, the Dirac-like band dispersion far from the Dirac point is strongly distorted,[11] and thus, the magnetoresistance can be observed by applying an external magnetic field which destroys the spin-momentum locking. Figure 2.3 shows the Dirac-dispersions and their spin distribution on the Fermi

surface, where the effective Hamiltonian includes a $\boldsymbol{k}^2$-term. When an external magnetic field is applied along the *y*-direction, the spin-momentum locking parallel with the field is broken, as seen for the spins indicated by the black arrows in Figure 2.3(b) becomes not orthogonal to each other anymore. Then a resistance parallel to the field increases because the back scattering along that direction is allowed due to broken of the spin-momentum locking. Such an anisotropic change of resistance caused by the external field can generate AMR and planar Hall effect (PHE) even in a non-magnetic material, and there are many reports on AMR and PHE originated from TSS in TIs.[12-15] Note that these magnetoresistances are proportional to the square of an external magnetic field without saturation, which is different from those in ferromagnetic materials.[12-15] Therefore, one can confirm the existence of TSS by measuring the AMR or PHE.

2.5 Rashba–Edelstein effect

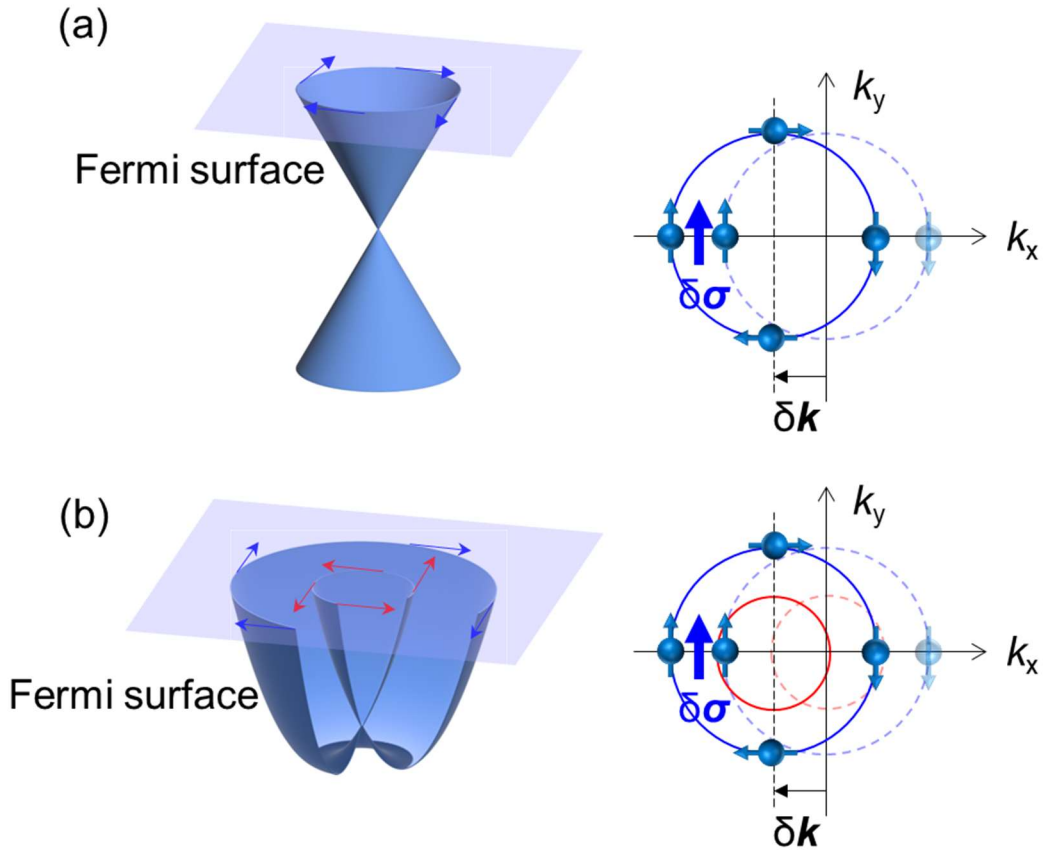

Figure 2.4. (a) Spin-momentum-locked Dirac-like dispersion (left hand side), and its spin accumulation caused by the shift of Fermi surface (right hand side), called as the Edelstein effect. (b) Rashba-splitting bulk state (left hand side), and its spin accumulation (right hand side), called as the Rashba effect, where spins for inside band depicted by red circle are omitted for simplify. Here, blue and red arrows in the left figures for (a) and (b) indicate the spin direction.

When an electric field is applied to a TI, a current will flow resulting in a shift of $\delta \boldsymbol{k}$ on the Fermi surface. Then, a spin accumulation $\delta \boldsymbol{\sigma}$ occurs on the surface due to the spin-momentum locking of the TSS, as shown in Figure 2.4(a). Although this accumulated spin cannot diffuse into other adjacent layers, it can show its effect via an exchange interaction if the adjacent layer is a ferromagnetic material.[16] Such 2D spin accumulation on a TSS is called as the Edelstein effect.[17] Similar effect can

be observed at the interface without spatial inversion symmetry. In the system whose spatial inversion symmetry is broken, the spin degeneracy of the band is removed because the band should follow the condition $E(\boldsymbol{k},\uparrow) \neq E(-\boldsymbol{k},\uparrow)$ except for the TRIM. Then, the band structure on the Fermi surface has the spin texture, as shown in Figure 2.4(b). Similar to the TSS case, this spin texture also generates a spin accumulation when an electric field is applied, and it can propagate the spin angular momentum. This effect originated from the lack of spatial reversal symmetry at the interface is called the Rashba effect.[18] In generally, we call the spin momentum generation via 2D spin accumulation as the Rashba-Edelstein effect.

2.6 Spin Hall effect

In this session, we explain the SHE which plays the most important role for magnetization manipulation. The SHE can generate a spin accumulation because electrons having opposite spins are deflected to opposite directions due to the spin orbit interaction, as mentioned in Section 1.2.[19] Different from the Rashba-Edelstein effect,[17,18] the accumulated spin caused by the SHE can diffuse into the adjacent ferromagnetic layer, and then, the damping-like SOT acts on the magnetization by following the conservation of angular momentum, similar to the STT.[20,21]

Here, two extrinsic mechanisms and one intrinsic mechanism can contribute to the SHE similar to the anomalous Hall effect (AHE).[4,22] Both extrinsic mechanisms originate from the scattering by impurities with strong spin orbit interaction. One of the extrinsic mechanisms is skew scattering which is caused by the shift of the Fermi distribution function depending on the spins, and the other is side-jump which is caused by the anomalous velocity given by the spin orbit interaction of impurities.

On the other hand, the intrinsic mechanism is originated from the Berry curvature, namely, it is only related to the band structure of the spin Hall material. Because the Berry curvature acts an effective magnetic field, electrons get the anomalous velocity perpendicular to their original velocities. Note that the band structure far from the Fermi surface also contributes to the SHE because the intrinsic spin Hall conductivity σ_{SH} is given by the integral of the spin Berry curvature multiplied by the Fermi distribution function.

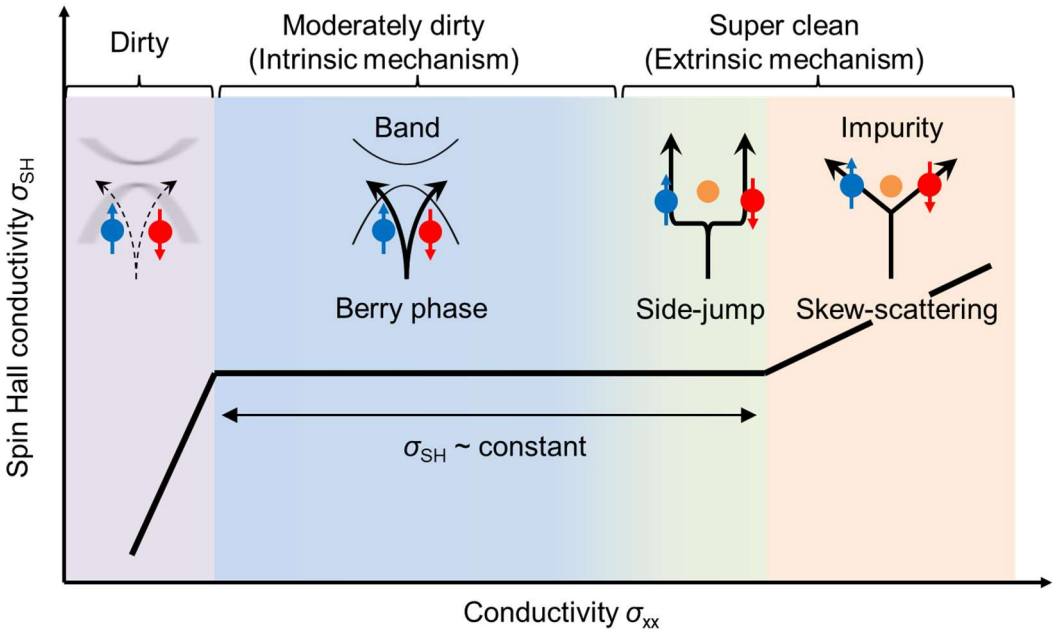

Figure 2.5. Schematic illustration of conductivity dependence of spin Hall conductivity. The SHE is originated from three kinds of mechanisms, the skew-scattering, side-jump, and Berry phase, and dominated one changes depending on its conductivity.

Although these three mechanisms can contribute to the SHE, the dominating mechanism for the SHE depends on the conductivity of spin Hall materials. Figure 2.5 shows the schematic illustration of σ_{SH} as a function of the conductivity σ_{xx}. When

a spin Hall material have high σ_{xx}, skew scattering dominates the SHE. In the skew scattering region, σ_{SH} is proportional to σ_{xx}. When σ_{xx} is degraded, the main mechanism for the SHE is switched to side-jump, and then, σ_{SH} becomes constant against the change of σ_{xx}. Further degradation of σ_{xx} changes the main mechanism from the extrinsic to intrinsic one. Similar to the side-jump case, σ_{SH} originated from the intrinsic mechanism is also independent of the change of σ_{xx}. In the poor σ_{xx} region, σ_{SH} suddenly drops due to degradation of the Berry curvature caused by fluctuation of their band structure. Because each mechanism shows unique σ_{xx} dependence of σ_{SH}, one can investigate the origin of the SHE by measuring σ_{SH} at various σ_{xx}. Although the side-jump and the intrinsic mechanism have same σ_{xx} dependence, the strength of the side-jump mechanism also depends on the resistivity contribution of impurities. Therefore, one can distinguish all mechanisms by using following equation,[23]

$$\sigma_{\mathrm{SH}} = \alpha_{\mathrm{SS}}\rho_{xx}^{\mathrm{imp}}\sigma_{xx}^{2} + \alpha_{\mathrm{SJ}}{\rho_{xx}^{\mathrm{imp}}}^{2}\sigma_{xx}^{2} + \sigma_{\mathrm{SH}}^{\mathrm{int}},$$

where α_{SS}, α_{SJ} are coefficients for the skew scattering and side-jump, respectively, ρ_{xx}^{imp} is a resistivity contribution from impurities, and $\sigma_{\mathrm{SH}}^{\mathrm{int}}$ is a spin Hall conductivity originated from the intrinsic mechanism. According to this equation, we cannot separate the contribution of the skew scattering and side-jump without changing ρ_{xx}^{imp}. However, the contribution of skew scattering is negligibly smaller than that of side-jump in almost samples except for very conductive samples grown by the molecular beam epitaxy or electron beam evaporation methods. Meanwhile, samples grown by the sputtering technique generally have relatively large resistivity.[22]

2.7 Magnetization dynamics in ferromagnetic materials

In this session, we explain the magnetization dynamics. When a spin current is injected into a ferromagnetic layer, the time evolution of the magnetization is given by the following the Landau-Lifshitz-Gilbert (LLG) equation,

$$\frac{d\boldsymbol{m}}{dt} = -\gamma \boldsymbol{m} \times \boldsymbol{H}_{\mathbf{eff}} + \alpha \boldsymbol{m} \times \frac{d\boldsymbol{m}}{dt} - \gamma H_{\mathrm{DL}} \boldsymbol{m} \times (\boldsymbol{m} \times \boldsymbol{p}_{\mathbf{S}}) - \gamma H_{\mathrm{FL}} \boldsymbol{m} \times \boldsymbol{p}_{\mathbf{S}},$$

where $\boldsymbol{m}$ is the unit vector of magnetization, γ is the gyromagnetic ratio for electrons, α is the Gilbert damping factor, $\boldsymbol{p}_{\mathbf{S}}$ is the spin polarization vector, which is opposite to the spin angular momentum of injected electrons. Here, H_{DL} and H_{FL} are the damping-like and field-like effective fields, and they are originated from the SHE and the Rashba-Edelstein effect, respectively. The effective magnetic field $\boldsymbol{H}_{\mathbf{eff}}$ is defined as the gradient of the magnetization energy. In the macrospin model, $\boldsymbol{H}_{\mathbf{eff}}$ is generally given by,

$$\boldsymbol{H}_{\mathbf{eff}} = \boldsymbol{H}_{\mathbf{ext}} + \boldsymbol{H}_{\mathbf{D}} + \boldsymbol{H}_{\mathbf{k}} = \boldsymbol{H}_{\mathbf{ex}} \ - 4\pi M_{\mathrm{S}} N \boldsymbol{m} + \frac{2K_{\mathrm{u}}}{M_{\mathrm{S}}} (\boldsymbol{n} \cdot \boldsymbol{m}) \boldsymbol{m},$$

where $\boldsymbol{H}_{\mathbf{ext}}$ is an external magnetic field, M_{S} is the saturation magnetization, N is the demagnetizing tensor, K_{u} is the uniaxial magnetic anisotropy energy, and $\boldsymbol{n}$ is the unit vector of a uniaxial easy axis. Although one can study the dynamics of the magnetization by solving the LLG equation analytically, it is very difficult to solve it in general case, because the LLG equation is a 3D non-linear differential equation. Here, one can reduce the dimension of the LLG equation by using the definition of the effective magnetic field $\boldsymbol{H}_{\mathbf{eff}} = -dE/d\boldsymbol{M}$,

$$\frac{dE}{dt} = -M_S \boldsymbol{H}_{\mathbf{eff}} \cdot \frac{d\boldsymbol{m}}{dt}.$$

Because this LLG equation in the energy-space treats the time evolution of energy, we can easily predict the magnetization trajectory between the typical energy without

considering any complicating motion. Especially, the LLG equation in the energy-space is useful when we predict the magnetization dynamics on a constant energy curve such as a sustainable oscillation state.

2.8 Magnetoresistance and magneto thermoelectric effects in ferromagnetic materials

In this section, we explain the magnetoresistance and magneto thermoelectric effects by phenomenological ways. When a current flows in a ferromagnetic material, conduction electrons are scattered depending on the magnetization direction because localized electrons, which form the magnetization, and conduction electrons interact via the spin orbit interaction or exchange interaction, resulting in the magnetoresistance. According to the vector analysis, Ohm's law with reference to the magnetization direction is given by,

$$\boldsymbol{\varepsilon} = \rho_{\parallel}(\boldsymbol{m}\cdot\boldsymbol{J}_{\mathbf{C}})\boldsymbol{m} + \rho_{\mathrm{AHE}}\boldsymbol{m}\times\boldsymbol{J}_{\mathbf{C}} + \rho_{\perp}\boldsymbol{m}\times(\boldsymbol{m}\times\boldsymbol{J}_{\mathbf{C}}),$$

where $\rho_{\parallel}$ and $\rho_{\perp}$ are resistivities when the current is parallel or perpendicular to the magnetization direction, respectively, and ρ_{AHE} is the resistivity for the AHE. By deforming the Ohm's law, one can obtain the following expression,

$$\boldsymbol{\varepsilon} = \rho_{\perp}\boldsymbol{J}_{\mathbf{C}} + (\rho_{\parallel}-\rho_{\perp})(\boldsymbol{m}\cdot\boldsymbol{J}_{\mathbf{C}})\boldsymbol{m} + \rho_{\mathrm{AHE}}\boldsymbol{m}\times\boldsymbol{J}_{\mathbf{C}}.$$

When the current is applied along the *x*-direction, the *x* and *y* components of resistivity are given by,

$$\rho_{xx} = \rho_{\perp} + (\rho_{\parallel}-\rho_{\perp})m_x^2,$$

$$\rho_{xy} = (\rho_{\parallel}-\rho_{\perp})m_x m_y + \rho_{\mathrm{AHE}}m_z.$$

Then, by adopting the spherical coordinate system for $\boldsymbol{m}$, one can obtain,

$$\rho_{xx} = \rho_{\perp} + (\rho_{\parallel}-\rho_{\perp})\sin^2\theta_0\cos^2\phi_0,$$

$$\rho_{xy} = \frac{\rho_{\parallel} - \rho_{\perp}}{2} \sin\theta_0 \sin 2\phi_0 + \rho_{\mathrm{AHE}} \cos\theta_0,$$

where θ_0 and φ_0 are the polar and azimuth angles for the magnetization, respectively. Here, ρ_{xx} is so called the AMR, and the 1st and 2nd terms of ρ_{xy} correspond to the PHE and AHE, respectively.

Next, we consider the magneto thermoelectric effects. Conduction electrons driven by a thermal gradient also cause a magnetoresistance via interaction with localized electrons. The magneto thermoelectric effects caused by an external magnetic field and magnetization are called as the ordinary Nernst effect (ONE) and anomalous Nernst effect (ANE), respectively. When a thermal gradient along the *z*-direction exists, the Hall resistance originated from the ONE and ANE are given by,

$$\rho_{xy} = C_{\mathrm{ONE}}(\boldsymbol{H_{ext}} \times \boldsymbol{\nabla T_z})_y = -C_{\mathrm{ONE}} H_{\mathrm{ext}} \sin\theta_{\mathrm{H}} \cos\phi_{\mathrm{H}} \boldsymbol{\nabla T_z},$$

$$\rho_{xy} = C_{\mathrm{ANE}}(\boldsymbol{m} \times \boldsymbol{\nabla T_z})_y = -C_{\mathrm{ANE}} \sin\theta_0 \cos\phi_0 \boldsymbol{\nabla T_z},$$

where C_{ONE} and C_{ANE} are coefficients originated from the ONE and ANE, respectively, θ_{H} and φ_{H} are the polar and azimuth angles for the external magnetic field, respectively. Because the magnetoresistance and magneto thermoelectric effects convert the magnetization direction into electric signals, one can evaluate the magnetization direction via these effects, and thus, they are sometimes utilized for detection of a spin current.

2.9 Summary

In this chapter, we have explained the fundamental phenomena in spin Hall materials such as the spin orbit interaction, and SHE. We then emphasized the importance of the Berry phase on the SHE. We also have explained the magnetization dynamics and magnetoresistance in ferromagnetic materials. In the following

chapters, the investigation of the spin Hall physics, and development of spin Hall devices are conducted based on the fundamental physics introduced in this chapter.

2.10 References

[1] P. A, M, Dirac, Proc. R. Soc. A **117**, 610 (1928).

[2] E. O. Kane, J. Phys. Chem. Solids **1**, 249 (1957).

[3] M. V. Berry, Proc. R. Soc. London, Ser. A **392**, 45 (1984).

[4] N. Nagaosa, J. Sinova, S. Onoda, A. H. MacDonald and N. P. Ong, Rev. Mod. Phys. **82**, 1539 (2010).

[5] D. J. Thouless, M. Kohmoto, M. P. Nightingale, and M. den Nijs, Phys. Rev. Lett. **49**, 405 (1982).

[6] L. Fu, and C. L. Kane, Phys. Rev. B **74**, 195312 (2006).

[7] L. Fu, C. L. Kane, and E. J. Mele, Phys. Rev. Lett. **98**, 106803 (2007).

[8] L. Fu, and C. L. Kane, Phys. Rev. B **76**, 045302 (2007).

[9] M. Z. Hasan, C. L. Kane, Rev. Mod. Phys. **82**, 3045 (2010).

[10] S.-H. Zheng, H.-J. Duan, J.-K. Wang, J.-Y. Li, M.-X. Deng, and R.-Q. Wang, Phys. Rev. B **101**, 041408(R) (2020).

[11] H. Zhang, C.-X. Liu, X.-L. Qi, X. Dai, Z. Fang, and S.-C. Zhang, Nat. Phys. **5**, 438 (2009).

[12] A. A. Taskin, H. F. Legg, F. Yang, S. Sasaki, Y. Kanai, K. Matsumoto, A. Rosch, and Y. Ando, Nat. Commun. **8**, 1340 (2017).

[13] L. Zhou, B. C. Ye, H. B. Gan, J. Y. Tang, P. B. Chen, Z. Z. Du, Y. Tian, S. Z. Deng, G. P. Guo, H. Z. Lu, *et al*. Phys. Rev. B **99**, 155424 (2019).

[14] A. Bhardwaj, P. S. Prasad, K. V. Raman, and D. Sur Appl. Phys. Lett. **118**, 241901

(2021).

[15] R. C. Budhani, J. S. Higgins, D. McAlmont, and J. Paglione, AIP Advances **11**, 055020 (2021).

[16] S. Emori, T. Nan, A. M. Belkessam, X. Wang, A. D. Matyushov, C. J. Babroski, Y. Gao, H. Lin, and N. X. SunPhys. Rev. B **93**, 180402(R) (2016).

[17] V. M. Edelstein, Solid State Commun. **73**, 233 (1990).

[18] E. I. Rashba, Sov. Phys. Solid State **1**, 368 (1959).

[19] J. E. Hirsch, Phys. Rev. Lett. **83**, 1834 (1999).

[20] J. C. Slonczewski, J. Magn. Magn. Mater. **159**, L1 (1996).

[21] L. Berger, Phys. Rev. B **54**, 9353 (1996).

[22] E. Sagasta, Y. Omori, M. Isasa, M. Gradhand, L. E. Hueso, Y. Niimi, Y. Otani and F. Casanova, Phys. Rev. B **94**, 060412(R) (2016).

[23] 23 Y. Tian, L. Ye and X. Jin, Phys. Rev. Lett. **103**, 087206 (2009).

Chapter 3. Development of Angle resolved second harmonic technique for precise evaluation of spin orbit torque in strong perpendicular magnetic anisotropy systems

3.1 Introduction

As described in Chapter 1, SOT is an innovative technology for spintronic devices because it can manipulate magnetization with small current, ultra-high speed, and low damage. For development of SOT devices, it is essential to evaluate the strength of SOT or charge-to-spin conversion efficiency.[1,2] A low field second harmonic technique has been used for quantitative evaluation of SOT thanks to its simple experimental setup and high throughput.[3,4] In non-magnetic/magnetic bilayers with strong PMA, SOT is evaluated from the first and second harmonic Hall resistances (R_{xy}^{ω} and $R_{xy}^{2\omega}$) under an alternating current (AC) while sweeping a small in-plane external magnetic field $H_{\mathrm{ext}} << H_{\mathrm{k}}^{\mathrm{eff}}$ along the current direction (x-direction), where $H_{\mathrm{k}}^{\mathrm{eff}}$ is the effective magnetic anisotropy field of the magnetic layer. When the contribution of the field-like SOT effective field and Oersted field $H_{\mathrm{FL+OF}}$ through the planar Hall effect is negligible, the damping-like SOT effective field H_{DL} is given by $H_{\mathrm{DL}} = -2\frac{\partial R_{\mathrm{xy}}^{2\omega}/\partial H_{\mathrm{ext}}}{\partial^2 R_{\mathrm{xy}}^{\omega}/\partial H_{\mathrm{ext}}^2}$.[3] In principle, the low field technique cannot distinguish SOT from various magneto thermoelectric effects such as the ONE, ANE and spin Seebeck effect (SSE), because contributions of those thermal effects to $R_{\mathrm{xy}}^{2\omega}$ are also proportional to small H_{ext}, i.e. $R_{\mathrm{xy}}^{2\omega}$(ONE) ~ H_{ext} and $R_{\mathrm{xy}}^{2\omega}$(ANE/SSE) ~ M_x ~ $H_{\mathrm{ext}}/H_{\mathrm{k}}^{\mathrm{eff}}$, where M_x is the x-component of the magnetization. Nevertheless, the low field technique has been widely used to estimate the strength of SOT while neglecting contributions from those thermal effects.[5-9]

One way to avoid this problem is to apply a large $H_{ext} >> H_k^{eff}$, so called the high field second harmonic technique.[10-12] At high fields, we can distinguish SOT from thermal effects thanks to their different H_{ext}-dependency; $R_{xy}^{2\omega}$ (SOT) ~ $H_{DL}/(H_{ext} - H_k^{eff})$, $R_{xy}^{2\omega}(\text{ONE}) \sim H_{ext}$, while $R_{xy}^{2\omega}$(ANE/SSE) becomes a constant.[4] However, when it is difficult to realize the condition $H_{ext} >> H_k^{eff}$ in samples with very large H_k^{eff}, the low field second harmonic technique is the only option. Thus, it is essential to find a way to disentangle SOT from those thermal effects in such samples. Recently, Yang *et al.* have shown that it is possible to disentangle SOT from ANE by using an angle resolved second harmonic technique in samples with relatively weak PMA.[13] However, their technique does not include ONE which is important in several materials such as topological materials.[14]

In this chapter, we generalize their technique by including ONE. We demonstrate that the generalized angle resolved second harmonic technique can be applied to resolve SOT, ANE/SSE, and ONE in samples with large H_k^{eff}, which is the case of interest. These results remind the importance of eliminating contributions from thermal effects in low field second harmonic measurements, and provide an effective way to precisely estimate SOT in samples with large H_k^{eff}. We then apply this method to evaluate θ_{SH} in CoPt/YPtBi films having strong PMA in Chapter 5.

3.2 Thermal effects on low field second harmonic signal

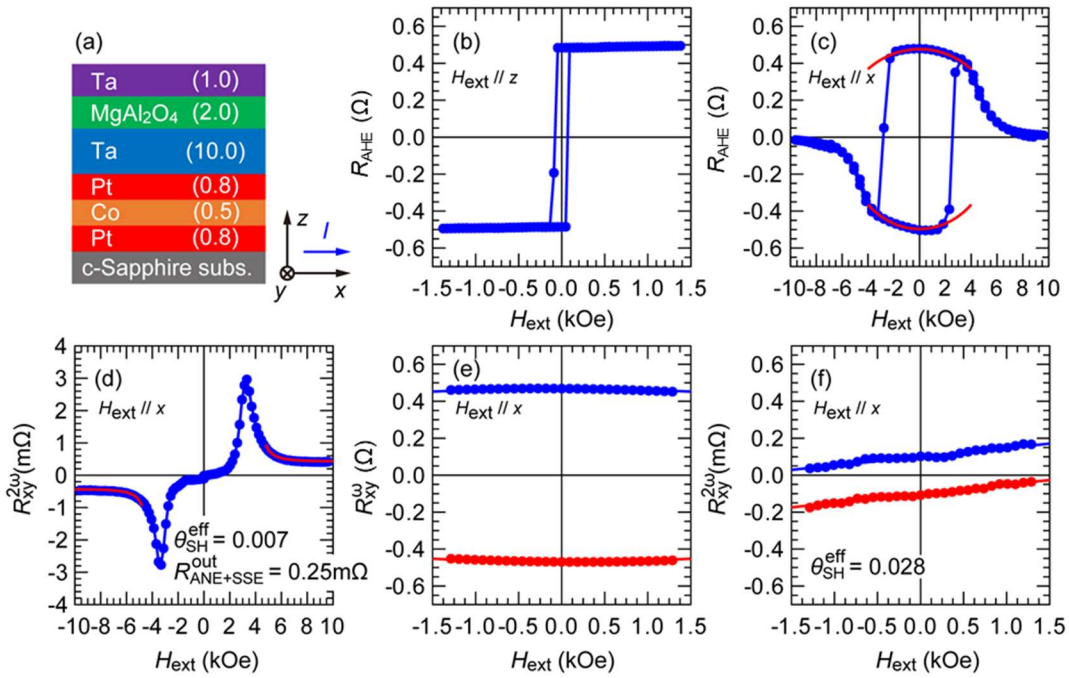

Figure 3.1. (a) Schematic structure of sample A and the coordination system. (b), (c) DC anomalous Hall resistance with H_{ext} applied along the *z*- and *x*- direction, respectively. (d) High field second harmonic Hall resistance as a function of H_{ext} measured with an AC current of 7.0 mA. Fitting to high field data yields an effective spin Hall angle θ_{SH}^{eff} of 0.007 and the contribution $R_{ANE+SSE}^{out}$ from the ANE/SSE. (e), (f) Low field first and second harmonic Hall resistance as a function of small in-plane H_{ext} at 7.0 mA, respectively. Fittings using the low field data yields θ_{SH}^{eff} of 0.028, which is overestimated by a factor of 4.

We first demonstrate that contamination from thermal effects can lead to significant overestimation of SOT in a sample with small spin Hall angle. For this purpose, we deposited a heterostructure of Ta (1.0) / $MgAl_2O_4$ (2.0) / Ta (10) / Pt (0.8) / Co (0.5) / Pt (0.8) / c-Sapphire substrate (sample A), where the layer thicknesses are in nm, as shown in Figure 3.1(a). The laminated Pt/Co/Pt stack is referred below as CoPt for short. Here, the parasitic SHE from the two Pt layers is negligible because the Pt thickness of 0.8 nm is few times thinner than the typical

spin relaxation length of Pt, and the Pt/Co/Pt stack is symmetric.[12,15-17] The main non-magnetic layer, Ta (10), is designed to have a high conductivity of 8.4×10^5 $\Omega^{-1}m^{-1}$ so that its spin Hall angle is small. In addition, large spin loss at the Ta/Pt interface due to spin back-flow and spin loss inside the Pt (0.8) layer further reduce the spin current from Ta, resulting in a small effective spin Hall angle θ_{SH}^{eff}. The multilayers were patterned into 10×60 μm^2 Hall bar devices by optical lithography and lift-off techniques for transport measurements. We assume that the top Ta (1.0) capping layer is fully oxidized after exposure to the atmosphere. Figures 3.1(b) and 3.1(c) show the anomalous Hall resistance measured by a direct current (DC) with H_{ext} applied along the z- and x-direction, respectively, where the x-direction is parallel to the applied current direction. By fitting the low field data in Figure 3.1(c) to $R_{AHE}(H_{ext}) = R_{AHE}(0)\sqrt{1-(H_{ext}/H_k^{eff})^2}$, we estimated H_k^{eff} = 6.3 kOe, which is moderately large. We first use the well-established high field second harmonic technique to evaluate θ_{SH}^{eff}. Figure 1(d) shows $R_{xy}^{2\omega}$ as a function of H_{ext} applied along the x-direction, measured with an AC current of 7.0 mA at 259.68 Hz, which shows typical behavior for a PMA sample.[10,12] We estimate SOT effective fields by fitting high field data using the following equation,[10-12]

$$R_{xy}^{2\omega} = \frac{R_{AHE}}{2}\frac{H_{DL}}{|H_{ext}| - H_k^{eff}} + R_{PHE}\frac{H_{FL+OF}}{|H_{ext}|} + \alpha_{ONE}^{out}|H_{ext}| + R_{ANE+SSE}^{out}, \quad (3.1)$$

where R_{AHE} is the anomalous Hall resistance, R_{PHE} is the planar Hall resistance, α_{ONE}^{out} and $R_{ANE+SSE}^{out}$ correspond to the contribution from ONE and ANE/SSE caused by a temperature gradient along the z-direction. Using M_S = 321 emu/cc measured by a superconducting quantum interference device (SQUID), t_{CoPt} = 2.1 nm for the thickness of CoPt layer, and the current shunting ratio for the Ta (10) layer of

0.69 for calculating the current density J_{Ta} in Ta, we obtained $\theta_{SH}^{eff} = \frac{2e}{\hbar} M_S t_{CoPt} \frac{H_{DL}}{J_{Ta}}$ = 0.007, which is ~20 times smaller than that of resistive Ta with a lower conductivity of 5×10^5 $\Omega^{-1}m^{-1}$ and an intrinsic spin Hall angle of 0.12-0.15.[18] We also obtained $R_{ANE+SSE}^{out}$= 0.25 mΩ in this sample. Figures 3.1(e) and 3.1(f) show the low field R_{xy}^{ω} and $R_{xy}^{2\omega}$, where dots and solid lines are experimental results and fittings $(\frac{\partial^2 R_{xy}^{\omega}}{\partial H_{ext}^2}, \frac{\partial R_{xy}^{2\omega}}{\partial H_{ext}})$ for the conventional low field technique, respectively. From the fittings, we obtained θ_{SH}^{eff} = 0.028, which is 4 times higher than that estimated from the high field technique. This discrepancy comes from the large contribution from ANE/SSE in low field $R_{xy}^{2\omega}$: the slope due to ANE/SSE at low field is $R_{ANE+SSE}^{out}/H_k^{eff}$= 0.039 mΩ/kOe, which is 75% of the observed slope $\frac{\partial R_{xy}^{2\omega}}{\partial H_{ext}}$ = 0.048 mΩ/kOe.

3.3 Proposal of angle resolved second harmonic technique and its validity

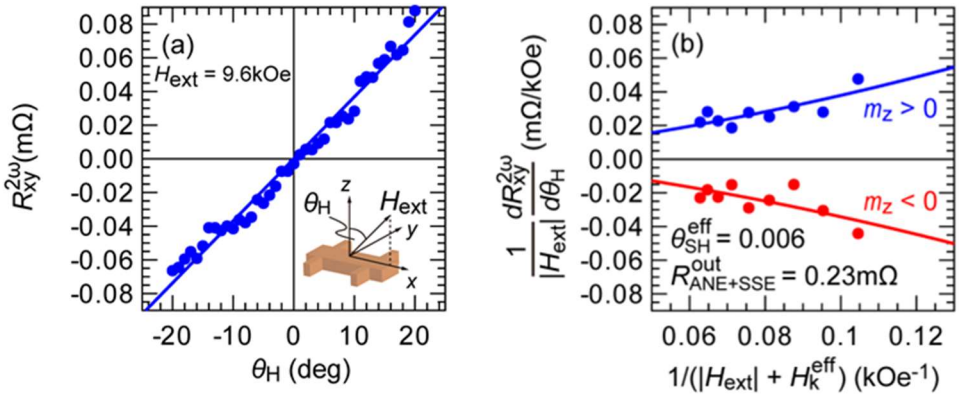

Figure 3.2. Angle resolved second harmonic Hall resistance measured at 7.0 mA with H_{ext} = 9.6 kOe applied in the *xz*-plane at varying polar angle θ_H in sample A. (b) $|H_{ext}|^{-1} dR_{xy}^{2\omega}/d\theta_H$ as a function of $(|H_{ext}| + H_k^{eff})^{-1}$ at 7.0 mA. Solid lines are fittings by equation (3.3), which yields θ_{SH}^{eff} = 0.006 and $R_{ANE+SSE}^{out}$= 0.23 mΩ, consistent with those estimated from the high field data.

In case that the high field second harmonic data are not available, one can

disentangle SOT from thermal effects by the angle resolved technique. Here, we generalize this technique to include ONE, which has not been considered in previous works,[13,19] and demonstrates the validity of the generalized angle resolved second harmonic technique. When H_{ext} is applied in the *xz*-plane at a small polar angle θ_H, $R_{xy}^{2\omega}$ is given by, (See derivation of this equation in the appendix)

$$R_{xy}^{2\omega} = \pm\left(\frac{R_{AHE}}{2}H_{DL} + R_{PHE}H_{FL+OF}\right)\frac{|H_{ext}|\theta_H}{(|H_{ext}| + H_k^{eff})^2} \mp \alpha_{ONE}^{in}|H_{ext}| \pm\alpha_{ONE}^{out}\theta_H|H_{ext}| \mp R_{ANE+SSE}^{in} \pm R_{ANE+SSE}^{out}\frac{|H_{ext}|\theta_H}{|H_{ext}| + H_k^{eff}}, \quad (3.2)$$

where α_{ONE}^{in} and $R_{ANE+SSE}^{in}$ corresponds to contribution of the ONE and ANE/SSE caused by a temperature gradient along the *x*-direction, respectively, and the sign $\pm$ corresponds to the up/down direction of H_{ext} or magnetization. Differentiating equation (3.2) with θ_H, one can obtain

$$\frac{1}{|H_{ext}|}\frac{dR_{xy}^{2\omega}}{d\theta_H} = \pm\left(\frac{R_{AHE}}{2}H_{DL} + R_{PHE}H_{FL+OF}\right)(|H_{ext}| + H_k^{eff})^{-2} \pm R_{ANE+SSE}^{out}(|H_{ext}| + H_k^{eff})^{-1} \pm \alpha_{ONE}^{out}. \quad (3.3)$$

Equation (3.3) indicates that one can disentangle contributions of SOT, ANE/SSE, and ONE, by fitting the $|H_{ext}|^{-1}dR_{xy}^{2\omega}/d\theta_H$ data to a polynomial function of $(|H_{ext}| + H_k^{eff})^{-1}$. On the other hand, the low field technique with H_{ext} applied along the *y*-direction can be used to estimate $\frac{1}{2}R_{AHE}H_{FL+OF} + R_{PHE}H_{DL}$ since there is no contribution of thermal effects in this case, thus the angle resolved measurement in the *yz*-plane is not required. Figure 3.2(a) shows a representative θ_H-dependence of $R_{xy}^{2\omega}$ measured with an AC current of 7.0 mA and H_{ext} = 9.6 kOe applied in the *xz*-plane. Figure 3.2(b) shows $|H_{ext}|^{-1}dR_{xy}^{2\omega}/d\theta_H$ as a function of $(|H_{ext}| + H_k^{eff})^{-1}$, where dots are experimental results, and solid lines are fittings by equation (3.3). From the fittings, we obtained θ_{SH}^{eff} = 0.006 and $R_{ANE+SSE}^{out}$ = 0.23 mΩ,

which were consistent with the high field technique. Therefore, the angle resolved method can accurately evaluate SOT by eliminating contributions from thermal effects.

3.4 Angle resolved second harmonic measurement in strong perpendicular magnetic anisotropy system

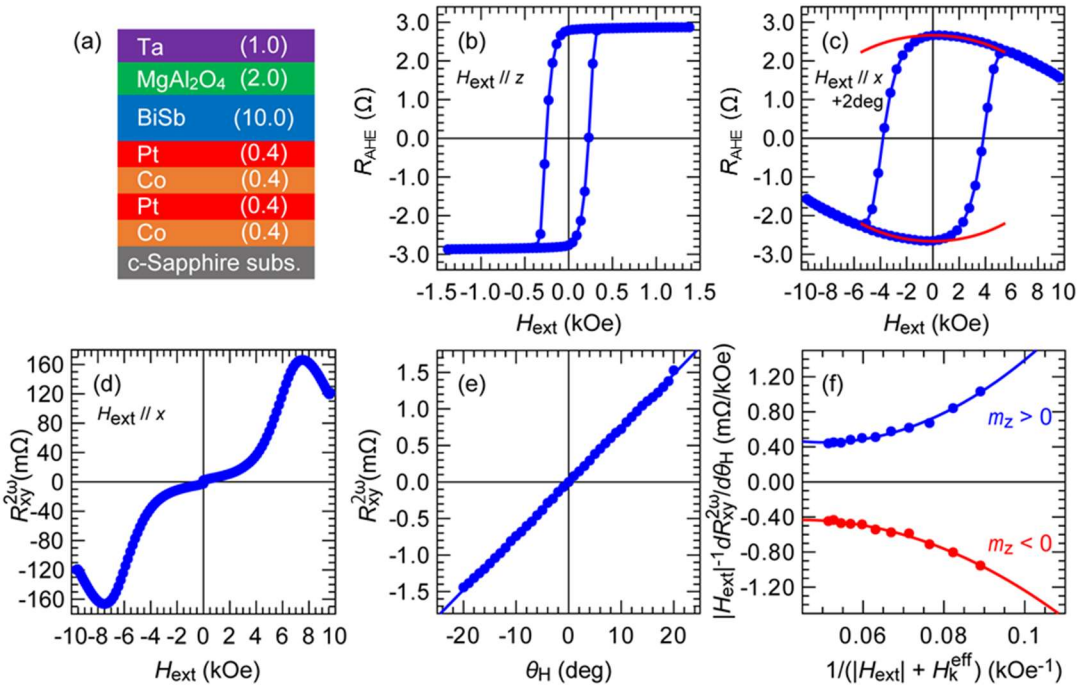

Figure 3.3. (a) Schematic structure of sample B. (b), (c) DC anomalous Hall resistance with H_{ext} applied along the *z*- and *x*- direction, respectively. (d) High field second harmonic Hall resistance as a function of H_{ext} at 3.4 mA. (e) Angle resolved second harmonic Hall resistance measured at 3.4 mA with H_{ext} = 9.6 kOe applied in the *xz*-plane at varying polar angle θ_H in sample B. (f) $|H_{ext}|^{-1}dR_{xy}^{2\omega}/d\theta_H$ as a function of $(|H_{ext}| + H_k^{eff})^{-1}$ at 3.4 mA. Solid lines are fittings by equation (3.3).

With the angle resolved technique validated, we now demonstrate our technique in a sample with large H_k^{eff} where high field data are not available. For this purpose, we prepare a heterostructure of Ta (1.0) / $MgAl_2O_4$ (2.0) / $Bi_{0.85}Sb_{0.15}$ (10.0) / [Pt (0.4)

/ Co (0.4)]$_2$ / c-Sapphire (sample B), as shown in Figure 3.3(a). Here, BiSb is a TI with a giant spin Hall angle[20] and high electrical conductivity.[21] The BiSb layer was deposited by sputtering using $Bi_{0.85}Sb_{0.15}$ single target and has an electrical conductivity of 1.5×10^5 $\Omega^{-1}m^{-1}$. The [Pt (0.4)/ Co (0.4)]$_2$ multilayers were chosen for their large H_k^{eff}. This stack was also patterned into 10×60 μm^2 Hall bar devices. Figures 3.3(b) and 3.3(c) show the DC anomalous Hall resistance with H_{ext} applied along the *z*- and *x*-direction, respectively. We obtained a large H_k^{eff} = 9.9 kOe from Figure 3.3(c). Figure 3.3(d) shows the high field $R_{xy}^{2\omega}$ measured with an AC current of 3.4 mA and H_{ext} applied along the *x*-direction. Since H_k^{eff} is large, we cannot obtain enough high field data for a reliable fitting using equation (3.1). Thus, we conducted the angle resolved second harmonic measurements. Figure 3.3(e) shows a representative θ_H-dependence of $R_{xy}^{2\omega}$ measured with the same AC current of 3.4 mA and H_{ext} = 9.6 kOe applied in the *xz*-plane at varying θ_H. Figure 3.3(f) shows $|H_{ext}|^{-1}dR_{xy}^{2\omega}/d\theta_H$ as a function of $(|H_{ext}|+H_k^{eff})^{-1}$, where dots are experimental results, and solid lines are fittings by equation (3.3). A parabolic $(|H_{ext}|+H_k^{eff})^{-2}$ term owing to strong SOT was clearly observed. In addition, there exists both α_{ONE}^{out} and $^{out}_{ANE+SSE}$, where the former originates from the ONE in the BiSb layer.

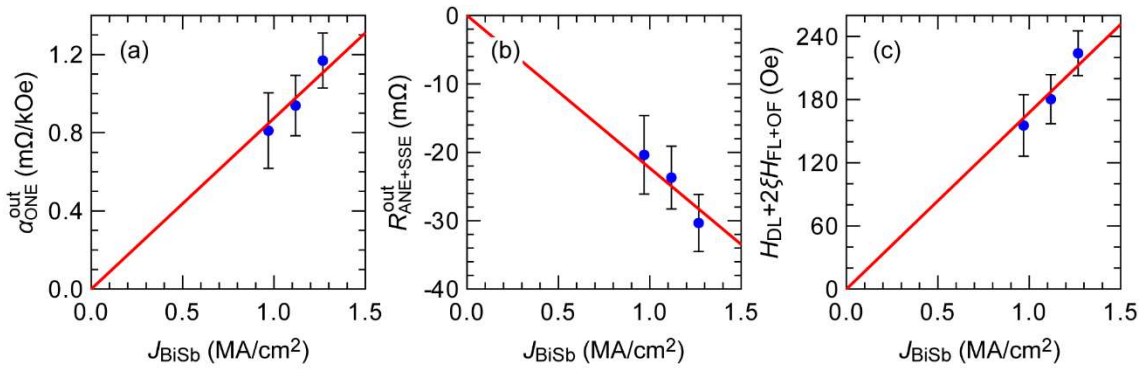

Figure 3.4. (a) α^{out}_{ONE}, (b) $R^{out}_{ANE+SSE}$, and (c) $H_{DL}+2\xi H_{FL}$ of sample B as a function of the current density in the BiSb layer, extracted by the angle resolved second harmonic technique.

Figures 3.4(a) – 3.4(c) show the fitting results of α^{out}_{ONE}, $R^{out}_{ANE+SSE}$ and $H_{DL}+2\xi H_{FL+OF}$ parameters at various current density in the BiSb layer J_{BiSb}, respectively, where $\xi = R_{PHE}/R_{AHE}$. We note that $R^{out}_{ANE+SSE}$ is negative, while α^{out}_{ONE} is positive. Since ANE, SSE, and ONE are independent phenomena, it is not unusual that $R^{out}_{ANE+SSE}$ and α^{out}_{ONE} have different sign. Because our sample is placed in vacuum, the heat generated by Joule heating inside the BiSb and CoPt would flow toward the substrate, and we can expect the thermal gradient $\nabla T_z > 0$ for both BiSb and CoPt. Therefore, the sign difference between $R^{out}_{ANE+SSE}$ and α^{out}_{ONE} is likely due to the opposite sign of the magneto thermoelectric coefficient of ANE/SSE and ONE.

By combining with the $2\xi H_{DL}+H_{FL+OF}$ data obtained from low field $R^{2\omega}_{xy}$ measured with H_{ext} applied along the *y*-direction, we can further deconvolute H_{DL} and H_{FL+OF}. Using M_S = 579 emu/cc, t_{CoPt} = 1.6 nm, and the current shunting ratio of 0.37 for the BiSb layer, we obtained θ^{eff}_{SH} of 4.7. We note that there is a self-SOT originated from the CoPt layer in this sample because of its asymmetric structure, which needed to be subtracted from the total SOT.[22] We evaluated the self-SOT of a

stand-alone CoPt layer without the BiSb layer on top, which shows θ_{SH}^{eff}=0.26, consistent that observed in Pt/CoPt.[22] Subtracting the self-SOT contribution from the CoPt layer, we obtain θ_{SH}^{eff} of 2.0 for the BiSb layer.

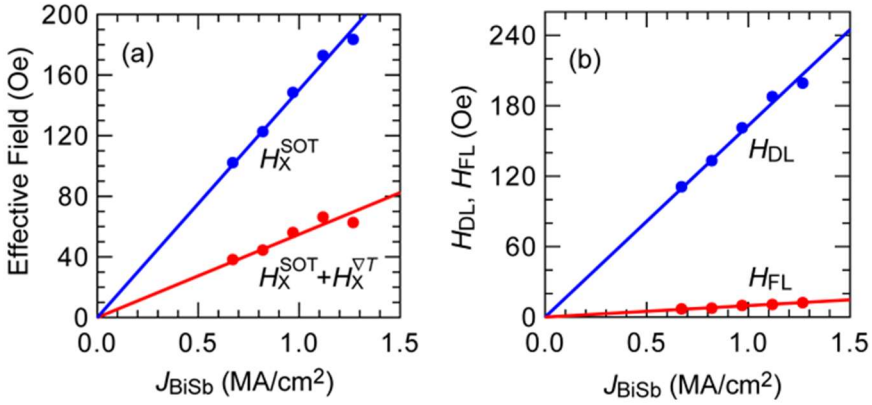

Figure 3.5. $H_X^{SOT} = H_{DL} + 2\xi H_{FL}$ and the apparent SOT field $H_X = H_X^{SOT} + H_X^{\nabla T}$ estimated from the low field data. The thermal contribution $H_X^{\nabla T}$ leads to underestimation of H_X^{SOT} by nearly 3 times. (b) Corrected H_{DL} and H_{FL} as a function of the current density in the BiSb layer.

To see how the thermal effects influence estimation of SOT from the low field data of the sample B, we measured the low field $R_{xy}^{2\omega}$ with H_{ext} applied along the *x*-direction, and then subtracted α_{ONE}^{out} and $R_{ANE+SSE}^{out}/H_k^{eff}$ from the gradient of $R_{xy}^{2\omega}$ to estimate the intrinsic SOT contribution. Figure 5(a) shows the apparent SOT field H_X estimated by,

$$H_X = -2\frac{\dfrac{\partial R_{xy}^{2\omega}}{\partial H_{ext}}}{\dfrac{\partial^2 R_{xy}^{\omega}}{\partial H_{ext}^2}} = [H_{DL} + 2\xi H_{FL}] + \frac{2H_k^{eff\,2}}{R_{AHE}}\left[\alpha_{ONE}^{out} + \frac{R_{ANE+SSE}^{out}}{H_k^{eff}}\right] = H_X^{SOT} + H_X^{\nabla T}. \quad (3.4)$$

As shown in Figure 3.5(a), the apparent H_X (red) are about 3 times smaller than $H_X^{SOT} = H_{DL} + 2\xi H_{FL}$ (blue) due to the large negative $R_{ANE+SSE}^{out}$ contribution. In this case, the contributions of thermal effects lead to underestimation of SOT. By

combining with the $2\xi H_{\mathrm{DL}} + H_{\mathrm{FL+OF}}$ data obtained from low field $R_{\mathrm{xy}}^{2\omega}$ measured with H_{ext} applied along the y-direction, we estimated H_{DL} and H_{FL}. Here, we used $\xi = 0.020$ and calculated the Oersted field by $\frac{1}{2}\mu_0 t_{\mathrm{BiSb}} J_{\mathrm{BiSb}}$,[13] where μ_0 and t_{BiSb} are the vacuum permeability and the thickness of BiSb layer, respectively. Figure 3.5(b) shows H_{DL} and H_{FL} as a function of J_{BiSb}. H_{FL} was about 10 times smaller than H_{DL} which is consistent with the previous report.[17] Subtracting contribution from the self-SOT effect in the CoPt layer, we obtained $\theta_{\mathrm{SH}}^{\mathrm{eff}}$=1.9 for BiSb, consistent with that estimated from the angle resolved technique, as shown in Figure 3.4(c). If we did not consider the thermal effects, $\theta_{\mathrm{SH}}^{\mathrm{eff}}$ estimated after subtracting the self-SOT contribution of CoPt from the apparent SOT field $H_{\mathrm{X}} = -2\frac{\partial R_{\mathrm{xy}}^{2\omega}/\partial H_{\mathrm{ext}}}{\partial^2 R_{\mathrm{xy}}^{\omega}/\partial H_{\mathrm{ext}}^2}$ data would be -1.1, whose magnitude and polarity are both different, highlighting the importance of eliminating contributions of the thermal effects.

3.5 Summary

In this chapter, we have shown how thermal effects can contaminate the low field second harmonic signals and reminded the importance of eliminating contributions from thermal effects in low field data. We then generalized the angle resolved second harmonic technique to include the ONE contribution, and demonstrated its effectiveness in disentangling SOT, ONE, and ANE/SSE. These results provide an accurate way to precisely estimate SOT in sample with large $H_{\mathrm{k}}^{\mathrm{eff}}$ where high field second harmonic data are not available. The generalized angle resolved second harmonic is applied to YPtBi films with strong PMA CoPt layer discussed in Chapter 5.

3.6 Appendix

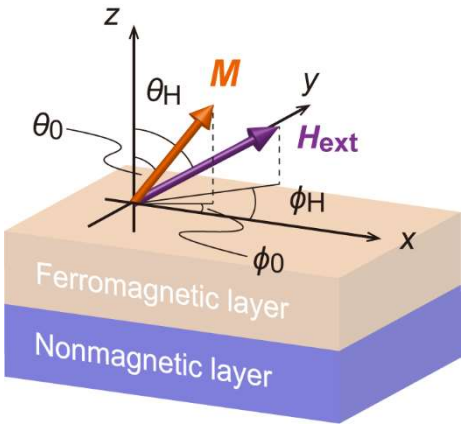

Figure 3.6. Coordination system and schematic illustration for angle resolved second harmonic measurement.

We derive the formulas for the second harmonic measurement. For this purpose, we assume a heterostructure of a nonmagnetic layer and a ferromagnetic layer, as shown in Figure 3.6. First, we consider an equilibrium state of magnetization under H_{ext} without spin current. Then, the magnetic energy E can be written by,

$$\frac{E}{M_{\mathrm{S}}} = -\frac{1}{2}\boldsymbol{m}\cdot\boldsymbol{H}_{\mathbf{k}}^{\mathbf{eff}} - \boldsymbol{m}\cdot\boldsymbol{H}_{\mathbf{ext}}, \tag{3.5}$$

where, $\boldsymbol{m}$ is a magnetization unit vector and $\boldsymbol{H}_{\mathbf{k}}^{\mathbf{eff}}$ is given by,

$$\boldsymbol{H}_{\mathbf{k}}^{\mathbf{eff}} = H_{\mathrm{k}}^{\mathrm{eff}} m_{\mathrm{z}}\hat{\boldsymbol{z}} = \left(\frac{2K_{\mathrm{U}}}{M_{\mathrm{S}}} - 4\pi M_{\mathrm{S}}\right) m_{\mathrm{z}}\hat{\boldsymbol{z}}, \tag{3.6}$$

where K_{U} is a unidirectional magnetic anisotropy energy. By using the spherical coordination system for the magnetization unit vector as shown in Figure 3.6, equation (3.5) can be written as,

$$\frac{E}{M_{\mathrm{S}}} = -\frac{1}{2}H_{\mathrm{k}}^{\mathrm{eff}}\cos^2\theta_0 - [(H_{\mathrm{ext}}^{\mathrm{x}}\cos\phi_0 + H_{\mathrm{ext}}^{\mathrm{y}}\sin\phi_0)\sin\theta_0 + H_{\mathrm{ext}}^{\mathrm{z}}\cos\theta_0], \tag{3.7}$$

where θ_0 and ϕ_0 are polar and azimuth angles of an equilibrium point for the magnetization, respectively. When the magnetization points an equilibrium direction, differentials of equation (3.7) by θ_0 and ϕ_0 should be 0, thus

$$\frac{1}{M_{\mathrm{S}}}\frac{\partial E}{\partial \theta_0} = \frac{1}{2}H_{\mathrm{k}}^{\mathrm{eff}}\sin 2\theta_0 - [(H_{\mathrm{ext}}^{\mathrm{x}}\cos\phi_0 + H_{\mathrm{ext}}^{\mathrm{y}}\sin\phi_0)\cos\theta_0 - H_{\mathrm{ext}}^{\mathrm{z}}\sin\theta_0] = 0, \quad (3.8)$$

$$\frac{1}{M_{\mathrm{S}}}\frac{\partial E}{\partial \phi_0} = (H_{\mathrm{ext}}^{\mathrm{x}}\sin\phi_0 - H_{\mathrm{ext}}^{\mathrm{y}}\cos\phi_0)\sin\theta_0 = 0. \quad (3.9)$$

If a current is applied, the equilibrium direction of magnetization will slightly change due to a spin induced effective filed $\Delta\boldsymbol{H}_{\mathbf{SOT}}$. These changes $\Delta\theta$ and $\Delta\phi$ can be written by,

$$\Delta\theta = \frac{\partial\theta_0}{\partial H_{\mathrm{SOT}}^{\mathrm{x}}}\Delta H_{\mathrm{SOT}}^{\mathrm{x}} + \frac{\partial\theta_0}{\partial H_{\mathrm{SOT}}^{\mathrm{y}}}\Delta H_{\mathrm{SOT}}^{\mathrm{y}} + \frac{\partial\theta_0}{\partial H_{\mathrm{SOT}}^{\mathrm{z}}}\Delta H_{\mathrm{SOT}}^{\mathrm{z}}, \quad (3.10)$$

$$\Delta\phi = \frac{\partial\phi_0}{\partial H_{\mathrm{SOT}}^{\mathrm{x}}}\Delta H_{\mathrm{SOT}}^{\mathrm{x}} + \frac{\partial\phi_0}{\partial H_{\mathrm{SOT}}^{\mathrm{y}}}\Delta H_{\mathrm{SOT}}^{\mathrm{y}} + \frac{\partial\phi_0}{\partial H_{\mathrm{SOT}}^{\mathrm{z}}}\Delta H_{\mathrm{SOT}}^{\mathrm{z}}. \quad (3.11)$$

Here, we approximate $\partial\theta_0/\partial H_{\mathrm{SOT}}^{\mathrm{i}}$ and $\partial\phi_0/\partial H_{\mathrm{SOT}}^{\mathrm{i}}$ by $\partial\theta_0/\partial H_{\mathrm{ext}}^{\mathrm{i}}$ and $\partial\phi_0/\partial H_{\mathrm{ext}}^{\mathrm{i}}$ (i = x, y, z), respectively. $\partial\theta_0/\partial H_{\mathrm{ext}}^{\mathrm{i}}$ and $\partial\phi_0/\partial H_{\mathrm{ext}}^{\mathrm{i}}$can be obtained from equations (3.8) and (3.9) with differentials by $H_{\mathrm{ext}}^{\mathrm{i}}$,

$$\frac{1}{M_{\mathrm{S}}}\frac{\partial^2 E}{\partial H_{\mathrm{ext}}^{\mathrm{i}}\partial\theta_0} = [H_{\mathrm{k}}^{\mathrm{eff}}\cos 2\theta_0 + (H_{\mathrm{ext}}^{\mathrm{x}}\cos\phi_0 + H_{\mathrm{ext}}^{\mathrm{y}}\sin\phi_0)\sin\theta_0 + H_{\mathrm{ext}}^{\mathrm{z}}\cos\theta_0]\frac{\partial\theta_0}{\partial H_{\mathrm{ext}}^{\mathrm{i}}}$$
$$+(H_{\mathrm{ext}}^{\mathrm{x}}\sin\phi_0 - H_{\mathrm{ext}}^{\mathrm{y}}\cos\phi_0)\cos\theta_0\frac{\partial\phi_0}{\partial H_{\mathrm{ext}}^{\mathrm{i}}} - f_{\mathrm{i}} = 0, \quad (3.12)$$

$$\frac{1}{M_{\mathrm{S}}}\frac{\partial^2 E}{\partial H_{\mathrm{ext}}^{\mathrm{i}}\partial\phi_0} = (H_{\mathrm{ext}}^{\mathrm{x}}\sin\phi_0 - H_{\mathrm{ext}}^{\mathrm{y}}\cos\phi_0)\cos\theta_0\frac{\partial\theta_0}{\partial H_{\mathrm{ext}}^{\mathrm{i}}}$$
$$+(H_{\mathrm{ext}}^{\mathrm{x}}\cos\phi_0 + H_{\mathrm{ext}}^{\mathrm{y}}\sin\phi_0)\sin\theta_0\frac{\partial\phi_0}{\partial H_{\mathrm{ext}}^{\mathrm{i}}} - g_{\mathrm{i}} = 0, \quad (3.13)$$

where, $\boldsymbol{f}$ and $\boldsymbol{g}$ are given by

$$\boldsymbol{f} = (\cos\theta_0\cos\phi_{\mathrm{H}}, \quad \cos\theta_0\sin\phi_{\mathrm{H}}, \quad -\sin\theta_0), \quad (3.14)$$

$$\boldsymbol{g} = (-\sin\theta_0\sin\phi_{\mathrm{H,}} \quad \sin\theta_0\cos\phi_{\mathrm{H}}, \quad 0). \quad (3.15)$$

For simplicity, we assume that an in-plane component of magnetization is determined by the direction of H_{ext}, which is reasonable except for samples with a strong in-plane easy axis such as nano wires. When H_{ext} is applied in the *xz*-plane under this approximation, equations (3.12) and (3.13) are written as,

$$[H_{\mathrm{k}}^{\mathrm{eff}}\cos 2\theta_0 + |H_{\mathrm{ext}}|\cos(\theta_{\mathrm{H}}-\theta_0)]\frac{\partial\theta_0}{\partial H_{\mathrm{ext}}^{\mathrm{i}}} = f_{\mathrm{i}}, \tag{3.16}$$

$$|H_{\mathrm{ext}}|\sin\theta_{\mathrm{H}}\sin\theta_0\frac{\partial\phi_0}{\partial H_{\mathrm{ext}}^{\mathrm{i}}} = g_i, \tag{3.17}$$

$$f_{\mathrm{i}} = (\cos\theta_0\,, \quad 0, \quad -\sin\theta_0), \tag{3.18}$$

$$g_i = (0, \quad \sin\theta_0, \quad 0). \tag{3.19}$$

Therefore, $\Delta\theta$ and $\Delta\phi$ are given by,

$$\Delta\theta = \frac{\Delta H_{\mathrm{SOT}}^{\mathrm{x}}\cos\theta_0 - \Delta H_{\mathrm{SOT}}^{z}\sin\theta_0}{H_{\mathrm{k}}^{\mathrm{eff}}\cos 2\theta_0 + |H_{\mathrm{ext}}|\cos(\theta_{\mathrm{H}}-\theta_0)}, \tag{3.20}$$

$$\Delta\phi = \frac{\Delta H_{\mathrm{SOT}}^{\mathrm{y}}}{|H_{\mathrm{ext}}|\sin\theta_{\mathrm{H}}}. \tag{3.21}$$

Here, when a current is applied along the *x*-direction with $\boldsymbol{p_S} = (0 \quad -1 \quad 0)$, $\Delta\boldsymbol{H}_{\mathbf{SOT}}$ is given by,

$$\begin{aligned}\Delta\boldsymbol{H}_{\mathbf{SOT}} &= (H_{\mathrm{DL}}\cos\theta_0\,, \quad -H_{\mathrm{FL+OF}}, \quad -H_{\mathrm{DL}}\sin\theta_0\cos\phi_H)\\ &= (H_{\mathrm{DL}}\cos\theta_0\,, \quad -H_{\mathrm{FL+OF}}, \quad -H_{\mathrm{DL}}\sin\theta_0),\end{aligned} \tag{3.22}$$

and thus, we finally obtain $\Delta\theta$ and $\Delta\phi$ as,

$$\Delta\theta = \frac{H_{\mathrm{DL}}}{H_{\mathrm{k}}^{\mathrm{eff}}\cos 2\theta_0 + |H_{\mathrm{ext}}|\cos(\theta_{\mathrm{H}}-\theta_0)}, \tag{3.23}$$

$$\Delta\phi = -\frac{H_{\mathrm{FL+OF}}}{|H_{\mathrm{ext}}|\sin\theta_{\mathrm{H}}}. \tag{3.24}$$

When an AC current is applied, $\Delta\theta$ and $\Delta\phi$ also change with the same frequency with the current. Then, the effects of $\Delta\theta$ and $\Delta\phi$ appear in a second harmonic Hall resistance because the anomalous Hall and planar Hall resistances can be expressed as follows by using Taylor expansion,

$$R_{\mathrm{AHE}}\cos(\theta_0+\Delta\theta) \sim R_{\mathrm{AHE}}\cos\theta_0 - R_{\mathrm{AHE}}\sin\theta_0\,\Delta\theta, \tag{3.25}$$

$$\begin{aligned}&R_{\mathrm{PHE}}\sin^2(\theta_0+\Delta\theta)\sin 2(\phi_0+\Delta\phi) \sim R_{\mathrm{PHE}}\sin^2\theta_0\sin 2\phi_0\\ &+R_{\mathrm{PHE}}\sin 2\theta_0\sin 2\phi_0\,\Delta\theta + 2R_{\mathrm{PHE}}\sin^2\theta_0\cos 2\phi_0\,\Delta\phi.\end{aligned} \tag{3.26}$$

By considering the ONE, ANE and SSE induced by a temperature gradient along the *z*- and *x*-directions, the first and second harmonic Hall resistance at ϕ_0= 0 is given

by,

$$R_{\mathrm{xy}}^{\omega} = R_{\mathrm{AHE}} \cos\theta_0 \,, \tag{3.27}$$

$$R_{\mathrm{xy}}^{2\omega} = \frac{R_{\mathrm{AHE}}}{2} \sin\theta_0 \,\Delta\theta - R_{\mathrm{PHE}} \sin^2\theta_0 \,\Delta\phi - (\alpha_{\mathrm{ONE}}^{\mathrm{in}} \cos\theta_{\mathrm{H}} - \alpha_{\mathrm{ONE}}^{\mathrm{out}} \sin\theta_{\mathrm{H}})|H_{\mathrm{ext}}|$$
$$-(R_{\mathrm{ANE+SSE}}^{\mathrm{in}} \cos\theta_0 - R_{\mathrm{ANE+SSE}}^{\mathrm{out}} \sin\theta_0), \tag{3.28}$$

where magneto thermoelectric effects in R_{xy}^{ω} is omitted due to its smaller contribution comparing with the AHE. By substituting equation (3.23) and (3.24) into equation (3.28), we obtain

$$R_{\mathrm{xy}}^{2\omega} = \frac{R_{\mathrm{AHE}}}{2} \frac{H_{\mathrm{DL}} \sin\theta_0}{H_{\mathrm{K}}^{\mathrm{eff}} \cos 2\theta_0 + |H_{\mathrm{ext}}| \cos(\theta_{\mathrm{H}} - \theta_0)} + R_{\mathrm{PHE}} \frac{H_{\mathrm{FL+OF}} \sin^2\theta_0}{|H_{\mathrm{ext}}| \sin\theta_{\mathrm{H}}}$$
$$-(\alpha_{\mathrm{ONE}}^{\mathrm{in}} \cos\theta_{\mathrm{H}} - \alpha_{\mathrm{ONE}}^{\mathrm{out}} \sin\theta_{\mathrm{H}})|H_{\mathrm{ext}}| - (R_{\mathrm{ANE+SSE}}^{\mathrm{in}} \cos\theta_0 - R_{\mathrm{ANE+SSE}}^{\mathrm{out}} \sin\theta_0). \tag{3.29}$$

Equation (3.29) is the basement for all equations of second harmonic measurement. First, we derive the equation for the high field method. In the high field method, H_{ext} larger than $H_{\mathrm{K}}^{\mathrm{eff}}$ is applied along the *x*-direction. Then, the condition $\theta_0 = \theta_{\mathrm{H}} = \pi/2$ should be satisfied, and thus, one can obtain,

$$R_{\mathrm{xy}}^{2\omega} = \frac{R_{\mathrm{AHE}}}{2} \frac{H_{\mathrm{DL}}}{|H_{\mathrm{ext}}| - H_{\mathrm{K}}^{\mathrm{eff}}} + R_{\mathrm{PHE}} \frac{H_{\mathrm{FL+OF}}}{|H_{\mathrm{ext}}|} + \alpha_{\mathrm{ONE}}^{\mathrm{out}} |H_{\mathrm{ext}}| + R_{\mathrm{ANE+SSE}}^{\mathrm{out}}. \tag{3.30}$$

Next, we derive the equation for the low field method. When a small H_{ext} is applied in the *xy*-plane, θ_0 will take small values. Under this situation, from equation (3.8), θ_0 is written by,

$$\theta_0 = \pm \frac{|H_{\mathrm{ext}}|}{H_{\mathrm{k}}^{\mathrm{eff}}}, \tag{3.31}$$

where, the sign $\pm$ corresponds to the *z*-direction of $\boldsymbol{m}$. By using (11.31), R_{xy}^{ω} given by equation (3.27) can be expanded as,

$$R_{\mathrm{xy}}^{\omega} = R_{\mathrm{AHE}} \cos\theta_0 \approx \pm R_{\mathrm{AHE}} \left[1 - \frac{1}{2} \left(\frac{|H_{\mathrm{ext}}|}{H_{\mathrm{k}}^{\mathrm{eff}}} \right)^2 \right]. \tag{3.32}$$

In the same manner, one can obtain $R_{\mathrm{xy}}^{2\omega}$ with H_{ext} along the *x*- and *y*-direction as

follows.

$$R_{\mathrm{xy}}^{2\omega}\big|_{\mathrm{x}} = \frac{R_{\mathrm{AHE}}}{2}\frac{H_{\mathrm{DL}}\sin\theta_0}{H_{\mathrm{k}}^{\mathrm{eff}}\cos 2\theta_0 + |H_{\mathrm{ext}}|\sin\theta_0} + R_{\mathrm{PHE}}\frac{H_{\mathrm{FL+OF}}\sin^2\theta_0}{|H_{\mathrm{ext}}|}$$
$$+\alpha_{\mathrm{ONE}}^{\mathrm{out}}|H_{\mathrm{ext}}| - R_{\mathrm{ANE+SSE}}^{\mathrm{in}}\cos\theta_0 + R_{\mathrm{ANE+SSE}}^{\mathrm{out}}\sin\theta_0$$
$$\approx \left[\frac{R_{\mathrm{AHE}}}{2}H_{\mathrm{DL}} + R_{\mathrm{PHE}}H_{\mathrm{FL}}\right]\frac{|H_{\mathrm{ext}}|}{{H_{\mathrm{k}}^{\mathrm{eff}}}^2} + \left[\alpha_{\mathrm{ONE}}^{\mathrm{out}}|H_{\mathrm{ext}}| \mp R_{\mathrm{ANE}}^{\mathrm{in}} + R_{\mathrm{ANE}}^{\mathrm{out}}\frac{|H_{\mathrm{ext}}|}{H_{\mathrm{k}}^{\mathrm{eff}}}\right]. \quad (3.33)$$

$$R_{\mathrm{xy}}^{2\omega}\big|_{\mathrm{y}} = -\frac{R_{\mathrm{AHE}}}{2}\frac{H_{\mathrm{FL+OF}}\sin\theta_0\cos\theta_0}{H_{\mathrm{k}}^{\mathrm{eff}}\cos 2\theta_0 + |H_{\mathrm{ext}}|\sin\theta_0} - R_{\mathrm{PHE}}\frac{H_{\mathrm{DL}}\cos\theta_0\sin^2\theta_0}{|H_{\mathrm{ext}}|} - R_{\mathrm{ANE}}^{\mathrm{in}}\cos\theta_0$$
$$\approx \mp\left[\frac{R_{\mathrm{AHE}}}{2}H_{\mathrm{FL+OF}} + R_{\mathrm{PHE}}H_{\mathrm{DL}}\right]\frac{|H_{\mathrm{ext}}|}{{H_{\mathrm{k}}^{\mathrm{eff}}}^2} \mp R_{\mathrm{ANE}}^{\mathrm{in}}. \quad (3.34)$$

Therefore, the second derivative of R_{xy}^{ω} and first derivative of $R_{\mathrm{xy}}^{2\omega}$ by H_{ext} are given by,

$$\frac{d^2R_{\mathrm{xy}}^{\omega}}{dH_{\mathrm{ext}}^2} = \mp\frac{R_{\mathrm{AHE}}}{{H_{\mathrm{k}}^{\mathrm{eff}}}^2}, \quad (3.35)$$

$$\frac{dR_{\mathrm{xy}}^{2\omega}\big|_{\mathrm{x}}}{dH_{\mathrm{ext}}} = \frac{1}{{H_{\mathrm{k}}^{\mathrm{eff}}}^2}\left[\frac{R_{\mathrm{AHE}}}{2}H_{\mathrm{DL}} + R_{\mathrm{PHE}}H_{\mathrm{FL}}\right] + \left[\alpha_{\mathrm{ONE}}^{\mathrm{out}} + \frac{R_{\mathrm{ANE}}^{\mathrm{out}}}{H_{\mathrm{k}}^{\mathrm{eff}}}\right], \quad (3.36)$$

$$\frac{dR_{\mathrm{xy}}^{2\omega}\big|_{\mathrm{y}}}{dH_{\mathrm{ext}}} = \mp\frac{1}{{H_{\mathrm{k}}^{\mathrm{eff}}}^2}\left[\frac{R_{\mathrm{AHE}}}{2}H_{\mathrm{FL+OF}} + R_{\mathrm{PHE}}H_{\mathrm{DL}}\right]. \quad (3.37)$$

Then, we obtain the effective fields H_{X} and H_{Y} from (3.35) – (3.37) as follows.

$$H_{\mathrm{X}} = -2\frac{\dfrac{dR_{\mathrm{xy}}^{2\omega}\big|_{\mathrm{x}}}{dH_{\mathrm{ext}}}}{\dfrac{d^2R_{\mathrm{xy}}^{\omega}}{dH_{\mathrm{ext}}^2}} = \pm[H_{\mathrm{DL}} + 2\xi H_{\mathrm{FL}}] \pm \frac{2(H_{\mathrm{k}}^{\mathrm{eff}})^2}{R_{\mathrm{AHE}}}\left[\alpha_{\mathrm{ONE}}^{\mathrm{out}} + \frac{R_{\mathrm{ANE}}^{\mathrm{out}}}{H_{\mathrm{k}}^{\mathrm{eff}}}\right]. \quad (3.38)$$

$$H_{\mathrm{Y}} = -2\frac{\dfrac{dR_{\mathrm{xy}}^{2\omega}\big|_{\mathrm{y}}}{dH_{\mathrm{ext}}}}{\dfrac{d^2R_{\mathrm{xy}}^{\omega}}{dH_{\mathrm{ext}}^2}} = -[H_{\mathrm{FL}} + 2\xi H_{\mathrm{DL}}]. \quad (3.39)$$

$$\xi = \frac{R_{\mathrm{PHE}}}{R_{\mathrm{AHE}}}. \quad (3.40)$$

One can see that H_{X} contains contributions from the thermal effects, which can be very large when the sample has large $H_{\mathrm{k}}^{\mathrm{eff}}$. On the other hand, H_{Y} does not contain contributions from thermal effects. Therefore, the low field method with H_{ext} applied

along the *y*-direction can precisely evaluate the spin orbit torque. However, one has to combine the angle-resolved method with H_{ext} applied along the *x*-direction because H_{DL} and H_{FL} are entangled.

Finally, we derive the equation for the angle resolved method. When H_{ext} is applied in the *xz*-plane, one can obtain the following equation from equation (3.8) for small θ_0 and θ_H,

$$\theta_0 = \frac{|H_{ext}|}{|H_{ext}| + H_k^{eff}} \theta_H. \tag{3.41}$$

Therefore, equation (3.29) with small θ_0 and θ_H also can be written as,

$$R_{xy}^{2\omega} = \pm \left(\frac{R_{AHE}}{2} H_{DL} + R_{PHE} H_{FL+OF} \right) \frac{|H_{ext}| \theta_H}{(|H_{ext}| + H_k^{eff})^2} \mp \alpha_{ONE}^{in} |H_{ext}|$$
$$\pm \alpha_{ONE}^{out} \theta_H |H_{ext}| \mp R_{ANE+SSE}^{in} \pm R_{ANE+SSE}^{out} \frac{|H_{ext}| \theta_H}{|H_{ext}| + H_k^{eff}}, \tag{3.42}$$

where, the sign $\pm$ corresponds to the up/down-direction of H_{ext} or $\boldsymbol{m}$. By calculating the differential of (3.42) by θ_H, we obtain

$$\frac{1}{|H_{ext}|} \frac{dR_{xy}^{2\omega}}{d\theta_H} = \pm \left(\frac{R_{AHE}}{2} H_{DL} + R_{PHE} H_{FL+OF} \right) (|H_{ext}| + H_k^{eff})^{-2}$$
$$\pm R_{ANE+SSE}^{out} (|H_{ext}| + H_k^{eff})^{-1} \pm \alpha_{ONE}^{out}. \tag{3.43}$$

From equation (3.43), we can see that the SOT contribution has a $(|H_{ext}| + H_k^{eff})^{-2}$ dependence, the ANE and SSE contribution have a $(|H_{ext}| + H_k^{eff})^{-1}$ dependence, while the ONE has a constant contribution to $|H_{ext}|^{-1} dR_{xy}^{2\omega}/d\theta_H$. Thus, by measuring $dR_{xy}^{2\omega}/d\theta_H$ as a function of H_{ext} at various small θ_H and fitting to equation (3.43), we can separate the SOT contribution from that of the thermal effects.

3.7 References

[1] I. M. Miron, K. Garello, G. Gaudin, P-J. Zermatten, M. V. Costache, S. Auffret, S. Bandiera, B. Rodmacq, A. Schuhl, and P. Gambardella, Nature **476**, 189 (2011).

[2] S. Fukami, T. Anekawa, C. Zhang, and H. Ohno, Nat. Nanotech. **11**, 621 (2016).

[3] M. Hayashi, J. Kim, M. Yamanouchi, and H. Ohno, Phys Rev. B **89**, 144425 (2014).

[4] C. O. Avci, K. Garello, M. Gabureac, A. Ghosh, A. Fuhrer, S. F. Alvarado, and P. Gambardella, Phys. Rev. B **90**, 224427 (2014).

[5] J. Kim, J. Sinha, M. Hayashi, M. Yamanouchi, S. Fukami, T. Suzuki, S. Mitani, and H. Ohno, Nat. Mater. **12**, 240 (2013).

[6] J. Torrejon, J. Kim, J. Sinha, S. Mitani, M. Hayashi, M. Yamanouchi, and H. Ohno, Nat. Commun. **5**, 4655 (2014).

[7] S.-H. C. Baek, V. P. Amin, Y.-W. Oh, G. Go, S.-J. Lee, G.-H. Lee, K.-J. Kim, M. D. Stiles, B.-G. Park, and K.-J. Lee, Nat. Mater. **17**, 509 (2018).

[8] L. Zhu, L. Zhu, M. Sui, D. C. Ralph, and R. A. Buhrman, Sci. Adv. 2019 **5**, eaav8025 (2019).

[9] T-Y. Chen, C-W. Peng, T-Y. Tsai, W-B. Liao, C-T. Wu, H-W. Yen, and C-F. Pai, ACS Appl. Mater. Interfaces **12**, 7788 (2020).

[10] Y. Fan, P. Upadhyaya, X. Kou, M. Lang, S. Takei, Z. Wang, J. Tang, L. He, L-T. Chang, M. Montazeri, *et al*. Nat. Mater. **13**, 699 (2014).

[11] H, Wu, P. Zhang, P. Deng, Q. Lan, Q. Pan, S. A. Razavi, X. Che, L. Huang, B. Dai, K. Wong, *et al*. Phys. Rev. Lett. **123**, 207205 (2019).

[12] N. H. D. Khang, S. Nakano, T. Shirokura, Y. Miyamoto, and P. N. Hai, Sci. Rep. **10**, 12185 (2020).

[13] H. Yang, H. Chen, M. Tang, S. Hu, and X. Qiu, Phys. Rev. B **102**, 024427 (2020).

[14] N. Roschewsky, E. S. Walker, P. Gowtham, S. Muschinske, F. Hellman, S. R. Bank, and S. Salahuddin, Phys. Rev. B **99**, 195103 (2019).

[15] M.-H. Nguyen, D. C. Ralph, and R. A. Buhrman, Phys. Rev. Lett. **116**, 126601 (2016).

[16] Y. Wang, P. Deorani, X. Qiu, J. H. Kwon, and H. Yang, Appl. Phys. Lett. **105**, 152412 (2014).

[17] N. H. D. Khang and P. N. Hai, Appl. Phys. Lett. **117**, 252402 (2020).

[18] L. Liu, C-F. Pai, Y. Li, H. W. Tseng, D. C. Ralph, and R. A. Buhrman, Science **336**, 555 (2012).

[19] K. Garello, I. M. Miron, C. O. Avci, F. Freimuth, Y. Mokrousov, S. Blügel, S. Auffret, O. Boulle, G. Gaudin, P. Gambardella, Nat. Nanotech. **8**, 587 (2013).

[20] N. H. D. Khang, Y. Ueda, P. N. Hai, Nat. Mater. **17**, 808 (2018).

[21] Y. Ueda, N. H. D. Khang, K. Yao, and P. N. Hai, Appl. Phys. Lett. **110**, 062401 (2017).

[22] B. Jinnai, C. Zhang, A. Kurenkov, M. Bersweiler, H. Sato, S. Fukami, and H. Ohno, Appl. Phys. Lett. 111, 102402 (2017).

Chapter 4.Spin Hall effect in YPt alloy

4.1 Introduction

Research on the SHE has been carried out focusing on materials with strong spin orbit interaction, such as HMs[1-4] and topological materials[5-8] because the spin orbit interaction is the origin of the SHE as described in Chapter 2. Although both HMs and topological materials show large θ_{SH}, the contribution of TSSs to the SHE is definitely important. In the case of our material, YPtBi, large contribution of TSS to the SHE is expected because YPtBi is a kind of HHA-TSM, while the SHE in its components Y, Pt, Bi has no contribution from TSS. Here, to clarify the role of TSS for the SHE in YPtBi, we compare the SHE in its contributing elements and alloys. Among these elements, sputtered Pt films have demonstrated the largest θ_{SH} (0.05 – 0.16).[2,9-11] Although both the intrinsic mechanism (Berry phase) and the extrinsic mechanisms (skew scattering and the side-jump) can contribute to the SHE similar to the AHE,[9,12-14] the intrinsic Berry phase mechanism dominates the SHE in sputtered Pt films due to their poor conductivity. Because σ_{SH} takes a constant value when the SHE originates from the intrinsic mechanism, θ_{SH} is proportional to the resistivity of Pt films, indicating that resistivity control techniques can realize large θ_{SH}.

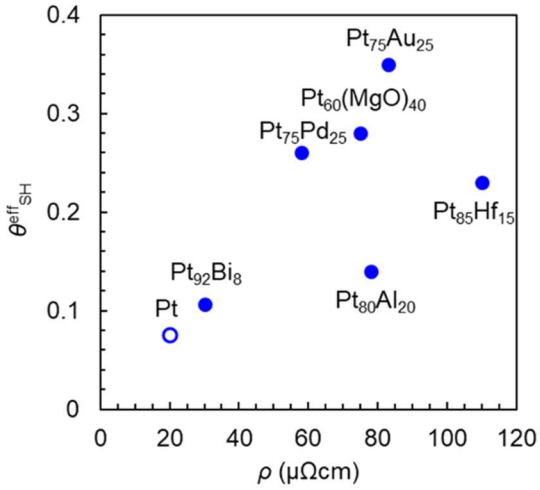

Figure 4.1. Benchmark of θ_{SH}^{eff} in Pt-based alloys.[2,15,16,18,20,21]

Alloying is one of the effective methods to increase Pt resistivity by increasing scattering centers or change of the Fermi level. There are many reports on θ_{SH} for Pt-based alloys utilizing wide variety of dopants from light metals, such as Al,[15,16] to HMs, such as Au.[15,17-22] Figure 4.1 shows the benchmark of θ_{SH} in Pt-based alloys. Alloying technique successfully realize large θ_{SH} by increasing their resistivity. Here, one of the components of YPtBi, $Pt_{1-x}Bi_x$, shows larger θ_{SH} than that for Pt by slightly increasing its resistivity.[21] However, there is no research on θ_{SH} in YPt despite its much higher resistivity caused by heavy doping.

In this chapter, we focused on the SHE in sputtered YPt films to clarify the importance of TSS in YPtBi via benchmark of θ_{SH} in Pt-based alloys. We investigated the origin of the SHE and its spin relaxation length λ_S of YPt by measuring the resistivity and thickness dependence of the SHE in YPt. We found the SHE in YPt is governed by both the intrinsic mechanism and the extrinsic side-jump mechanism with opposite polarity, and very long λ_S comparing with that expected in a Pt-based alloy with the same resistivity assuming the Elliott-Yafet (EY) mechanism.[23,24]

However, the maximum value of θ_{SH} of YPt was 0.081 despite its high resistivity, which is much smaller than that of YPtBi as shown later in Chapter 5. This result highlights the importance of the contribution of TSS to the SHE in YPtBi as described in Chapter 5.

4.2 Crystal analysis for YPt alloy and sample fabrication

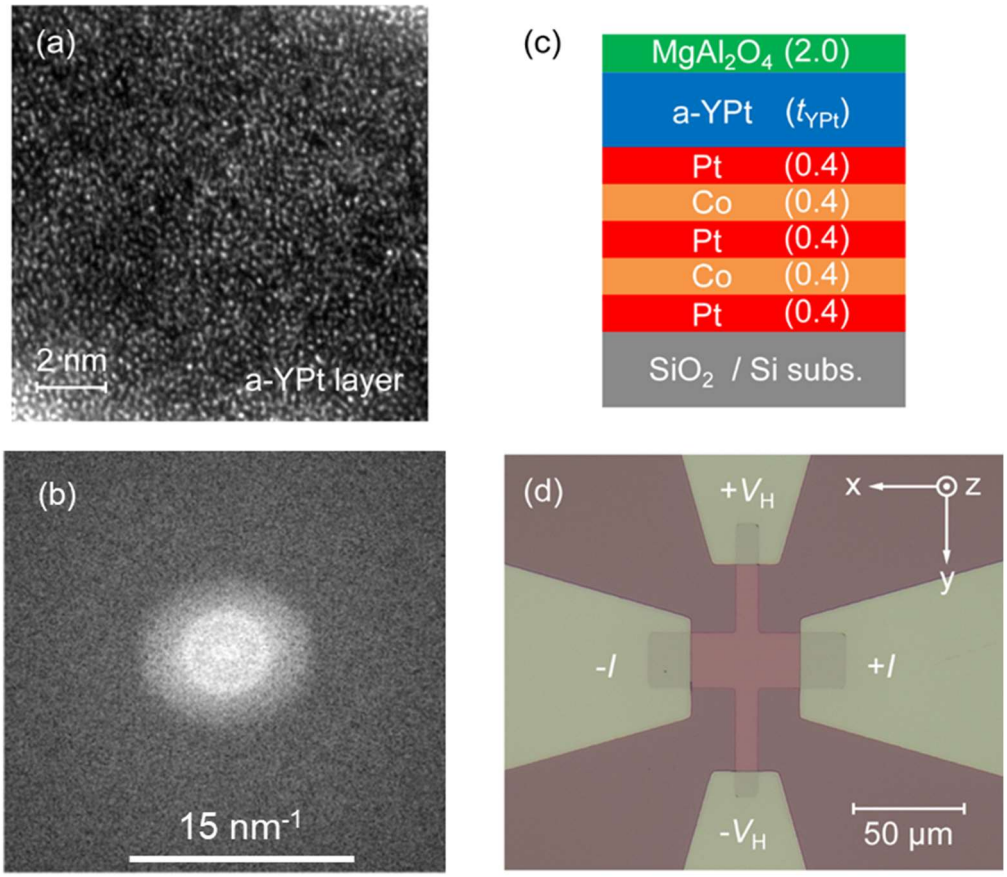

Figure 4.2 (a) Cross-sectional transmission electron microscopy (TEM) image of an YPt layer. (b) Fast Fourier transform of the TEM image. (c) Schematic structure of $MgAl_2O_4$ (2.0) / YPt (t_{YPt}) / [Pt (0.4) / Co (0.4)]$_2$ / Pt (0.4) deposited on oxidized Si substrates. (d) Optical image of a Hall bar device and coordination system for second harmonic measurements.

The YPt layers were deposited by magnetron sputtering at room temperature from an YPt target sintered from stoichiometric YPt powders. Stoichiometry of YPt

thin films were confirmed by X-ray fluorescence spectrometry (XRF) measurements. Figure 4.2(a) shows a cross-sectional transmission electron microscopy (TEM) image of an YPt layer, which show no long-range atomic ordering. Figure 4.2(b) shows the fast Fourier transformation (FFT) of the TEM image. The FFT image shows a single ring with diameter of 3.90 nm^{-1} followed by a halo pattern, corresponding to the nearest interatomic distance of 0.256 nm, which is different from that of crystallized orthorhombic YPt.[25] This value was also different from both the lattice constant and nearest interatomic distance for both face-centered cubic (fcc)-Pt and hexagonal close pack (hcp)-Y. Thus, the TEM and FFT images confirmed that our sputtered YPt alloy thin films are amorphous.

For evaluation of the SHE, we prepared $MgAl_2O_4$ (2.0) / YPt (t_{YPt}) / [Pt (0.4) / Co (0.4)]$_2$ / Pt (0.4) / SiO_2 / Si substrates by magnetron sputtering, as shown in Figure 4.2(c) (the unit of thickness for each layer is nanometer). The YPt layer thickness t_{YPt} ranges from 1.0 to 14.5 nm. The laminated [Pt (0.4) / Co (0.4)]$_2$ / Pt (0.4) multilayers are referred below as CoPt (2 nm) for short. Here, the 0.4 nm-thick Pt layers reduce H_k^{eff} of Co by their interfacial uniaxial magnetic anisotropy, which is essential for accurate estimation of the effective spin Hall angle from the second harmonic measurements. Note that the SHE from Pt layers are negligible because the Pt thickness of 0.4 nm is few times to one magnitude thinner than typical λ_S of Pt,[10,11,26,27] and the Pt/Co multilayers are laminated in a symmetric fashion. We fabricated 25×50 μm^2 Hall bars with Ta electrodes for second harmonics measurements. Figure 4.2(d) shows an optical image of a device and definition of the coordination system. We also fabricated four-terminal 60×100 μm^2 Hall bars to evaluate the sample conductance by the four-probe technique, which is essential for

calculation of the resistivity of the YPt and CoPt layers, as well as the current density in the YPt layer.

4.3 Ar pressure dependence of spin Hall effect for YPt alloy

Table 4.1. List of samples with structure of $MgAl_2O_4$ (2.0) / YPt (t_{YPt}) / [Pt (0.4) / Co (0.4)]$_2$ / Pt (0.4) studied in this work.

Samples	YPt thickness t_{YPt} (nm)	Sputtering Ar pressure (Pa)
A1	14.5	0.3
A2	12.8	0.5
A3	12.3	0.7
A4	13.0	1.0
A5	11.0	2.0
B1	8.9	0.3
B2	7.5	0.3
B3	6.0	0.3
B4	4.6	0.3
B5	3.2	0.3
B6	2.0	0.3
B7	1.0	0.3

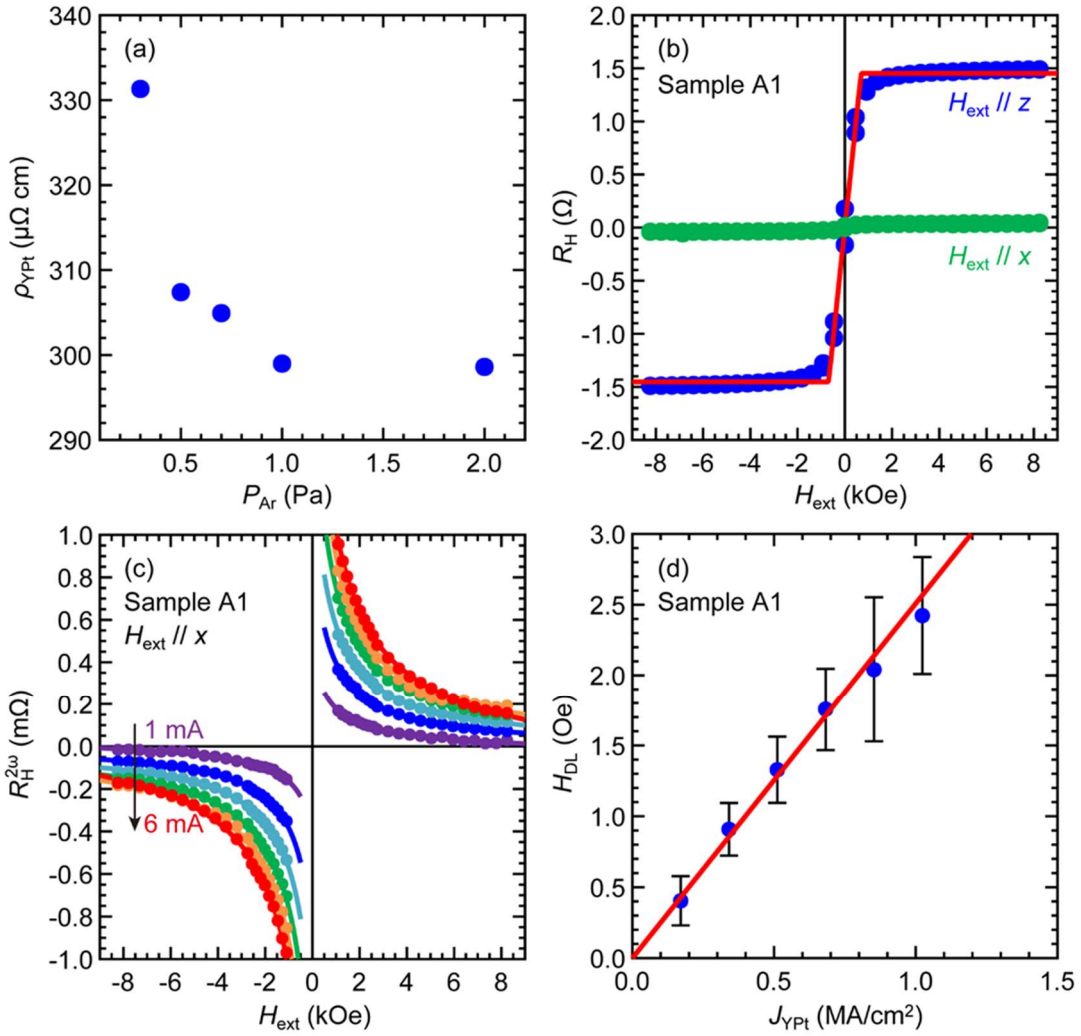

Figure 4.3 (a) Resistivity of YPt thin films deposited with various Ar pressure during sputtering deposition. (b) Anomalous Hall resistance of sample A1 with 14.5 nm-thick YPt deposited at Ar pressure of 0.3 Pa, measured with H_{ext} applied along the *x*- (green) and *z*-directions (blue). (c) Second harmonic Hall resistance of sample A1 measured with H_{ext} applied in-plane along the *x*-direction and bias currents of 1 – 6 mA (1 mA step). Solid lines are fitting curves using equation (4.1). (d) H_{DL} as a function of the current density in the YPt layer for sample A1.

To investigate the physical origins of the SHE in YPt, we prepared a series of samples $MgAl_2O_4$ (2.0) / YPt (11.0–14.5) / CoPt (2) with different Ar pressure of 0.3, 0.5, 0.7, 1.0, and 2.0 Pa during YPt sputtering deposition (Samples A1-A5 in Table 4.1). The corresponding YPt thickness t_{YPt} is 14.5, 12.8, 12.3, 13.0 and 11.0 nm,

respectively, as determined in advance by XRF for YPt stand-alone thin films deposited with the same condition. Figure 4.3(a) shows the resistivity of YPt layer ρ_{YPt} in each sample measured by the four-probe technique. ρ_{YPt} is 331 μΩcm at 0.3 Pa but gradually decreases and saturates at 299 μΩcm when the Ar pressure is increased to 2.0 Pa. These values are 1.5 – 10 times larger than those of other Pt-based alloys,[15-22] and comparable to that of β-W.[3]

Figure 4.3(b) shows the anomalous Hall resistance of a Hall bar device of sample A1 with 14.5 nm-thick YPt deposited at 0.3 Pa, measured with H_{ext} applied along the x (green) and z-directions (blue). The dots and the red solid line are the experimental data and fitting curve, respectively. The anomalous Hall resistance was negligible when H_{ext} was applied along the x-direction, indicating that the CoPt magnetic layer has in-plane magnetic anisotropy (IMA). H_k^{eff} of -0.7±0.1 kOe was obtained from the anomalous Hall resistance data with H_{ext} applied along the z-direction. We then evaluate the spin orbit torque of this sample by the second harmonic technique with alternating currents at 259.68 Hz. In the case of IMA, $R_{xy}^{2\omega}$ measured at high enough H_{ext} applied along the x-direction is given by,[28,29]

$$R_{xy}^{2\omega} = \frac{R_{AHE}}{2}\frac{H_{DL}}{|H_{ext}| - H_k^{eff}} + R_{PHE}\frac{H_{FL+OF}}{|H_{ext}|} + \alpha_{ONE}|H_{ext}| + R_{ANE+SSE}, \qquad (4.1)$$

where α_{ONE} is a coefficient reflecting contribution from the ONE, and $R_{ANE+SSE}$ is a constant reflecting contribution from the ANE and SSE. Fitting was performed between 8.5 to 1 kOe and -8.5 to -1 kOe to extract the four parameters H_{DL}, H_{FL+OF}, α_{ONE} and $R_{ANE+SSE}$. Representative second harmonics data and the corresponding fitting for sample A1 at bias currents of 1 – 6 mA (1 mA step) are shown in Figure 4.3(c), where the dots and solid lines are the experimental data and fitting curves using equation (4.1), respectively. Figure 4.3(d) summarizes the obtained H_{DL} as a

function of the YPt current density J_{YPt}, which shows that the H_{DL} term increases with increasing charge current. Here J_{YPt} is determined using the parallel conduction model. Error bars include the fitting uncertainty of H_{DL} for the total of 44 data points in each curve, and the uncertainty of H_k^{eff} and R_{AHE} estimated from Figure 4.3(b). On the other hand, the H_{FL+OF} term was negligibly small and beyond the fitting uncertainty in our measurements, which is similar to heavily doped Pt(MgO) alloy.[16] We then calculate θ_{SH}^{eff} of YPt films by,

$$\theta_{SH}^{eff} = \frac{2eM_S t_{CoPt}}{\hbar} \frac{H_{DL}}{J_{YPt}}, \tag{4.2}$$

where parameters M_S and t_{CoPt} are 532±3 emu/cc and 2 nm, respectively. Here, the slope H_{DL}/J_{YPt} was calculated by the weighted least squares method, and then, θ_{SH}^{eff} of 0.081±0.007 was obtained for sample A1.

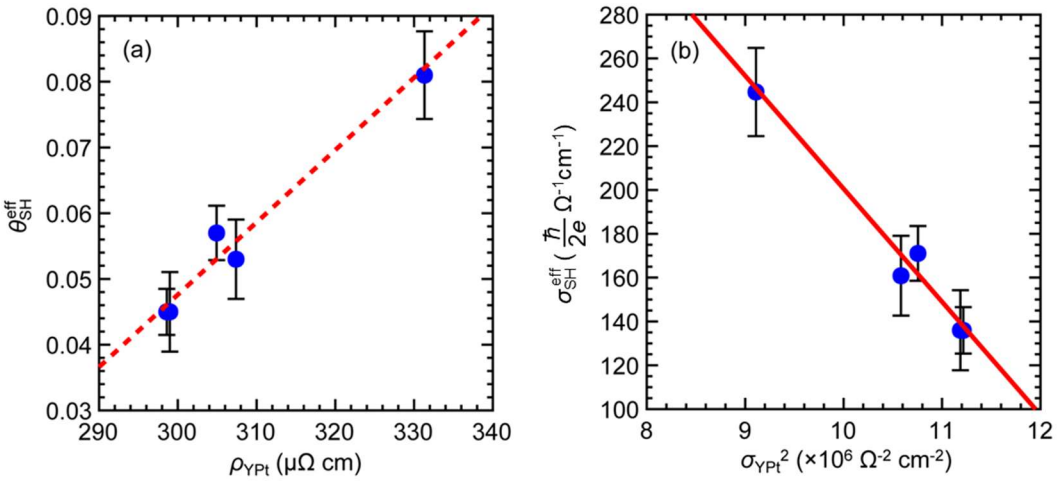

Figure 4.4 (a) θ_{SH}^{eff} of samples A1-A5 with various YPt deposited at different Ar pressure, as a function of their ρ_{YPt}. Dashed line is an approximation line. (b) σ_{SH}^{eff} of samples A1-A5 as a function of σ_{YPt}^2. Solid line is fitting using equation (4.3).

Figure 4.4(a) summarizes θ_{SH}^{eff} of samples A1-A5 with various YPt deposited at

different Ar pressure, as a function of their ρ_{YPt}. Note that the intrinsic θ_{SH} may be higher than θ_{SH}^{eff} if we consider correction due to the spin memory loss,[30,31] the spin back flow at the YPt/CoPt interface,[32] and the Hall bar geometry effect.[33] However, we will not attempt such correction here due to the lack of critical parameters such as spin mixing conductance at the YPt/CoPt interface. We observed a linear dependence of θ_{SH}^{eff} on ρ_{YPt}, which suggests that the intrinsic mechanism and/or the extrinsic side-jump mechanism dominate the SHE in YPt films. We note that, however, θ_{SH}^{eff} of YPt films is nearly doubled when ρ_{YPt} increases only by 10% from 299 to 331 μΩcm. To explain this high sensitivity of θ_{SH}^{eff} to ρ_{YPt}, we deconvolute the contribution of the intrinsic mechanism and the extrinsic side-jump mechanism by plotting the effective spin Hall conductivity $\sigma_{SH}^{eff} = \frac{\hbar}{2e}\theta_{SH}^{eff}\sigma_{YPt}$ as a function of σ_{YPt}^2 in Figure 4.4(b). We fit the $\sigma_{SH}^{eff} - \sigma_{YPt}^2$ relationships by (red line),[13]

$$\sigma_{SH}^{eff} = \alpha_{ext}\sigma_{YPt}^2 + \sigma_{SH}^{int}, \tag{4.3}$$

where α_{ext} is a coefficient reflecting contribution from the extrinsic side-jump mechanism. We obtained α_{ext} = (-5±1)×10^{-5} ($\hbar$/2e) Ωcm and σ_{SH}^{int} = 700±100 ($\hbar$/2e) Ω^{-1}cm^{-1}. Note that, the intrinsic mechanism, whose σ_{SH}^{int} was smaller but comparable to that of Pt,[9] contributes to the SHE in YPt films despite its amorphous structure and no Pt-precipitation in the films. This result shows that although there is no long-range atomic ordering in YPt alloy, there exists a finite Berry phase for the intrinsic SHE. Furthermore, our result indicates the contribution of the extrinsic and intrinsic mechanism has opposite polarity, which is a unique feature of YPt comparing with other crystallized Pt-based alloys. Due to the opposite polarity, YPt has a strong sensitivity of θ_{SH}^{eff} to ρ_{YPt} because the extrinsic term drastically reduces the contribution of the intrinsic term with a small decrease in ρ_{YPt}.

4.4 Thickness dependence of spin Hall effect for YPt alloy

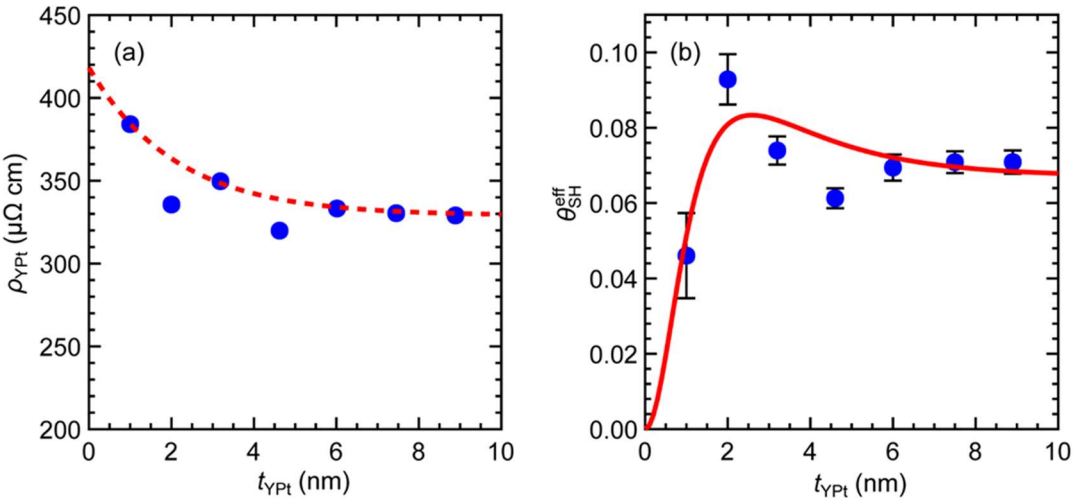

Figure 4.5. (a) Thicknesses dependence of ρ_{YPt} for YPt thin films deposited with Ar pressure of 0.3 Pa. Dashed line is an approximation curve. (b) θ_{SH}^{eff} of samples B1-B7 as a function of the YPt layer thickness. Solid line is a fitting curve using equation (4.4).

Next, we investigate the spin relaxation length in YPt. For this purpose, we prepared another series of samples with different t_{YPt} ranging from 1.0 to 8.9 nm deposited with Ar pressure of 0.3 Pa (samples B1-B7 in Table 4.1). Figure 4.5(a) shows t_{YPt}-dependence of ρ_{YPt}, where the blue dots and the red dashed line are experimental data and an approximation curve, respectively. ρ_{YPt} tends to increase with decrease of t_{YPt}, similar to previous reports on HMs.[10,15] The blue dots in Figure 4.5(b) show the experimental values of θ_{SH}^{eff} as a function of t_{YPt}. θ_{SH}^{eff} is about 0.07 for thick t_{YPt} but increases up to about 0.09 at 2 nm, then dropped to about 0.04 at 1 nm. This behavior can be explained by the tradeoff between enhancement of θ_{SH}^{eff} due to increase in ρ_{YPt} and suppression of θ_{SH}^{eff} due to diffusion of opposite spins from the rear side at small t_{YPt}, similar to Pt films on Ta buffers with strong thickness dependence of resistivity.[10] In our case, although ρ_{YPt} increased only 17% at small

t_{YPt}, the high sensitivity of θ_{SH}^{eff} to ρ_{YPt} causes the peak at 2 nm. We fit the experimental data by utilizing the following function,[2,34]

$$\theta_{SH}^{eff} = \theta_{SH0}[\rho_{YPt}(t_{YPt})]\left[1 - \mathrm{sech}\left(\frac{t_{YPt}}{\lambda_S}\right)\right]. \quad (4.4)$$

Here, $\theta_{SH0}(\rho_{YPt}) = \sigma_{SH0}/\sigma_{YPt} = \alpha_{ext}/\rho_{YPt} + \sigma_{SH}^{int}\rho_{YPt}$ is given by the fitting result of Figure 4.4(b), while $\rho_{YPt}(t_{YPt})$ is approximated by the red dashed line in Figure 4.5(a). The red solid line in Figure 4.5(b) shows the best fit curve with λ_S = 0.9 nm. In Pt-based alloys with the fcc structure, λ_S can be calculated from their resistivity and λ_S of Pt assuming the EY mechanism.[16] The estimated value of λ_S using the Pt-based alloy model is 0.3 nm,[11] which is smaller than the obtained value of 0.9 nm for YPt. This result is surprising given the amorphous nature of YPt.

4.5 Summary

In this chapter, we have investigated the SHE and its mechanism in YPt alloy thin films with various resistivity and thickness. It was found that θ_{SH}^{eff} of YPt increased linearly but drastically from 0.045 to 0.081 for a slight increase of ρ_{YPt} from 299 to 331 μΩcm. This strong sensitivity of θ_{SH}^{eff} to ρ_{YPt} was found to be governed by both the intrinsic mechanism and the extrinsic side-jump mechanism with opposite polarity. By deconvoluting the contribution of the intrinsic and extrinsic side-jump mechanisms, the large intrinsic spin Hall conductivity of 700±100 $\hbar/2e$ Ω^{-1}cm^{-1} was obtained despite its amorphous structure. Furthermore, we found that spin relaxation length λ_S of 0.9 nm for YPt is larger than that expected for a crystallized Pt-based alloy with the same resistivity. Although these unique results are very different from the conventional Pt-based alloys, YPt also cannot realize θ_{SH}^{eff} larger than unity. This result highlights the importance of the

contribution of a TSS to the giant SHE in YPtBi discussed in Chapter 5.

4.6 References

[1] L. Liu, C.-F. Pai, Y. Li, H. W. Tseng, D. C. Ralph and R. A. Buhrman, Science **336**, 555 (2012).

[2] L. Liu, T. Moriyama, D. C. Ralph and R. A. Buhrman, Phys. Rev. Lett. **106**, 036601 (2011).

[3] C.-F. Pai, L. Liu, Y. Li, H. W. Tseng, D. C. Ralph and R. A. Buhrman, Appl. Phys. Lett. **101**, 122404 (2012).

[4] Y. Takeuchi, C. Zhang, A. Okada, H. Sato, S. Fukami and H. Ohno, Appl. Phys. Lett. **112**, 192408 (2018).

[5] A. R. Mellnik, J. S. Lee, A. Richardella, J. L. Grab, P. J. Mintun, M. H. Fischer, A. Vaezi, A. Manchon, E.-A. Kim, N. Samarth and D. C. Ralph, Nature **511**, 449 (2014).

[6] M. DC, R. Grassi, J. Y. Chen, M. Jamali, D. R. Hickey, D. Zhang, Z. Zhao, H. Li, P. Quarterman, Y. Lv, M. Li, A. Manchon, K. A. Mkhoyan, T. Low and J. P. Wang, Nat. Mater. **17**, 800 (2018).

[7] H. Wu, P. Zhang, P. Deng, Q. Lan, Q. Pan, S. A. Razavi, X. Che, L. Huang, B. Dai, K. Wong, X. Han and K. L. Wang, Phys. Rev. Lett. **123**, 207205 (2019).

[8] N. H. D. Khang, Y. Ueda and P. N. Hai, Nat. Mater. **17**, 808 (2018).

[9] E. Sagasta, Y. Omori, M. Isasa, M. Gradhand, L. E. Hueso, Y. Niimi, Y. Otani and F. Casanova, Phys. Rev. B **94**, 060412(R) (2016).

[10] M.-H. Nguyen, D. C. Ralph and R. A. Buhrman, Phys. Rev. Lett. **116**, 126601 (2016).

[11] Y. Wang, P. Deorani, X. Qiu, J. H. Kwon and H. Yang, Appl. Phys. Lett. **105**, 152412 (2014).

[12] S. Sangiao, L. Morellon, G. Simon, J. M. De Teresa, J. A. Pardo, J. Arbiol and M. R. Ibarra, Phys. Rev. B **79**, 014431 (2009).

[13] Y. Tian, L. Ye and X. Jin, Phys. Rev. Lett. **103**, 087206 (2009).

[14] N. Nagaosa, J. Sinova, S. Onoda, A. H. MacDonald and N. P. Ong, Rev. Mod. Phys. **82**, 1539 (2010).

[15] M.-H. Nguyen, M. Zhao, D. C. Ralph and R. A. Buhrman, Appl. Phys. Lett. **108**, 242407 (2016).

[16] L. Zhu, L. Zhu, M. Sui, D. C. Ralph and R. A. Buhrman, Sci. Adv. 2019, **5**, eaav8025 (2019).

[17] M. Obstbaum, M. Decker, A. K. Greitner, M. Haertinger, T. N. G. Meier, M. Kronseder, K. Chadova, S. Wimmer, D. Ködderitzsch, H. Ebert and C. H. Back, Phys. Rev. Lett. **117**, 167204 (2016).

[18] L. Zhu, D. C. Ralph and R. A. Buhrman, Phys. Rev. Appl. **10**, 031001 (2018).

[19] M.-H. Nguyen, S. Shi, G. E. Rowlands, S. V. Aradhya, C. L. Jermain, D. C. Ralph and R. A. Buhrman, Appl. Phys. Lett. **112**, 062404 (2018).

[20] L. Zhu, K. Sobotkiewich, X. Ma, X. Li, D. C. Ralph and R. A. Buhrman, Adv. Funct. Mater. **29**, 1805822 (2019).

[21] C. Hong, L. Jin, H. Zhang, M. Li, Y. Rao, B. Ma, J. Li, Z. Zhong, and Q. Yang, Adv. Electron. Mater. **4**, 1700632 (2018).

[22] M. Li, L. Jin, Y. H. Rao, Z. Zhong, X. Tang, B. Liu, H. Meng, Q. Yang, Y. Lin and H. Zhang, J. Magn. Magn. Mater. **507**, 166860 (2020).

[23] R. J. Elliott, Phys. Rev. **96**, 266 (1954).

[24] Y. Yafet, Phys. Rev. **85**, 478 (1952).

[25] N. H. Krikorian, J. Less-Common Met. **23**, 271 (1971).

[26] N. H. D. Khang and P. N. Hai, Appl. Phys. Lett. **117**, 252402 (2020).

[27] N. H. D. Khang, S. Nakano, T. Shirokura, Y. Miyamoto, P. N. Hai, Sci. Rep. **10**, 12185 (2020).

[28] M. Hayashi, J. Kim, M. Yamanouchi and H. Ohno, Phys Rev. B **89**, 144425 (2014).

[29] C. O. Avci, K. Garello, M. Gabureac, A. Ghosh, A. Fuhrer, S. F. Alvarado and P. Gambardella, Phys. Rev. B **90**, 224427 (2014).

[30] C.-F. Pai, Y. Ou, L. H. Vilela-Leao, D. C. Ralph and R. A. Buhrman, Phys. Rev. B **92**, 064426 (2015).

[31] L. Zhu, D. C. Ralph and R. A. Buhrman, Phys. Rev. Lett. **122**, 077201 (2019).

[32] P. M. Haney, H.-W. Lee, K.-J. Lee, A. Manchon and M. D. Stiles, Phys. Rev. B **87**, 174411 (2013).

[33] L. Neumann and M. Meinert, AIP Adv. **8**, 095320 (2018).

[34] Y.-T. Chen, S. Takahashi, H. Nakayama, M. Althammer, S. T. B. Goennenwein, E. Saitoh and G. E. W. Bauer, Phys. Rev. B **87**, 144411 (2013).

Chapter 5. Development of efficient spin source using a half-Heusler alloy topological semimetal YPtBi with Back-End-of-Line compatibility

5.1 Introduction

As introduced in Chapter 1, there are two families of materials that are currently studied for efficient spin current sources: HMs and TIs. HMs, such as Ta,[1] W,[2] Pt,[3] and their alloys with other elements, have the advantages of high melting point and non-toxicity. Furthermore, some of them have been already adopted as buffering or lining materials in silicon BEOL process. Thus, these HMs, considered as the first-generation spin Hall materials, have been heavily studied by the industry as candidates for spin current sources in spintronic devices. However, the spin Hall performance of HMs is insufficient because their θ_{SH} is usually smaller than 1. On the hand, TIs with TSSs, such as Bi_2Se_3, $(Bi,Sb)Te_3$, and BiSb, have demonstrated very high θ_{SH} larger than 1 at room temperature in epitaxial TI thin films prepared by molecular beam epitaxy.[4-6] Moreover, the high θ_{SH} is maintained even in non-epitaxial TIs prepared by the industry-friendly sputtering technique.[7-10] Thus, TIs are very promising for magnetization manipulation with ultralow power consumption, and considered as the second-generation of spin Hall materials. However, the observed room-temperature high θ_{SH} is so far limited to only a few chalcogenide TIs with toxic elements of either Se, Sb, or Te. Furthermore, those TIs have low melting points, making them challenging for device integration during the silicon BEOL process, which usually involves high temperature up to 400°C. As a result, despite having very high θ_{SH}, the TI-based second-generation spin Hall materials have not yet been adopted by the industry as candidates for spin current sources. In recent year,

the research field of the SHE is expanded to other topological materials beyond TIs, such as Weyl semimetals[11,12] and Dirac semimetals.[13,14] However, the realization of a spin Hall material having both high θ_{SH} (>1) and BEOL compatibility is still challenging.

In this chapter, we demonstrate a spin Hall material that combines the advantage of HMs and TIs, using an HHA-TSM, YPtBi. We demonstrate that YPtBi can have a high θ_{SH} up to 4.1, rivaling that of TIs, and a high thermal stability up to 600°C, comparable to that of HMs. We show that the giant θ_{SH} can be explained by the SHE of TSS rather the bulk states. We then demonstrate magnetization switching of a CoPt thin film using the giant SHE of YPtBi by current densities lower than those of HMs by one order of magnitude. Since HHA-TSM includes a group of three-element topological materials with great flexibility, our work opens the door to the third-generation spin Hall materials with both high θ_{SH} and high compatibility with the BEOL process that would be easily adopted by the industry.

5.2 Comparison between conventional topological insulator and half-Heusler alloy topological semimetal

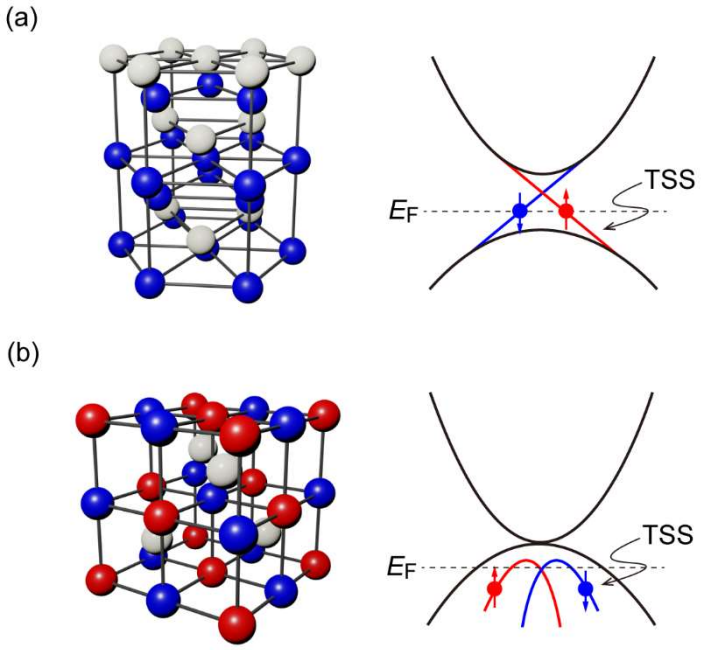

Figure 5.1. Comparison of the crystal structure and band structure of (a) topological insulator and (b) half-Heusler alloy topological semimetal. In the band structures, TSS indicates topological surface states.

Figure 5.1 compares the crystal structure and the band structure of TI and HHA-TSM. Most TIs crystallize in the trigonal or rhombohedral lattices including two dimensional atomic sheets interacting via Vander Waal bonding, as schematically shown in the left panel of Figure 5.1(a). While this crystal structure makes it easy to grow high-quality TIs on many substrates, it results in low mechanical strength and low melting points that in turn increase the crystal grain and surface roughness, which are not favored for device integration. The schematic band structure of TIs is shown in the right panel of Figure 5.1(a), which consists of a bulk band gap and one or multi

TSS with Dirac-like dispersion and spin-momentum locking. The large Berry phase curvature originating from the monopole at the Dirac cones of TSS is the key for obtaining the giant spin Hall angle in TIs. The left panel in Figure 5.1(b) shows the schematic crystal structure of HHA-TSMs, which are constructed from three kinds of element XYZ, where X and Y are transition or rare-earth metals, and Z is the main-group element, and thus possesses high controllability of lattice constant and band structure via material combination.[15-19] Unlike TIs, the crystal structure of HHA-TSMs are cubic, matching those of many ferromagnetic materials and the MgO insulating material typically used in realistic spintronic devices. Furthermore, HHA-TSMs have high melting points, which make them compatible with the BEOL process. In numerous combinations of X, Y, and Z, an inversion of the *s*-orbital band with Γ_8 symmetry and the *p*-orbital band with Γ_6 symmetry occurs around the Γ point, and then TSS is generated through the change of band topology,[20,21] as schematically shown in the right panel of Figure 5.1(b). An ideal topological HHA would have zero band gap and no Fermi surface. In reality, due to crystal defects, there can exist a significant number of carriers and thus non-zero Fermi surface, making topological HHA semi-metal rather than zero-gap insulator. Numerous works have successfully observed such a Fermi surface and TSS in several HHA such as LuPtBi, YPtBi, and LuPtSb using ARPES,[22-25] confirming that they are HHA-TSMs. Nevertheless, there is no report on the spin Hall performance of these compounds.

5.3 Deposition and characterization of YPtBi stand-alone thin films

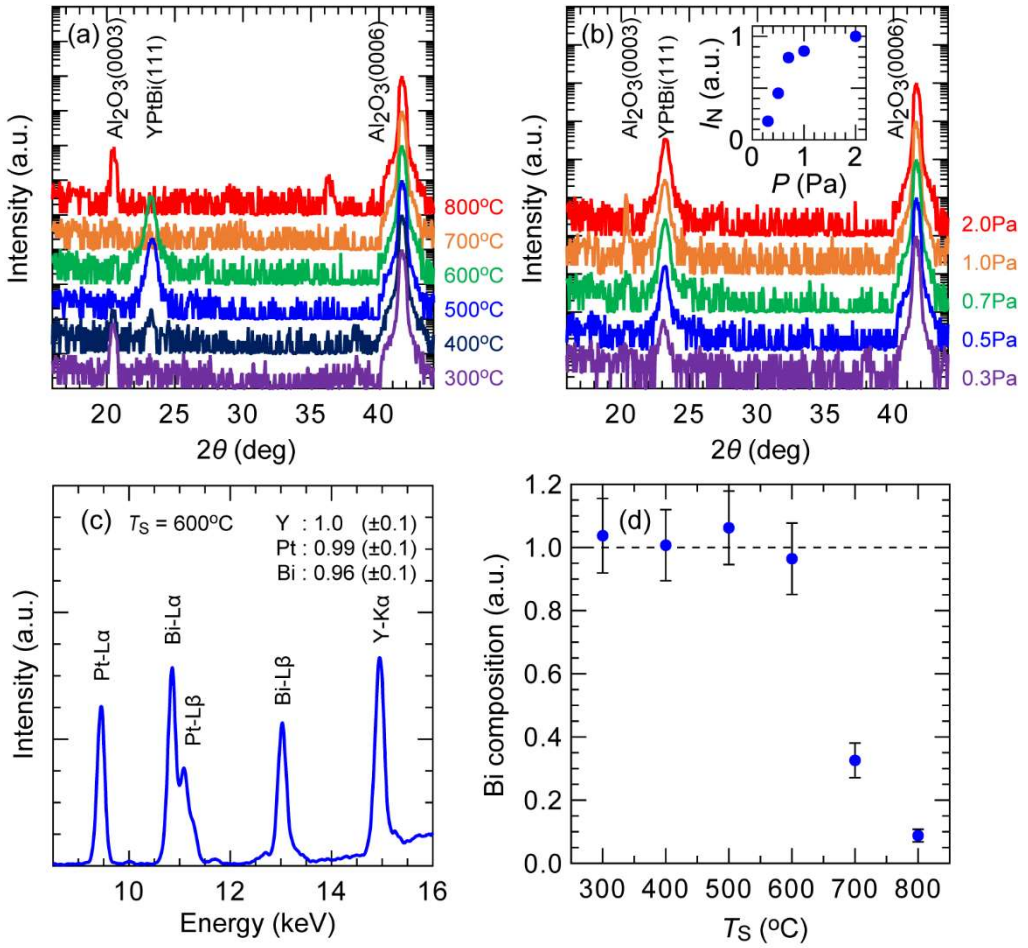

Figure 5.2. Crystal structure analysis of YPtBi thin films. (a) XRD θ-2θ spectra of 50 nm-thick YPtBi films deposited on c-Sapphire at different substrate temperature ranging from 300°C to 800°C and the Ar pressure of 0.2 Pa. (b) XRD θ-2θ spectra of YPtBi films deposited at different Ar pressure ranging from 0.3 to 2.0 Pa at the substrate temperature of 600°C. Inset shows the peak intensity of YPtBi(111) normalized by that at 2.0 Pa as a function of Ar pressure. (c) XRF spectrum of an YPtBi thin film deposited at 600°C. (d) Bi composition at different substrate temperature. YPtBi is stable up to 600°C.

Here, we chose to investigate the SHE in YPtBi as a proof of concept for several reasons. First, the band inversion between Γ_8 and Γ_6 of YPtBi are among the largest as predicted from first principle calculation.[13,14] Furthermore, this compound does not contain toxic elements, such as Pb,Th, or Sb. Finally, Y is stable in air and is easy

to handle than other rare-earth elements, such as Lu, Ce, and La. We grew YPtBi thin films on c-Sapphire substrate by co-sputtering multi targets. In this section, to demonstrate the high thermal stability of YPtBi, we prepared two different series of samples with different substrate temperature and Ar gas pressure. The sample structure is $MgAl_2O_4$ (2.0) / YPtBi (~50) / c-Sapphire, where the layer thicknesses are in nm. The cap $MgAl_2O_4$ (2.0) layer was deposited at room temperature. Figure 5.2(a) shows the X-ray diffraction (XRD) θ-2θ spectra for YPtBi films deposited at different substrate temperature T_S ranging from 300ºC to 800ºC and the Ar pressure of 2.0 Pa. Clear YPtBi(111) peaks were observed at T_S = 300ºC ~ 600ºC, indicating that YPtBi is stable up to 600ºC. The lattice constant of 6.62 Å evaluated from the peak position of YPtBi(111) is consistent with the bulk value of 6.64 Å.[26] Therefore, a strain effect on the band structure is negligibly small in our YPtBi films. Figure 5.2(b) shows the XRD θ-2θ spectra for YPtBi films deposited at different Ar pressure ranging from 0.3 to 2.0 Pa at T_S = 600ºC. Peaks of YPtBi(111) were observed under the whole Ar pressure range. The inset in Figure 5.2(b) shows the peak intensity I_N of YPtBi(111) normalized by that at the Ar pressure of 2.0 Pa. I_N increases with increasing Ar pressure up to 1 Pa, above which I_N saturates because higher Ar pressure reduces the recoil energy of Ar ions which may implant into the YPtBi thin films and reduce their crystal quality. We then used XRF to characterize the elemental composition of the YPtBi thin film. A representative XRF spectrum of the YPtBi thin film deposited at T_S = 600ºC is shown in Figure 5.2(c). Fitting to the intensity of the characteristic X-ray energy of each element allows us to determine that the atomic composition Y:Pt:Bi of this sample is close to 1:1:1. Figure 5.2(d) shows the relative atomic composition of Bi as a function of T_S. Since Bi is the most volatile among the

three elements, this data allows us to determine whether YPtBi is stable or not at a particular substrate temperature. The result in Figure 5.2(d) reveals that YPtBi is stable up to 600ºC, above which Bi composition significantly decreases due to desorption from YPtBi, consistent with the XRD spectra in Figure 5.2(a). These results demonstrate that YPtBi has a high thermal stability up to 600ºC, higher than the required 400ºC of the BEOL process. This is a significant advantage of HHA-TSMs compared with TIs.

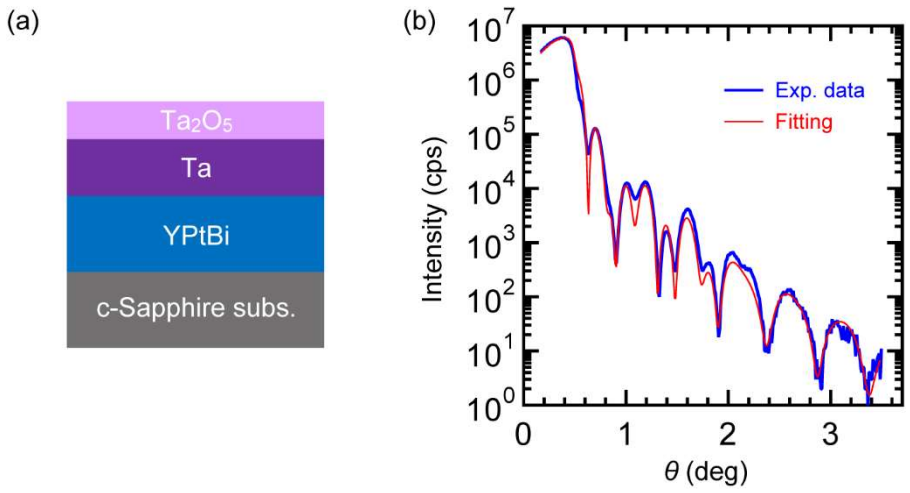

Figure 5.3. (a) Model of the YPtBi stack used for fitting of an XRR spectrum. (b) XRR spectrum for the YPtBi stack, where the blue and red solid lines are the experimental and fitting results, respectively.

Next, we investigated the surface roughness of YPtBi film which is one of the most important parameters for realistic spintronic devices because the thickness of adjacent ferromagnetic layer is ranging from several Å to few nm. The X-ray reflectivity (XRR) method was employed to evaluate the surface roughness of YPtBi with a Ta cap layer, where Ta layer is necessary for protection of YPtBi from surface oxidization, and thus it is impossible to evaluate the surface roughness of YPtBi by

conventional surface analysis method such as the atomic force microscopy (AFM). For XRR measurement, we deposited ~10 nm-thick YPtBi with a 10 nm-thick Ta capping layer on a c-Sapphire substrate. Because Ta is partly oxidized after exposure to the atmosphere, we employed a structure of Ta_2O_5/Ta/YPtBi/c-Sapphire for fitting, as shown in Figure 5.3(a). Figure 5.3(b) shows a XRR spectrum of this stack, where the blue and red solid lines are the experimental and fitting results, respectively. The fitting is in good agreement with the experimental result. Surprisingly we obtained the YPtBi surface roughness of 2.4 Å, which is 3 times smaller than the surface roughness of BiSb topological insulator, despite high Ar pressure during the sputtering. This atomically flat surface of YPtBi is a strong advantage for spintronic devices such as MRAM with strong PMA.

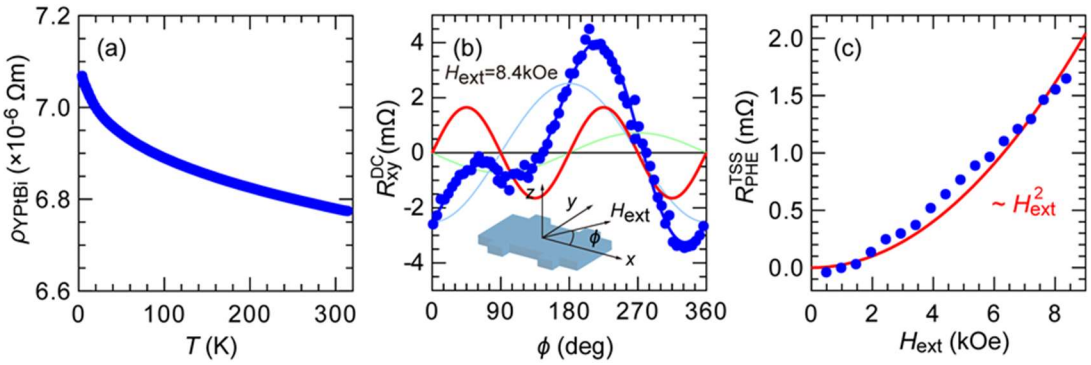

Figure 5.4. (a) Temperature dependence of the resistivity of a 11.8 nm-thick YPtBi film. (b) Planar Hall resistance measured with an in-plane rotating H_{ext} of 8.4 kOe measured at 4K, where dots are experimental data and the solid curve is a fitting given by equation (5.1). Inset shows the coordination system and definition for the azimuth angle ϕ_H of H_{ext}. The sin2ϕ_H dependence of the Hall resistance originates from the spin-momentum locking of TSS. (c) Amplitude of the sin2ϕ_H planar Hall resistance as a function of H_{ext}, which increases as H_{ext}^2, similar to those observed in TIs.

Next, we investigated the electrical properties of YPtBi. For this purpose, we

prepared a thinner $MgAl_2O_4$ (2.0) / YPtBi (11.8) / c-Sapphire stand-alone sample. We fabricated a 4-terminal Hall bar structure with size of 60×100 μm^2 by optical lithography and ion-milling for electrical measurements. We obtained the charge conductivity σ_{YPtBi} of 1.5×10^5 $\Omega^{-1}m^{-1}$, which is similar to that of bulk YPtBi.[27] From the Hall measurement, we confirmed a large carrier density of 7.1×10^{22} cm^{-3}. Figure 5.4(a) shows the temperature dependence of the resistivity ρ_{YPtBi} of this YPtBi film. We observed that ρ_{YPtBi} increases with lowering temperature, consistent with the semi-metallic behavior observed in bulk YPtBi.[25] However, the change of ρ_{YPtBi} at low temperature is only 4%, which is one order of magnitude smaller than that (~50%) observed in bulk YPtBi. This can be explained by the increasing contribution of metallic surface conduction at small thickness. We then employ the planar Hall effect measurement to detect the existence of the spin-momentum locking of TSS in YPtBi. Figure 5.4(b) shows the DC planar Hall resistance measured at 4 K with an in-plane rotating magnetic field H_{ext} of 8.4 kOe. Here, dots show experimental data and the solid curve is a fitting result by,[28]

$$R_{xy}^{DC}=R_{PHE}^{TSS}\sin 2\phi_H+R_{OHE}^{x}\cos\phi_H+R_{OHE}^{y}\sin\phi_H, \quad (5.1)$$

where R_{PHE}^{TSS} is a planar Hall resistance originated from spin-momentum locking of TSS, R_{OHE}^{x} and R_{OHE}^{y} are an ordinary Hall resistance caused by the misalignment of H_{ext} from the *xy*-plane, ϕ_H is the azimuth angle for H_{ext}, as shown in the inset. We observed a clear $\sin 2\phi_H$ planar Hall effect despite YPtBi is a non-magnetic material. Such a $\sin 2\phi_H$ planar Hall effect has been reported in many non-magnetic TIs with TSS crossing the Fermi level.[26,29-31] Because H_{ext} breaks the time-reversal-symmetry of TSS, back scattering increases due to selective destruction of spin-momentum-locking along the H_{ext} direction, resulting in the $\sin 2\phi_H$ planar Hall

effect.[26] To further confirm this scenario, we shows in Figure 5.4(c) the amplitude R_{PHE}^{TSS} measured at various H_{ext}, where dots are experimental data and the solid line is a fitting result by a quadratic function. The observed $R_{PHE}^{TSS} \sim H_{ext}^2$ is consistent with previous reports on the planar Hall effect of TIs,[26-29] which provide evidence that our YPtBi films have TSS crossing the Fermi level. Thus, a large SHE from the Berry phase of TSS can be expected.

5.4 Spin Hall effect in YPtBi

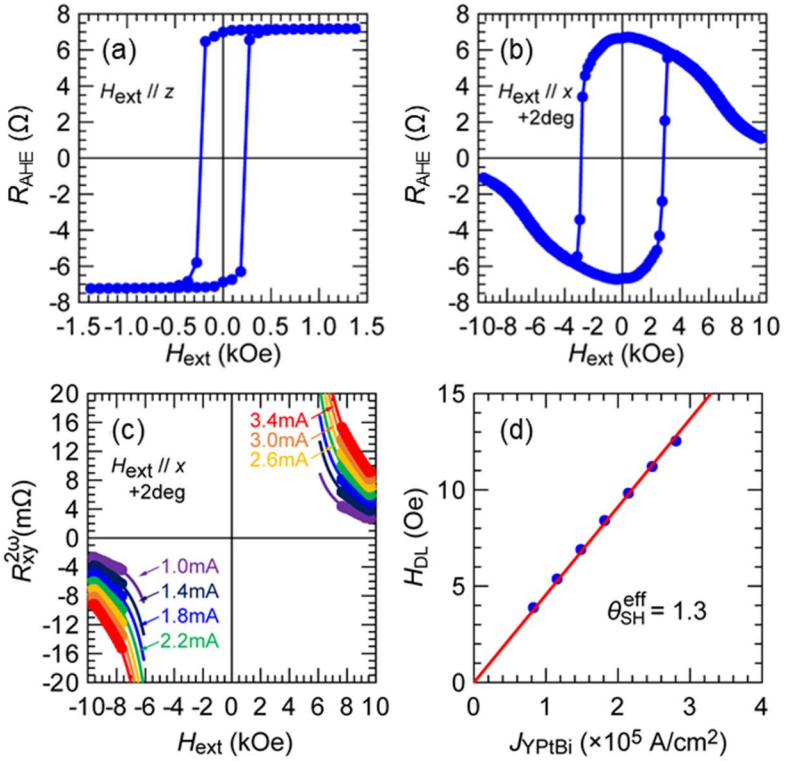

Figure 5.5. (a), (b) DC anomalous Hall resistance for sample A (σ_{YPtBi} = 0.38×10^5 Ω^{-1}m^{-1} and t_{Co}=0.5 nm) measured with H_{ext} applied along the z-direction and the x+2°-direction, respectively. (c) Second harmonic Hall resistance of sample A measured with H_{ext} applied along the x-direction and an AC current ranging from 1.0 to 3.4 mA, where dots are experimental data and solid curves show fitting results given by equation (5.2). (d) H_{DL} as a function of the current density in the YPtBi layer.

We now investigate θ_{SH} of YPtBi in three samples with different σ_{YPtBi} of 0.38, 1.2, and 1.5×10^5 $\Omega^{-1}m^{-1}$ (referred below as sample A, B, C). We prepared multilayers of $MgAl_2O_4$ (2.0) / Pt (0.5) / Co (t_{Co}) / Pt (0.5) / YPtBi (t_{YPtBi}) / c-Sapphire. The YPtBi layers were deposited by co-sputtering YPt and Bi targets. The Pt/Co/Pt ferromagnetic multilayers have PMA, and referred below as CoPt for short. Here, the parasitic SHE from the Pt layers is negligible because the Pt thickness of 0.5 nm is few times to one magnitude thinner than the typical spin relaxation length of Pt, and the Pt/Co/Pt stack is symmetric.[9,32-34] The thickness of the Co layer t_{Co} is 0.5 nm for sample A and B, and 0.8 nm for sample C. The YPtBi layer thickness t_{YPtBi} for sample A, B, and C is 9.3, 11.5 and 11.8, respectively, as measured by XRR for stand-alone YPtBi thin films deposited at the same conditions. After the deposition, these film stacks were patterned into 25×50 μm^2 Hall bar devices for transport measurements. Figures 5.5(a) and 5.5(b) show the DC anomalous Hall resistance for sample A measured at room temperature with H_{ext} applied along the z-direction and x+2°-direction. Strong PMA with H_k^{eff} of 6.1 kOe was obtained thanks to the very flat interface of YPtBi. Quantitative evaluation of θ_{SH} in sample A was carried out by using the high-field second harmonic technique at room temperature with alternating currents at 259.68 Hz. In the case of PMA, $R_{xy}^{2\omega}$ measured at H_{ext} higher than H_k^{eff} applied along the x-direction is given by,[35,36]

$$R_{xy}^{2\omega}=\frac{R_{AHE}}{2}\frac{H_{DL}}{|H_{ext}|-H_k^{eff}}+R_{PHE}\frac{H_{FL+OF}}{|H_{ext}|}+\alpha_{ONE}|H_{ext}|+R_{ANE+SSE}, \quad (5.2)$$

Here, fitting parameters are H_{DL}, H_k^{eff}, H_{FL+OF}, α_{ONE}, and $R_{ANE+SSE}$. Figure 5.5(c) shows the high-field second harmonics data and the corresponding fitting for sample A at bias currents of 1.0 to 3.4 mA, where the dots and solid curves are the experimental data and fitting using equation (5.2), respectively. Figure 5.5(d) shows

the relationship between the extracted values of H_{DL} and the current density in the YPtBi layer J_{YPtBi} for sample A. Then, the effective spin Hall angle θ_{SH}^{eff} was calculated from the slope of H_{DL}/J_{YPtBi} by,

$$\theta_{SH}^{eff} = \frac{2eM_S t_{CoPt}}{\hbar} \frac{H_{DL}}{J_{YPtBi}}, \tag{5.3}$$

with the parameters of M_S = 633 emu/cc and t_{CoPt} = 1.5 nm. Thanks to the contribution of TSS, large θ_{SH}^{eff} of 1.3 was observed in sample A. Furthermore, our fittings to high-field second harmonic data indicate that the thermal contribution is negligible in sample A, thus the low-field second harmonic technique[33] can also be used to double check the value of θ_{SH}^{eff}.

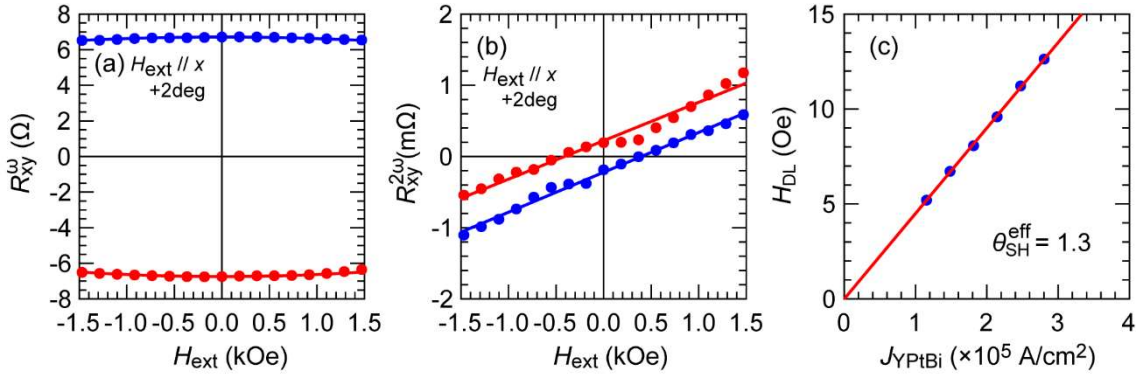

Figure 5.6. (a) First harmonic Hall resistance and (b) Second harmonic Hall resistance as a function of H_{ext} applied along the *x*-direction for sample A with an applied alternating current of 1.4 mA. Here, dots and solid lines are experimental results and eye-guides, respectively. Blue (red) correspond to the up (down) direction of the magnetization. (c) H_{DL} as a function of the current density in the YPtBi layer.

Figures 5.6(a) and 5.6(b) show the low field first harmonic resistance R_{xy}^{ω} and $R_{xy}^{2\omega}$ as a function of H_{ext}, respectively. Here, an alternating current of 1.4 mA at 259.68 Hz was applied. At low fields, R_{xy}^{ω} and $R_{xy}^{2\omega}$ show quadratic and linear

dependence of H_{ext}. We then evaluated H_{DL} by using following equation,

$$H_{\mathrm{DL}} = -2\frac{\partial R_{\mathrm{xy}}^{2\omega}/\partial H_{\mathrm{ext}}}{\partial^2 R_{\mathrm{xy}}^{\omega}/\partial H_{\mathrm{ext}}^2}. \tag{5.4}$$

Here, we neglect the contribution of H_{FL} because this term was undetectable in the high-field second harmonic measurements with large H_{ext}. Figure 5.6(c) shows H_{DL} as a function of J_{YPtBi}. The value of θ_{SH}^{eff} calculated from the slope of H_{DL}/J_{YPtBi} is 1.3, which is consistent with that estimated by the high-field second harmonic technique. Therefore, we confirmed that sample A really has large θ_{SH}^{eff} of 1.3. This large θ_{SH}^{eff} is comparable with those reported in TIs such as Bi_2Se_3 and $(BiSb)_2Te_3$,[4,5] and larger than that of topological Weyl semimetals.[11,12] Furthermore, this value is one order magnitude larger than θ_{SH}^{eff} of its contributing elements such as Bi, Pt, and their alloys including YPt discussed in Chapter 4. This big difference strongly supports the importance of TSS in YPtBi, which is the main difference between YPtBi and those materials.

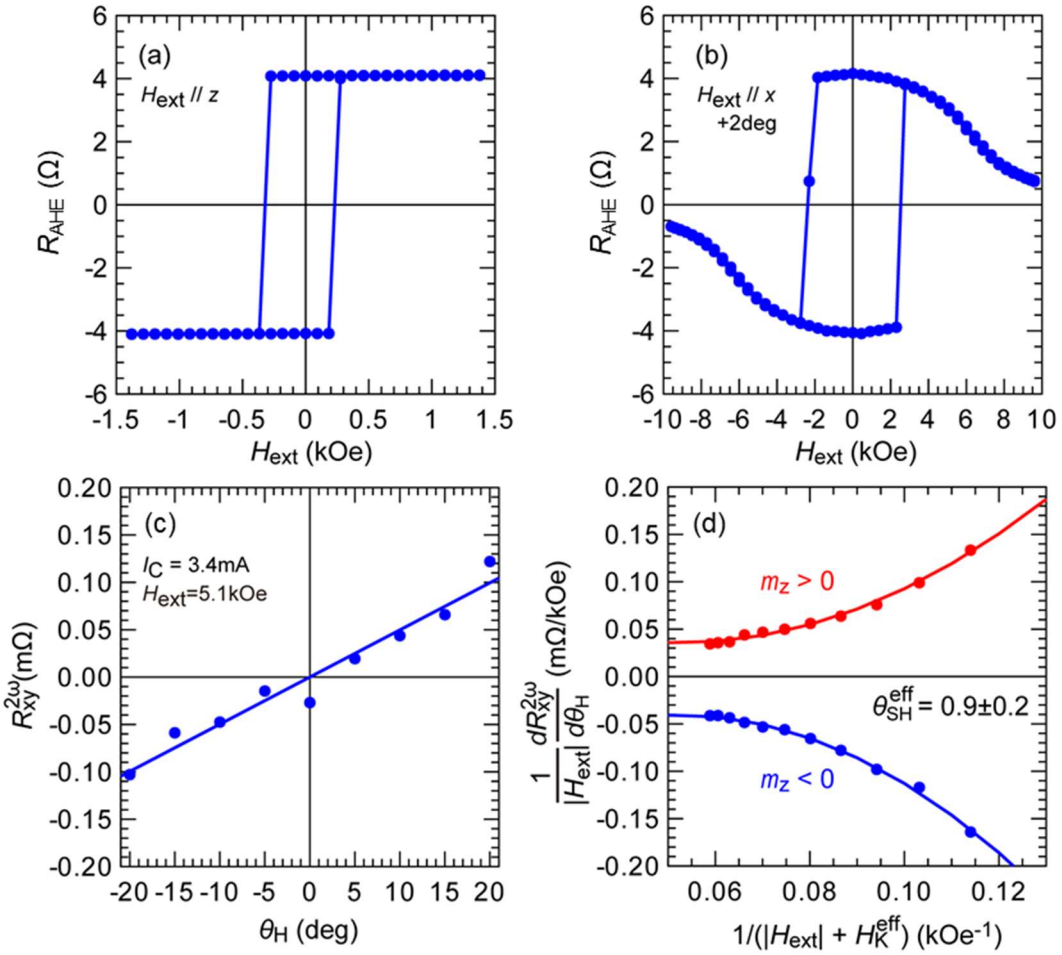

Figure 5.7. DC anomalous Hall resistance for sample B (σ_{YPtBi} = 1.2×10^5 Ω^{-1}m^{-1} and t_{Co}=0.5 nm) measured with H_{ext} applied along (a) the z-direction and (b) the x+2°-direction. (c) Second harmonic Hall resistance of sample B as a function of θ_H measured with H_{ext} = 5.1 kOe and an AC current of 3.4 mA, where dots are experimental data and the solid line shows the gradient $dR^{2\omega}_{xy}/d\theta_H$. (d) $|H_{ext}|^{-1}dR^{2\omega}_{xy}/d\theta_H$ (dots) as a function of $(|H_{ext}| + H^{eff}_k)^{-1}$ and the corresponding fitting curves using equation (5.5).

We then investigate the SHE in sample B and C with higher σ_{YPtBi} of 1.2 and 1.5×10^5 Ω^{-1}m^{-1}, respectively. Figures 5.7(a) and 5.7(b) show the DC anomalous Hall resistance for sample B measured at room temperature with H_{ext} applied along the z-direction and x+2°-direction. From Figure 5.7(b), we found that H^{eff}_K of sample B

is as large as 7.4 kOe. This makes it difficult to estimate the effective spin Hall angle by the high-field second harmonic technique in this sample. Instead, we performed the angle-resolved second harmonic technique for this sample, which is described in Chapter 3. Figure 5.7(c) show a representative $R_{xy}^{2\omega} - \theta_H$ data measured at H_{ext} = 5.1 kOe and an AC current of 3.4 mA. The slopes correspond to $dR_{xy}^{2\omega}/d\theta_H$ in the following equation (5.5),

$$\frac{1}{|H_{ext}|}\frac{dR_{xy}^{2\omega}}{d\theta_H} = \pm\left(\frac{R_{AHE}}{2}H_{DL} + R_{PHE}H_{FL+OF}\right)(|H_{ext}| + H_k^{eff})^{-2} \pm R_{ANE+SSE}(|H_{ext}| + H_k^{eff})^{-1} \pm \alpha_{ONE}. \quad (5.5)$$

Figure 5.7(d) shows $|H_{ext}|^{-1}dR_{xy}^{2\omega}/d\theta_H$ as a function of $(|H_{ext}| + H_k^{eff})^{-1}$ and the corresponding fitting at bias currents of 3.4 mA, where the dots and solid curves are the experimental data and fitting results given by equation (5.5), respectively. From the coefficient of $(|H_{ext}| + H_k^{eff})^{-2}$ term (ignoring the $R_{PHE}H_{FL+OF}$ contribution), M_S = 729 emu/cc and t_{CoPt} = 1.5 nm, we obtained θ_{SH}^{eff} = 0.9±0.2 for sample B.

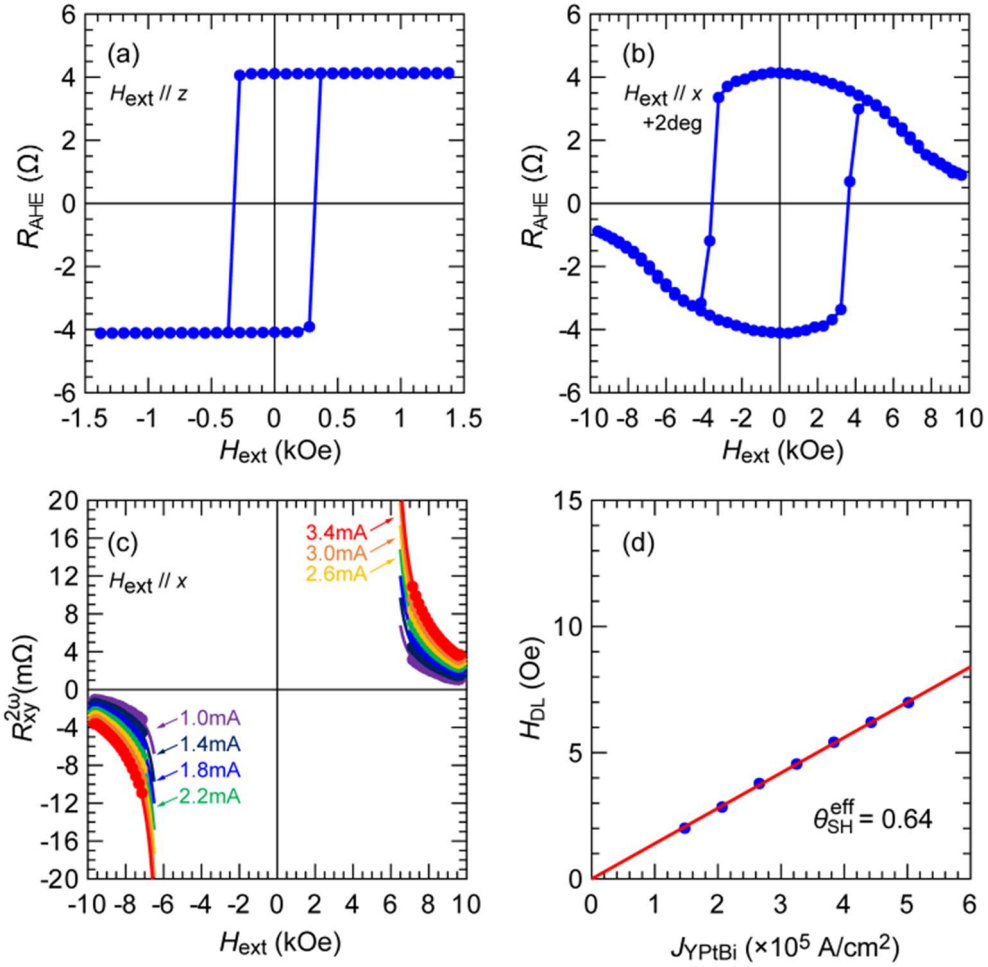

Figure 5.8. (a), (b) DC anomalous Hall resistance for sample C (σ_{YPtBi} = 1.5×10^5 Ω^{-1}m^{-1} and t_{Co}=0.8 nm) measured with H_{ext} applied along the z-direction and the x+2°-direction, respectively. (c) Second harmonic Hall resistance of sample C measured with H_{ext} applied along the x-direction and an AC current ranging from 1.0 to 3.4 mA, where dots are experimental data and solid curves show fitting results given by equation (5.2). (d) H_{DL} as a function of the current density in the YPtBi layer.

On the other hand, since the sample C has the highest surface quality, H_k^{eff} of CoPt could be even larger than that of sample B. To reduce H_k^{eff}, we increased the Co thickness from 0.5 nm to 0.8 nm in sample C. This allows us to perform the high-field second harmonic measurement on sample C, which is faster and more simple

than the angle-resolved second harmonic technique. Figures 5.8(a) and 5.8(b) show the DC anomalous Hall resistance for sample C measured with H_{ext} applied along the z-direction and x+2°-direction. We obtain H_k^{eff} = 6.1 kOe from Figure 5.8(b). Figure 5.8(c) shows the high-field second harmonics data and the corresponding fitting for sample C at bias currents of 1.0 to 3.4 mA, where the dots and solid curves are the experimental data and fitting using equation (5.2), respectively. Figure 5.8(d) shows the relationship between the extracted values of H_{DL} and J_{YPtBi} for sample C. From the slope H_{DL}/J_{YPtBi}, M_S = 837 emu/cc and t_{CoPt} = 1.8 nm, we obtained θ_{SH}^{eff} = 0.64 in sample C.

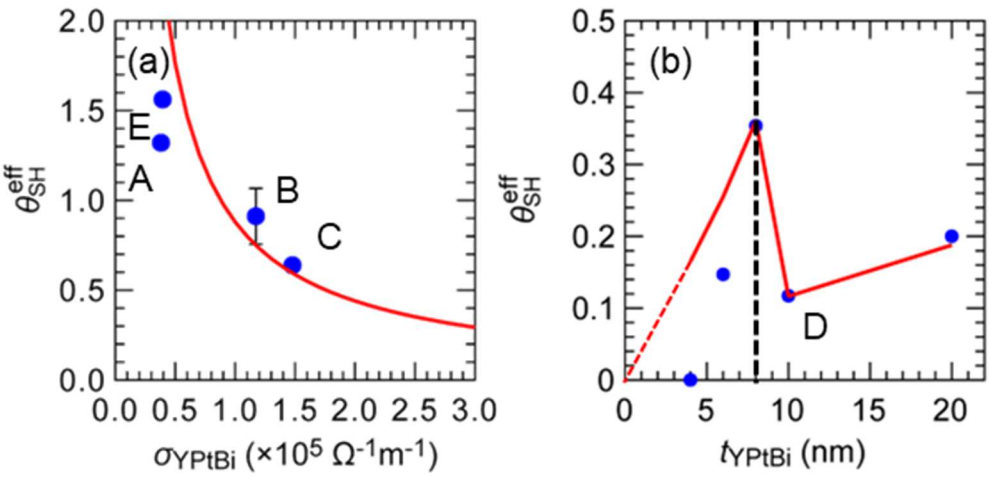

Figure 5.9. (a) Relationship between the effective spin Hall angle and the conductivity of the YPtBi layer observed in sample A, sample B (σ_{YPtBi} = 1.2×10^5 Ω^{-1}m^{-1} and t_{Co}=0.5 nm), sample C (σ_{YPtBi} = 1.5×10^5 Ω^{-1}m^{-1} and t_{Co}=0.8 nm), and sample E (σ_{YPtBi} = 0.39×10^5 Ω^{-1}m^{-1} and t_{Co}=0.5 nm). (b) Thickness dependence of the effective spin Hall angle in another series of samples. Sample D (σ_{YPtBi} = 2.0×10^5 Ω^{-1}m^{-1} and t_{Co}=0.5 nm) is a representative sample in this series.

Figure 5.9(a) summarizes the θ_{SH}^{eff} – σ_{YPtBi} relation for each sample. θ_{SH}^{eff} for sample E which is discussed in the next section is also plotted. Here, sample E

consists of an YPtBi layer with the same conductivity with that in sample A but deposited by co-sputtering Y, Pt, and Bi target. Its θ_{SH}^{eff} is even larger, reaching 1.6. We model the spin Hall angle by considering the contribution from a TSS spin Hall conductivity σ_{SH}^{TSS} and a bulk spin Hall conductivity σ_{SH}^{B},

$$\theta_{SH}^{eff}=\frac{\sigma_{SH}^{TSS}+\sigma_{SH}^{B}}{\sigma_{YPtBi}}. \quad (5.6)$$

Thus, $\theta_{SH}^{eff}\sim\sigma_{SH}^{TSS}/\sigma_{YPtBi}$ if TSS dominates the SHE, and $\theta_{SH}^{eff}\sim\sigma_{SH}^{B}/\sigma_{YPtBi}$ if otherwise. Regardless of which dominates, because the spin Hall conductivity is constant in the moderately dirty regime with the dominating Berry phase mechanism,[37,38] θ_{SH}^{eff} is inversely proportional to σ_{YPtBi}. The red solid curve in Figure 5.9(a) is a fitting result of the θ_{SH}^{eff} – σ_{YPtBi} relation by equation (5.6), which reasonably agrees with the experimental results and indicates that the SHE in YPtBi is indeed governed by the Berry phase.

In order to see which of σ_{SH}^{TSS} or σ_{SH}^{B} dominates the SHE, we studied the YPtBi thickness dependence of θ_{SH}^{eff} in another series of samples with structure of Ta (1.0) / $MgAl_2O_4$ (2.0) / Pt (0.8) / Co (0.5) / Pt (0.8) / YPtBi (t_{YPtBi}) / c-Sapphire, whose t_{YPtBi} are 4, 6, 8, 10, and 20 nm. The YPtBi layers in this series were deposited by co-sputtering Y, Pt, and Bi targets. A representative sample D with t_{YPtBi} = 10 nm and high $\sigma_{YPtBi} = 2.0\times10^5\ \Omega^{-1}m^{-1}$ shows θ_{SH}^{eff} = 0.12. Figure 5.9(b) shows the thickness dependence of θ_{SH}^{eff} in this series, where the dots and solid line indicate the experimental data and fitting result by equation (5.6). At $t_{YPtBi} \geq 8$ nm, equation (5.6) explains the experimental results very well. At $t_{YPtBi} < 8$ nm, θ_{SH}^{eff} rapidly decreases to below that expected from the equation (5.6). Notably, θ_{SH}^{eff} reaches 0 at t_{YPtBi} = 4 nm. This behavior cannot be explained by the bulk SHE, whose thickness dependence should follow $\theta_{SH}^{eff}=\theta_{SH}^{B}[1-\mathrm{sech}(t_{YPtBi}/\lambda_S)]$, which means $\theta_{SH}^{eff} \sim \theta_{SH}^{B}$ at $t_{YPtBi} >> \lambda_S$

and $\theta_{SH}^{eff} \sim \frac{1}{2}\theta_{SH}^{B}(t_{YPtBi}/\lambda_S)^2$ at $t_{YPtBi} << \lambda_S$. Thus, the bulk θ_{SH}^{eff} should approach zero only at t_{YPtBi} = 0 nm (dashed line in Figure 5.9(b)). Meanwhile, if θ_{SH}^{eff} is governed TSS, the observed rapid decrease and disappearance of θ_{SH}^{eff} at t_{YPtBi} = 4 nm can be explained by destruction of TSS due to interference of TSS on the top and bottom surface of YPtBi, a phenomenon well known in TIs.[39] Thus, our results indicate that the SHE in YPtBi is dominated by the intrinsic Berry phase mechanism from TSS.

5.5 Magnetization switching by ultralow DC and pulse currents

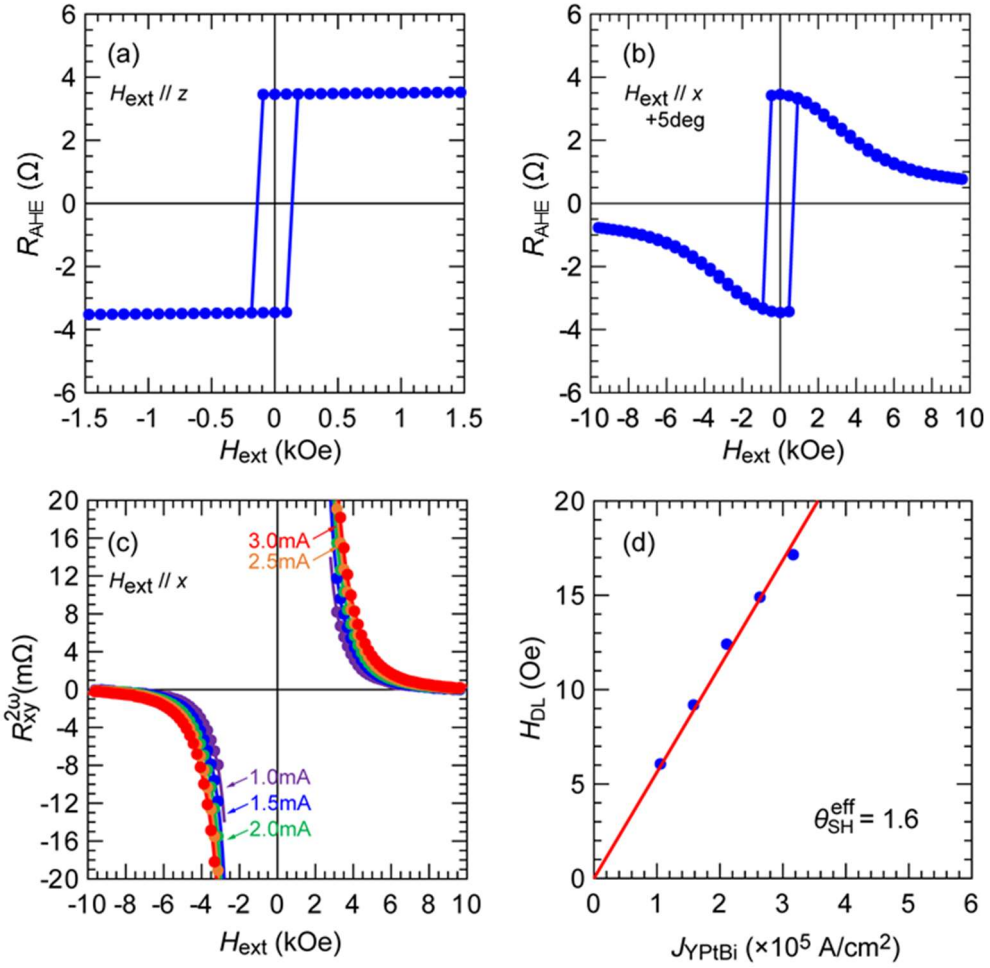

Figure 5.10. (a), (b) DC anomalous Hall resistance for sample E (σ_{YPtBi} = 0.39×10^5 Ω^{-1}m^{-1} and t_{Co}=0.5 nm) measured with H_{ext} applied along the *z*-direction and the *x*+5°-direction, respectively. (c) Second harmonic Hall resistance of sample E measured with H_{ext} applied along the *x*-direction and an AC current ranging from 1.0 to 3.0 mA, where dots are experimental data and solid curves show fitting results given by equation (5.2). (d) H_{DL} as a function of the current density in the YPtBi layer.

To demonstrate the magnetization switching by the SOT effect generated by YPtBi, we prepared a stack of Ta (1.0) / $MgAl_2O_4$ (2.0) / Pt (0.8) / Co (0.5) / Pt (0.8) / YPtBi (11.3) / c-Sapphire (sample E). Here, σ_{YPtBi} was tuned to 0.39 × 10^5 Ω^{-1}m^{-1} to

maximize θ_{SH}^{eff}. We then fabricated a Hall bar device with size of 10×60 μm^2 of this stack for current-induced magnetization switching. Figures 5.10(a) and 5.10(b) show the DC anomalous Hall resistance for sample E measured at room temperature with H_{ext} applied along the z-direction and x+5°-direction. We obtained H_k^{eff} = 3.4 kOe from Figure 5.10(b). Figure 5.10(c) shows the high-field second harmonics data and the corresponding fitting for sample E at bias currents of 1.0 to 3.0 mA, where the dots and solid curves are the experimental data and fitting using equation (5.2), respectively. Figure 5.2(d) shows the relationship between the extracted values of H_{DL} and J_{YPtBi} for sample E. From the slope H_{DL}/J_{YPtBi}, M_S = 435 emu/cc and t_{CoPt} = 2.1 nm, θ_{SH}^{eff} of 1.6 was obtained in sample E.

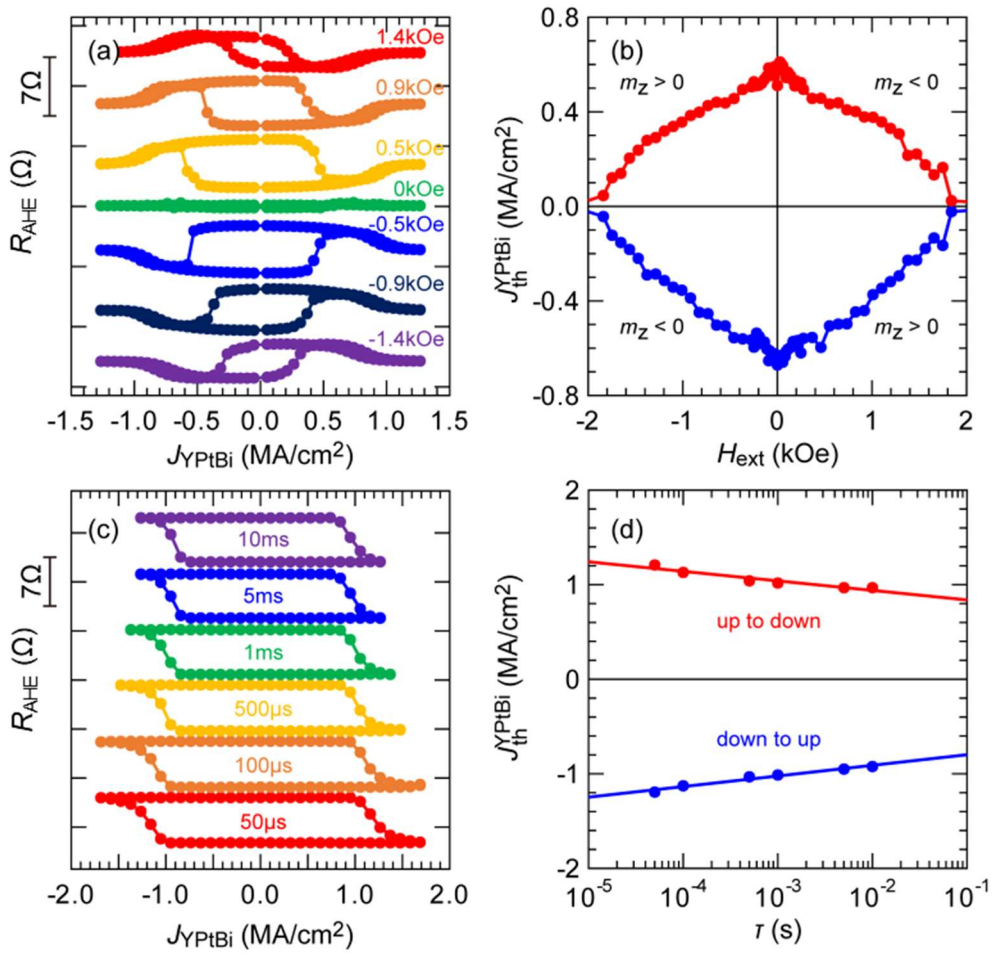

Figure 5.11. Ultralow current-induced magnetization switching in sample E (σ_{YPtBi} = 0.39×10^5 Ω^{-1}m^{-1} and t_{Co}=0.5 nm). (a) SOT magnetization switching by DC currents with various in-plane H_{ext} (-1.4 to 1.4 kOe) applied along the x-direction. (b) Threshold switching current density in YPtBi as a function of H_{ext}. (c) SOT magnetization switching by pulse currents with various pulse width ranging from 50 μs to 10 ms and H_{ext} of 0.5 kOe. (d) Threshold switching current density in YPtBi as a function of pulse width, where dots are experimental data and solid lines show fitting results given by equation (5.7).

Figure 5.11(a) shows the SOT magnetization switching loops at room temperature by DC currents under an in-plane bias magnetic field H_{ext} (-1.4 ~ 1.4 kOe) applied along the x-direction. The switching polarity was reversed when H_{ext} with opposite direction was applied, indicating the switching was governed by SOT.

Furthermore, the observed switching direction shows that the spin Hall angle of YPtBi has the same polarity with that of Pt,[40] and is similar to that of other Bi-based TIs.[4-6] Figure 5.11(b) shows the threshold current density J_{th}^{YPtBi} as a function of H_{ext}. Low J_{th}^{YPtBi} on the order of 10^5 Acm^{-2} was achieved for entire H_{ext}. Figure 5.11(c) shows the full SOT switching loops by pulse currents with various pulse width τ from 50μs to 10 ms under H_{ext} of 0.5 kOe applied along the x-direction. Figure 5(d) shows J_{th}^{YPtBi} as a function of τ. For a reasonable benchmarking, we note that the switching current density in 10×60 μm^2 Hall bar of Pt (3) / [Co (0.4) / Pt (0.4)]$_n$ stacks is 3.2×10^7, 4.6×10^7, and 5.4×10^7 Acm^{-2} at the pulse width of 100 ms for n = 1, 2, 4, respectively.[41] Thus, the switching current density in YPtBi is one order of magnitude lower than that of Pt, demonstrating that YPtBi is as efficient as TIs.

We then fit J_{th}^{YPtBi} by the thermal fluctuation model,[42,43]

$$J_{th}^{YPtBi} = J_{th0}^{YPtBi}\left[1-\frac{1}{\Delta}\ln\left(\frac{\tau}{\tau_0}\right)\right], \tag{5.7}$$

where, J_{th0}^{YPtBi} is the threshold current density for YPtBi layer at 0 K, Δ is the thermal stability factor, and $1/\tau_0$ (10 GHz) is the attempt frequency associated with the precession frequency of a magnetization. From the fitting, we obtained Δ = 39 and J_{th0}^{YPtBi} = 1.8×10^6 A/cm^2. Δ is similar to that of CoFeB/MgO in perpendicular magnetic tunnel junctions with diameter of 20 ~ 30 nm.

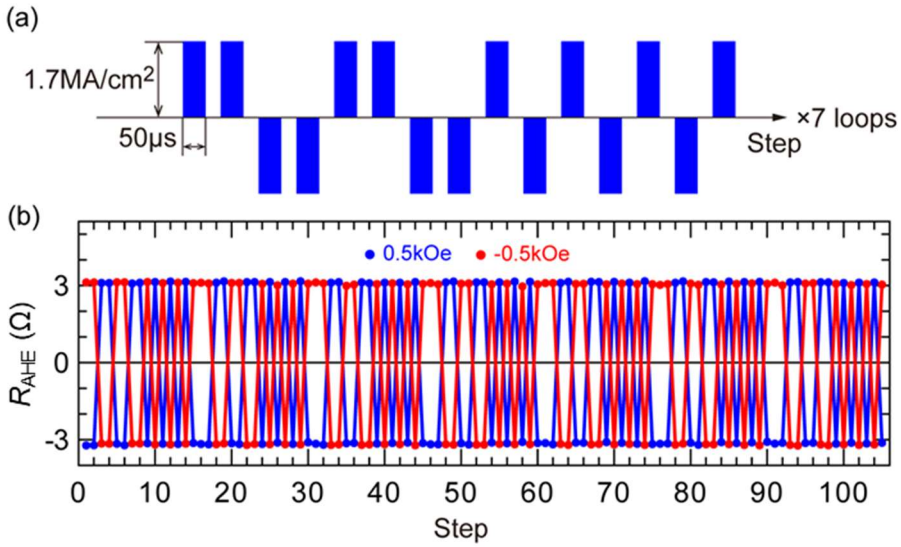

Figure 5.12. Robust SOT magnetization switching by YPtBi in sample E. (a) Sequence of 105 pulses with the current density in YPtB of 1.7×10^{6} Acm^{-2} and the pulse width of 50 μs. (b) Hall resistance data measured for a total of 210 pulses under a bias field of ±0.5 kOe.

Finally, to demonstrate robust SOT switching using YPtBi, we applied a sequence of 105 pulses with J_{YPtBi} of 1.7 MA/cm^2 and τ of 50 μs, as shown in Figure 5.12(a). Figure 5.12(b) shows the Hall resistance data measured for a total of 210 pulses under the bias field of H_{ext} = ±0.5 kOe. We observed very robust SOT switching by YPtBi, indicating that the spin Hall characteristics of YPtBi were unchanged during the pulse sequences.

5.6 Further improvement of spin Hall angle

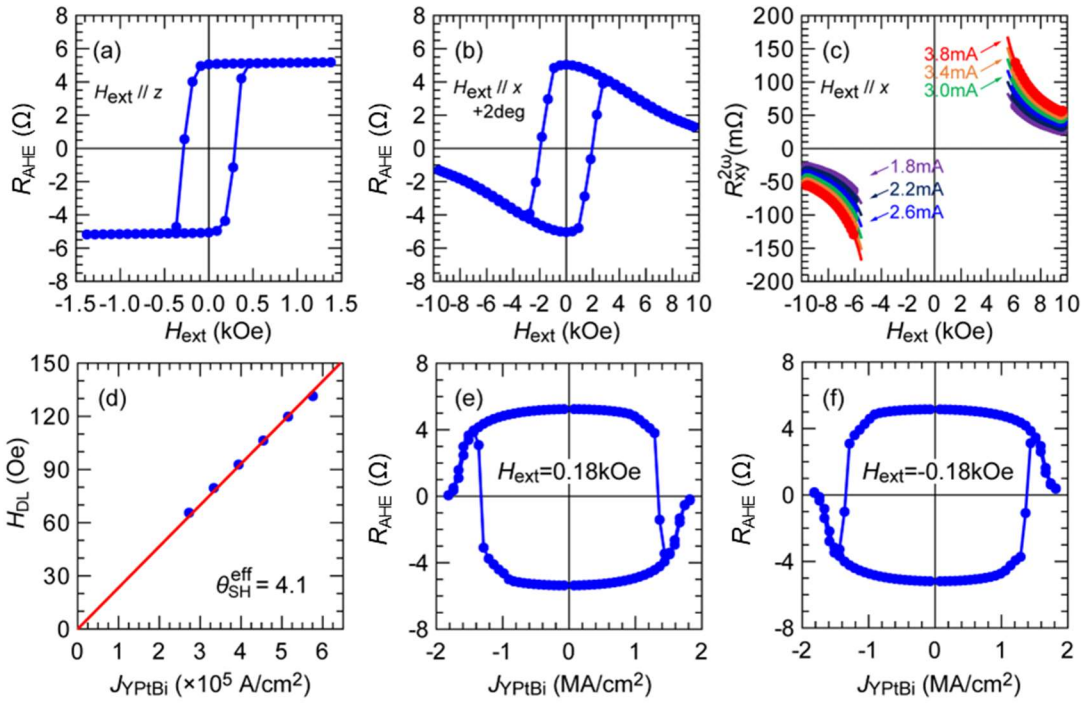

Figure 5.13. (a), (b) DC anomalous Hall resistance in sample F (σ_{YPtBi} = 0.36×10^5 Ω^{-1}m^{-1} and t_{Co}=0.5 nm) measured with H_{ext} applied along the *z*-direction and the *x*+2°-direction, respectively. (c) Second harmonic Hall resistance of sample F measured with H_{ext} applied along the *x*-direction and an AC current ranging from 1.8 to 3.8 mA, where dots are experimental data and solid curves show fitting results given by equation (2). (d) H_{DL} as a function of the current density in the YPtBi layer. (e), (f) SOT magnetization switching by DC currents with in-plane H_{ext} of 0.18 and -0.18 kOe applied along the *x*-direction, respectively.

In this section, we demonstrate the improvement of θ^{eff}_{SH} in YPtBi by improving spin transparency at the YPtBi interface. In previous sections, we have inserted an interfacial Pt layer between the YPtBi and Co layers to make the Pt/Co/Pt structure symmetric and to enhance the interfacial PMA between Co and Pt. However, spin dissipation can occur in the interfacial Pt layer and reduces the effective spin Hall angle of YPtBi. To eliminate this spin dissipation, we prepared a stack of Ta (1.0) / $MgAl_2O_4$ (2.0) / Pt (0.8) / Co (0.5) / YPtBi (10) / c-Sapphire (sample F). Figures

5.13(a) and 5.13(b) show the DC anomalous Hall resistance of sample F measured at room temperature with H_{ext} applied along the z-direction and x+2°-direction. Despite there is no Pt interfacial layer, we obtained PMA with H_k^{eff} = 4.6 kOe as shown in Figure 5.13(b), which is larger than that of sample E (H_k^{eff} = 3.4 kOe), thanks to the flat surface of the YPtBi layer. Figure 5.13(c) shows the high-field second harmonics data and the corresponding fitting for sample F at bias currents of 1.8 to 3.8 mA, where the dots and solid curves are the experimental data and fitting using equation (5.2), respectively. Figure 5.13(d) shows the relationship between the extracted values of H_{DL} and J_{YPtBi} for sample F. From the slope H_{DL} / J_{YPtBi}, M_S = 443 emu/cc and t_{CoPt} = 1.3 nm, we obtain θ_{SH}^{eff} = 4.1 for sample F, which is not only 2.6 times larger than that in sample E but also larger than that of several conventional TIs such as Bi_2Se_3, $(BiSb)_2Te_3$, and Bi_xTe_{1-x}.[4,5,7] Note that, the improvement factor of 2.6 cannot be explained only by the elimination of spin dissipation in the Pt interfacial layer, which is given by $\mathrm{sech}(t_{Pt}/\lambda_S^{Pt})$ = 0.78, where t_{Pt} and λ_S^{Pt} of 1.1 nm are thickness and spin relaxation length for Pt, respectively. This result indicates that additional spin dissipation due to other mechanisms at the interface between the YPtBi and Co layers, such as spin memory loss[44,45] and spin back flow,[46] is also smaller than those between YPtBi and Pt. Figure 5.13(e) and 5.13(f) show the SOT magnetization switching loops at room temperature by DC currents with H_{ext} of 0.18 and -0.18 kOe applied along the x-direction, respectively. The switching polarity in Figures 5.13(e) and 5.13(f) is similar to that of sample E, but opposite to what expected from the SHE of the top Pt layer, indicating that the observed SOT switching is governed by the SHE of YPtBi.

5.7 Summary

In this chapter, we have demonstrated a proof of concept that by using an HHA-TSM, we can combine the advantage of the high spin Hall performance of TIs ($\theta_{SH}^{eff} > 1$) and the high thermal stability (> 400°C) of HMs, which make it much easier for industrial adoption than the case of TIs. Our results open the door to the third-generation spin Hall materials with both high θ_{SH} and high compatibility with the BEOL process. Since HHA-TSMs include a group of three-element topological materials with great flexibility for material choice, we call for further investigation of the spin Hall performance of this family. Indeed, first principle calculations have suggested at least ten materials in this group.[13,14] Although the YPtBi thin films in this chapter were deposited by using multi target sputtering, bulk single crystal of some bismuthides, such as HoPdBi, LuPdBi, LuPtBi, YPtBi, GdPdBi, and DyPdBi have been synthesized by the Bi-flux technique,[25] indicating that it is possible to make large single crystal targets of HHA-TSM for mass production. Contrasting to the case of TIs, we found that there is no obvious physical nor technical difficulty for HHA-TSMs to be used in realistic spintronic applications.

5.8 References

1 Liu, L. *et al.* Spin-torque switching with the giant spin Hall effect of tantalum. *Science* **336**, 555–558 (2012).

2 Pai, C.-F. *et al*. Spin transfer torque devices utilizing the giant spin Hall effect of tungsten. *Appl. Phys. Lett.* **101**, 122404 (2012).

3 Liu, L., Lee, O. J., Gudmundsen, T. J., Ralph, D. C. & Buhrman, R. A. Current-Induced Switching of Perpendicularly Magnetized Magnetic Layers Using Spin Torque from the Spin Hall Effect. *Phys. Rev. Lett.* **109**, 096602 (2012).

[4] Mellnik, A. R. *et al*. Spin-transfer torque generated by a topological insulator. *Nature* **511**, 449-451 (2014).

[5] Wu, H. *et al*. Room-Temperature Spin-Orbit Torque from Topological Surface States. *Phys. Rev. Lett.* **123**, 207205 (2019).

[6] Khang, N. H. D. *et al*. A conductive topological insulator with large spin Hall effect for ultralow power spin–orbit torque switching. *Nat. Mater.* **17**, 808-813 (2018).

[7] Chen, T., Peng, C., Tsai, T., Liao, W., Wu, C., Yen, H., and Pai, C. Efficient Spin−Orbit Torque Switching with Nonepitaxial Chalcogenide Heterostructures. *ACS Appl. Mater. Interfaces* **12**, 7788 (2020).

[8] Mahendra, DC. *et al*. Room-temperature high spin–orbit torque due to quantum confinement in sputtered Bi_xSe_{1-x} films. *Nat. Mat.* **17**, 800–807 (2018).

[9] Khang, N. H. D., Nakano, S., Shirokura, T., Miyamoto, Y., Hai, P. N. Ultralow power spin–orbit torque magnetization switching induced by a non-epitaxial topological insulator on Si substrates. *Sci. Rep.* **10**, 12185 (2020).

[10] Fan, T., Khang, N. H. D., Shirokura, T., Huy, H. H., Hai, P. N. Low power spin–orbit torque switching in sputtered BiSb topological insulator/perpendicularly magnetized CoPt/MgO multilayers on oxidized Si substrate. *Appl. Phys. Lett.* **119**, 082403 (2021).

[11] Shi, S. *et al.* All-electric magnetization switching and Dzyaloshinskii-Moriya interaction in WTe_2/ferromagnet heterostructures. *Nat. Nanotechnol.* **14**, 945-949 (2019).

[12] Kimata, M., Chen, H., Kondou, K., Sugimoto, S., Muduli, P. K., Ikhlas, M., Omori, Y., Tomita, T., MacDonald, A. H., Nakatsuji, S. *et al.* Magnetic and magnetic inverse spin Hall effects in a non-collinear antiferromagnet. *Nature* **565**, 627–630 (2019).

[13] Ding, J. *et al*. Switching of a Magnet by Spin-Orbit Torque from a Topological Dirac

Semimetal. *Adv. Mater.* **33**, 2005909 (2021).

[14] Binda, F. *et al*. Spin-orbit torques and magnetotransport properties of α-Sn and β-Sn heterostructures. *Phys. Rev. B* **103**, 224428 (2021).

[15] Chadov, S. *et al*. Tunable multifunctional topological insulators in ternary Heusler compounds. *Nat. Mater.* **9**, 541-545 (2010).

[16] Lin, H. *et al*. Half-Heusler ternary compounds as new multifunctional experimental platforms for topological quantum phenomena. *Nat. Mater.* **9**, 546-549 (2010).

[17] Al-Sawai, W. *et al*. Topological electronic structure in half-Heusler topological insulators. *Phys. Rev. B* **82**, 125208 (2010).

[18] Müchler, L. *et al.* Topological Insulators from a Chemist's Perspective. *Angew. Chem., Int. Ed. Engl.* **51**, 7221 (2012).

[19] Nakajima, Y. *et al.* Topological *R*PdBi half-Heusler semimetals: A new family of noncentrosymmetric magnetic superconductors. *Sci. Adv*. **1**, e1500242 (2015).

[20] Yan, B. and de Visser, A. Half-Heusler topological insulators. *MRS Bull.* **39**, 859-66 (2014).

[21] Armitage, N. P. *et al*. Weyl and Dirac semimetals in three-dimensional solids. *Rev. Mod. Phys.* **90**, 015001 (2018).

[22] Liu, Z. K. *et al.* Observation of unusual topological surface states in half-Heusler compounds LnPtBi (Ln = Lu, Y). *Nat. Commun.* **7**, 12924 (2016).

[23] Logan, J. A. *et al.* Observation of a topologically non-trivial surface state in half-Heusler PtLuSb (001) thin films. *Nat. Commun.* **7**, 11993 (2016).

[24] Kronenberg, A. *et al.* Dirac cone and pseudogapped density of states in the topological half-Heusler compound YPtBi. *Phys. Rev B* **94**, 161108(R) (2016).

[25] Hosen, M. M. *et al.* Observation of Dirac state in half-Heusler material YPtBi. *Sci.*

Rep. **10**, 12343 (2020).

[26] Haase, M. G. *et al.* Equiatomic rare earth (Ln) transition metal antimonides LnTSb (T = Rh, Ir) and bismuthides LnTBi (T = Rh, Ni, Pd, Pt). *J. Solid State Chem.* **168**, 18–27 (2002).

[27] Pavlosiuk, O. *et al.* Magnetic and Transport Properties of Possibly Topologically Nontrivial Half-Heusler Bismuthides RMBi (R = Y, Gd, Dy, Ho, Lu; M = Pd, Pt). *Acta Phys. Pol. A* **130**, 573 (2016).

[28] Taskin, A. A. *et al.* Planar Hall effect from the surface of topological insulators. *Nat. Commun.* **8**, 1340 (2017).

[29] Zhou, L. *et al.* Surface-induced positive planar Hall effect in topological Kondo insulator SmB_6 microribbons. *Phys. Rev. B* **99**, 155424 (2019).

[30] Bhardwaj, A. *et al.* Observation of planar Hall effect in topological insulator-Bi_2Te_3. *Appl. Phys. Lett.* **118**, 241901 (2021).

[31] Budhani, R. C., Higgins, J. S., McAlmont, D. and Paglione, J. Planar Hall effect in c-axis textured films of $Bi_{85}Sb_{15}$ topological insulator. *AIP Advances* **11**, 055020 (2021).

[32] Nguyen, M.-H. *et al.* Spin Torque Study of the Spin Hall Conductivity and Spin Diffusion Length in Platinum Thin Films with Varying Resistivity. *Phys. Rev. Lett.* **116**, 126601 (2016).

[33] Wang,Y. *et al.* Determination of intrinsic spin Hall angle in Pt. *Appl. Phys. Lett.* **105**, 152412 (2014).

[34] Khang, N. H. D. and Hai, P. N. Spin-orbit torque as a method for field-free detection of in-plane magnetization switching. *Appl. Phys. Lett.* **117**, 252402 (2020).

[35] Hayashi, M. *et al.* Quantitative characterization of the spin-orbit torque using

harmonic Hall voltage measurements. *Phys Rev. B* **89**, 144425 (2014).

[36] Avci, C. O. *et al.* Interplay of spin-orbit torque and thermoelectric effects in ferromagnet/normal-metal bilayers. *Phys. Rev. B* **90**, 224427 (2014).

[37] Tanaka, T. *et al*. Intrinsic spin Hall effect and orbital Hall effect in 4*d* and 5*d* transition metals. *Phys. Rev. B* **77**, 165117 (2008).

[38] Sagasta, E. *et al*. Tuning the spin Hall effect of Pt from the moderately dirty to the superclean regime. *Phys. Rev. B* **94**, 060412(R) (2016).

[39] Zhang, Y. *et al.* Crossover of the three-dimensional topological insulator Bi_2Se_3 to the two-dimensional limit. *Nat. Phys.* **6**, 584-588 (2010).

[40] Liu, L. *et al.* Current-Induced Switching of Perpendicularly Magnetized Magnetic Layers Using Spin Torque from the Spin Hall Effect. *Phys. Rev. Lett.* **109**, 096602 (2012).

[41] Jinnai, B., Zhang, C., Kurenkov, A., Bersweiler, M., Sato, H., Fukami, S., Ohno, H. Spin-orbit torque induced magnetization switching in Co/Pt multilayers. *Appl. Phys. Lett.* **111**, 102402 (2017).

[42] Coffey, W. T. and Kalmykov, Y. P. Thermal fluctuations of magnetic nanoparticles: Fifty years after Brown. *J. Appl. Phys.* **112**, 121301 (2012).

[43] Koch, R. H. *et al.* Time-resolved reversal of spin-transfer switching in a nanomagnet. *Phys. Rev. Lett.* **92**, 088302 (2004).

[44] Pai, C-F. *et al.* Dependence of the efficiency of spin Hall torque on the transparency of Pt/ferromagnetic layer interfaces. *Phys. Rev. B* **92**, 064426 (2015).

[45] Zhu, L. *et al.* Spin-Orbit Torques in Heavy-Metal–Ferromagnet Bilayers with Varying Strengths of Interfacial Spin-Orbit Coupling. *Phys. Rev. Lett.* **122**, 077201 (2019).

[46] Haney, P. M. *et al.* Current induced torques and interfacial spin-orbit coupling: Semiclassical modeling. *Phys. Rev. B* **87**, 174411 (2013).

Chapter 6. Effect of Stoichiometry on the spin Hall angle in YPtBi

6.1 Introduction

In Chapter 5, we successfully developed an efficient spin source by using a kind of HHA-TSM, YPtBi, which has both large θ_{SH} (>1) and high thermal stability (600oC) that are important for BEOL processes. Although ideal HHA-TSM are zero-gap TIs with no Fermi surface,[1] there are extrinsic carriers due to various crystal defects that make those alloys semimetal with a finite Fermi surface. As described in Chapter 5, we shown that θ_{SH}^{eff} of YPtBi is sensitive to its electrical conductivity, which depends on the crystal growth parameters. However, the effect of stoichiometry on θ_{SH} in this alloy is not well understood. It is well-known that the SHE in TIs, such as Bi_2Se_3, strongly depends on stoichiometry, which brought controversy about the value of θ_{SH}^{eff} and is a big problem for using TIs in realistic spin devices. Because YPtBi is classified as a zero-gap TI, there is a possibility that the SHE in YPtBi can have a strong stoichiometry dependence. Thus, it is important to understand the effect of stoichiometry on the SHE in YPtBi.

In this work, we investigate θ_{SH}^{eff} of YPtBi when changing the composition ratio of Y/Pt (denoted as r) from 0.5 to 1.9. From XRD analysis, we found that YPtBi is highly ordered up to r = 1.5. Furthermore, the carrier concentration is minimized, and the mobility is maximized, thus σ_{YPtBi} is minimized (~0.36×10^5 $\Omega^{-1}m^{-1}$) when the alloy was tuned to the exact stoichiometry condition (r = 1.0), at which θ_{SH}^{eff} reached a maximum value of 1.7 in junctions with Pt/Co/Pt. Furthermore, we found that the $\theta_{SH}^{eff} - \sigma_{YPtBi}$ relationships is similar to that observed in Chapter 5 in samples with exact stoichiometry, indicating that the SHE in YPtBi is robust against the change of

its stoichiometry.

6.2 Crystallinity and the electric properties of YPtBi at various stoichiometry

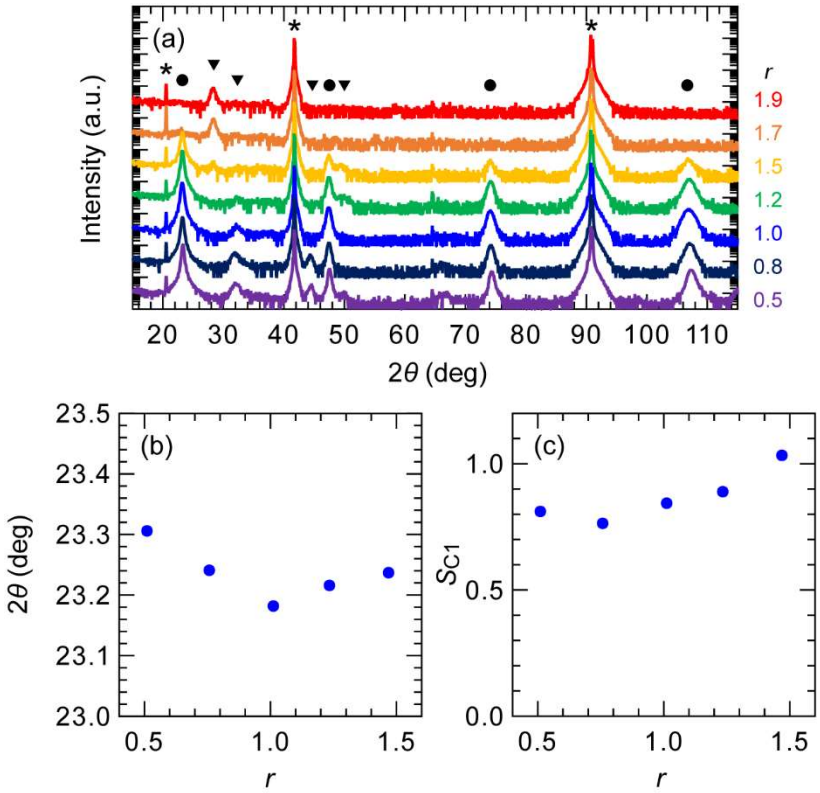

Figure 6.1. (a) XRD spectra depending on *r*. Asterisks denote, from left to right, the Al2O3(0003), (0006), and (00012) peaks of c-Sapphire substrate. Circles denote, from left to right, the YPtBi(111), (222), (333), (444) peaks. Triangles denote, from left to right, the peaks of parasitic alloys of Y(100), YPtx(110), YPtx(200), and YPtx(222). (b) *r* dependence of the peak position for YPtBi(111). (c) Order parameter of the C1 structure at various *r*.

First, we investigated the relationship between the crystallinity and the electric properties of YPtBi prepared by magnetron sputtering. For this purpose, we deposited 30 nm-thick YPtBi films on c-Sapphire substrate by co-sputtering from Y, Bi, and Pt targets. To change *r*, we kept the sputtering power of the Bi and Pt target constant, while changing the sputtering power of the Y target. The substrate temperature and

Ar pressure were kept at 600 °C and 2.0 Pa, respectively. A Ta capping layer was deposited on top of YPtBi to prevent oxidation of YPtBi for XRD measurements. Figure 6.1(a) shows the XRD spectra of the 30 nm-thick YPtBi samples at various *r*. XRD peaks of the YPtBi(111) plane (filled circles) were clearly observed for *r* between 0.5 and 1.5. However, except for the exact stoichiometry conduction $r = 1$, notable peaks from undesirable parasitic alloys (filled triangles) were also observed; Pt-rich YPtx alloys emerged at $r < 1.0$, while Y was observed at $r > 1.5$ due to oversupply of Pt or Y atoms. Figure 6.1(b) shows the *r* dependence of the peak position of YPtBi(111). The shift of the YPtBi(111) peak indicates that not all oversupplied atoms precipitates into undesirable parasitic alloys but parts of them entered substitutional sites in the YPtBi crystal, which means that YPtBi is non-stoichiometry at $r \neq 1$. We calculate the order parameter S_{C1} for Y and Bi against Pt in the C1 structure by using the integrated intensity ratio of YPtBi(222) at ~47° and YPtBi(444) at ~107°, which affects the density of state (DOS) around the Fermi level.[2] For the calculation, we took into account the powder ring distribution factor and absorption factor corrections.[3] Figure 6.1(b) shows the *r* dependence of S_{C1}. S_{C1} varied from 0.8 to 1.0 with increasing *r*. In this range of S_{C1}, the effect of disorder on DOS around Fermi level is limited.[2]

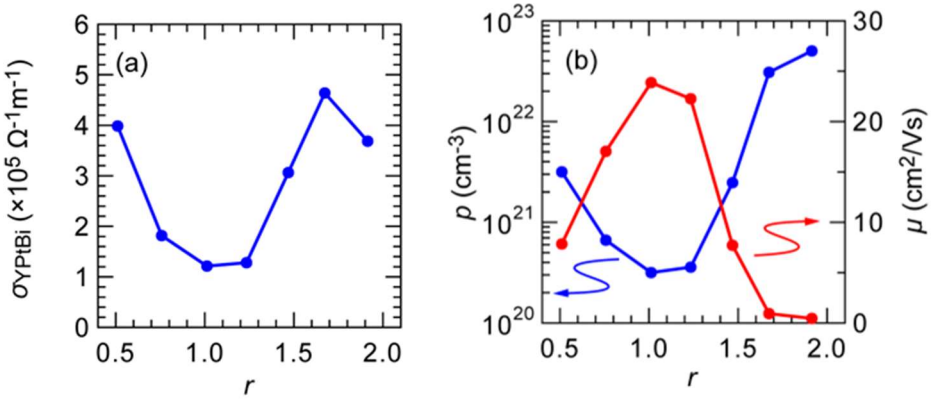

Figure 6.2. *r* dependence of (a) σ_{YPtBi}, (b) hole concentration *p* and mobility μ of 30 nm-thick YPtBi samples.

We then conducted the electrical transport measurements for 30 nm-thick YPtBi by using the van der Pauw method at room temperature. According to the Hall measurement results, the carrier type in our 30 nm-thick YPtBi is hole, consistent with observation by angle resolved photoemission spectroscopy.[4,5] Figure 6.2(a) shows the *r* dependence of σYPtBi. We observed that σ_{YPtBi} takes a minimum value at $r = 1.0$. Figure 6.2(b) shows the *r* dependence of the hole density *p* (blue circles) and mobility μ (red circles). At low $r = 0.5$ and high $r \geq 1.5$, *p* is as high as 10^{21}–10^{22} cm^{-3} and μ is less than 10 cm^2/Vs. However, at $r = 1$, *p* is drastically reduced to 3×10^{20} cm^{-3}, while μ is improved up to 24 cm^2/Vs. As discussed above, this dramatic change of *p* cannot be explained only by the change of the S_{C1} parameter. Rather, the extra carriers at $r \neq 1$ may be caused by extra electronic states arising from the defects such as anti-site due to non-stoichiometry of YPtBi.[6]

6.3 Spin Hall properties of YPtBi films at various stoichiometry

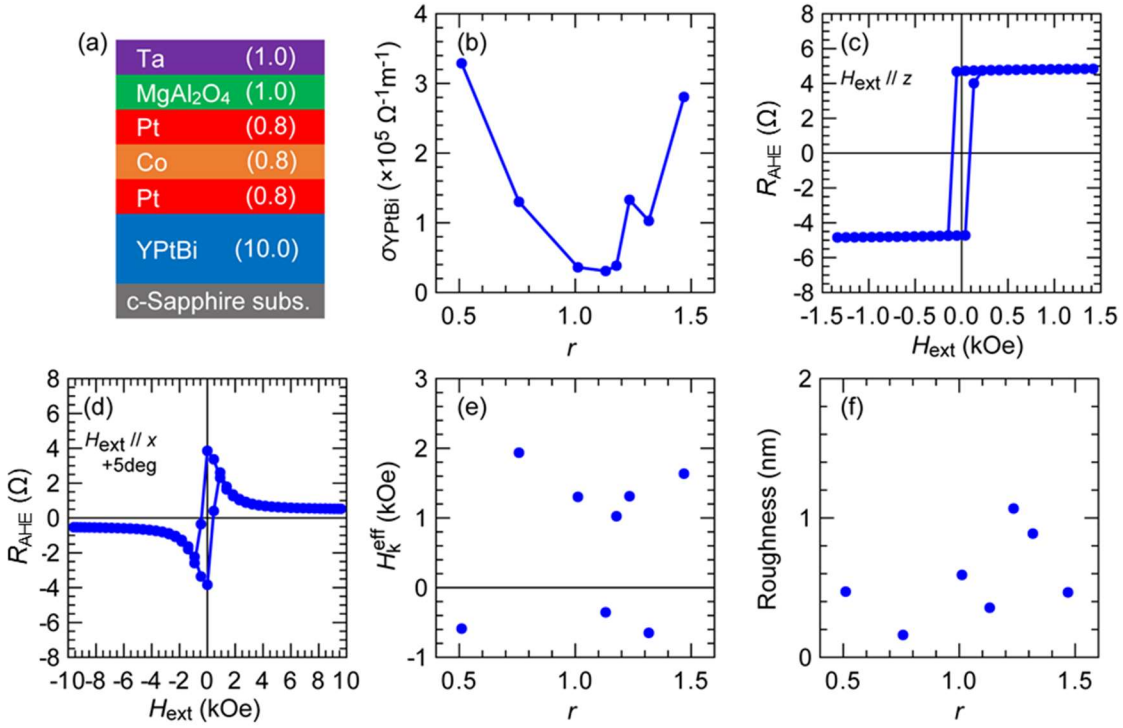

Figure 6.3. (a) Schematic illustration of sample structure for spin Hall measurements. (b) *r* dependence of σ_{YPtBi} in CoPt/YPtBi heterostructures. (c), (d) Anomalous Hall resistance at *r* = 1.0 with H_{ext} applied along the *z*-direction and *x*+5°-direction, respectively, measured by a direct current. (e), (f) *r* dependence of H_k^{eff} and surface roughness.

Next, we investigated the spin Hall properties of YPtBi films at various *r*. For this purpose, we prepared heterostructures of Ta (1.0) / $MgAl_2O_4$ (1.0) / CoPt (2.4) / YPtBi (10), as shown in Figure 6.3(a), where CoPt (2.4) = Pt (0.8) / Co (0.8) / Pt (0.8) (the number are the layer thicknesses in nm). Here, we assumed that the 1 nm-thick Ta layer on $MgAl_2O_4$ was fully oxidized after exposure to the air. The parasitic SHE from Pt layers is negligible because the thickness of Pt layer is few times thinner than the spin relaxation length of Pt layer and the structure of CoPt is symmetric.[7-9] After the deposition, these film stacks were patterned into 10 × 60 μm^2 Hall bar devices

with Pt/Ta electrodes for transport measurements. Figure 6.3(b) shows the r dependence of σ_{YPtBi}, which was calculated from the total conductivity of the CoPt/YPtBi heterostructures and the conductivity of a CoPt (2.4) standalone reference sample measured by a four-terminal method. σ_{YPtBi} of 10 nm-thick YPtBi in the heterostructure samples has similar r dependency with 30 nm-thick YPtBi. Figures 6.3(c) and 6.3(d) show the anomalous Hall resistance at r = 1.0 with H_{ext} applied along the z-direction and x + 5°-direction, measured by a direct current. By applying the generalized Sucksmith–Thompson method to Figure 6.3(d),[10] we achieved $H_{\mathrm{k}}^{\mathrm{eff}}$ of 1.3 kOe. Figure 6.3(e) shows the r dependence of $H_{\mathrm{k}}^{\mathrm{eff}}$ where the positive (negative) value of $H_{\mathrm{k}}^{\mathrm{eff}}$ correspond to PMA (IMA). Here, PMA was realized at most of r values thanks to the flat interface of YPtBi. However, $H_{\mathrm{k}}^{\mathrm{eff}}$ suddenly drops at r = 0.5 and around r ~ 1.2. Figure 6.3(f) shows the r dependence of the surface roughness of the CoPt/YPtBi heterostructures evaluated by AFM. We can see a correlation between Figures 6.3(e) and 6.3(f); samples with small surface roughness tend to have high $H_{\mathrm{k}}^{\mathrm{eff}}$. Therefore, the degradation of $H_{\mathrm{k}}^{\mathrm{eff}}$ was likely caused by an increase in the surface roughness.

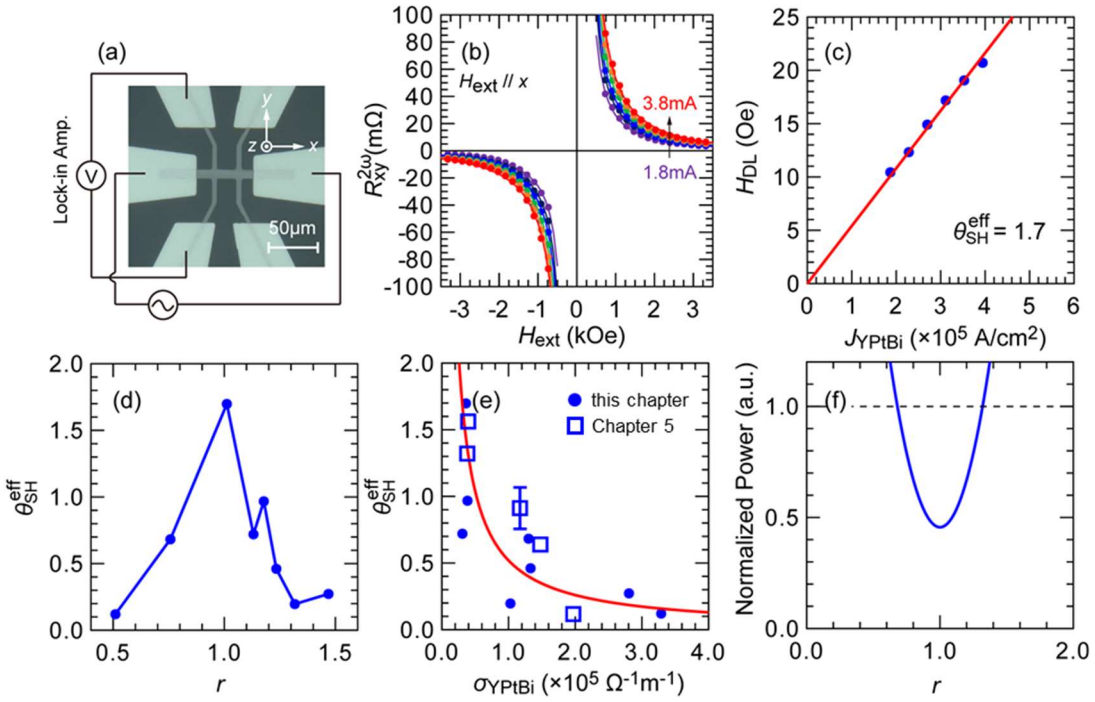

Figure 6.4. (a) Schematic illustration of the experimentally set up for the high-field second harmonic measurement and coordination system. (b) Representative high-field second harmonics data (r = 1.0) and the corresponding fitting at alternating bias currents of 1.8 to 3.8 mA (0.4 mA step), where the dots and solid curves are the experimental data and fitting using equation (6.1), respectively. (c) Relationship between the extracted values of H_{DL} and J_{YPtBi} at r = 1.0. (d) r dependence of θ^{eff}_{SH}. (e) Correlation between θ^{eff}_{SH} and σ_{YPtBi}. The red solid line indicates θ^{eff}_{SH} is inversely proportional to σ_{YPtBi}. (f) r dependence of the power consumption of SOT magnetization switching for YPtBi normalized by that for W in a bi-layer model.

We then evaluated θ^{eff}_{SH} by using the high-field second harmonic technique with an alternating current at 259.68 Hz. Figure 6.4(a) shows the experimental set up for the high-field second harmonic measurement and coordination system. In the high-field second harmonic method, $R^{2\omega}_{xy}$ measured at H_{ext} higher than H^{eff}_{k} applied along the x-direction is given by,[9,11,12]

$$R^{2\omega}_{xy} = \frac{R_{AHE}}{2}\frac{H_{DL}}{|H_{ext}| - H^{eff}_{k}} + \alpha_{ONE}|H_{ext}| + R_{ANE+SSE}. \quad (6.1)$$

Here, fitting parameters are H_{DL}, H_k^{eff}, α_{ONE}, and $R_{ANE+SSE}$. Figure 6.4(b) shows the representative high-field second harmonics data for the stoichiometry sample (r = 1.0) and the corresponding fitting using equation (6.1) at bias currents of 1.8–3.8 mA (0.4 mA step), where the dots and solid curves are the experimental data and fitting curves, respectively. Figure 6.4(c) shows the relationship between the extracted values of H_{DL} and J_{YPtBi} for this sample. Then, θ_{SH}^{eff} was calculated from the slope of H_{DL}/J_{YPtBi} by,

$$\theta_{SH}^{eff} = \frac{2eM_S t_{CoPt}}{\hbar} \frac{H_{DL}}{J_{YPtBi}}. \quad (6.2)$$

where the parameters M_S and t_{CoPt} are 431 emu/cc and 2.4 nm, respectively. Thanks to the large Berry phase of TSS and suppression of the shunting current to the bulk state by reducing extra carriers, large θ_{SH}^{eff} of 1.7 was observed. Note that, θ_{SH}^{eff} larger than 1 is very rare in topological semimetals because of large shunting current into the conductive bulk. Figure 6.4(d) shows the r dependence of θ_{SH}^{eff}. θ_{SH}^{eff} is maximum at stoichiometry (r = 1.0) but drops quickly at other non-stoichiometry conditions. This behavior is opposite that of σ_{YPtBi} shown in Figure 6.3(b). Figure 6.4(e) shows the correlation between σ_{YPtBi} and θ_{SH}^{eff} where blue circles are experimental results. Although the data was scattering, we can see a general trend that θ_{SH}^{eff} was inversely proportional to σ_{YPtBi} (red line). Furthermore, the θ_{SH}^{eff}–σ_{YPtBi} relationships is similar to that observed in Chapter 5 in samples with exact stoichiometry depicted in Figure 6.4(e) as rectangles. This implies that the SHE in YPtBi is robust against the change of its stoichiometry, which is another evidence that the SHE in YPtBi is originated from the intrinsic Berry phase mechanism of a TSS because the bulk origin one should strongly depend on its bulk band structure and change of Fermi level due to the change of its stoichiometry. This also explains

why there is no correlation between the order parameter in Figure 6.1(c) and θ_{SH}^{eff} in Figure 6.4(d). Rather, the spin Hall angle is affected indirectly through the change of σ_{YPtBi}.

Finally, we investigated how changing r affects the power consumption of SOT magnetization switching. For this purpose, we consider a bi-layer of a spin Hall layer and a ferromagnetic layer.[13] In this model, the power consumption P_{SOT} is proportional to $\frac{\sigma_{SOT}t_{SOT}+\sigma_{FM}t_{FM}}{(\sigma_{SOT}t_{SOT}\theta_{SH})^2}$, where σ_{SOT}, t_{SOT} and σ_{FM}, t_{FM} are the conductivity and thickness of the spin Hall layer and the ferromagnetic layer (assumed to be CoFeB), respectively. Figure 6.4(f) shows the r dependence of P_{SOT} for YPtBi normalized by P_{SOT} for W, where we assumed $t_{YPtBi} = 10$ nm, $t_W = 4$ nm, $\sigma_W = 4.7\times10^5$ $\Omega^{-1}m^{-1}$, $\theta_{SH}^{W} = 0.3$,[14] $t_{CoFeB} = 1$ nm, and $\sigma_{CoFeB} = 6.0\times10^5$ $\Omega^{-1}m^{-1}$. Here, the r dependence of σ_{YPtBi} was approximated by a quadratic function best fitted to data in Figure 6.3(b). We found that YPtBi provides smaller P_{SOT} than W within $0.7 < r < 1.3$, and the smallest power consumption is realized at the exact stoichiometry condition $r = 1.0$.

6.4 Summary

In this chapter, we have investigated the SHE in YPtBi while changing the Y/Pt composition ratio r. We successfully grew highly ordered YPtBi films at $r = 0.5$– 1.5. Furthermore, the extra carrier density was minimized, and mobility was maximized at the exact stoichiometry of $r = 1.0$, resulting in the minimum σ_{YPtBi}. We achieved a large θ_{SH}^{eff} of 1.7 at $r = 1.0$, where the power consumption of magnetization manipulation was minimized. We also found that the θ_{SH}^{eff}–conductivity relationship is robust against the change of its stoichiometry unlike the conventional TIs, which

is strong advantage of this alloy for spintronic applications.

6.5 References

[1] S. Chadov, X. Qi, J. Kübler, G. H. Fecher, C. Felser, and S. C. Zhang, Nat. Mater. **9**, 541-545 (2010).

[2] H. Narita, Y. Niimi, T. Miyawaki, N. Tanaka, and H. Asano, Jpn. J. Appl. Phys. **54**, 093002 (2015).

[3] E. Yang, D. E. Laughlin, and J-G. Zhu, IEEE Trans. Magn. **48**, 7 (2012).

[4] Z. K. Liu, L. X. Yang, S-C. Wu, C. Shekhar, J. Jiang, H. F. Yang, Y. Zhang, S-K. Mo, Z. Hussain, B. Yan, *et al*. Nat. Commun. **7**, 12924 (2016).

[5] M. M. Hosen, G. Dhakal, K. Dimitri, H. Choi, F. Kabir, C. Sims, O. Pavlosiuk, P. Wiśniewski, T. Durakiewicz, J-X. Zhu, *et al*. Sci. Rep. **10**, 12343 (2020).

[6] Y. G. Yu, X. Zhang, and A. Zunger, Phys. Rev. B **95**, 085201 (2017).

[7] Y. Wang, P. Deorani, X. Qiu, J. H. Kwon, and H. Yang, Appl. Phys. Lett. **105**, 152412 (2014).

[8] M.-H. Nguyen, D. C. Ralph, and R. A. Buhrman, Phys. Rev. Lett. **116**, 126601 (2016).

[9] N. H. D. Khang, S. Nakano, T. Shirokura, Y. Miyamoto, and P. N. Hai, Sci. Rep. **10**, 12185 (2020).

[10] H. Sato, M. Pathak, D. Mazumdar, X. Zhang, G. J. Mankey, P. LeClair, and A. Gupta, J. Appl. Phys. **109**, 103907 (2011).

[11] H. Wu, P. Zhang, P. Deng, Q. Lan, Q. Pan, S. A. Razavi, X. Che, L. Huang, B. Dai, K. Wong, *et al*. Phys. Rev. Lett. **123**, 207205 (2019).

[12] Y. Fan, P. Upadhyaya, X. Kou, M. Lang, S. Takei, Z. Wang, J. Tang, L. He, L-T. Chang, M. Montazeri, *et al*. Nat. Mater. **13**, 699 (2014).

[13] T. Fan, N. H. D. Khang, S. Nakano, and P. N. Hai, Sci. Rep. **12**, 2998 (2022).

[14] C.-F. Pai, L. Liu, Y. Li, H. W. Tseng, D. C. Ralph, and R. A. Buhrman, Appl. Phys. Lett. **101**, 122404 (2012).

Chapter 7.Giant spin Hall effect in YPtBi grown at low temperature

7.1 Introduction

In Chapter 5 and 6, we have demonstrated that YPtBi has not only large θ_{SH}^{eff} up to 4.1 but also high thermal stability of 600ºC, which is favorable for BEOL process. In YPtBi, suppression of bulk carrier or bulk conductivity is a key to achieve large θ_{SH}^{eff}. Since YPtBi is basically a zero-gap TI, the bulk carriers are generated by crystal defects. Therefore, previous chapters adopted high growth temperature of 600ºC during sputtering to improve the crystal quality. However, such a high growth temperature exceeds the limitation of 400ºC of BEOL process. For fabrication of realistic SOT devices on top of silicon electronics during BEOL process, it is essential to reduce the growth temperature to below 400ºC.

In this chapter, we investigate the SHE of YPtBi grown at lower temperature down to 300°C. We found that θ_{SH}^{eff} and σ_{SH}^{eff} of YPtBi decrease with lowering the growth temperature from θ_{SH}^{eff} = 2.8 and σ_{SH}^{eff} = 0.89×10^5 ($\hbar$/2e) Ω^{-1}m^{-1} at 600ºC to θ_{SH}^{eff} = 1.2 and σ_{SH}^{eff} = 0.33×10^5 ($\hbar$/2e) Ω^{-1}m^{-1} at 300ºC due to degradation of the crystallinity and spin transparency at the interface of CoPt/YPtBi. On the other hand, we found that by decreasing the sputtering Ar gas pressure, σ_{SH}^{eff} can be recovered by improving spin transparency thanks to higher migration energy of sputtered atoms. We realized a giant θ_{SH}^{eff} up to 8.2, and then performed SOT magnetization switching by ultralow current density in the YPtBi layer grown at 300°C with the Ar gas pressure of 1 Pa. Our results open up a way to achieve giant θ_{SH}^{eff} in YPtBi grown at low growth temperature suitable for BEOL process.

7.2 Effect of growth temperature on the crystallinity and spin Hall effect of YPtBi

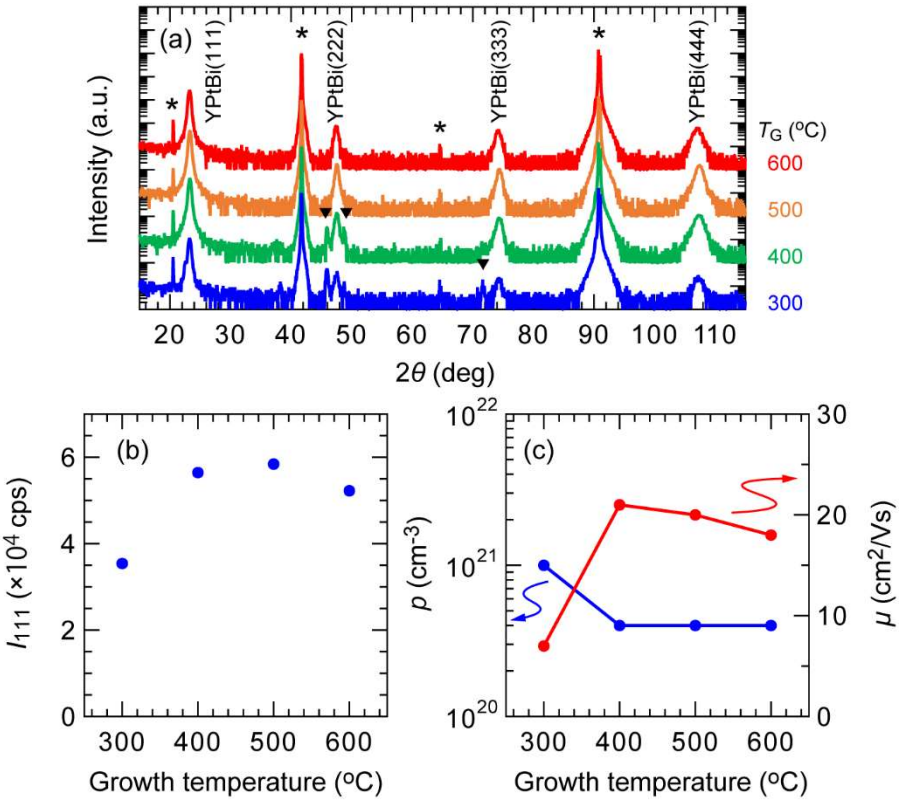

Figure 7.1 (a) XRD spectra of 30 nm-thick stand-alone YPtBi films deposited at various growth temperature (T_G). Asterisks denote, from left to right, the Al_2O_3(0003), (0006), (0009), and (00012) peaks of c-Sapphire substrate. Triangles denote, from left to right, the peaks of Bi(006), (202), and (300). (b) Growth temperature dependence of the integrated peak intensity of YPtBi(111) with the powder ring correction. (c) Growth temperature dependence of the hole carrier density p and mobility μ.

First, we investigated how the growth temperature (T_G) affects the SHE of YPtBi. We prepared 30 nm-thick YPtBi films grown at T_G = 300, 400, 500 and 600°C by co-sputtering Y, Pt, and Bi targets. The Ar gas pressure during YPtBi sputtering was fixed to 2.0 Pa, and the atomic Y/Pt composition ratio was fixed to the exact stoichiometry of 1.0 to minimize the bulk carriers by following Chapter 6. The sample structure was Ta (1.0) / $MgAl_2O_4$ (5.0) / YPtBi (30) / c-Sapphire (the number

are the layer thicknesses in nm). Here, we assumed that the 1 nm-thick Ta layer on $MgAl_2O_4$ was fully oxidized after exposure to the air. Figure 7.1(a) shows the XRD spectra for the YPtBi samples grown at various temperature. Peaks from YPtBi(111) orientations were clearly observed in all samples. Peaks from residual Bi (filled triangles) were also observed at T_G below 400°C, when the Bi de-absorption rate from the YPtBi films is lower. Figure 7.1(b) shows the T_G dependence of the integrated peak intensity of YPtBi(111) with the powder ring correction.[1] Although the integrated peak intensity is nearly unchanged at $T_G \geq 400$°C, it dropped at $T_G = 300$°C indicating degradation of the crystallinity. Figure 7.1(c) shows the T_G dependence of the hole carrier density p and mobility μ measured by using the van der Pauw method at room temperature. p and μ are nearly unchanged at $T_G \geq 400$°C and comparable to those reported in another sputtered Bi-based half Heusler alloy.[2] However, p increased to 10^{21} cm^{-3} while μ dropped to 7 cm^2/Vs at $T_G = 300$°C, reflecting degradation of the crystallinity. Therefore, weaker SHE is expected for the sample grown at 300°C due to its poor crystallinity.

We then investigate the relationship between the growth temperature and the SHE. For this purpose, we fabricated heterostructure samples consisting of Ta (1.0) / $MgAl_2O_4$ (1.0) / Pt (0.8) / Co (0.8) / Pt (0.8) / YPtBi (10) / c-Sapphire, where the YPtBi layer was grown at 300, 400, 500 and 600°C, and the Pt / Co / Pt layers were grown at room temperature. Below, we will refer Pt (0.8) / Co (0.8) / Pt (0.8) as CoPt (2.4) for short. Here, the parasitic SHE from the two Pt layers is negligible because the thickness of the Pt layers is few times thinner than the spin relaxation length of Pt and the layer structure of CoPt is symmetric.[3-6] After deposition, these samples were patterned into 10×60 μm^2 Hall bar devices with Pt/Ta electrodes for transport

measurements.

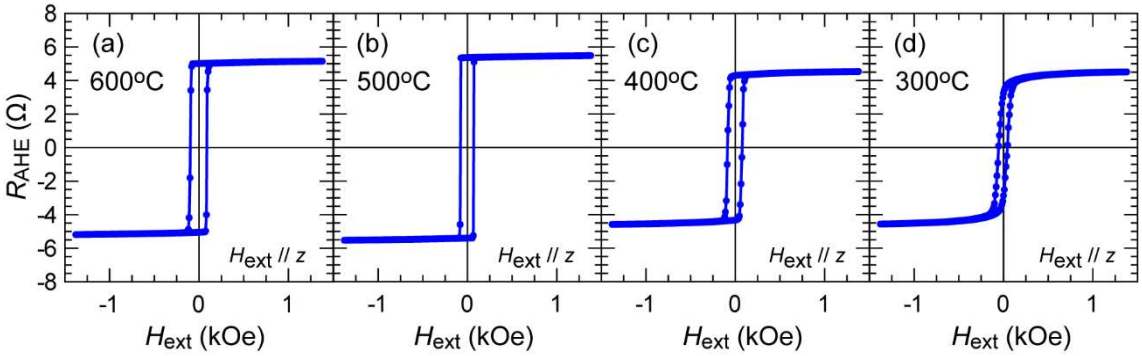

Figure 7.2. (a) – (d) Anomalous Hall resistance of 10×60 μm^2 Hall bar devices of Ta (1.0) / $MgAl_2O_4$ (1.0) / Pt (0.8) / Co (0.8) / Pt (0.8) / YPtBi (10) heterostructures, whose YPtBi layer was grown at 300, 400, 500 and 600ºC, respectively.

Figures 7.2(a) – (d) show the anomalous Hall resistance of the Hall bar devices measured with H_{ext} applied along the z-direction (film normal). Although all samples show PMA, the squareness ratio of the hysteresis of R_{AHE} becomes less than 1 at 300ºC. These results suggest that the quality of CoPt on YPtBi also degrades with decreasing T_G. Next, we used the high-field second harmonic Hall effect measurement technique with an alternating current at 259.68 Hz for evaluation of θ_{SH}^{eff}. In the high-field second harmonic Hall effect method, $R_{xy}^{2\omega}$ measured with H_{ext} applied along the x-direction (parallel to the current direction) and higher than H_k^{eff} is given by,[7,8]

$$R_{xy}^{2\omega} = \frac{R_{AHE}}{2}\frac{H_{DL}}{|H_{ext}| - H_k^{eff}} + \alpha_{ONE}|H_{ext}| + R_{ANE+SSE}. \quad (7.1)$$

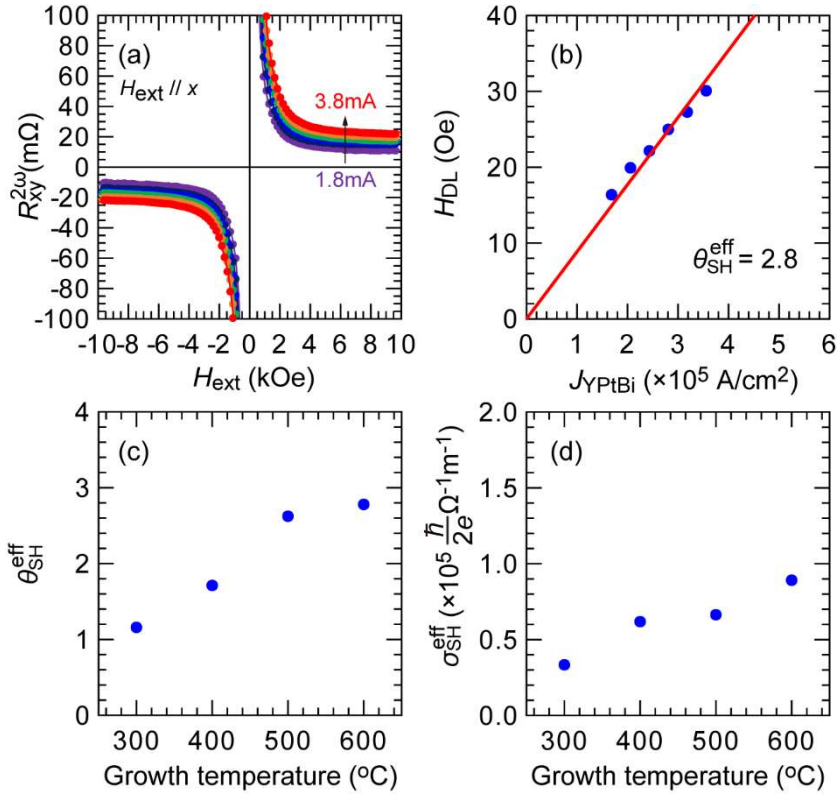

Figure 7.3. (a) Representative high-field second harmonic Hall resistance data for the heterostructure sample grown at 600°C, measured with alternating bias currents of 1.8 to 3.8 mA (0.4 mA step). Dots and solid curves are the experimental data and fitting curves using equation (7.1), respectively. (b) Relationship between the extracted values of H_{DL} and J_{YPtBi} for this sample. (c), (d) Growth temperature dependence of θ_{SH}^{eff} and σ_{SH}^{eff}, respectively.

Figure 7.3(a) shows the representative high-field second harmonic Hall resistance data for the sample grown at 600°C and the corresponding fitting using equation (7.1) at bias currents of 1.8 to 3.8 mA (0.4 mA step), where the dots and solid curves are the experimental data and fitting curves, respectively. Figure 7.3(b) shows the relationship between the extracted values of H_{DL} and J_{YPtBi} for this sample. Then, θ_{SH}^{eff} was calculated from the slope of H_{DL}/J_{YPtBi} by,

$$\theta_{SH}^{eff} = \frac{2eM_S t_{CoPt}}{\hbar} \frac{H_{DL}}{J_{YPtBi}}, \tag{7.2}$$

where the parameters M_S and t_{CoPt} are 431 emu/cc and 2.4 nm, respectively. We obtained large θ_{SH}^{eff} of 2.8 in the sample grown at 600ºC thanks to the large Berry phase of TSS and its high crystallinity. By this way, we estimated θ_{SH}^{eff} and $\sigma_{SH}^{eff} = \frac{\hbar}{2e}\theta_{SH}^{eff}\sigma_{YPtBi}$ for all samples. Here, σ_{YPtBi} is the conductivity of the 10 nm-thick YPtBi layer, estimated from the total resistance of the heterostructures and that of a reference Ta (1.0) / $MgAl_2O_4$ (1.0) / Pt (0.8) / Co (0.8) / Pt (0.8) sample without the 10 nm-thick YPtBi layer. Figures 7.3(c) and 7.3(d) show the T_G dependence of θ_{SH}^{eff} and σ_{SH}^{eff}, respectively. Both θ_{SH}^{eff} and σ_{SH}^{eff} monotonically decreases with lowering T_G, even though the crystal quality is maintained for $T_G \geq 400$ºC. Degradation of θ_{SH}^{eff} and σ_{SH}^{eff} at $T_G \geq 400$ºC is seemingly caused by the poor spin transparency due to degraded interface quality between CoPt and YPtBi, while further degradation of θ_{SH}^{eff} and σ_{SH}^{eff} at $T_G = 300$ºC is caused by the poor crystallinity of YPtBi.

7.3 Effect of sputtering Ar gas pressure on the crystallinity and spin Hall effect of YPtBi

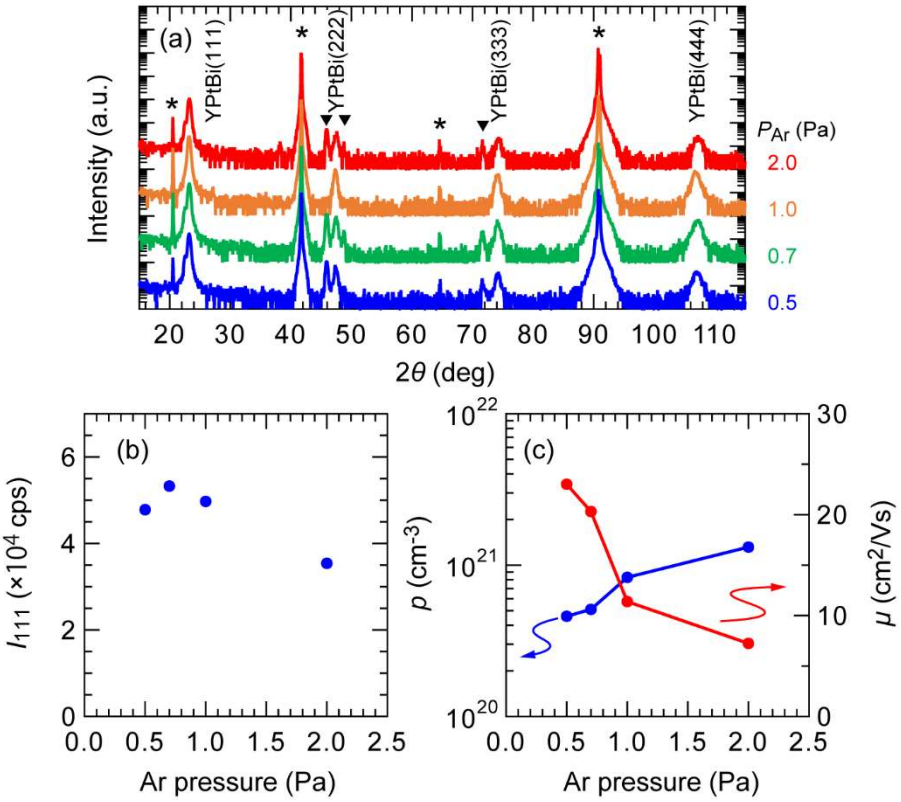

Figure 7.4. (a) XRD spectra of 30 nm-thick stand-alone YPtBi films deposited at 300°C with various Ar gas pressure (P_{Ar}). Asterisks denote, from left to right, the Al_2O_3(0003), (0006), (0009), and (00012) peaks of c-Sapphire substrate. Triangles denote, from left to right, the peaks of Bi(006), (202), and (300). (b) Ar pressure dependence of the integrated peak intensity of YPtBi(111) with the powder ring correction. (c) Ar pressure dependence of p and μ.

Next, we investigated the effect of sputtering Ar pressure (P_{Ar}) on the SHE of the sample grown at 300°C. Improvement of the bulk crystallinity and interface quality of YPtBi is expected by lowering P_{Ar} during YPtBi deposition, because lower P_{Ar} provides higher kinetic energy of sputtered Y/Pt/Bi atoms and recoil Ar atoms, leading to higher migration energy for the atoms that arrive on the film surface.[9] Figure 7.4(a) shows the P_{Ar} dependence of the XRD spectra for 30 nm-thick stand-

alone YPtBi samples grown at 300ºC. We found that YPtBi(111) orientation is maintained at lower P_{Ar}. Figure 7.4(b) shows the P_{Ar} dependence of the integrated peak intensity of YPtBi(111). The intensity was improved by reducing P_{Ar}, indicating improvement of the crystallinity. Figure 7.4(c) shows the P_{Ar} dependence of p and μ in 30 nm-thick stand-alone YPtBi thin films measured by using the van der Pauw method at room temperature. p monotonically decreases while μ monotonically increases with lowering P_{Ar}, indicating improvement of their crystallinity, which is consistent with the XRD results.

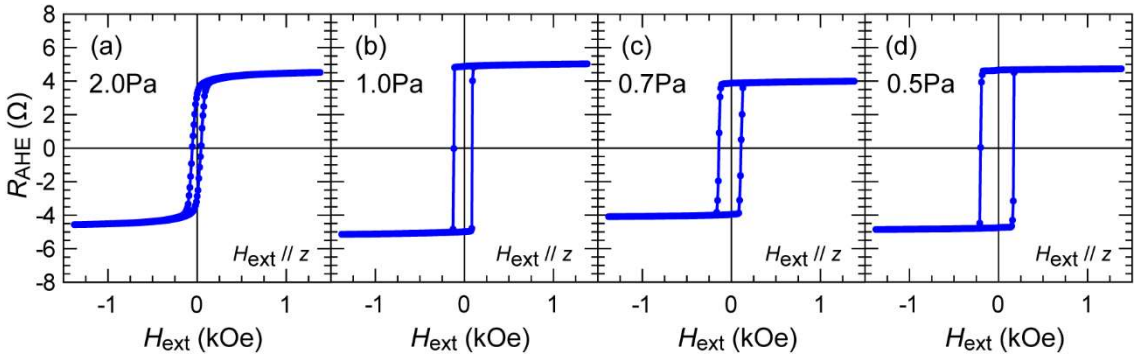

Figure 7.5. (a) – (d) Anomalous Hall resistance of 10×60 μm^2 Hall bar devices of Ta (1.0) / $MgAl_2O_4$ (1.0) / Pt (0.8) / Co (0.8) / Pt (0.8) / YPtBi (10) heterostructure samples, whose YPtBi layer was grown at 300°C with P_{Ar} of 2.0, 1.0, 0.7 and 0.5 Pa, respectively.

Next, we investigated the SHE of YPtBi grown at 300°C with various P_{Ar} in heterostructures of Ta (1.0) / $MgAl_2O_4$ (1.0) / Pt (0.8) / Co (0.8) / Pt (0.8) / YPtBi (10) / c-Sapphire. Figures 7.5(a) – (d) show R_{AHE} of 10×60 μm^2 Hall bar devices of those samples measured with H_{ext} applied along the z-direction. We found that the squareness ratio of the R_{AHE} hysteresis was recovered by reducing P_{Ar}.

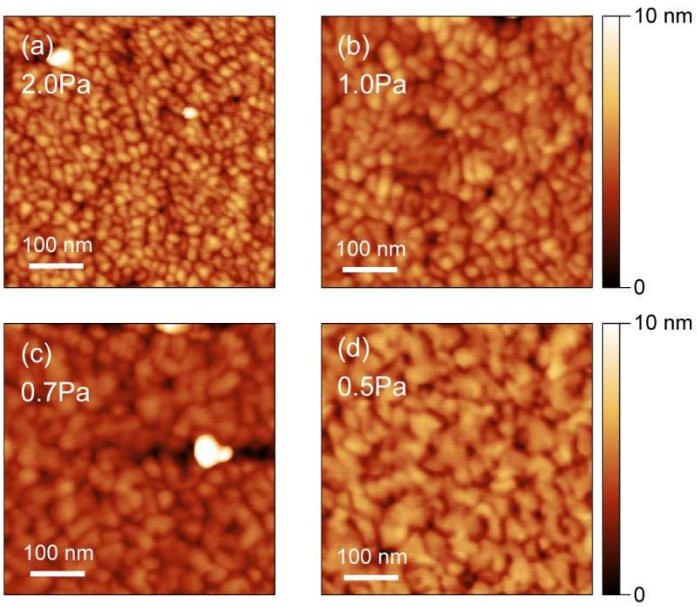

Figure 7.6. (a) – (d) Surface morphology measured by atomic force microscopy for the heterostructure samples, whose YPtBi layer was grown at 300°C with P_{Ar} of 2.0, 1.0, 0.7 and 0.5 Pa, respectively.

Figures 7.6(a) – (d) show the surface morphology for these samples measured by atomic force microscopy. We observed that the grain size becomes larger as expected from the higher migration energy of atoms arrived on the surface of YPtBi at low P_{Ar}, consistent of the improved bulk crystal quality shown in Figure 7.4 and the enhanced hysteresis of R_{AHE} in Figure 7.5.

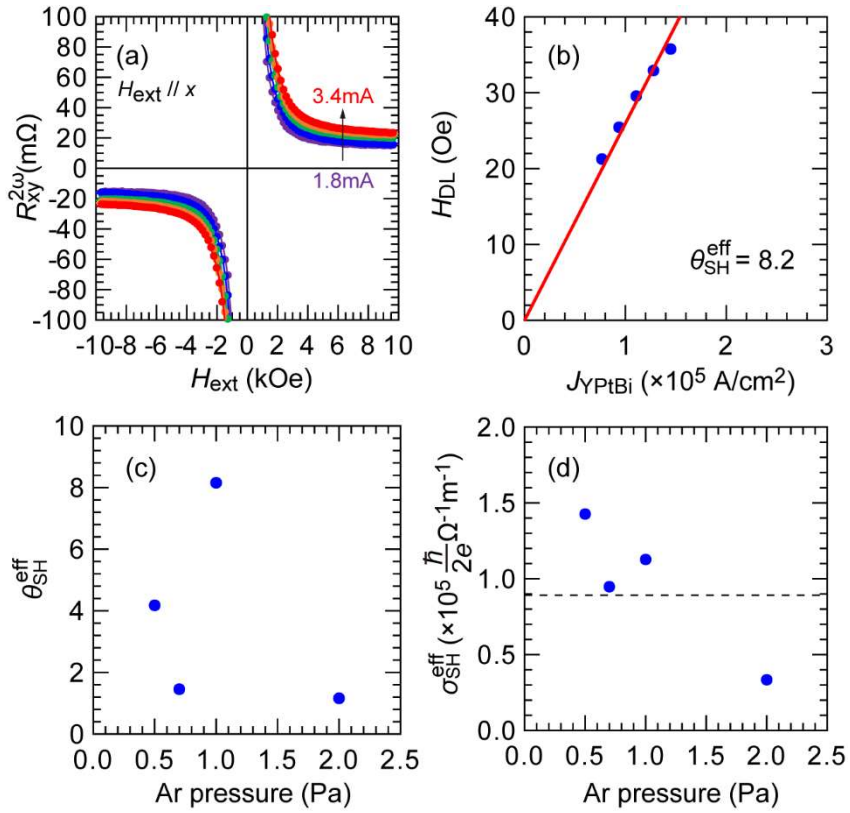

Figure 7.7. (a) Representative high-field second harmonic Hall resistance data for the heterostructure sample whose YPtBi layer was grown at 300°C with P_{Ar} = 1.0 Pa, measured by alternating bias currents of 1.8 to 3.4 mA (0.4 mA step). Dots and solid curves are the experimental data and fitting using equation (7.1), respectively. (b) Relationship between the extracted values of H_{DL} and J_{YPtBi} for this sample. (c) Ar pressure dependence of θ_{SH}^{eff} of heterostructure samples with YPtBi grown at 300°C. (d) Ar pressure dependence of σ_{SH}^{eff}, where the black dashed line indicates the σ_{SH}^{eff} value of the sample grown at 600°C with P_{Ar} = 2.0 Pa.

Figure 7.7(a) shows the representative high-field second harmonic Hall resistance data for the sample grown at P_{Ar} = 1.0 Pa with low conductivity σ_{YPtBi} of 0.14×10^5 $\Omega^{-1}m^{-1}$, and the corresponding fitting using equation (7.1) at bias currents of 1.8 to 3.4 mA (0.4 mA step), where the dots and solid curves are the experimental data and fitting curves, respectively. Figure 7.7(b) shows the relationship between the extracted values of H_{DL} and J_{YPtBi} for this sample. From this slope, we obtained a

giant θ_{SH}^{eff} of 8.2 thanks to suppression of bulk shunting current in this sample. This value is larger than θ_{SH}^{eff} of many conventional chalcogenide-based TIs,[10-12] and comparable to that of sputtered BiSb topological insulator.[13] Figure 7.7(c) shows the P_{Ar} dependence of θ_{SH}^{eff}. Although θ_{SH}^{eff} does not increase monotonously with lowering P_{Ar}, we achieved large θ_{SH}^{eff} of 1.5 at P_{Ar} = 0.7 Pa and 4.2 at P_{Ar} = 0.5 Pa. Figure 7.7(d) shows the P_{Ar} dependence of σ_{SH}^{eff}. σ_{SH}^{eff} is drastically improved at P_{Ar} ≤ 1 Pa by recovering spin transparency at the interface between CoPt and YPtBi, and exceeds that of the sample grown at 600ºC with P_{Ar} = 2.0 Pa denoted by the dashed line.

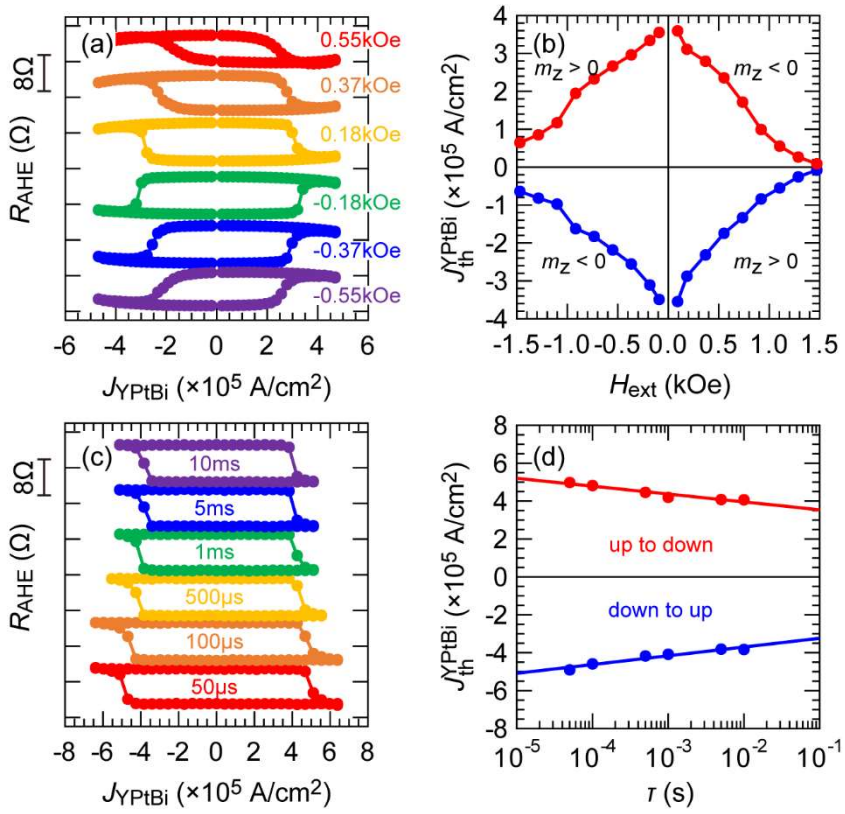

Figure 7.8. Current-induced SOT magnetization switching in the heterostructure sample whose YPtBi was grown at 300°C with P_{Ar} = 1.0 Pa. (a) SOT magnetization switching by direct currents with various in-plane H_{ext} (-0.55 to 0.55 kOe) applied along the *x*-direction. (b) Threshold switching current density in YPtBi as a function of H_{ext}. (c) SOT magnetization switching by pulse currents with various pulse width ranging from 50 μs to 10 ms and H_{ext} of 0.18 kOe. (d) Threshold switching current density in YPtBi as a function of pulse width, where dots are experimental data and solid lines show fitting results given by equation (7.3).

Finally, we demonstrated SOT magnetization switching by ultralow current density in the sample with giant θ_{SH}^{eff} of 8.2. Figure 7.8(a) shows DC-induced SOT magnetization switching with H_{ext} (-0.55 ~ 0.55 kOe) applied along the *x*-direction. The switching polarity was inverted when the direction of H_{ext} was reversed, consistent with the feature of SOT switching. Here, the switching polarity was same as Pt.[14] Figure 7.8(b) shows J_{th}^{YPtBi} as a function of H_{ext}. Low J_{th}^{YPtBi} on the order of

10^5 Acm^{-2} was achieved for entire H_{ext}. Figure 7.8(c) shows the pulse current-induced SOT switching with H_{ext} of 0.18 kOe applied along the x-direction, where the pulse width τ was set to 50 μs ~ 10 ms. Figure 7.8(d) shows J_{th}^{YPtBi} as a function of τ. The switching current density in YPtBi is two orders of magnitude smaller than that in Pt with CoPt ferromagnetic layer at 100 ms pulse current.[15] We then fit J_{th}^{YPtBi} by the thermal activation model,[16,17]

$$J_{th}^{YPtBi} = J_{th0}^{YPtBi}\left[1-\frac{1}{\Delta}\ln\left(\frac{\tau}{\tau_0}\right)\right], \tag{7.3}$$

From the fitting, we obtained $\Delta = 39$ and $J_{th0}^{YPtBi} = 7.3\times10^5$ A/cm^2.

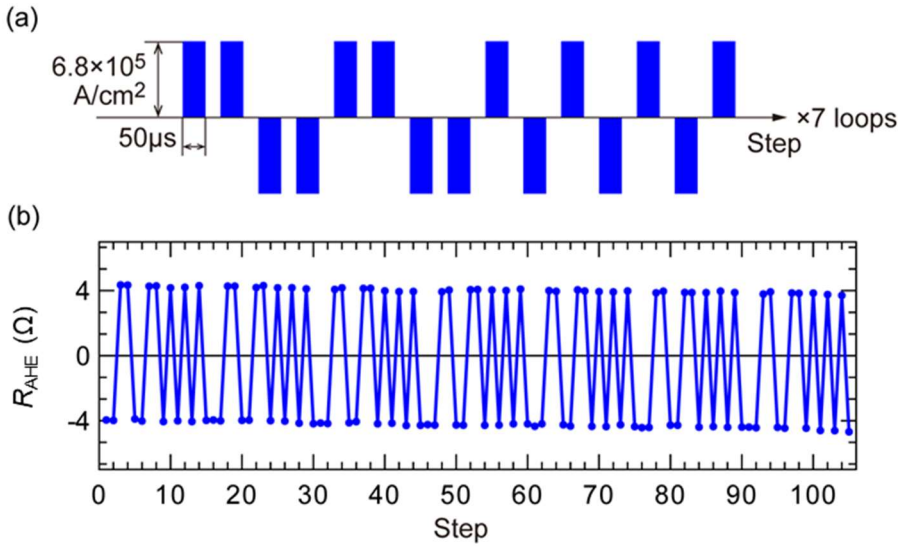

Figure 7.9. Robust SOT magnetization switching in the heterostructure sample whose YPtBi was grown at 300°C with P_{Ar} = 1.0 Pa. (a) Sequence of 105 pulses with the current density in YPtBi of 6.8×10^5 Acm^{-2} and the pulse width of 50 μs. (b) Hall resistance data measured under an in-plane bias field of 0.18 kOe.

Finally, we demonstrate repeating SOT switching by pulse currents of J_{YPtBi} = 6.8×10^5 A/cm^2 and τ = 50 μs. Figure 7.9(a) shows the sequence of total 105 pulse currents. Figure 7.9(b) shows the Hall resistance data measured with H_{ext} = 0.18 kOe

applied along the *x*-direction. We observed very robust switching by YPtBi. These results indicate that the YPtBi film grown at 300°C and low P_{Ar} has SOT performance not inferior to that of the sample grown at 600°C.

7.4 Summary

In this chapter, we have investigated the SHE of YPtBi films grown at lower temperature. When we reduced the growth temperature from 600°C to 300°C, both θ_{SH}^{eff} and σ_{SH}^{eff} decrease due to degradation of crystallinity of YPtBi and spin transparency at the interface between CoPt and YPtBi. To improve the SHE for samples grown at 300°C, we reduced the Ar gas pressure to increase the migration energy of atoms arrived on the surface of YPtBi. We obtained better crystallinity of YPtBi and achieved giant θ_{SH}^{eff} up to 8.2 by recovering spin transparency at the interface of CoPt/YPtBi, which is larger than those of most TIs. We demonstrated current-induced SOT magnetization switching with ultralow current density of 10^5 A/cm^2 in the YPtBi layer grown at 300°C by both DC and pulse currents. These results indicate the potential of YPtBi as an efficient spin source and open up a way to achieve a giant θ_{SH}^{eff} in YPtBi grown at low growth temperature suitable for BEOL process.

7.5 References

1 E. Yang, D. E. Laughlin, and J-G. Zhu, IEEE Trans. Magn. **48**, 7 (2012).

2 H. Narita, Y. Niimi, T. Miyawaki, N. Tanaka, and H. Asano, Jpn. J. Appl. Phys. **54**, 093002 (2015).

3 Y. Wang, P. Deorani, X. Qiu, J. H. Kwon, and H. Yang, Appl. Phys. Lett. **105**, 152412 (2014).

[4] M.-H. Nguyen, D. C. Ralph, and R. A. Buhrman, Phys. Rev. Lett. **116**, 126601 (2016).

[5] N. H. D. Khang, S. Nakano, T. Shirokura, Y. Miyamoto, and P. N. Hai, Sci. Rep. **10**, 12185 (2020).

[6] N. H. D. Khang and P. N. Hai, Appl. Phys. Lett. **117**, 252402 (2020).

[7] M. Hayashi, J. Kim, M. Yamanouchi and H. Ohno, Phys Rev. B **89**, 144425 (2014).

[8] C. O. Avci, K. Garello, M. Gabureac, A. Ghosh, A. Fuhrer, S. F. Alvarado and P. Gambardella, Phys. Rev. B **90**, 224427 (2014).

[9] J. A. Thornton, Ann. Rev. Mater. Sci. **7**, 239 (1977).

[10] A. R. Mellnik, J. S. Lee, A. Richardella, J. L. Grab, P. J. Mintun, M. H. Fischer, A. Vaezi, A. Manchon, E.-A. Kim, N. Samarth, and D. C. Ralph, Nature **511**, 449 (2014).

[11] H. Wu, P. Zhang, P. Deng, Q. Lan, Q. Pan, S. A. Razavi, X. Che, L. Huang, B. Dai, K. Wong, *et al*. Phys. Rev. Lett. **123**, 207205 (2019).

[12] T.-Y. Chen, C-W. Peng, T.-Y. Tsai, W.-B. Liao, C.-T. Wu, H.-W. Yen, and C.-F. Pai, ACS Appl. Mater. Interfaces **12**, 7788 (2020).

[13] T. Fan, N. H. D. Khang, S. Nakano, and P. N. Hai, Sci. Rep. **12**, 2998 (2022).

[14] L. Liu, O. J. Lee, T. J. Gudmundsen, D. C. Ralph, and R. A. Buhrman, Phys. Rev. Lett. **109**, 096602 (2012).

[15] B. Jinnai, C. Zhang, A. Kurenkov, M. Bersweiler, H. Sato, S. Fukami, and H. Ohno, Appl. Phys. Lett. **111**, 102402 (2017).

[16] W. T. Coffey, and Y. P. Kalmykov, J. Appl. Phys. **112**, 121301 (2012).

[17] R. H. Koch, J. A. Katine, and J. Z. Sun, Phys. Rev. Lett. **92**, 088302 (2004).

Chapter 8. Strong spin Hall effect in conductive YPtBi sputtered on oxidized Si substrate

8.1 Introduction

Through Chapter 5 to 7, we have demonstrated the novel spin Hall properties of YPtBi deposited on crystalized c-Sapphire substrates. However, realistic SOT devices are fabricated on bare SiO_2/Si substrates. Therefore, investigation of SOT properties of YPtBi deposited on SiO_2/Si substrates is strongly required for development of next generation SOT devices with YPtBi.

In this chapter, we investigate the SHE in sputtered YPtBi films grown on SiO_2/Si substrates. Although crystallinity of YPtBi films on SiO_2/Si were degraded compared to that deposited on crystallized substrates, their spin Hall conductivity is maintained, which may be attributed to the robustness of TSS in YPtBi. We revealed that inserting an 1nm-thick Ta buffer layer can yield a giant θ_{SH} of 1.3 and high conductivity of 1.4×10^5 $\Omega^{-1}m^{-1}$ at the same time by improving the crystallinity of YPtBi. We then demonstrate pulse current induced SOT magnetization switching with low current density of 10^6 A/cm^2, which is one order smaller than that of heavy metals. Our results demonstrate the feasibility of YPtBi-based SOT devices with ultralow power consumption on SiO_2/Si substrates.

8.2 Characterization of crystal quality and electrical property of YPtBi single layer

We prepared three kinds of YPtBi thin films: one grown directly on bare SiO_2/Si substrate, and two grown on a 1 nm-thick Ta buffer layer, or a 10 nm-thick CrO_x insulating buffer layers. YPtBi was deposited by the co-sputtering Y, Pt, and Bi targets. The substrate temperature and Ar pressure during deposition were fixed to

300°C and 0.5 Pa to improve σ_{SH}^{eff}. The stoichiometry ratio of Y:Pt was set to exact stoichiometry of 1:1 to maximize θ_{SH}. First, we investigated the crystallinity of 30 nm-thick YPtBi films with Ta (1.0) / $MgAl_2O_4$ (5.0) capping layer (the number are the layer thicknesses in nm). Here, the 1 nm-thick Ta on $MgAl_2O_4$ layer was assumed to be fully oxidized after exposure to the air.

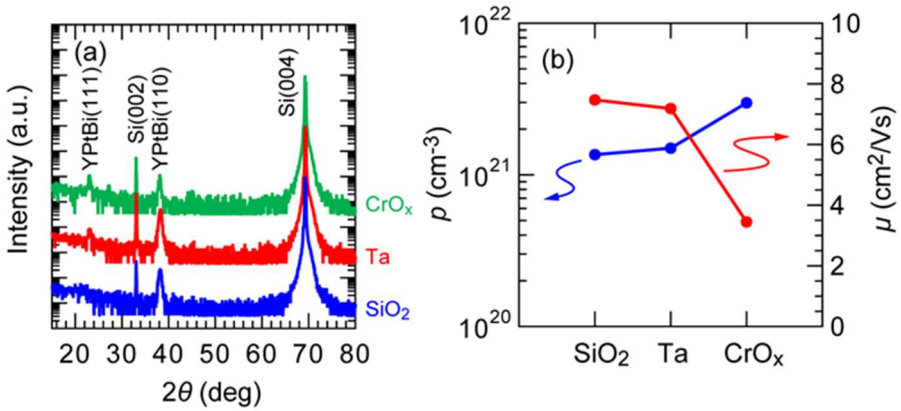

Figure 8.1. (a) XRD spectra of 30 nm-thick stand-alone YPtBi films deposited directly on SiO_2/Si, and on Ta, or CrO_x buffer layers. (b) Buffer layer dependence of carrier density and mobility for 30 nm-thick stand-alone YPtBi films measured by the van der Pauw method.

Figure 8.1(a) shows the X-ray diffraction (XRD) spectra for each sample. The (110) orientation dominated in the sputtered YPtBi films grown on amorphous SiO_2/Si substrate because the (110) plane corresponds to the close-packed plane for half Heusler alloys, while YPtBi was oriented to (111) on c-Sapphire in Chapters 5 – 7. Here, such a difference of orientation may not affect the spin Hall properties because the number of TSS does not depend on the crystal orientation in YPtBi[1] unlike the topological insulator BiSb.[2] By comparing the peak intensity of YPtBi(220) in all samples, the Ta-sample has the strongest intensity, indicating the best crystal quality

among them. Figure 8.1(b) shows the carrier density and mobility measured by the van der Pauw method. Their carrier density (mobility) is one order higher (lower) than that grown on a c-Sapphire substrate, indicating the degradation of the crystallinity.

8.3 Spin Hall properties of YPtBi

Next, we investigated the spin Hall effect in sputtered YPtBi films on SiO_2/Si substrate. For this purpose, we fabricated heterostructures of Ta (1.0) / $MgAl_2O_4$ (1.0) / Pt (0.8) / Co (0.8) / Pt (0.8) / YPtBi (10) / buffer layer / SiO_2 / Si. The sample with no buffer layer, 1 nm-thick Ta, and 10 nm-thick CrO_x buffer layers are referred as SiO_2-, Ta-, and CrO_x-samples, respectively. After deposition, these samples were patterned into 10×60 μm^2 Hall bar devices with Pt/Ta electrodes for transport measurements. Here, it is known that the parasitic spin Hall effect from Pt layers is negligible thanks to the symmetric structure of CoPt and negligible thickness of Pt layer comparing with its spin relaxation length.[3-6]

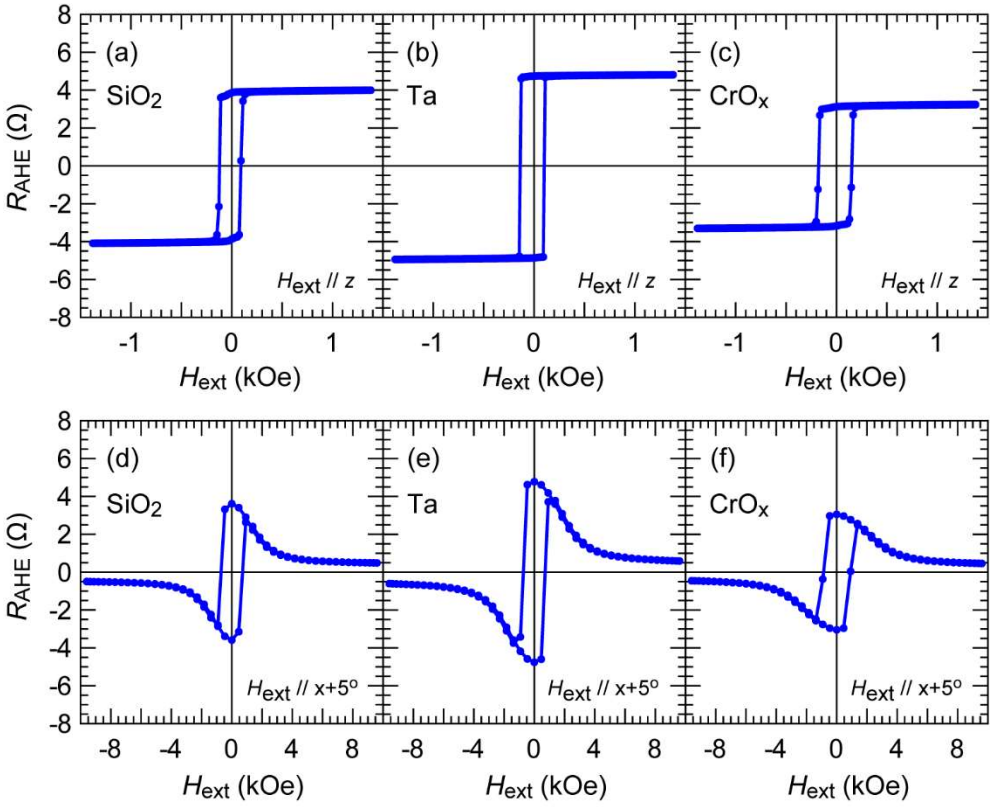

Figure 8.2. Anomalous Hall resistance for SiO_2-, Ta-, and CrO_x-samples, where H_{ext} is applied along (a) – (c) the *z*-axis (perpendicular to the films), and (d) – (f) the *x*-axis + 5° (the *x*-axis is parallel to the current).

Figures 8.2(a) – (c) show the anomalous Hall resistance with H_{ext} applied along the *z*-direction (film normal), and Figures 8.2(d) – (f) show that with H_{ext} applied along the *x*+5°-direction (the *x*-direction is parallel to the current) for SiO_2-, Ta-, and CrO_x-samples, respectively. The CoPt layers showed PMA in all samples, and their H_k^{eff} were 1.6, 2.0, and 2.3 kOe in SiO_2-, Ta-, and CrO_x- samples, respectively.

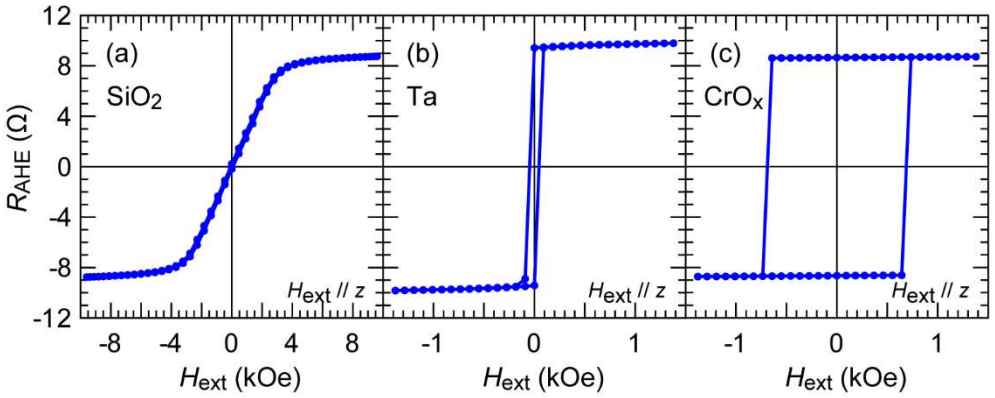

Figure 8.3. Anomalous Hall resistance for CoPt controlled stacks grown on (a) bare SiO_2 / Si, (b) 1 nm-thick Ta, and (c) 10 nm-thick CrOx buffer layers, respectively. Here, H_{ext} was applied along the *z*-direction.

Interestingly, PMA disappeared when CoPt was deposited on bare SiO_2/Si without a 10 nm-thick YPtBi layer. Figures 8.3 (a) – (c) show the anomalous Hall resistance with H_{ext} applied along the *z*-direction in CoPt controlled stacks grown on bare SiO_2/Si, 1 nm-thick Ta, and 10 nm-thick CrO_x buffer layers, respectively. Although PMA was observed in the samples with Ta and CrO_x buffer layer, CoPt became IMA when deposited directly on bare SiO_2/Si. This result indicates that 10 nm-thick YPtBi acts as an efficient buffer layer for PMA-CoPt, which is an advantage for high bit density magnetic memory devices.

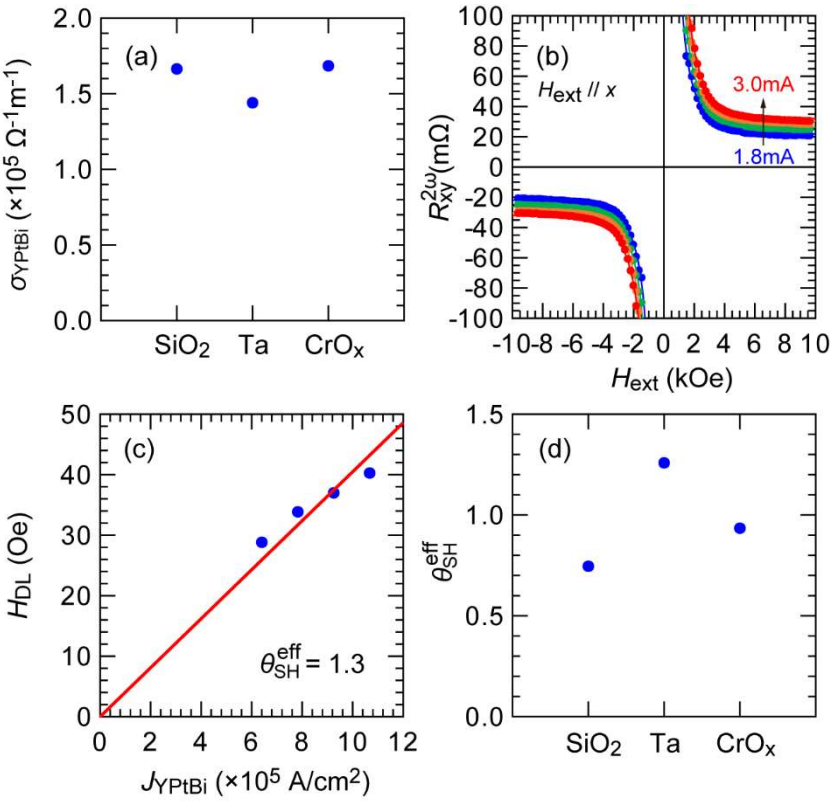

Figure 8.4. (a) Buffer layer dependence of conductivity for SiO_2-, Ta-, and CrO_x-samples. (b) Representative high-field second harmonic Hall resistance data for Ta-sample measured by alternating bias currents of 1.8, 2.2, 2.6, and 3.0 mA. Dots and solid curves are the experimental data and fitting using equation (8.1), respectively. (c) Relationship between the extracted values of H_{DL} and J_{YPtBi} for Ta-sample. (d) Buffer layer dependence of the effective spin Hall angle.

Figure 8.4(a) shows the electrical conductivities σ_{YPtBi} of the 10 nm-thick YPtBi layers, which were calculated from the four-terminal resistance of the whole stacks and that of the CoPt controlled stacks. These values of 10^5 $\Omega^{-1}m^{-1}$ were one order higher than the typical value of 10 nm-thick sputtered YPtBi film grown on c-Sapphire due to higher carrier density. We evaluated θ^{eff}_{SH} by using the high-field second harmonic technique with an alternating current at 259.68 Hz at room temperature. When we applied H_{ext} higher than H^{eff}_{k} along the x-direction, the second harmonic Hall resistance $R^{2\omega}_{xy}$ is given by,[7,8]

$$R_{xy}^{2\omega}=\frac{R_{AHE}}{2}\frac{H_{DL}}{|H_{ext}|-H_k^{eff}}+\alpha_{ONE}|H_{ext}|+R_{ANE+SSE}, \quad (8.1)$$

Here, fitting parameters are H_{DL}, H_k^{eff}, α_{ONE}, and $R_{ANE+SSE}$. Figure 8.4(b) shows a representative high-field second harmonics data for the Ta-sample and the corresponding fitting using equation (8.1) at bias currents of 1.8, 2.2, 2.6, and 3.0 mA, where the dots and solid curves are the experimental data and fitting curves, respectively. Figure 8.4(c) shows the relationship between the extracted values of H_{DL} and the current density in the YPtBi layer J_{YPtBi} for Ta-sample. θ_{SH}^{eff} can be obtained from the slope of H_{DL}/J_{YPtBi} by,

$$\theta_{SH}^{eff}=\frac{2eM_S t_{CoPt}}{\hbar}\frac{H_{DL}}{J_{YPtBi}}, \quad (8.2)$$

where, M_S and t_{CoPt} are 426 emu/cc and 2.4 nm, respectively. Large θ_{SH}^{eff} of 1.3 was obtained in the Ta-sample. Figure 8.4(d) shows the buffer layer dependence of θ_{SH}^{eff}. Ta-sample shows the largest θ_{SH}^{eff} among them thanks to its high crystallinity. Note that the Ta-sample shows not only large θ_{SH}^{eff} (> 1) but also high σ_{YPtBi} of 1.4×10^5 $\Omega^{-1}m^{-1}$ at the same time. Such a high conductivity of 10^5 $\Omega^{-1}m^{-1}$ is very important to minimize the power consumption for SOT-MRAM because a spin Hall layer also works as a bit line, and thus, low conductive spin Hall materials causes large power dissipation there.[9] One can also confirm that their effective spin Hall conductivity σ_{SH}^{eff} of $1.2-1.8\times10^5$ $\hbar/2e$ $\Omega^{-1}m^{-1}$ are comparable to that in YPtBi films on c-Sapphire substrates, despite their poor crystallinity. These results indicate the robustness of the SHE originated by TSS in YPtBi.

8.4 Pulse current induced magnetization switching by using YPtBi on SiO_2 / Si

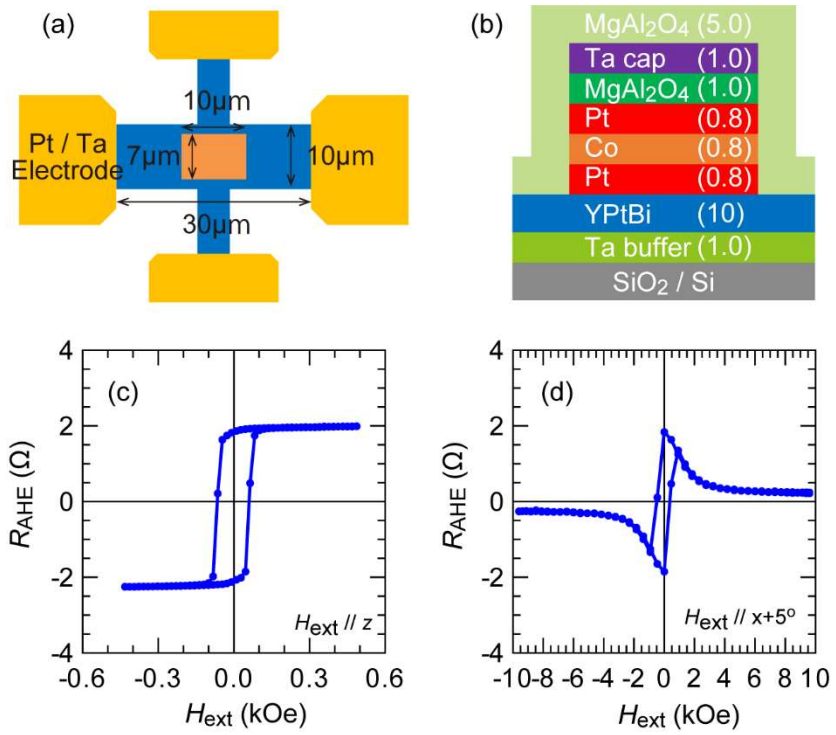

Figure 8.5. (a) Schematic illustration of Hall bar structure for SOT switching. (b) Cross-sectional image at the center of the Hall bar device, where the number for each layer is layer thickness in nm. (c), (d) Anomalous Hall resistance for Ta-sample patterned into the Hall bar structure with H_{ext} applied along the z- and x+5°-direction, respectively.

Next, we demonstrate the pulse current induced SOT magnetization switching in Ta-sample. For this purpose, we fabricated a small Hall bar device with a ferromagnetic pillar on top of YPtBi. Figures 8.5(a) and (b) show a schematic illustration of the Hall bar structure and cross-sectional stacking image at the center of the Hall bar device, respectively. Here, the size for the main Hall bar (blue region in Figure 8.5(a)) is 10 μm-width and 30 μm-effective length, where the effective length is determined by the distance between Pt/Ta electrodes. The size for the

ferromagnetic pillar (orange region in Figure 8.5(a)) is 7 μm-width and 10 μm-length. Figures 8.5(c) and (d) show the anomalous Hall resistance with H_{ext} applied along the z-direction and the x+5°-direction (the x-direction is parallel to the current), respectively. Because the CoPt layer was formed into the pillar in this device, the amplitude of the anomalous Hall resistance was reduced because less current flows into the CoPt layer with smaller width. The effective magnetic anisotropy field H_k^{eff} for this device was 1.4 kOe, whereas that of the Ta-sample for the second harmonic measurement was 2.0 kOe. This degradation may come from additional damages during the ion-milling and heating processes.

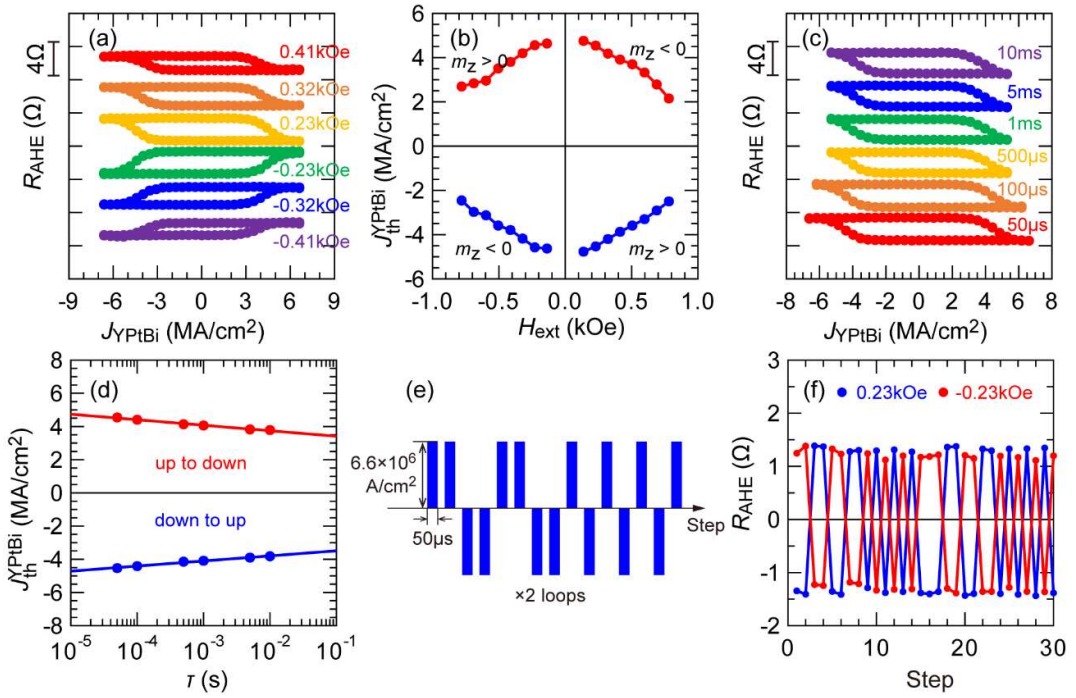

Figure 8.6. Pulse current-induced SOT magnetization switching in Ta-sample. (a) SOT magnetization switching with various in-plane H_{ext} (-0.41 to 0.41 kOe) applied along the *x*-direction. (b) Threshold switching current density in YPtBi as a function of H_{ext}. (c) SOT magnetization switching at various pulse width ranging from 50 μs to 10 ms wit H_{ext} of 0.23 kOe. (d) Threshold switching current density in YPtBi as a function of pulse width, where dots are experimental data and solid lines show fitting results given by the thermal fluctuation model. (e) Random pulse sequence of 30 pulses with the current density in YPtBi of 6.6 MA/cm^2 and the pulse width of 50 μs. (f) Anomalous Hall resistance data measured under an in-plane bias field of -0.23 and 0.23 kOe with random pulse sequence.

Figure 8.6(a) shows the current-induced SOT magnetization switching with the pulse width τ of 50 μs and various H_{ext} applied along the *x*-direction. The SOT switching with Pt-type polarity was observed which is consistent with the previous chapters. Figure 8.6(b) shows the threshold current density J_{th}^{YPtBi} as a function of H_{ext}. Low J_{th}^{YPtBi} on the order of 10^6 A/cm^2 were achieved for entire H_{ext}, which are one order of magnitude smaller than that in Pt with CoPt ferromagnetic layer at 100 ms pulse

current.[10] Here, the total current density including the shunting current in the CoPt layer is still on the order of 10^6 A/cm^2 thanks to the high current flow ratio of 44% in the YPtBi layer with high σ_{YPtBi}. Figures 8.6(c) and (d) show the pulse current-induced SOT switching with H_{ext} of 0.23 kOe applied along the x-direction and J_{th}^{YPtBi} as a function of τ, respectively. By considering the thermal fluctuation model with the attempt frequency associated with the magnetization of 10 GHz,[11,12] we obtained the thermal stability factor Δ of 46 which is larger than that for the MgO/CoFeB system (~38). We then conducted repeating SOT switching by pulse currents with J_{YPtBi} of 6.6×10^6 A/cm^2 and τ of 50 μs. Figure 8.6(e) shows the random sequence of applied pulse currents. Totally 60 of pulse currents were applied. Figure 8.6(f) shows the Hall resistance data with H_{ext} = 0.23 kOe applied along the x-direction. Robust switching was successfully observed by using YPtBi grown on SiO_2/Si substrate.

8.5 Benchmark of spin Hall materials grown by sputtering on SiO_2 / Si substrate

Table 8.1. Comparison of σ, θ_{SH}^{eff}, BEOL compatibility and normalized switching power consumption P_N for spin Hall materials deposited by sputtering on SiO_2/Si substrate. The bi-layer model is assumed for P_N calculation, where the thickness of the spin Hall layer is 4 nm for heavy metals and 10 nm for topological materials, and the thickness and conductivity of CoFeB layer are 1 nm and 6×10^5 $\Omega^{-1}m^{-1}$, respectively.

Materials	σ ($\Omega^{-1}m^{-1}$)	$\lvert\theta_{SH}^{eff}\rvert$	BEOL compatibility	P_N
Ta[14]	5.3×10^5	0.15	○	1
Pt[15]	4.2×10^6	0.08	○	3.6×10^{-1}
W[16]	4.7×10^5	0.3	○	2.9×10^{-1}
Bi_xSe_{1-x}[17]	5.5×10^4	2.9	×	1.7×10^{-2}
BiSb[18]	1.0×10^5	2.4	×	1.0×10^{-2}
YPtBi (this work)	1.4×10^5	1.3	○	2.3×10^{-2}

Finally, we compared the switching power consumption for typical spin Hall materials grown on SiO_2/Si substrates by using the sputtering method. Table 1 summarizes σ, θ_{SH}^{eff}, BEOL compatibility and the normalized switching power consumption P_N. To calculate the P_N, we assumed a bi-layer model of a spin Hall layer (thickness t = 4 nm for heavy metals and t = 10 nm for topological materials) and CoFeB (thickness t_{FM} = 1 nm and $\sigma_{CoFeB} = 6\times10^5$ $\Omega^{-1}m^{-1}$),[13] where the switching power consumption is proportional to $(\sigma t + \sigma_{FM}t_{FM})/(\sigma t\theta_{SH}^{eff})^2$ in this model. As

shown in Table 8.1, sputtered YPtBi has the same potential as the conventional topological materials in term of low power consumption, and has better compatibility with BEOL processes. Furthermore, YPtBi can reduce the switching power of 92% comparing with W which is a well-known heavy metal for SOT devices, demonstrating the advantage of YPtBi-based spintronic devices.

8.6 Summary

In this chapter, we have investigated the SHE in YPtBi deposited by the sputtering technique on SiO_2/Si substrates. Although the crystallinity of YPtBi on SiO_2 substrate was degraded from those deposited on c-Sapphire, the spin Hall conductivity was maintained, which may be attributed to the robustness of the TSS. By using the 1 nm-thick Ta buffer layer, we successfully obtained not only large $\theta_{\mathrm{SH}}^{\mathrm{eff}}$ of 1.3 but also high conductivity of 1.4×10^5 $\Omega^{-1}\mathrm{m}^{-1}$ which is a desirable feature for low power SOT-MRAM. Our results demonstrate the feasibility of YPtBi-based SOT devices such as SOT-MRAM and racetrack memory on SiO_2/Si substrate.

8.7 References

1 Z. K. Liu, L. X. Yang, S.-C. Wu, C. Shekhar, J. Jiang, H.F. Yang, Y. Zhang, S.-K. Mo, Z. Hussain, B. Yan, *et al*, Nat. Commun. **7**, 12924 (2016).

2 X.-G. Zhu, M. Stensgaard, L. Barreto, W. S. Silva, S. Ulstrup, M. Michiardi, M. Bianchi, M. Dendzik, and P. Hofmann, New J. Phys. **15**, 103011 (2013).

3 M.-H. Nguyen, D. C. Ralph and R. A. Buhrman, Phys. Rev. Lett. **116**, 126601 (2016).

4 Y. Wang, P. Deorani, X. Qiu, J. H. Kwon, and H. Yang, Appl. Phys. Lett. **105**, 152412 (2014).

5 N. H. D. Khang, S. Nakano, T. Shirokura, Y. Miyamoto, and P. N. Hai, Sci. Rep. **10**,

12185 (2020).

[6] N. H. D. Khang and P. N. Hai, Appl. Phys. Lett. **117**, 252402 (2020).

[7] M. Hayashi, J. Kim, M. Yamanouchi and H. Ohno, Phys Rev. B **89**, 144425 (2014).

[8] C. O. Avci, K. Garello, M. Gabureac, A. Ghosh, A. Fuhrer, S. F. Alvarado and P. Gambardella, Phys. Rev. B **90**, 224427 (2014).

[9] X. Li, S.-J. Lin, M. DC, Y.-C. Liao, C. Yao, A. Naeemi, W. Tsai, and S. X. Wang, IEEE J. Electron Devices Soc. **8**, 674–680 (2020).

[10] B. Jinnai, C. Zhang, A. Kurenkov, M. Bersweiler, H. Sato, S. Fukami, and H. Ohno, Appl. Phys. Lett. **111**, 102402 (2017).

[11] W. T. Coffey, and Y. P. Kalmykov, J. Appl. Phys. **112**, 121301 (2012).

[12] R. H. Koch, J. A. Katine, and J. Z. Sun, Phys. Rev. Lett. **92**, 088302 (2004).

[13] T. Fan, N. H. D. Khang, S. Nakano, and P. N. Hai, Sci. Rep. **12**, 2998 (2022).

[14] L. Liu, C.-F. Pai, Y. Li, H. W. Tseng, D. C. Ralph, and R. A. Buhrman, Science **336**, 555 (2012).

[15] L. Liu, T. Moriyama, D. C. Ralph, and R. A. Buhrman, Phys. Rev. Lett. **106**, 036601 (2011).

[16] C.-F. Pai, L. Liu, Y. Li, H. W. Tseng, D. C. Ralph, and R. A. Buhrman, Appl. Phys. Lett. **101**, 122404 (2012).

[17] M. DC, R. Grassi, J. Y. Chen, M. Jamali, D. R. Hickey, D. Zhang, Z. Zhao, H. Li, P. Quarterman, Y. Lv, M. Li, A. Manchon, K. A. Mkhoyan, T. Low and J. P. Wang, Nat. Mater. **17**, 800 (2018).

[18] T. Fan, N. H. D. Khang, T. Shirokura, H. H. Huy, and P. N. Hai, Appl. Phys. Lett. **119**, 082403 (2021).

Chapter 9. Theoretical study on bias-field-free spin Hall oscillators with an out-of-plane precession mode and improvement of their properties by YPtBi

9.1 Introduction

As introduced in Chapter 1, STOs are promising candidates for next generation microwave generators[1] and neuromorphic computing.[2] Although the oscillation properties for STOs are promising in term of its oscillation frequency and quality factor, their large driving current (requested several tens to several hundred μA at least) caused by their small charge-to-spin conversion efficiency bottleneck because such a large current degrades the reliability of STO.[3]

To deal with the large driving current problem, spin Hall oscillator (SHO) has attracted much attention in recent years.[4-7] Because SHOs utilize the SHE for spin current generation, the charge-to-spin conversion efficiency is much higher than that for STOs in which is given by P (< 1). Furthermore, in principle, SHOs have higher reliability since the driving current does not pass through the insulating layer of MTJ unlike STOs. Until now, several type of SHOs with a MTJ,[4] nanowire,[5] and nanogaps[6,7] have been proposed, and high frequency oscillations like STOs have been successfully obtained. However, all of proposed SHOs request an external magnetic field to obtain stable oscillations because their magnetization trajectory is IPP mode.

In this chapter, we propose and theoretically analyze a two-terminal bias-field-free SHO with OPP mode by solving the LLG equation with macrospin approximation numerically and analytically. Although we focus on a two-terminal version from the viewpoint of the fabrication cost and device size, our analysis is also available to design the three-terminal structures. We show the strategy to improve the

performance of the bias-field-free SHO. Finally, we demonstrate how YPtBi improves the performance of the bias-field-free SHO.

9.2 Proposal of device structure for bias-field-free spin Hall oscillator

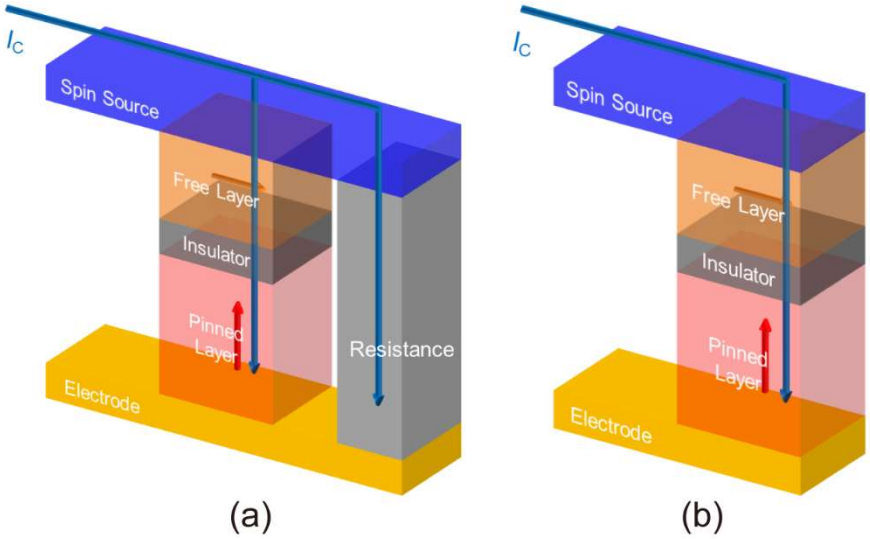

Figure 9.1. Schematic device structures of two-terminal bias-field-free SHO (a) with a parallel resistance, and (b) without a parallel resistance.

Figure 9.1 (a), (b) show two schematic device structures of our proposed two-terminal bias-field-free SHO. The spin Hall layer (spin source) is contact with the free layer of the MTJ. The spin Hall layer is composed of a material having a strong spin-orbit interaction such as HMs and topological materials. The free layer has an in-plane hard axis parallel to the spin polarization vector of the spin current. The pinned layer also has an in-plane hard axis parallel to that of the free layer to maximize the TMR effect. Here, the in-plane component of the charge current in the spin Hall layer plays an important role for the precession excitation because the SHE converts only that into the pure spin current. In the SHO with a parallel resistance as shown in Figure 9.1(a), any spin Hall materials are available since the parallel

resistance provides the in-plane charge current path. Meanwhile, the perpendicular current flowing through the MJT converts the magnetization precession of the free layer into the electrical signal with microwave frequency. Here, we assume that the insulating layer in the MTJ is thick enough so that the perpendicular current is small and the contribution of STT from this current is negligible compared with SOT. On the other hand, by comparing with the previous structure, the in-plane component of charge current is small in the SHO without the parallel resistance as shown in Figure 9.1(b). In this case, small cross-sectional area and/or large θ_{SH} for the spin Hall layer is required to drive it with small current via improving its charge-to-spin conversion efficiency. Here, one can omit the insulating and pinned layer in the MTJ if one uses the microwave stray-field as an output like microwave assisted magnetic recording (MAMR). Then the SHO has simplest structure although output power becomes small.

9.3 Strategy to realize bias-field-free spin Hall oscillator and simulation conditions

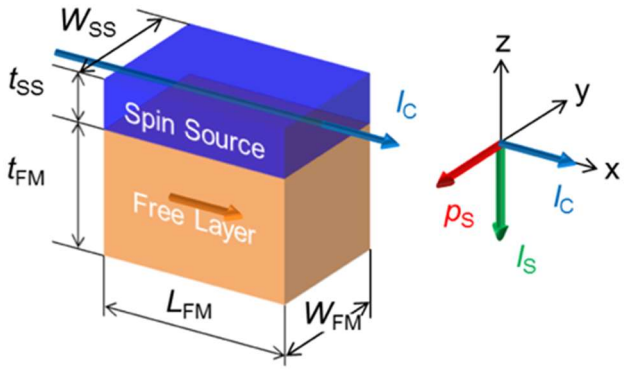

Figure 9.2. Coordination system and simulation parameters. The orange and red arrows show the magnetization of the free and pinned layer, respectively. The blue arrows show the current flow paths.

Table 9.1. Simulation parameters.

Parameters	Values	Parameters	Values
W_{SS} (nm)	10 ~ 19	M_S (emu/cc)	1200
t_{SS} (nm)	2	L_{FM} (nm)	20 ~ 35
θ_{SH}	0.4	W_{FM} (nm)	10 ~ 19
α	0.005	t_{FM} (nm)	20

In case of OPP-STOs, bias-field-free oscillation is achieved by using a demagnetization field as a repulsive force instead of an external magnetic field. To realize such a situation, the spin polarization direction for a spin current is set along the film normal which corresponds to the magnetic hard axis for the free layer. These results imply that one can obtain bias-field-free oscillations by setting the magnetic hard axis parallel to the spin polarization direction even in SHOs.

To check our assumptions, we conducted numerical simulations. The magnetization dynamics in the free layer is governed by the LLG equation with damping-like SOT term,[8,9]

$$\frac{d\boldsymbol{m}}{dt} = -\gamma \boldsymbol{m} \times \boldsymbol{H}_{\mathbf{eff}} + \alpha \boldsymbol{m} \times \frac{d\boldsymbol{m}}{dt} - \gamma H_{\mathrm{DL}} \boldsymbol{m} \times (\boldsymbol{m} \times \boldsymbol{p}_{\mathbf{S}}), \tag{9.1}$$

where γ is the gyromagnetic ratio, α is the Gilbert damping constant, $\boldsymbol{m}$ is the magnetization unit vector, $\boldsymbol{H}_{\mathbf{eff}}$ is the effective magnetic field, $\boldsymbol{p}_{\mathbf{S}}$ is the spin polarization unit vector, and H_{DL} is given by,

$$H_{\mathrm{DL}} = \frac{\hbar \theta_{\mathrm{SH}}}{2eM_{\mathrm{S}} t_{\mathrm{FM}}} \frac{I_{\mathrm{C}}}{t_{\mathrm{SS}} W_{\mathrm{SS}}}, \tag{9.2}$$

where, t_{FM} is the thickness of the free layer, t_{SS} and W_{SS} are the thickness and the width of the spin source, respectively. Here, we first focus on the damping-like SOT term originated from the SHE by ignoring the field-like SOT term originating from the Rashba-Edelstein effect.[10] The general case with both the damping-like and field-like SOT term is discussed in Section 9.6. Figure 9.2 shows the schematic illustration of our simulation target: heterostructure of a spin source and free layers, and the coordination system for our simulation, where W_{FM} and L_{FM} are the width and the length of the free layer, respectively. Here, we assume $W_{SS} = W_{FM}$. When the current flows along the *x*-direction in the spin source, the spin current is injected to the –*z*-direction with the spin polarization along the –*y*-direction. In this setup, bias-field-free oscillation would be realized by setting the magnetic hard axis to the *y*-axis, namely, $N'_y > N'_x, N'_z$ should be satisfied, where N'_x, N'_y and N'_z are the effective anisotropic coefficients with respect to the *x*-, *y*-, and *z*-direction, respectively. N'_x, N'_y and N'_z can be controlled by the shape of the free layer, the bulk crystalline anisotropy, the interfacial anisotropy, among others. Here, we assume that the effective anisotropic coefficients are controlled by only the shape of the free layer without the loss of generality to simplify the simulation. Table 1 shows the simulation parameters. We assume Tungsten (W) for the spin source material,[11] and CoFeB for the free layer material,[12] The shape anisotropy is calculated by using the demagnetizing tensor of a rectangular shape.[13] We emphasize here that the size of the free layer with the rectangular shape assumed in Table 9.1 is for controlling the condition $N'_y > N'_x, N'_z$ poorly by the shape anisotropy, which is for the sake of simplicity and not suitable for realistic devices. In reality, the free layer should be a nano wire along the *x*-direction with the thickness of only a few nm to avoid the

current shunting effect. In this case, we can obtain a large magnetic anisotropy constant K_{uz} along the z-direction by utilizing the bulk crystalline magnetic anisotropy or the interfacial magnetic anisotropy. Similarly, we can obtain a large K_{ux} by using uniaxial strain-induced magnetic anisotropy and field annealing-induced magnetic anisotropy, in addition to shape anisotropy along the x direction. For example, N'_x with the shape anisotropic coefficient N_x and large K_{ux} is given by $N'_x = N_x - K_{ux}/2\pi M_S^2$.

9.4 Numerical simulation and analytical analysis

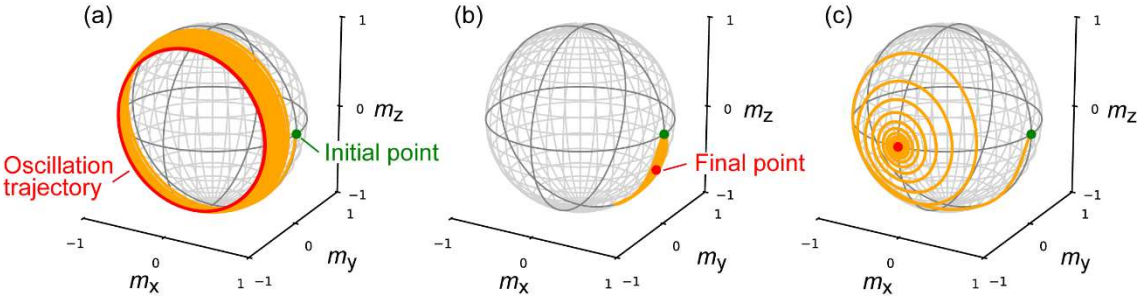

Figure 9.3. Time evolution of the magnetization unit vector *m* when (a) L_{FM} = W_{FM} = 20 nm and t_{FM} = 15 nm at I_C = 2 μA, (b) L_{FM} is changed to 21 nm at I_C = 45 μA, and (c) L_{FM} = 21 nm at I_C = 46 μA. The green points, the orange solid lines, the red solid line, and the red points show the initial points, the trajectories of the magnetization, the oscillation trajectory in a self-oscillation state, and the final points, respectively.

Figure 9.3 (a) shows the time evolution of ***m*** with L_{FM} = t_{FM} = 20 nm and W_{FM} = 15 nm at the constant bias current of I_C = 2 μA. We successfully observed the OPP stable precession around the y-axis without any bias fields and at arbitrary small bias currents. However, such a precession requires the strict condition of L_{FM} = t_{FM}. Figures 9.3(b) and 9.3(c) show the time evolution of ***m*** when L_{FM} is slightly changed to 21 nm at I_C = 45 μA and 46 μA, respectively. As shown in Figures 9.3(b) and 9.3(c),

the magnetization stopped at an equilibrium point (I_C = 45 μA) or immediately relaxed to the –y-direction (I_C = 46 μA) without sustainable oscillation. The same magnetization behaviors were observed at other $L_{FM} \neq t_{FM}$.

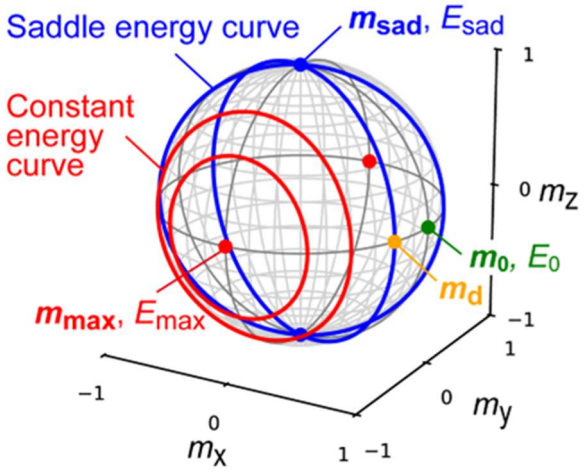

Figure 9.4. Schematic illustration of the constant energy curves and important points in the magnetization unit vector space. Green m_0 and E_0 indicate the initial point and the minimum energy. Blue m_{sad} and E_{sad} indicate the saddle point and the saddle energy curves. Orange m_d indicates the nearest point to m_0 in the saddle energy curves. Red m_{max} and E_{max} indicate the maximum point and maximum energy. Red curves indicate constant energy curves for $E_{max} > E > E_{sad}$.

To understand these behaviors and find a way to obtain OPP stable oscillations in the general case of $L_{FM} \neq t_{FM}$, we analytically solve the time evolution of the energy of the magnetization.[14,15] In the following derivation, we consider the case of $N'_x < N'_z$ ($t_{FM} < L_{FM}$) without the loss of generality. In this situation, one can define the three kinds of typical magnetization energy: the minimum energy E_{min} on the x-axis $\boldsymbol{m}_0 = (\pm 1, 0, 0)$, maximum energy E_{max} on the y-axis $\boldsymbol{m}_{max} = (0, \pm 1, 0)$, and saddle point energy E_{sad} on the z-axis $\boldsymbol{m}_{sad} = (0, 0, \pm 1)$. Then, we found that OPP

stable precession is obtained at $E_{max} > E > E_{sad}$, whose constant energy curves are shown by red curves in Figure 9.4(a). This condition is consistent with that for the STO's oscillation condition for the OPP mode with a bias-field.[14] Next, we calculate the current required for OPP stable precessions. The time evolution of the magnetization energy traveling from the initial state $\boldsymbol{m_0} = (\pm 1, 0, 0)$ to an arbitrary state is given by,

$$\int_{t_0}^{t} dt' \frac{dE}{dt'} = W_{\mathrm{D}} + W_{\mathrm{DL}} + W_{\mathrm{FL}}. \tag{9.3}$$

Here, the work done by the damping torque W_{D}, the damping-like torque W_{DL}, and the field-like torque W_{FL} are given by,

$$W_{\mathrm{D}} = \gamma \alpha M_{\mathrm{S}} \int_{t_0}^{t} dt' \, [(\boldsymbol{m} \cdot \boldsymbol{H}_{\mathbf{eff}})^2 - \boldsymbol{H}_{\mathbf{eff}}^2], \tag{9.4}$$

$$W_{\mathrm{DL}} = \gamma M_{\mathrm{S}} H_{\mathrm{DL}} \int_{t_0}^{t} dt' \, [(\boldsymbol{m} \cdot \boldsymbol{p}_{\mathbf{S}})(\boldsymbol{m} \cdot \boldsymbol{H}_{\mathbf{eff}}) - \boldsymbol{p}_{\mathbf{S}} \cdot \boldsymbol{H}_{\mathbf{eff}}], \tag{9.5}$$

$$W_{\mathrm{FL}} = -\gamma \alpha M_{\mathrm{S}} H_{\mathrm{DL}} \int_{t_0}^{t} dt' \, \boldsymbol{H}_{\mathbf{eff}} \cdot (\boldsymbol{m} \times \boldsymbol{p}_{\mathbf{S}}). \tag{9.6}$$

Note that the work done by the field-like term is not originated from the field-like SOT due to the Rashba-Edelstein effect but from the damping-like SOT due to the SHE since now we exclude the field-like SOT term. This field-like term appears when we convert the LLG equation into the Landau Lifshitz (LL) equation, while this field-like torque originated from the SHE is weaker than the general field-like torque originated from the Rashba-Edelstein effect. In a self-oscillation state, the average value of the time derivative of the magnetization energy should be zero during a precession period. Hence, the left-hand side of equation (9.3) becomes zero, and then, the current required to excite a self-oscillation on an arbitrary energy curve of $E_{max} > E > E_{sad}$ is given by,

$$I_{\mathrm{C}}(E) = -\frac{2\alpha e M_{\mathrm{S}} t_{\mathrm{FM}} t_{\mathrm{SS}} W_{\mathrm{SS}}}{\hbar \theta_{\mathrm{SH}}} \frac{\oint dt\,[(\boldsymbol{m}\cdot\boldsymbol{H}_{\mathbf{eff}})^2 - \boldsymbol{H}_{\mathbf{eff}}^2]}{\oint dt\,[(\boldsymbol{m}\cdot\boldsymbol{p}_{\mathbf{S}})(\boldsymbol{m}\cdot\boldsymbol{H}_{\mathbf{eff}}) - \boldsymbol{p}_{\mathbf{S}}\cdot\boldsymbol{H}_{\mathbf{eff}}]}, \tag{9.7}$$

where the integral interval is a precession period, and W_{FL} becomes zero in this integral interval. Here, we assume that the magnetization precesses on the constant energy curve, although the actual trajectory of the magnetization has fluctuations around the constant energy curve. This approximation allows us to replace the time integral by the angle integral on the constant energy curve which is derived from the damping-less LLG equation.[16] Then, the integrals of the numerator and the denominator in equation (9.7) are,

$$\oint dt\,[(\boldsymbol{m}\cdot\boldsymbol{H}_{\mathbf{eff}})^2 - \boldsymbol{H}_{\mathbf{eff}}^2]$$

$$= -\frac{16\pi M_{\mathrm{S}}(N'_{\mathrm{y}} - N'_{\mathrm{x}})}{\gamma k}\sqrt{1-p^2}[p^2\mathrm{K}(\beta) + k^2\{\mathrm{E}(\beta) - \mathrm{K}(\beta)\}], \tag{9.8}$$

$$\oint dt\,[(\boldsymbol{m}\cdot\boldsymbol{p}_{\mathbf{S}})(\boldsymbol{m}\cdot\boldsymbol{H}_{\mathbf{eff}}) - \boldsymbol{p}_{\mathbf{S}}\cdot\boldsymbol{H}_{\mathbf{eff}}] = \frac{2\pi p^2}{\gamma k}. \tag{9.9}$$

Therefore, equation (9.7) becomes

$$I_{\mathrm{C}}(E) = \frac{16\alpha e M_{\mathrm{S}}^2 t_{\mathrm{FM}} t_{\mathrm{SS}} W_{\mathrm{SS}}(N'_{\mathrm{y}} - N'_{\mathrm{x}})}{\hbar \theta_{\mathrm{SH}} p^2}\sqrt{1-p^2}[p^2\mathrm{K}(\beta) + k^2\{\mathrm{E}(\beta) - \mathrm{K}(\beta)\}], \tag{9.10}$$

where K(β) and E(β) are the first and second kinds of complete elliptic integral, respectively, k, p, and β are defined as follows

$$k = \sqrt{\frac{N'_{\mathrm{y}} - N'_{\mathrm{z}}}{N'_{\mathrm{y}} - N'_{\mathrm{x}}}}, \tag{9.11}$$

$$p = \sqrt{\frac{N'_{\mathrm{y}} - E/2\pi M_{\mathrm{S}}^2}{N'_{\mathrm{y}} - N'_{\mathrm{x}}}}, \tag{9.12}$$

$$\beta = \frac{p}{k}\sqrt{\frac{1-k^2}{1-p^2}}. \tag{9.13}$$

Then, the oscillation frequency is given by,

$$f(E) = \frac{\pi M_{\mathrm{S}} \gamma k (N'_{\mathrm{y}} - N'_{\mathrm{x}}) \sqrt{1-p^2}}{\mathrm{K}(\beta)}. \tag{9.14}$$

In a self-oscillation state around the *y*-axis, the magnetization energy is larger than the saddle point energy E_{sad}. Therefore, the minimum current for sustainable oscillation around the *y*-axis is given by

$$I_{\mathrm{min}} = \lim_{E \to E_{\mathrm{sad}}} I(E) = \frac{16 \alpha e M_{\mathrm{S}}^2 t_{\mathrm{FM}} t_{\mathrm{SS}} W_{\mathrm{SS}} (N'_{\mathrm{y}} - N'_{\mathrm{x}})}{\hbar \theta_{\mathrm{SH}}} \sqrt{1-k^2}. \tag{9.15}$$

On the other hand, the current at which the magnetization is fully relaxed to –*y*-direction is given by

$$I_{\mathrm{max}} = \lim_{E \to E_{\mathrm{max}}} I(E) = \frac{4\pi \alpha e M_{\mathrm{S}}^2 t_{\mathrm{FM}} t_{\mathrm{SS}} W_{\mathrm{SS}} (N'_{\mathrm{y}} - N'_{\mathrm{x}})}{\hbar \theta_{\mathrm{SH}}} (1+k^2). \tag{9.16}$$

Then, the precession frequency takes a maximum value f_{max},

$$f_{\mathrm{max}} = \lim_{E \to E_{\mathrm{max}}} f(E) = 2 M_{\mathrm{S}} \gamma k (N'_{\mathrm{y}} - N'_{\mathrm{x}}). \tag{9.17}$$

To begin the precession around the *y*-axis, the magnetization must overcome the energy barrier ΔE between the initial and saddle points by the spin torque. The minimum current for overcoming ΔE can be evaluated by solving equation (9.3) with the integral interval from the initial to saddle points. However, the magnetization travels from the initial to saddle points with complicating trajectory, which makes difficult to solve the LLG equation analytically. Here, we approximate the trajectory between the initial and saddle points to the saddle energy curve, whose trajectory is shown by the blue curves in Figure 9.4(a).[14] In the case of $N'_{\mathrm{x}} < N'_{\mathrm{z}}$, the initial point $\boldsymbol{m_0}$ = (1, 0, 0) is replaced by the nearest point on the saddle energy curve $\boldsymbol{m_{\mathrm{d}}}$ = (k, $-\sqrt{1-k^2}$, 0). Then, we obtain following equations,

$$\int_{t_0}^{t} dt' \frac{dE}{dt'} = E_{\mathrm{sad}} - E_0, \tag{9.18}$$

$$\int_{t_0}^{t} dt' \left[(\boldsymbol{m} \cdot \boldsymbol{H_{\mathrm{eff}}})^2 - \boldsymbol{H_{\mathrm{eff}}}^2 \right] = -\frac{4\pi M_{\mathrm{S}} (N'_{\mathrm{y}} - N'_{\mathrm{x}})}{\gamma} k \sqrt{1-k^2}, \tag{9.19}$$

$$\int_{t_0}^{t} dt' \left[(\boldsymbol{m} \cdot \boldsymbol{p}_{\mathbf{S}})(\boldsymbol{m} \cdot \boldsymbol{H}_{\mathbf{eff}}) - \boldsymbol{p}_{\mathbf{S}} \cdot \boldsymbol{H}_{\mathbf{eff}} \right] = \frac{\pi k}{2\gamma}, \tag{9.20}$$

$$\int_{t_0}^{t} dt' \, \boldsymbol{H}_{\mathbf{eff}} \cdot (\boldsymbol{m} \times \boldsymbol{p}_{\mathbf{S}}) = -\frac{\sqrt{1-k^2}}{\gamma} \tag{9.21}$$

By substituting equations (9.18) – (9.21) to equation (9.3) and solving for the current, we obtain

$$I_{\mathrm{cri}} = \frac{8\pi e M_{\mathrm{S}}^2 t_{\mathrm{FM}} t_{\mathrm{SS}} W_{\mathrm{SS}} \left[(N'_{\mathrm{z}} - N'_{\mathrm{x}}) + 2\alpha (N'_{\mathrm{y}} - N'_{\mathrm{x}}) k \sqrt{1-k^2} \right]}{\hbar \theta_{\mathrm{SH}} \left(\pi k + 2\alpha \sqrt{1-k^2} \right)}. \tag{9.22}$$

I_{cri} contains two terms: the energy term which required to overcome ΔE (the first term inside of the square brackets), and the damping term which required to cancel out the damping torque from the demagnetizing field (the second term inside of the square brackets). According to equation (9.22), the energy term has more influence on I_{cri} than the damping term since α is typically much smaller than unity. When $N'_{\mathrm{z}} < N'_{\mathrm{x}}$, N'_{x} and N'_{z} are exchanged in equations (9.8) – (9.22). According to equations (9.15) and (9.22), I_{cri} is always larger than I_{min} at arbitrary$N'_{\mathrm{x}}, N'_{\mathrm{z}} < N'_{\mathrm{y}}$ Furthermore, I_{cri} easily exceeds I_{max} by a small difference between L_{FM} and t_{FM} because I_{cri} is much more sensitive to the change of ΔE than I_{max}, as shown in equations (9.16) and (9.22). These results indicate that the magnetization cannot reach the saddle point when we apply a constant current smaller than I_{cri}, while the magnetization immediately relaxes to the *y*-axis after passing through the saddle point without any stable precession when we apply a constant current larger than I_{cri}, which is consistent with the numerical simulation in Figures 9.3(b) and 9.3(c).

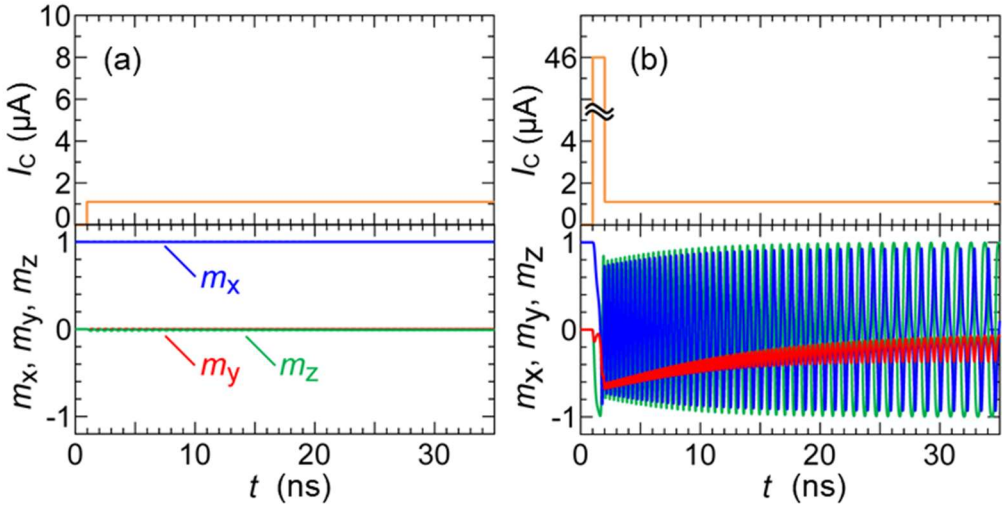

Figure 9.5. Time evolution of the current and the magnetization with (a) only a DC current of 1.1 μA and no initial pulse current, and (b) with a 46 μA pulse current excitation followed by a DC current of 1.1 μA.

Here, one can confirm that I_{min} is always smaller than I_{cri} by taking the ratio of equations (9.15) and (9.22). This relationship indicates that a sustainable oscillation can be obtained even in the case of $L_{FM} \neq t_{FM}$ if the magnetization overcome ΔE once. Such a sequence is possible by applying a very short initial pulse current larger than I_{cri} followed by small constant driving current whose amplitude is $I_{max} > I_C \geq I_{min}$. To check this assumption, we simulate the magnetization dynamics by applying an initial short pulse current with larger amplitude than I_{cri}. Figures 9.5(a) and 9.5(b) show the magnetic dynamics without and with the initial short pulse current at L_{FM} = 21 nm, respectively. The applied DC current in Figures 9.5(a) and 9.5(b) is 1.1 μA, which is larger than I_{min}. Without the short pulse current, the effective precession was not observed because the magnetization could not overcome ΔE. On the other hand, the sustainable OPP around the y-axis was observed by applying the pulse current whose amplitude and pulse width are 46 μA and 1 ns, respectively. Here, the rise and fall times for the pulse current were assumed to be zero. As shown in Figure 9.5(b),

one can realize the stable OPP without any bias-fields even in $L_{FM} \neq t_{FM}$ if the pulse width is longer than the traveling time for the magnetization between the initial to saddle points, which is typically shorter than 1 ns.

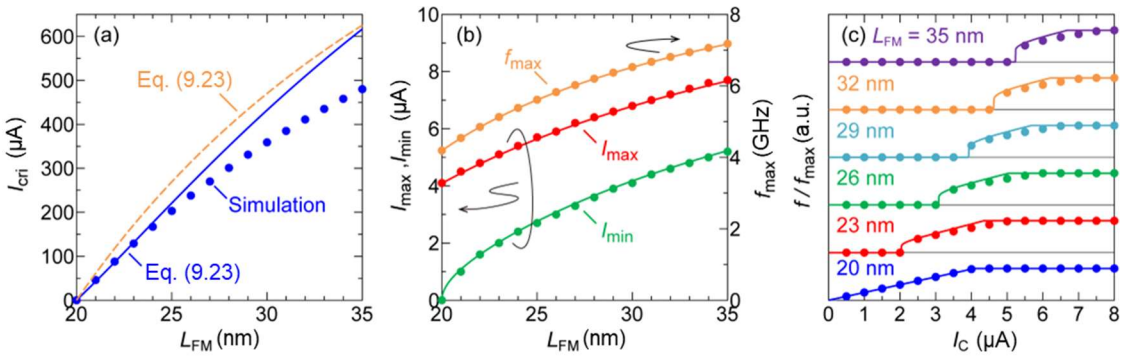

Figure 9.6. L_{FM}-dependence of (a) the critical current I_{cri}, (b) the maximum current I_{max} (red), the minimum current I_{min} (green), and the maximum precession frequency f_{max} (orange), respectively. (c) I_C-dependence of the normalized frequency f / f_{max} with L_{FM} ranging from 20 to 35 nm. The solid and dashed lines show the analytical results, and the dots show the numerical simulation results.

We then checked the validity of equations (9.10) – (9.22) by solving the LLG equation numerically while varying L_{FM} and W_{FM}. Figure 9.6(a) shows L_{FM}-dependence of I_{cri} (blue), and Figure 9.6(b) shows that of I_{max} (red), I_{min} (green), and f_{max} (orange), respectively. The solid lines show the analytical values given by equations (9.15), (9.16), (9.17), and (9.22), and the dots show the numerical simulation results. Here, the simulation results of I_{max}, I_{min}, and f_{max} in the region of $L_{FM} \geq 21$ nm were obtained with the pulse current excitation. For comparison, we also plot another critical current (orange dashed line) by using the torque valance approximation,[17]

$$I'_{\mathrm{cri}} = \frac{4\pi e M_{\mathrm{S}}^2 t_{\mathrm{FM}} t_{\mathrm{SS}} W_{\mathrm{SS}} (N'_{\mathrm{z}} - N'_{\mathrm{x}})}{\hbar \theta_{\mathrm{SH}}}. \tag{9.23}$$

The equation (9.23) says that only the energy term determines I_{cri}, while the damping term also affects I_{cri} in our derived equation (9.22). As shown in Figures 9.6(a) and 9.6(b), I_{cri} rapidly increased with an increase in L_{FM}, and immediately exceed I_{max}, which well explains why there is no oscillation for $L_{\mathrm{FM}} \neq t_{\mathrm{FM}}$. The analytical values are in good agreement with the numerical simulation results for I_{min}, I_{max}, f_{max}. However, equation (9.22) overestimates I_{cri} when L_{FM} is large, whereas equation (9.23) overestimates I_{cri} for entire L_{FM}. This difference between the simulation results and the analytical values of I_{cri} given by equation (9.22) is caused by the invalidity of the saddle energy curve approximation at large L_{FM}, discussed in detailed in the next session. Figure 9.6(c) shows the current dependence of the precession frequency with several L_{FM} ranging from 20 to 35 nm, where the solid lines are analytical values and dots are simulation results. The analytical values are also in good agreement with the simulation results. In the case of $L_{\mathrm{FM}} \neq t_{\mathrm{FM}}$, the magnetization starts to precess at I_{min}, after that, the precession frequency is roughly proportional to the current until it saturates at I_{max}. This current dependence of the precession frequency is consistent with the typical behavior for the bias-field-free OPP mode.[18-21] Note that the precession frequency is strictly proportional to the current in the case of $L_{\mathrm{FM}} = t_{\mathrm{FM}}$, and one can obtain the following relationship from equation (9.10) and equation (9.14), which is useful for design the oscillator,

$$f = \frac{\gamma \hbar \theta_{\mathrm{SH}}}{4\pi \alpha e M_{\mathrm{S}} t_{\mathrm{FM}} t_{\mathrm{SS}} W_{\mathrm{SS}}} I_{\mathrm{C}}. \tag{9.24}$$

9.5 Critical current evaluated by saddle energy curve and torque valance approximations

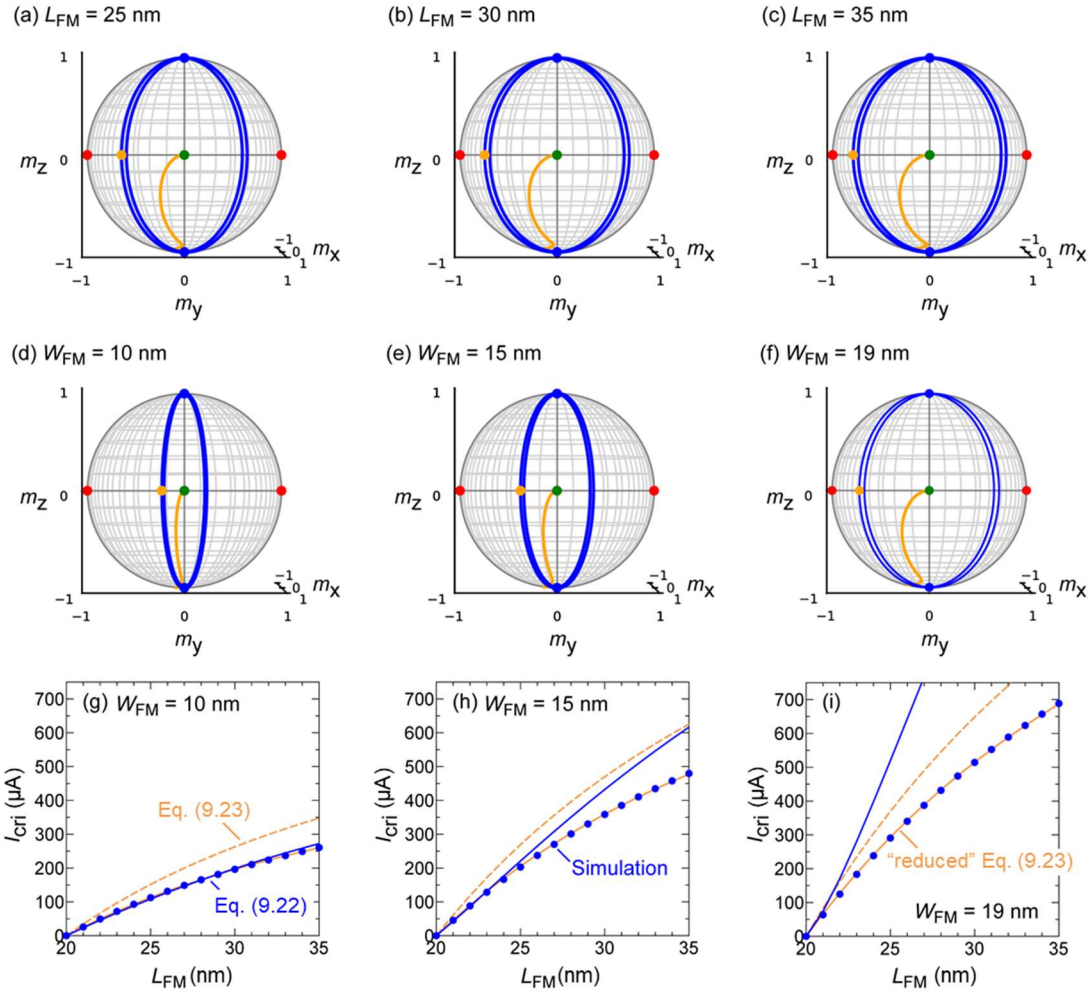

Figure 9.7. Schematic illustrations of (a) – (c) L_{FM}-dependence, and (d) – (f) W_{FM}-dependence of the actual trajectory (orange solid lines) and the saddle energy curves (blue solid lines) in the magnetization unit vector space. The green dot is m_0, the orange dot is m_d, the blue dots are m_{sad}, and the red dots are the maximum energy points. The structure parameters of L_{FM} : W_{FM} : t_{FM} are 25 – 35 nm : 15 nm : 20 nm in (a) – (c), and 21 nm : 10 – 19 nm : 20 nm in (d) – (f), respectively. (g) – (i) L_{FM}-dependence of I_{cri} with W_{FM} = 10, 15, and 19 nm, respectively, L_{FM} = 21 nm, and t_{FM} = 20 nm. The blue dots are the numerical simulation results, the blue solid lines are the analytical values given by equation (9.22), the orange dashed lines are the analytical values given by equation (9.23), and the orange solid lines are the analytical values given by "reduced" equation (9.23).

We have derived the analytical expression of I_{cri} by using the saddle energy curve approximation in Section 9.4. Although this approximation is accurate at small L_{FM}, it is not at large L_{FM}. In the saddle energy curve approximation, the actual trajectory of the magnetization from the initial point $\boldsymbol{m}_0$ to the saddle point $\boldsymbol{m}_{sad}$ is replaced by the trajectory on the saddle energy curves from $\boldsymbol{m}_d$ to $\boldsymbol{m}_{sad}$, where the actual trajectory exists between the saddle energy curves and the *xz*-plane. Figures 9.7(a) – (c) show the schematic illustrations of the actual trajectory (orange solid lines) and the saddle energy curves (blue solid lines) with various L_{FM} of 25 – 35 nm, where the green dot is $\boldsymbol{m}_0$, the orange dot is $\boldsymbol{m}_d$, the blue dots are $\boldsymbol{m}_{sad}$, and the red dots are maximum energy points. Here, we set W_{FM} and t_{FM} to 15 nm and 20 nm, respectively. One can confirm that the difference between the actual magnetization trajectory and the saddle energy curves increase with an increase in L_{FM}, and thus, the saddle energy curve approximation becomes invalid at large L_{FM}.

The validity of the saddle energy curve approximation also depends on W_{FM}. Figures 9.7 (d) – (f) show the schematic illustrations of the actual trajectory and the saddle energy curves with various W_{FM} of 10 – 19 nm, where L_{FM} and t_{FM} are 21 nm and 19 nm, respectively. The difference between the actual magnetization trajectory and the saddle energy curves decreases with decreasing W_{FM} because the saddle energy curves approach to the *xz*-plane. Furthermore, the sensitivity of N_x', N_y', and N_z' to L_{FM} becomes lower when W_{FM} becomes small. Therefore, the validity of the saddle energy curve approximation improves by decreasing W_{FM} even at the large L_{FM}.

Figures 9.7(g) – (i) show the L_{FM}-dependence of I_{cri}, where the blue dots are the numerical simulation results, the blue solid lines are the analytical values given by

equation (9.22), the orange solid lines are the analytical values given by equation (9.23), and the orange dashed lines are the analytical values given by "reduced" equation (9.23), where a "reduction factor", or a constant value of C, is multiplied to equation (9.23) which is discussed below. The analytical values given by equation (9.22) are in good agreement with the simulation results when W_{FM} is small, while those given by equation (9.23) are not.

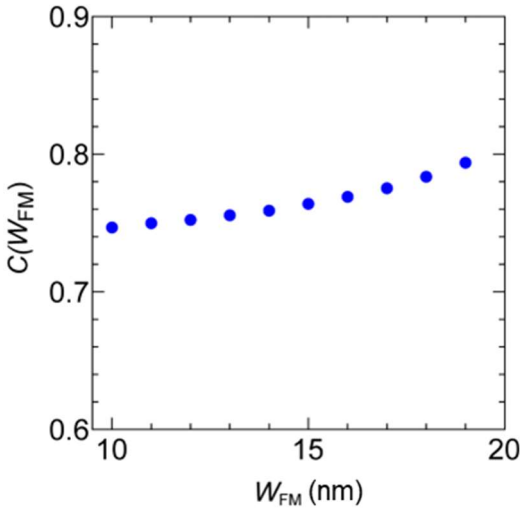

Figure 9.8. W_{FM} dependence of the reduction factor C in the "reduced" equation (9.23).

In contrast, the analytical values given by "reduced" equation (9.23) agree very well with the simulation results for whole L_{FM} and W_{FM}, while the reduction factor C has a W_{FM} dependence, as shown in Figure 9.8. The origin of the reduction factor is seemingly related to the assistance of the precession torque by the demagnetizing field whose contribution was neglected in the derivation process of equation (9.23). Although further investigations are necessary to clarify the origin of the reduction factor, the common point of equations (9.22), (9.23), and "reduced" equation (9.23)

is that the critical current is mainly proportional to ΔE, or $N'_z - N'_x$, and thus, we should reduce the energy imbalance between the *x*- and *z*-axes to reduce the critical current. Therefore, we should design the SHOs so that to have the same effective magnetic anisotropy along the *x*- and *z*-axes. In the ultimate with $N'_x = N'_z$, no I_{cri} is required as shown in Figure 9.3(a).

9.6 Analytical analysis in the general case with both the damping-like and field-like SOT term

In this section, we discuss about the effect of the field-like SOT. The LLG equation with the damping-like and field-like SOT terms is given by,

$$\frac{d\boldsymbol{m}}{dt} = -\gamma \boldsymbol{m} \times \boldsymbol{H}_{\mathbf{eff}} + \alpha \boldsymbol{m} \times \frac{d\boldsymbol{m}}{dt} - \gamma H_{\mathrm{DL}} \boldsymbol{m} \times (\boldsymbol{m} \times \boldsymbol{p}_{\mathbf{S}}) - H_{\mathrm{FL}} \boldsymbol{m} \times \boldsymbol{p}_{\mathbf{S}}, \quad (9.25)$$

By calculating the time evolution of the magnetization energy starting from equation (9.25), one can obtain the following expressions corresponding to equations (9.3) – (9.6).

$$\int_{t_0}^{t} dt' \frac{dE}{dt'} = W_{\mathrm{D}} + W_{\mathrm{DL}} + W_{\mathrm{FL}}. \quad (9.26)$$

$$W_{\mathrm{D}} = \gamma \alpha M_{\mathrm{S}} \int_{t_0}^{t} dt' \, [(\boldsymbol{m} \cdot \boldsymbol{H}_{\mathbf{eff}})^2 - \boldsymbol{H}_{\mathbf{eff}}^2], \quad (9.27)$$

$$W_{\mathrm{DL}} = \gamma M_{\mathrm{S}} (\alpha H_{\mathrm{FL}} + H_{\mathrm{DL}}) \int_{t_0}^{t} dt' \, [(\boldsymbol{m} \cdot \boldsymbol{p}_{\mathbf{S}})(\boldsymbol{m} \cdot \boldsymbol{H}_{\mathbf{eff}}) - \boldsymbol{p}_{\mathbf{S}} \cdot \boldsymbol{H}_{\mathbf{eff}}], \quad (9.28)$$

$$W_{\mathrm{FL}} = \gamma M_{\mathrm{S}} (H_{\mathrm{FL}} - \alpha H_{\mathrm{DL}}) \int_{t_0}^{t} dt' \, \boldsymbol{H}_{\mathbf{eff}} \cdot (\boldsymbol{m} \times \boldsymbol{p}_{\mathbf{S}}). \quad (9.29)$$

Because both H_{DL} and H_{FL} are proportional to a charge current I_{C}, we can solve equation (9.26) in the same manner as equation (9.3). By introducing the coefficients ξ_{DL} and ξ_{FL} defined by $H_{\mathrm{DL}} = \xi_{\mathrm{DL}} I_{\mathrm{C}}$ and $H_{\mathrm{FL}} = \xi_{\mathrm{FL}} I_{\mathrm{C}}$, respectively, we get the following formulas for $I_{\mathrm{C}}(E)$, I_{min}, I_{max}, and I_{cri} in the general case with both damping-like and fied-like SOT terms.

$$I_{\mathrm{C}}(E) = \frac{8\alpha M_{\mathrm{S}}(N'_{\mathrm{y}} - N'_{\mathrm{x}})}{(\alpha\xi_{\mathrm{FL}} + \xi_{\mathrm{DL}})p^2}\sqrt{1-p^2}[p^2\mathrm{K}(\beta) + k^2\{\mathrm{E}(\beta) - \mathrm{K}(\beta)\}], \tag{9.30}$$

$$I_{\mathrm{min}} = \frac{8\alpha M_{\mathrm{S}}(N'_{\mathrm{y}} - N'_{\mathrm{x}})}{\alpha\xi_{\mathrm{FL}} + \xi_{\mathrm{DL}}}\sqrt{1-k^2}, \tag{9.31}$$

$$I_{\mathrm{max}} = \frac{2\pi\alpha M_{\mathrm{S}}(N'_{\mathrm{y}} - N'_{\mathrm{x}})}{\alpha\xi_{\mathrm{FL}} + \xi_{\mathrm{DL}}}(1+k^2), \tag{9.32}$$

$$I_{\mathrm{cri}} = \frac{4\pi M_{\mathrm{S}}\left[(N'_{\mathrm{z}} - N'_{\mathrm{x}}) + 2\alpha(N'_{\mathrm{y}} - N'_{\mathrm{x}})k\sqrt{1-k^2}\right]}{(\alpha\pi k - 2\sqrt{1-k^2})\xi_{\mathrm{FL}} + (\pi k + 2\alpha\sqrt{1-k^2})\xi_{\mathrm{DL}}}. \tag{9.33}$$

According to equation (9.30), the effect of the field-like SOT term is small since α is typically much smaller than unity.

9.7 Improvement of performance for spin Hall oscillator

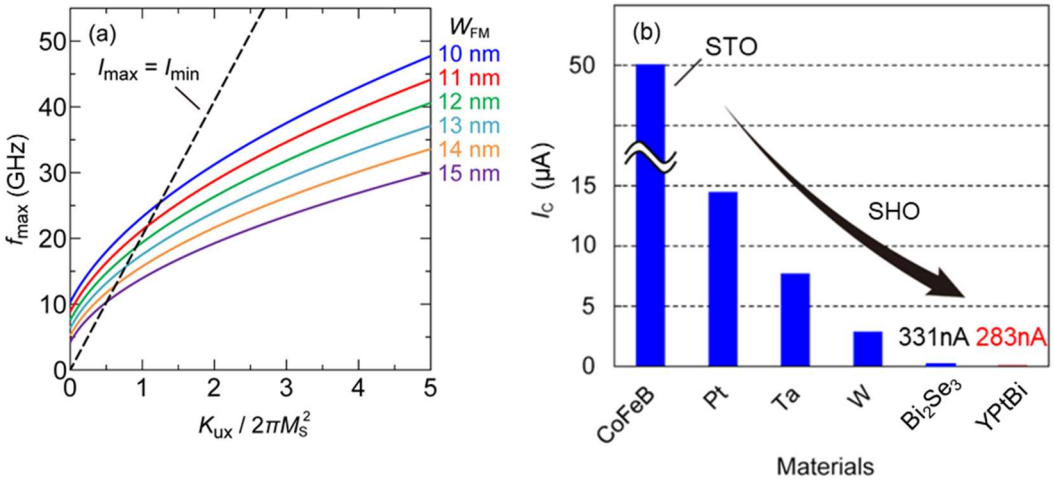

Figure 9.9. (a) Maximum precession frequency f_{max} as a function of the uniaxial crystalline anisotropy K_{ux} along the x-direction with different W_{FM} ranging from 10 to 15 nm. The dashed line shows the condition $I_{max} = I_{min}$. (b) Spin source material dependence of the driving current I_C for our SHOs. I_C for a STO with CoFeB as the spin polarizing layer is also shown for comparison.

The performance of our SHO can be improved by optimizing the materials for the spin source and free layers. First, we demonstrate the improvement of the oscillation frequency. So far, we have used only the shape anisotropy to control the

effective anisotropic coefficients in the above simulations. In this case, the maximum oscillation frequency is limited by the saturation magnetization because the driving force of the precession is only the demagnetizing field. On the other hand, the oscillation frequency can be improved by using the uniaxial bulk crystalline anisotropy and the interfacial anisotropy. Figure 9.9(a) shows the relationship between f_{max} and K_{ux} along the *x*-direction with different W_{FM} ranging from 10 to 15 nm. Here, f_{max} was calculated by using equation (9.17). One can understand this improvement of f_{max} originated from the uniaxial anisotropy by substituting the relationship $N_x' = N_x - K_{ux}/2\pi M_S^2$ into equation (9.14). The dashed line in Figure 9.9(a) shows the line for $I_{max} = I_{min}$, namely, precession cannot be obtained on the right side of this line. However, one can shift the dashed line to the right side by introducing anisotropy along the *z*-direction (for example, by perpendicular crystalline or interfacial magnetic anisotropy) because I_{min} decreases with a decrease in the energy imbalances in the *xz*-plane. Therefore, we can expand the effective precession region and obtain higher frequencies by controlling the magnetic anisotropy.

Although the main concept of our SHO is bias-field-free oscillation, one can improve f_{max} by applying an external magnetic field because it can accelerate the precession. In our setup, an external magnetic field applied along the +*y*-direction can improve f_{max} as follows,

$$f'_{max} = f_{max} + \frac{\gamma}{2\pi} H^y_{ext}. \tag{9.34}$$

or 2.8 GHz per 1 kOe, where H^y_{ext} is an external magnetic field applied along the +*y*-direction. Such an external magnetic field is readily available in MAMR applications because there is a very large magnetic field of ~10 kOe in the gap between the main

pole and the trailing shield of the write-head. Thus, high frequency of 25 GHz or higher is obtainable for MAMR applications with the write gap field of 10 kOe by using our OPP-SHO. Furthermore, I_{cri} decreases by applying small H^y_{ext} thanks to the precession torque from H^y_{ext}. However, large H^y_{ext} also increases I_{cri} because the damping term in equation (9.22) increases, and thus, I_{cri} takes a minimum value as a function of H^y_{ext} due to the trade-off between those effects.

Finally, we demonstrate the reduction of the driving current. In our simulations, we assumed W as a spin Hall material. Although W has the largest θ_{SH} of ~0.4 among HMs, much larger θ_{SH} are available by using topological materials. Figure 9.9(b) shows the comparison of the driving current for 3 GHz oscillation using HMs (W, Pt, Ta) and topological materials (Bi_2Se_3, YPtBi) for the spin source.[11,22-24] The structure of the SHO is assumed W_{SS} : t_{SS} = 15 nm : 2 nm for the spin source, and L_{FM} : W_{FM} : t_{FM} = 20 nm : 15 nm : 20 nm for the free layer. For comparison, we also simulated the bias-field-free OPP-STO with a perpendicular spin polarizing layer. The structure of the STO is assumed L_{FM} : W_{FM} : t_{FM} = 50 nm : 50 nm : 2 nm for the free layer whose volume is almost same with that for the SHO. CoFeB is assumed for the spin polarizing layer of the STO.[12] According to Figure 9.9(b), the driving currents of SHOs with HMs are already smaller than that of the STO. Note that, topological materials including YPtBi effectively reduce the driving currents of SHOs (~100 nA). These ultra-small driving currents improve long-term durability of the SHO, and this comparison also highlights the advantage of YPtBi.

9.8 Summary

In this chapter, we proposed OPP-SHOs which can oscillate without any bias-

fields, by controlling the hard axis. The effective oscillation can be excited at arbitrary situation N'_{x}, $N'_{\mathrm{z}} < N'_{\mathrm{y}}$, by applying an initial short pulse current I_{cri} followed by a small constant current $I_{\mathrm{max}} > I_{\mathrm{C}} > I_{\mathrm{min}}$. We derived analytical equations for I_{cri}, I_{max}, I_{min}, f_{max} and showed that they agreed well with numerical simulation results, indicating that these equations are useful for design of bias-field-free SHOs. Furthermore, we showed how to improve the performance of our SHOs in term of its frequency and drive current. Oscillation frequency can be increased by controlling the magnetic anisotropy, or by applying a magnetic field along the +*y*-direction. Although HMs can reduce drive currents, topological materials, especially YPtBi, can significantly reduce the driving current. Our results pave the way for bias-field-free SHO applications and highlight the high spin Hall performance of YPtBi.

9.9 Appendix

In this section, we derive equations (9.10), (9.14), and (9.22) under the assumption of $N'_{\mathrm{x}} \leq N'_{\mathrm{z}}$. The equations under the condition of $N'_{\mathrm{z}} \leq N'_{\mathrm{x}}$ can be obtained in the same manner. When ***m*** precesses on a constant energy curve of E, the following equations (9.35) and (9.36) should be satisfied.

$$m_{\mathrm{x}}^2 + m_{\mathrm{y}}^2 + m_{\mathrm{z}}^2 = 1, \tag{9.35}$$

$$E = 2\pi M_{\mathrm{S}}^2 (N'_{\mathrm{x}} m_{\mathrm{x}}^2 + N'_{\mathrm{y}} m_{\mathrm{y}}^2 + N'_z m_z^2). \tag{9.36}$$

Here, equation (9.35) is the definition of the magnetization unit vector, and equation (9.36) is the energy conservation under the zero-bias-field. By substituting equation (9.36) to equation (9.35), we obtain the following equations,

$$m_{\mathrm{x}}^2 + k^2 m_{\mathrm{z}}^2 = p^2, \tag{9.37}$$

$$m_{\mathrm{x}} = p \cos u(t)\,, \tag{9.38}$$

$$m_{\mathrm{z}} = \frac{p}{k}\sin u(t)\,, \tag{9.39}$$

$$k = \sqrt{\frac{N'_{\mathrm{y}} - N'_{\mathrm{z}}}{N'_{\mathrm{y}} - N'_{\mathrm{x}}}}, \tag{9.40}$$

$$p = \sqrt{\frac{N'_{\mathrm{y}} - E/2\pi M_{\mathrm{S}}^2}{N'_{\mathrm{y}} - N'_{\mathrm{x}}}}, \tag{9.41}$$

where *u* as a function of time is the angle with respect to the *x*-axis in the *xz*-plane. On the other hand, the dynamics of the magnetization on a constant energy curve is given by the damping-less LLG equation, and thus, the infinitesimal time *dt* is given by,

$$dt = \frac{du}{4\pi M_{\mathrm{S}}\gamma k(N'_{\mathrm{y}} - N'_{\mathrm{z}})m_{\mathrm{y}}} = \frac{-1}{4\pi M_{\mathrm{S}}\gamma k(N'_{\mathrm{y}} - N'_{\mathrm{z}})\sqrt{1-p^2}}\frac{du}{\sqrt{1-\beta^2\sin^2 u}}, \tag{9.42}$$

$$\beta = \frac{p}{k}\sqrt{\frac{1-k^2}{1-p^2}}. \tag{9.43}$$

Here, equation (9.14) can be obtained by integrating equation (9.42) with the integral interval of the one precession period,

$$f(E) = \frac{1}{\oint dt} = -\frac{\pi M_{\mathrm{S}}\gamma k(N'_{\mathrm{y}} - N'_{\mathrm{z}})\sqrt{1-p^2}}{\int_0^{\frac{\pi}{2}} du\,(1-\beta^2\sin^2 u)^{\frac{1}{2}}}. \tag{9.44}$$

Equation (9.10) can be obtained by replacing the integration variable of *t* by *u* in equation (9.7) by using equation (9.42) as follows,

$$\oint dt\,[(\boldsymbol{m}\cdot\boldsymbol{H}_{\mathbf{eff}})^2 - \boldsymbol{H}_{\mathbf{eff}}^2] = -(4\pi M_{\mathrm{S}})^2(N'_{\mathrm{y}} - N'_{\mathrm{x}})^2 p^2(1-p^2)\oint dt\left(1 - \frac{k^2}{p^2}\beta^2\sin^2 u\right)$$
$$= \frac{16\pi M_{\mathrm{S}}(N'_{\mathrm{y}} - N'_{\mathrm{x}})}{\gamma k}\sqrt{1-p^2}\int_0^{\frac{\pi}{2}} du\left(\frac{p^2-k^2}{\sqrt{1-\beta^2\sin^2 u}} + k^2\sqrt{1-\beta^2\sin^2 u}\right), \tag{9.45}$$

$$\oint dt\,[(\boldsymbol{m}\cdot\boldsymbol{p}_{\mathbf{S}})(\boldsymbol{m}\cdot\boldsymbol{H}_{\mathbf{eff}}) - \boldsymbol{p}_{\mathbf{S}}\cdot\boldsymbol{H}_{\mathbf{eff}}]$$
$$= -4\pi M_{\mathrm{S}}(N'_{\mathrm{y}} - N'_{\mathrm{x}})p^2\oint dt\, m_{\mathrm{y}} = -\frac{4p^2}{\gamma k}\int_0^{\frac{\pi}{2}} du\,. \tag{9.46}$$

$$\oint dt\, \boldsymbol{H}_{\mathbf{eff}} \cdot (\boldsymbol{m} \times \boldsymbol{p}_{\mathbf{S}}) = 4\pi M_{\mathrm{S}} (N'_{\mathrm{y}} - N'_{\mathrm{x}}) \frac{p^2}{k} \oint dt \cos u \sin u = 0. \tag{9.47}$$

Equation (9.22) also can be obtained by the same way of integration variable replacement. Because $p = k$ and $\beta = 1$ are held on the saddle energy curve, the integration for equations (9.19), (9.20) and (9.21) becomes very simple as shown below,

$$\int_{t_0}^{t} dt' \, [(\boldsymbol{m} \cdot \boldsymbol{H}_{\mathbf{eff}})^2 - \boldsymbol{H}_{\mathbf{eff}}^2] = -(4\pi M_{\mathrm{S}})^2 (N'_{\mathrm{y}} - N'_{\mathrm{x}})^2 k^2 (1 - k^2) \int_{t_0}^{t} dt' \, (1 - \sin^2 u)$$

$$= \frac{4\pi M_{\mathrm{S}} (N'_{\mathrm{y}} - N'_{\mathrm{x}})}{\gamma} k \sqrt{1 - k^2} \int_{0}^{-\frac{\pi}{2}} du \cos u \,, \tag{9.48}$$

$$\int_{t_0}^{t} dt' \, [(\boldsymbol{m} \cdot \boldsymbol{p}_{\mathbf{S}})(\boldsymbol{m} \cdot \boldsymbol{H}_{\mathbf{eff}}) - \boldsymbol{p}_{\mathbf{S}} \cdot \boldsymbol{H}_{\mathbf{eff}}]$$

$$= -4\pi M_{\mathrm{S}} (N'_{\mathrm{y}} - N'_{\mathrm{x}}) k^2 \int_{t_0}^{t} dt' \, m_{\mathrm{y}} = -\frac{k}{\gamma} \int_{0}^{-\frac{\pi}{2}} du \,, \tag{9.49}$$

$$\int_{t_0}^{t} dt' \, \boldsymbol{H}_{\mathbf{eff}} \cdot (\boldsymbol{m} \times \boldsymbol{p}_{\mathbf{S}}) = 4\pi M_{\mathrm{S}} (N'_{\mathrm{y}} - N'_{\mathrm{x}}) k \int_{t_0}^{t} dt' \cos u \sin u$$

$$= -\frac{N'_{\mathrm{z}} - N'_{\mathrm{x}}}{\gamma (N'_{\mathrm{y}} - N'_{\mathrm{x}}) \sqrt{1 - k^2}} \int_{0}^{-\frac{\pi}{2}} du \frac{\cos u \sin u}{\sqrt{1 - \sin^2 u}}. \tag{9.50}$$

9.10 References

[1] S. I. Kiselev, J. C. Sankey, I. N. Krivorotov, N. C. Emley, R. J. Schoelkopf, R. A. Buhrman, and D. C. Ralph, Nature **425**, 308 (2003).

[2] J. Torrejon, M. Riou, F. A. Araujo, S. Tsunegi, G. Khalsa, D. Querlioz, P. Bortolotti, V. Cros, K. Yakushiji, A. Fukushima, H. Kubota, S. Yuasa, M. D. Stiles, and J. Grollier, Nature **547**, 428 (2017).

[3] Z. Zeng, G. Finocchio, B. Zhang, P. K. Amiri, J. A. Katine, I. N. Krivorotov, Y. Huai, J. Langer, B. Azzerboni, K. L. Wang, and H. Jiang, Sci. Rep. **3**, 1426 (2013).

[4] L. Liu, C.-F. Pai, D. C. Ralph, and R. A. Buhrman, Phys. Rev. Lett. **109**, 186602

(2012).

[5] Z. Duan, A. Smith, L. Yang, B. Youngblood, J. Lindner, V. E. Demidov, S. O. Demokritov, and I. N. Krivorotov, Nat. Commun. **5**, 5616 (2014).

[6] V. E. Demidov, S. Urazhdin, H. Ulrichs, V. Tiberkevich, A. Slavin, D. Baither, G. Schmitz, and S. O. Demokritov, Nat. Mater. **11**, 1028 (2012).

[7] V. E. Demidov, S. Urazhdin, A. Zholud, A. V. Sadovnikov, and S. O. Demokritov, Appl. Phys. Lett. **105**, 172410 (2014).

[8] J. C. Slonczewski, J. Magn. Magn. Mater. **159**, L1 (1996).

[9] L. Berger, Phys. Rev. B **54**, 9353 (1996).

[10] V. M. Edelstein, Solid State Commun. **73**, 233 (1990).

[11] C.-F. Pai, L. Liu, Y. Li, H. W. Tseng, D. C. Ralph, and R. A. Buhrman, Appl. Phys. Lett. **101**, 122404 (2012).

[12] S. Ikeda, K. Miura, H. Yamamoto, K. Mizunuma, H. D. Gan, M. Endo, S. Kanai, J. Hayakawa, F. Matsukura, and H. Ohno, Nat. Mater. **9**, 721 (2010).

[13] A. Aharoni, J. Appl. Phys. **83**, 3432 (1998).

[14] T. Taniguchi, Phys. Rev. B **91**, 104406 (2015).

[15] T. Taniguchi and H. Kubota, Phys. Rev. B **93**, 174401 (2016).

[16] G. Bertotti, I. Mayergoyz, and C. Serpico, *Nonlinear Magnetization Dynamics in Nanosystems* (Elsevier, Oxford, 2009), Chap. 4.

[17] R. Matsumoto and H. Imamura, AIP Adv. **6**, 125033 (2016).

[18] X. Zhu and J. G. Zhu, IEEE Trans. Magn. **42**, 2670 (2006).

[19] D. Houssameddine, U. Ebels, B. Delaet, B. Rodmacq, I. Firastrau, F. Ponthenier, M. Brunet, C. Thirion, J.-P. Michel, L. Perjbeanu-Buda, M.-C. Cyrille, O. Redon, and B. Dieny, Nat. Mater. **6**, 447 (2007).

[20] Y. Zhou, H. Zhang, Y. Liu, and J. Åkerman, J. Appl. Phys. **112**, 063903 (2012).

[21] G. Lv, H. Zhang, X. Cao, Y. Liu, Z. Hou, Y. Qin, G. Li, and L. Wang, AIP Adv. **5**, 077171 (2015).

[22] L. Liu, T. Moriyama, D. C. Ralph, and R. A. Buhrman, Phys. Rev. Lett. **106**, 036601 (2011).

[23] L. Liu, C.-F. Pai, Y. Li, H. W. Tseng, D. C. Ralph, and R. A. Buhrman, Science **336**, 555 (2012).

[24] A. R. Mellnik, J. S. Lee, A. Richardella, J. L. Grab, P. J. Mintun, M. H. Fischer, A. Vaezi, A. Manchon, E.-A. Kim, N. Samarth, and D. C. Ralph, Nature **511**, 449 (2014).

Chapter 10. Conclusion

In this research, an efficient spin source YPtBi with both large θ_{SH} and high thermal stability has been developed, and a spintronic application using YPtBi has also been proposed. Here, the important results are highlighted as follows.

In Chapter 1, we have introduced the background for this thesis. The spin current generation method and spintronic devices were reviewed, and the potential of a pure spin current generated by the SHE was emphasized.

In Chapter 2, we have explained the fundamental phenomena in spin Hall materials such as the spin orbit interaction and the SHE. We then emphasized the importance of the Berry phase on the SHE, and explained that TSSs in topological materials play an important role because their Dirac points are hot spots for Berry phase. We also explained the magnetization dynamics and magnetoresistance in ferromagnetic materials.

In Chapter 3, we have generalized the angle resolved second harmonic technique to include the ONE, and demonstrated that it can disentangle the contribution from SOT, ONE, and ANE/SSE. These results provide an accurate way to precisely estimate SOT in a sample with large H_k^{eff}. The generalized angle resolved second harmonic was applied to CoPt/YPtBi films with strong PMA.

In Chapter 4, we have investigated the SHE and its mechanism in YPt alloy thin films with various resistivity and thickness. It was found that θ_{SH}^{eff} of YPt increased linearly but drastically from 0.045 to 0.081 for a slight increase of ρ_{YPt} from 299 to 331 μΩcm. This strong sensitivity of θ_{SH}^{eff} to ρ_{YPt} was found to be governed by both the intrinsic mechanism and the extrinsic side-jump mechanism with opposite polarity. By deconvoluting the contribution of the intrinsic and extrinsic side-jump mechanisms, the

large intrinsic spin Hall conductivity of 700±100 $\hbar/2e$ $\Omega^{-1}cm^{-1}$ was obtained despite its amorphous structure. Furthermore, we found that spin relaxation length of 0.9 nm for YPt is larger than that expected for a crystallized Pt-based alloy with the same resistivity. Although these unique results are very different from the conventional Pt-based alloys, YPt also cannot realize θ_{SH}^{eff} larger than unity. This result highlighted the importance of the contribution of a TSS to the giant SHE in YPtBi.

In Chapter 5, we have successfully realized an efficient spin source by using a HHA-TSM, YPtBi, having both giant θ_{SH}^{eff} (> 1) and high thermal stability (> 400°C). The YPtBi layers were deposited using the co-sputtering technique, which makes it much easier for industrial adoption. Existence of a TSS in our sputtered YPtBi films was confirmed by using the planar Hall technique. We revealed that the SHE in YPtBi is dominated by the intrinsic SHE from its TSS by evaluating conductivity and thickness dependence of θ_{SH}^{eff}. We also performed current induced SOT switching by using CoPt/YPtBi heterostructure. Thanks to its giant θ_{SH}^{eff}, full switching with ultra-low pulse current density of 10^6 A/cm^2 was demonstrated. Although we focused on YPtBi in this thesis, there are a lot of material combinations since HHA-TSMs include a group of three-element topological materials, and thus, we call for further investigation of the spin Hall performance of this family. Indeed, first principle calculations have suggested at least ten materials in this group. Although the YPtBi thin films in this thesis were deposited using multi target sputtering, bulk single crystal of some bismuthides have been synthesized by the Bi-flux technique, indicating that it is possible to make large single crystal targets of HHA-TSM for mass production. Contrasting to the case of TIs, we found that there is no obvious physical nor technical difficulty for HHA-TSMs to be used in realistic spintronic applications.

In Chapter 6, we have evaluated the SHE in YPtBi while changing the Y/Pt composition ratio r to investigate the effect of stoichiometry on the SHE. We successfully grew highly ordered YPtBi films at r = 0.5– 1.5. Furthermore, the extra carrier density was minimized, and hole mobility was maximized at the exact stoichiometry of r = 1.0, resulting in the minimum σ_{YPtBi}. We achieved a large θ_{SH}^{eff} of 1.7 at r = 1.0, where the power consumption of magnetization manipulation was minimized. We also found that the θ_{SH}^{eff}–σ_{YPtBi} relationship is robust against the change of its stoichiometry unlike the conventional TIs, which is a strong advantage of this alloy for spintronic applications.

In Chapter 7, we have investigated the SHE of YPtBi films grown at lower temperature. When we reduced the growth temperature from 600ºC to 300ºC, both θ_{SH}^{eff} and σ_{SH}^{eff} decrease due to degradation of crystallinity of YPtBi and spin transparency at the interface between CoPt and YPtBi. We then reduced the Ar gas pressure to increase the migration energy of atoms arrived on the surface of YPtBi for 300ºC growth. By improving spin transparency via recovery of interfacial quality, we successfully achieved giant θ_{SH}^{eff} up to 8.2, which is larger than those of most TIs. We demonstrated current-induced SOT magnetization switching with ultralow current density of 10^5 A/cm^2 in the YPtBi layer grown at 300ºC by both DC and pulse currents.

In Chapter 8, we have investigated the SHE in YPtBi deposited by the sputtering technique on SiO_2/Si substrates. Although the crystallinity of YPtBi on a SiO_2/Si substrate was degraded, the spin Hall conductivity was maintained, which may be attributed to the robustness of the TSS. By using the 1 nm-thick Ta buffer layer, we successfully obtained not only large θ_{SH}^{eff} of 1.3 but also high conductivity of 1.4×10^5 Ω^{-1}m^{-1} which is desirable feature for low power SOT-MRAM. Our results successfully demonstrate the feasibility of YPtBi-based SOT devices such as SOT-MRAM and racetrack memory on SiO_2/Si

substrate.

In Chapter 9, we have proposed OPP-SHOs which can oscillate without any bias-fields by controlling the hard axis. The effective oscillation can be excited at arbitrary situation $N'_x,\ N'_z < N'_y$, by applying an initial short pulse current I_{cri} followed by a small constant current $I_{max} > I_C > I_{min}$. We derived analytical equations for I_{cri}, I_{max}, I_{min}, and f_{max}, and showed that they agreed well with numerical simulation results, which indicates that these equations are useful for design of bias-field-free SHOs. Furthermore, we showed how to improve the performance of our SHOs in term of its frequency and drive current. Oscillation frequency can be increased by controlling the magnetic anisotropy, or by applying a magnetic field along the $+y$-direction. Although HMs can reduce driving currents, topological materials, especially YPtBi, can significantly reduce the driving current.

Acknowledgments

First of all, I would like to express my gratitude to my supervisor, Prof. Pham Nam Hai who has greatly supported and guided me with his wisdom, enthusiasm and professionalism in these years. He not only taught me the knowledge and strategy to plan the experiments, but also stimulates my inspiration and supports my academic life. He paid plenty of effort on my way from a rookie to a Ph.D. candidate. His precious advice will forever be invaluable in my future career.

I would like to express my sincere thankfulness to our collaborator Tsuyoshi Kondo from Kioxia corporation for fruitful discussions.

I would like to especially thank Dr. Nguyen Huynh Duy Khang and Dr. Tuo Fan who are always my best friend and support me in this Ph. D. research via fruitful discussions. I have been cheered up and highly motivated thanks to conversations with them.

I would like to thank other members in my Lab, such as Dr. Tinh, Dr. Hiep, Mr. Arakawa, Mr. Nishijima, Mr. Yamane, Mr. Chonan, Mr. Ichimura, Mr. Sou, Mr. Takahashi, Mr. Nakano, Mr. Yu, Mr. Kevin, Mr. Sasaki, Mr. Kumada, Ms. Tao, Mr. Zhang, Mr. Ho, Mr. Fujiwara, Mr. Endo, Mr. Tran, Mr. Osada, Mr. Namba, Mr. Nishiyama, Mr. Takabayashi, Mr. Yamamoto, Mr. Kagami, and Mr. Arikawa, and especially Mr. Kenichiro Yao who had been my tutor in my fourth grade of bachelor course, for their help, technical supports and discussions.

I would like to thank the members of Nakagawa Lab. in Tokyo Institute of Technology who kindly supported me in the experiments structure analysis and magnetic property evaluation.

I wish to express my thankfulness to Mr. Iida, Mr. Suzuki, Mr. Ohta, Mr.

Hatakeyama, and other members in Materials Analysis Division, Open Facility Center for their technical supports in the thin film structure characterization.

I would like to acknowledge the Japan Society for the Promotion of Science (JSPS) Scholarship for their financial support in this Ph. D. study.

Finally, I would like to deeply thank my beloved family for your endless supports and encouragement.

Publications and presentations

Papers

[1] T. Shirokura, and P. N. Hai, "Bias-field-free spin Hall nano-oscillators with an out-of-plane precession mode", J. Appl. Phys. **127**, 103904 (2020).

[2] T. Shirokura, K. Fujiwara, and P. N. Hai, "Spin Hall effect in amorphous YPt alloy", Appl. Phys. Express **14**, 043002 (2021).

[3] T. Shirokura, and P. N. Hai, "Angle resolved second harmonic technique for precise evaluation of spin orbit torque in strong perpendicular magnetic anisotropy systems", Appl. Phys. Lett. **119**, 222402 (2021).

[4] T. Shirokura, T. Fan, N. H. D. Khang, T. Kondo, and P. N. Hai, "Efficient spin current source using a half-Heusler alloy topological semimetal with back end of line compatibility", Sci. Rep. **12**, 2426 (2022).

[5] T. Shirokura, T. Kondo, and P. N. Hai, "Effect of stoichiometry on the spin Hall angle of the half-Heusler alloy topological semimetal YPtBi", Jpn. J. Appl. Phys. **61**, 073001 (2022).

[6] T. Shirokura, and Pham Nam Hai, (under review).

[7] T. Shirokura, N. H. D. Khang, T. Kondo, and P. N. Hai, (under preparation).

Other co-authored papers

[8] T. Fan, M. Tobah, T. Shirokura, N. H. D. Khang, and P. N. Hai, "Crystal growth and characterization of topological insulator BiSb thin films by sputtering deposition on sapphire substrates", Jpn. J. Appl. Phys. **59**, 063001 (2020).

[9] N. H. D. Khang, S. Nakano, T. Shirokura, Y. Miyamoto, and P. N. Hai, "Ultralow power spin–orbit torque magnetization switching induced by a non-epitaxial topological insulator on Si substrates", Sci. Rep. **10**, 12185 (2020).

[10] S. Imai, T. Hamada, M. Hamada, T. Shirokura, I. Muneta, K. Kakushima, T. Tatsumi, S. Tomiya, K. Tsutsui, and H. Wakabayashi, "Importance of Crystallinity Improvement in MoS_2 film just after MoS_2-Compound Sputtering even followed by Post Sulfurization for Chip-Size Fabrication", Jpn. J. Appl. Phys. **60**, SBBH10 (2021).

[11] T. Fan, N. H. D. Khang, T. Shirokura, H. H. Huy, and P. N. Hai, "Low power spin–orbit torque switching in sputtered BiSb topological insulator/perpendicularly magnetized CoPt/MgO multilayers on oxidized Si substrate", Appl. Phys. Lett. **119**, 082403 (2021).

[12] H. Wu, A. Chen, P. Zhang, H. He, J. Nance, C. Guo, J. Sasaki, T. Shirokura, P. N. Hai, B. Fang, S. A. Razavi, K. Wong, Y. Wen, Y. Ma, G. Yu, G. P. Carman, X. Han, X. Zhang, and K. L. Wang. "Magnetic memory driven by topological insulators", Nat. Commun. **12**, 6251 (2021).

[13] N. H. D. Khang, T. Shirokura, T. Fan, M. Takahashi, N. Nakatani, D. Kato, Y. Miyamoto, and Pham Nam Hai. "Nanosecond ultralow power spin orbit torque magnetization switching driven by BiSb topological insulator", Appl. Phys. Lett. **120**, 152401 (2022).

International conferences

[1] T. Shirokura, and P. N. Hai, "Bias-field-free spin Hall oscillator with an out-of-plane precession mode", 2020 Magnetism and Magnetic Materials, Nov. 2020.

[2] T. Shirokura, K. Fujiwara, and P. N. Hai, “Non-conventional spin Hall effect in YPt alloy”, Intermag 2021, Apr. 2021.

[3] T. Shirokura, T. Fan, N. H. D. Khang, and P. N. Hai, “Giant spin Hall effect in a half-Heusler alloy topological semimetal with high thermal stability” 2022 Magnetism and Magnetic Materials, Nov. 2022.

Domestic conferences

[1] T. Shirokura, P. N. Hai, “Bias-field-free spin Hall oscillators with an out-of-plane precession mode”, The 67th JSAP Spring meeting, Mar. 2020.

[2] K. Fujiwara, T. Shirokura, P. N. Hai, “Evaluation of Spin Hall effect in YPt alloy”, The 68th JSAP Spring meeting, Mar. 2021.

[3] 白倉 孝典, ファム ナム ハイ, “角度分解二次高調波法による正確なスピン軌道トルクの定量評価”, PASPS-26, Dec. 2021.

[4] T. Shirokura, P. N. Hai, “Angle resolved second harmonic technique for precise evaluation of spin orbit torque in strong perpendicular magnetic anisotropy systems”, 2022 JSAP Spring meeting, Mar. 2022.

[5] T. Shirokura, T. Fan, N. H. D. Khang, P. N. Hai, “Efficient spin current source using a half-Heusler alloy topological semimetal with Back-End-of-Line compatibility”, 83rd JSAP Autumn meeting, Sept. 2022.

Patents

[1] ファムナムハイ, 白倉孝典. スピンホール発振器および磁気記録デバイス、計算機. 2020/02/21、 特願 PCT/JP2020/007010. 2020/09/10、 特願 WO 2020/179493.

[2] ファムナムハイ, グエン　フィン　ズィ　カン, 白倉孝典. 磁気記録デバイス. 2019/08/21、 特願 2019-151364. 2021/03/01、 特開 2021-034480.

[3] ファムナムハイ, 白倉孝典, 近藤　剛.スピン注入源、磁気メモリ、スピンホール発振器、計算機、及び磁気センサ.2021/8/31、特願 2021-141316.